UNIVERSITAT POLITÈCNICA DE CATALUNYA BARCELONATECH

Gas migration in deep argillaceous formations : Boom clay and indurated clays

Laura Gonzalez-Blanco

UNIVERSITAT POLITÈCNICA DE CATALUNYA
BARCELONATECH

Department of Civil and Environmental Engineering

Thesis submitted within the Doctoral Programme of:

Geotechnical Engineering

Presented by:

Laura Gonzalez-Blanco

Gas migration in deep argillaceous formations: Boom Clay and indurated clays

Supervised by:

Prof. Enrique Romero Morales

Barcelona, March 2017

This research was funded by:

Belgian National Agency for Radioactive Waste and enriched Fissile Material (ONDRAF/NIRAS) through a PhD collaboration agreement with Centre Internacional de Mètodes Numèrics a l'Enginyeria (CIMNE): 'Laboratory investigation of the gas transport processes in a repository located in Boom Clay', ref. XSI/AV/2012-1952, 2012-2016.

“Learn from yesterday,

live for today,

hope for tomorrow.

The important thing is

not to stop questioning”

Albert Einstein

ABSTRACT

Deep geological disposal remains the preferred option at present for the management of long-living and heat-emitting radioactive waste, which consists of confining the waste during a very long period (several hundreds of thousands of years) by placing them in a deep geological formation. Therefore, the understanding of the long-term behaviour of formations is becoming a key issue to ensure the feasibility of the geological disposal facilities, particularly regarding the generation and migration of gases. The present PhD work aims at better understanding the complex hydro-mechanical response of different argillaceous formations to gas migration process. To this end, gas flow through Boom Clay (one of the potential candidate plastic Paleogene clay formations to host nuclear waste in Belgium) has been deeply investigated on the basis of laboratory experiments at different scales and their numerical modelling. This main study has been complemented by presenting tests on two indurated and deeper claystone Mesozoic formations, considered as candidate host rocks in the Swiss programme for deep geological disposal, namely Opalinus Clay and 'Brauner Dogger'.

The different materials have been firstly characterised to evaluate mechanical (compressibility on loading) and two phase flow properties (water retention and permeability). Gas injection tests under oedometer and isotropic conditions have been performed following different testing protocols, in which boundary conditions have been carefully controlled. Major relevance has been given to restore the *in situ* stress state and to ensure full saturation conditions before the gas tests. Special emphasis has been placed in measuring sample deformation along the gas injection and dissipation process. The anisotropy of Boom Clay has been studied by carrying out tests with bedding planes parallel and normal to flow. Air injections have been performed at three different controlled-volume rates. The dissipation stages after shut-off have been also analysed to study air intrinsic permeability changes. Microstructure of samples before and after air injection tests has been evaluated by different techniques: mercury intrusion porosimetry, field-emission scanning electron microscopy and micro-focus X-ray computed tomography.

Gas migration turned out to be a fully coupled hydro-mechanical process. Air injection at constant stress induced expansion of the samples during pressure front propagation and compression during air pressure dissipation. The deformational behaviour was dependent on the injection rate. At slower injection rates expansion occurred during the injection while at higher rates it was delayed in time. Air intrinsic permeability resulted

higher than water permeability suggesting that air flow took place along preferential pathways. Evaluation of the microstructural changes induced by air migration revealed the opening of fissures and allowed quantifying their apertures and separation, as well as their volume and connectivity. Air intrinsic permeability was found to be dependent on the fissured volume.

To complete and better understand the gas transport mechanisms, numerical simulations of the experimental results have been performed using a fully coupled hydro-mechanical finite element code, which incorporates an embedded fracture permeability model to account for the correct simulation of the gas flow along preferential pathways. Clay intrinsic permeability and its retention curve have been made depend on strains through fracture aperture changes. Numerical results not only accounted for the correct simulation of the recorded upstream pressures and outflow volumes and pressures, but also for the volume change behaviour. The experimental and numerical information provided a good insight into the mechanisms of gas transport in deep clay formations and highlighted the role played by the deformational response on the air transport properties of argillaceous rock formations.

Keywords: gas migration; deep argillaceous formations; preferential pathways; microstructural analysis; coupled hydro-mechanical response; embedded fracture modelling.

RESUMEN

El almacenamiento geológico profundo es la solución actualmente aceptada para la gestión de los residuos radioactivos de alta actividad, que consiste en confinar dichos residuos durante un período muy largo de tiempo (varios cientos de miles de años) depositándolos en una formación geológica profunda. De ahí que el entendimiento del comportamiento a largo plazo se esté convirtiendo en una cuestión clave para asegurar la viabilidad de las instalaciones de almacenamiento de residuos, particularmente en lo que respecta a la generación y migración de gases. Este trabajo de doctorado tiene como objetivo mejorar la comprensión en lo que se refiere a la compleja respuesta hidro-mecánica de diferentes formaciones arcillosas frente a procesos de migración de gas. Con este objetivo, el flujo de gas a través de la arcilla Boom Clay (arcilla plástica del paleógeno candidata a alojar los residuos nucleares en Bélgica) se ha investigado en profundidad mediante experimentos de laboratorio a diferentes escalas y su modelación numérica. Este estudio principal se ha complementado con ensayos experimentales en dos formaciones arcillosas del mesozoico (más profundas y endurecidas), posibles candidatas a roca huésped en el programa suizo para el almacenamiento geológico profundo, llamadas Opalinus Clay y 'Brauner Dogger'.

Inicialmente, los diferentes materiales han sido caracterizados para evaluar sus propiedades mecánicas (compresibilidad en carga) e hidráulicas (retención de agua y permeabilidad). Los ensayos de inyección de gas, bajo condiciones edométricas e isótropas, se han realizado siguiendo diferentes protocolos de ensayo controlando cuidadosamente las condiciones de contorno, así como, dando prioridad al hecho de restaurar el estado tensional *in situ* y las condiciones de saturación antes de los ensayos de gas. Además, se ha hecho especial hincapié en la medición de la deformación de las muestras a lo largo de los procesos de inyección y disipación de gas. La anisotropía de la Boom Clay se ha tenido en cuenta realizando ensayos con los planos de estratificación dispuestos en paralelo y perpendicular al flujo. Las inyecciones de aire se han realizado a tres velocidades volumétricas diferentes. Las etapas de disipación se han analizado para evaluar los cambios en la permeabilidad intrínseca al aire. La microestructura de las muestras se ha evaluado antes y después de los ensayos de inyección de aire mediante tres técnicas diferentes: porosimetría de intrusión de mercurio, microscopía electrónica de barrido de emisión de campo y micro-tomografía computarizada.

La migración de gases en estas rocas arcillosas saturadas resultó ser un proceso hidro-mecánico totalmente acoplado. La inyección de aire a tensión constante produjo expansión de las muestras durante la propagación del frente de presión y compresión durante la disipación de la presión de aire. El comportamiento deformacional dependió de la velocidad de inyección. A velocidades de inyección más lentas, la expansión se produjo durante la inyección, mientras que, a velocidades más altas, ésta se retrasó en el tiempo. La permeabilidad intrínseca al aire resultó ser más alta que la permeabilidad al agua medida, lo que sugiere que el flujo de aire tuvo lugar a lo largo de vías preferenciales. La evaluación de los cambios microestructurales inducidos por la migración de aire reveló la apertura de fisuras, cuantificando sus aperturas y separación, así como su volumen y conectividad, lo que permitió encontrar una relación de dependencia entre la permeabilidad intrínseca al aire y el volumen fisurado.

Para completar la información experimental y comprender mejor los mecanismos de transporte de gas, se realizaron simulaciones numéricas de los resultados experimentales utilizando un código de elementos finitos acoplado, que incorpora un modelo de permeabilidad con fracturas embebidas para explicar el flujo de gas a lo largo de vías preferenciales. La permeabilidad intrínseca de la arcilla y su curva de retención dependen de la deformación a través de cambios en la apertura de la fractura. Los resultados numéricos no sólo reprodujeron de forma correcta las presiones registradas y los volúmenes de salida, sino también el comportamiento deformacional. Esta información experimental y numérica proporcionó una buena visión de los mecanismos de transporte de gas en formaciones arcillosas profundas y en los que destacó el papel desempeñado por la respuesta deformacional sobre las propiedades de transporte de aire.

AGRADECIMIENTOS

Quiero aprovechar la oportunidad que me brindan estas líneas para agradecer a todas las personas que, de alguna manera, ya sea en el ámbito científico o en el personal han contribuido a la realización de este trabajo.

En primer lugar, dar las gracias a mi director de tesis, Enrique Romero, por la confianza que ha depositado en mí desde mis comienzos en Barcelona, por su orientación, su atención y su apoyo. También a los profesores e investigadores del Departamento que han sido de gran ayuda en diversas etapas, en especial a Sebastiá Olivella por su inestimable colaboración con los aspectos numéricos de la tesis. Mi sincero agradecimiento a Cristina Jommi por su ayuda y amistad, y por abrirme las puertas durante mi estancia en Delft.

También quiero agradecer la financiación de las instituciones que han hecho posible el desarrollo de esta tesis doctoral, ONDRAF/NIRAS y NAGRA, sobre todo, a las personas que han estado implicadas en los diferentes proyectos: Xavier Sillen, Xiangling Li, Séverine Levaseur y Paul Marschall.

Al personal de secretaria del Departamento y del CIMNE, gracias por la amabilidad y la atención en la realización de todas las gestiones.

Por supuesto, al equipo del laboratorio, a los que siguen y a los que ya se han ido: José, Víctor, Tomás, Rodrigo, Ferrán, gracias por vuestra gran ayuda y por el compañerismo que ha hecho que las horas en el laboratorio se hicieran más amenas.

A mis compañeros de doctorado (no os voy a citar a todos porque seguro que me olvido de alguien) no puedo más que agradecerles la acogida, los buenos ratos, el apoyo en los malos, las horas en la terraza, las risas, los debates, todos esos momentos que hacen que me haya sentido en casa. En especial a Nuria y Roger que ya son parte de familia.

A mis amigos, a los “tullits”, a mi gran familia y muy especialmente a mis padres que siempre han sido un apoyo incondicional, no hay suficientes palabras para expresar mi agradecimiento.

Así que a todos:

Mil gracias!!!

TABLE OF CONTENTS

LIST OF FIGURES

LIST OF TABLES

1 INTRODUCTION

1.1. General context

The current use of nuclear energy in many countries produces radioactive waste presenting risks to humans and the environment. For this reason, this waste should be managed specifically according to their level of radioactivity and their lifetime. While a surface storage is considered for short-lived waste, a burial in shallow and impermeable geological strata is the solution envisaged at present for the management of long-lived and high-level radioactive waste. This solution consists of confining the waste a very long period (several hundreds of thousands of years) by placing them in a geological formation.

Geological Disposal Facility (GDF) (Figure 1-1) is the solution that is internationally accepted as a safer and viable final management of long-lived and high-level radioactive waste. It is based on the capacity of isolation and confinement of geological formations, provided with certain characteristics such as stability, strength (thickness), retention capacity and low permeability. This ability to confinement and isolation is complemented by placing an Engineered Barrier System (EBS) around the radioactive waste.

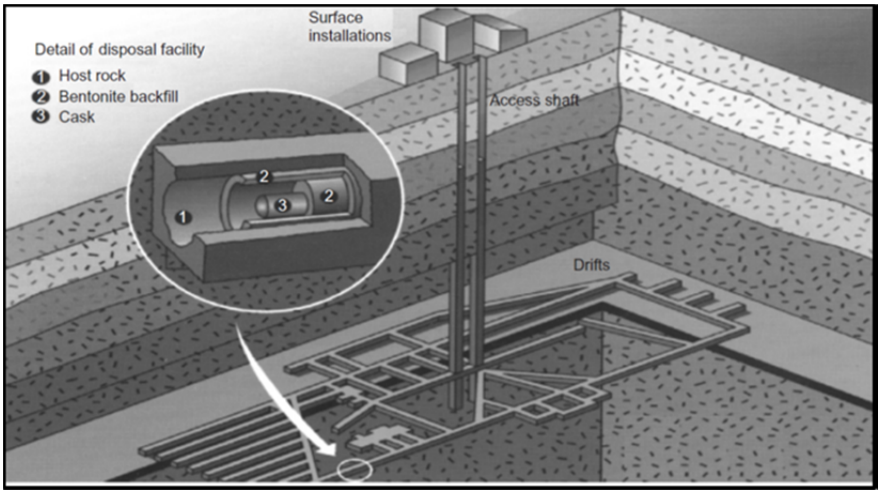

Figure 1-1. Conceptual scheme of deep geological repository for high-level nuclear waste (Gens et al. 2009).

Deep GDF is founded on the so-called multi-barrier principle which consists of a series of barriers between the waste and the biosphere (Figure 1-2). This management method is designed to delay the release and migration of radionuclides on a time scale consistent with their decay period. The multi-barrier design offers several protective layers, natural or artificial, of which the highest level is the geological formation itself. Other barriers in place are vitrified waste packages, the metal canister and any engineered bentonite or cement-based barriers. Each one will impose specific conditions of isolation and retardation, being a redundant system as a whole, resulting in the absence of undesirable impact to men and the environment.

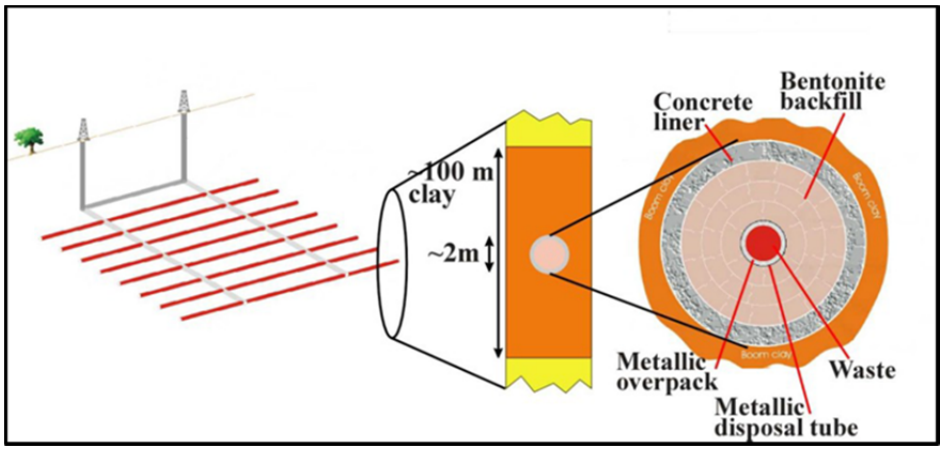

Figure 1-2. Schematic view of the SAFIR2 engineered barrier system for geological disposal of vitrified high-level waste in Boom Clay (ONDRAF/NIRAS 2013).

Nowadays, there are many Underground Research Laboratories (URLs) with the aim of studying *in situ* storage conditions for the radioactive waste located in Belgium, Canada, Finland, France, Sweden, Switzerland, and the United States. Several geological materials meet the requirements for radioactive waste disposal, although the most common are: crystalline rocks (granite, basalt), clays (indurated and plastic clays) and rock salts. In Europe, important research programmes are being carried out in clayey host formations, given their stability and low permeability, in which this Thesis is included.

1.1.1. Context of the investigation

This Thesis arises from the need of two national agencies to increase the knowledge and understanding of some of the candidate geological formations to host the nuclear waste.

ONDRAF/NIRAS (Belgian National Agency for Radioactive Waste and Enriched Fissile Material) in close collaboration with SCK•CEN (Belgian Nuclear Research Centre) and

EIG EURIDICE (European Underground Research Infrastructure for Disposal of nuclear waste In Clay Environment) have proposed Boom Clay as one of the host formations in Belgium. Boom Clay has been deeply studied since 1974. Recent contributions to the coupled Thermo-Hydro-Mechanical (THM) behaviour of this clayey formation under laboratory scale conditions have been published by Le (2008); Cui et al. (2010); Lima (2011); Deng et al. (2011); Andò et al. (2012); Bésuelle et al. (2014); Dao (2015); Nguyen (2013); Prime et al. (2016). The THM coupled response has also been investigated within the context of field-scale experiments carried out at the HADES URL in the site of Mol (François et al. 2009; Chen et al. 2011; Li et al. 2015).

Nagra (Swiss Cooperative for the Disposal of radioactive waste) has proposed six candidate regions for nuclear waste repositories. Most of the research about the THM behaviour of the disposal has been focused on the Mont Terri URL (near St-Ursanne in the Canton of Jura) in which the Opalinus Clay is the host formation (Nagra 2002). However, for the purpose of further site characterization, Nagra has an interest in the acquired data regarding geology, hydrogeology and rock mechanics for the extension of existing regional data bases and modelling of Northern Switzerland, which are used in the framework of its investigations for deep geological disposal of radioactive waste. Among other activities, Nagra took the opportunity to make the investigations in a few geothermal wells which went through the formations of interest. That was the case of the Schlattingen geothermal well, which is intended to provide thermal power for greenhouse farming. The investigations in the Schlattingen borehole included hydro-testing, geophysical logging and stress measurements (Frieg et al. 2015; Vietor et al. 2012). Furthermore, cores were retrieved from the sections of interest, ‘Brauner Dogger’ and Opalinus Clay, for laboratory investigations related to the feasibility of the nuclear waste storage in such indurated clayey rocks (Ferrari et al. 2012; Jahns 2013).

Most of this research work in the aforementioned materials concerns the initial transient processes of hydration under the combined action of the infiltrating water from the host rock and the heat generated by the canister. The experimental information concerning this transient process covers only a short time period of the expected lifetime of an engineered barrier. The long-term behaviour of clay barriers has received comparatively less attention. A significant issue in the long-term performance of clay buffers and the surrounding host rock concerns the generation and migration of gases. Therefore, improving the knowledge in this regard is becoming a keystone to ensure the feasibility of the geological disposal facilities. This PhD Thesis intents to shed light on some of the issues that concern gas migration in argillaceous rock formations.

The Thesis has been funded by ONFRAF/NIRAS through a PhD collaboration agreement with CIMNE entitled “Laboratory investigation of the gas transport processes in a repository located in Boom Clay” (ref. XSI/AV/2012-1952, 2012-2016). The Thesis has also been benefited from experimental work done on deep Opalinus Clay and ‘Brauner Dogger’ performed within the context of different research projects with NAGRA: “Water and air permeability tests on deep core samples from Schlattingen SLA-1 borehole” (NAGRA order 11695 (May 2013) (2013-2014)) whose results are published in NAB 13-51 (Romero & Gómez 2013); “Complementary water and air permeability tests on core samples from Schlattingen SLA-1 borehole” (NAGRA order 11695 (May 2013) (2013-2014)); and “Completion of water and air permeability tests on core samples from Schlattingen borehole” (NAGRA order 13132 (November 2014) (2014-2015)) whose results are published in NAB 15-06 (Romero & Gonzalez-Blanco 2015).

1.1.2. Gas generation

Gas is expected to be generated in underground repositories for radioactive wastes. The generation rates and quantities of gas that are expected to be produced will vary with the waste type and repository concept, but issues arising from gas generation need to be addressed in safety cases for all repositories (Rodwell et al. 2003).

There is general consensus about the mechanisms that may give rise to the generation of significant quantities of gases in repositories and that need to be considered in safety cases: anaerobic corrosion of metals (production of hydrogen); degradation of organic matter (production of methane and carbon dioxide); radiolysis (production of hydrogen, oxygen, carbon dioxide, methane, etc.); steam generation due to the high temperature at the surface of a vitrified high-level radioactive waste (HLW) canister or a spent fuel element; and helium production due to alpha decay. Radioactive gases will also be produced; radioisotopes like ^{129}I, ^{3}H, ^{14}C, and ^{85}Kr might be released as fission or activation products, while radon (^{222}Rn and ^{220}Rn) will be generated as a daughter product of uranium and thorium decay (Ortiz et al. 2002).

It is now generally accepted that the largest gas generation source will be the anaerobic corrosion. The gas generating materials will be principally the waste and their containers, but in some repository concepts, there may also be significant quantities of "construction" steel in the repository, including, for example, rock bolts, gallery linings, abandoned machinery, and concrete reinforcement (Volckaert et al. 1998).

Generally, a rather simple approach is followed in safety assessments for the estimation of the rate of hydrogen production from the corrosion of metals. The rate of gas production is proportional to the rate at which the metal corrodes. This is considered to occur uniformly and is calculated as the product of the corrosion rate constant ($m \cdot a^{-1}$) and the metal surface area (which may change with time, depending on the shape of the metal items in the waste). This is generally considered an appropriate model for long-term metal corrosion under repository conditions; although it may not adequately predict early gas production rates (i.e. the corrosion rates may not be constant, with the initial rates being higher than the long-term rates). Corrosion may occur as both localised and general corrosion. Localised corrosion is generally expected to be relatively more important during aerobic corrosion, because of its small scale, and is expected to be more important for container integrity, because of its potential to cause pitting, than for its contribution to the overall extent of corrosion. For carbon steel and cast iron, rates between 0.1 and 10 $\mu m \cdot a^{-1}$ have typically been used (Rodwell et al. 2003).

Despite the fact that gas generation rates are essential to predict the quantity of gases that might accumulate in the repository, this work will not focus on this issue since the main objective is to shed light on the consequences of gas migration through the host rocks in case the gas pressure increases. To this end, it is required using higher rates than the above-mentioned which allows laboratory testing to study different transport mechanisms.

1.1.3. Phenomenological considerations on gas migration

A crucial aspect of the assessment of the effects of gas generated in a repository is an analysis of how the gas will migrate away from the repository. It is still problematic, as it is not certain that conventional two-phase flow-models are properly applicable to the gas transport mechanisms operating in the clays and mud rocks, currently being investigated as potential repository sites. For these materials, experimental data so far available suggest that gas should be able to enter the rock at pressures below those required for macroscopic fracturing (usually equated with the sum of the minimum principal stress and the tensile strength of the rock). Gas transport through low-permeability rock formations seems to be controlled not only by the hydraulic and mechanical properties of the rock mass (intrinsic permeability, porosity, rock strength), but also by the gas pressure at the generation locus and the hydro-mechanical state of the rock (i.e. water saturation, pore-water pressure, stress state). Phenomenological considerations suggest the following subdivision of the basic transport mechanisms, some of which occur simultaneously (Marschall et al. 2005):

(i) Diffusive transport of gas dissolved in the pore-water: is characterised by two fundamental laws. Fick's law represents the diffusion of dissolved gas due to concentration gradients in the pore-water and Henry's law describes the solubility of gas in pore-water. The transport of dissolved gas occurs even at low (total) gas pressures. The main parameters affecting the transport behaviour of dissolved gas are Henry's coefficient, the diffusion coefficient of gas in water, the tortuosity, the accessible porosity and the hydraulic conductivity. The low hydraulic conductivity of argillaceous rock significantly restricts the efficiency of this transport mechanism.

(ii) Visco-capillary two-phase flow: is described as a transport process whereby pore-water in the pore volume of a rock formation is displaced by gas under the influence of viscous and capillary forces (Bear 1972). In a geomechanical sense, the rock mass behaves like an elastic medium, characterised by the porosity and the rock compressibility. The controlling factor for the two-phase flow characteristics of a porous medium is the gas entry pressure, also known as the capillary threshold pressure, which represents the difference between gas pressure and water pressure needed to displace the pore-water from the initially fully saturated medium. Once the gas entry pressure has been exceeded, the gas mobility is controlled mostly by the intrinsic permeability of the formation, the permeability-saturation relationship (relative permeability) and the relationship between the capillary pressure and the water saturation (suction or water retention curve).

(iii) Dilatancy-controlled gas flow: or "pathway dilation" (terminology after Horseman et al. 1996) is a transport mechanism of special importance for argillaceous media with low tensile strength. Clay-rich rock cannot withstand long-term gas pressures with a magnitude greater than the minimum principal stress acting on the rock mass. Due to the expected microscale variability of the geomechanical rock properties, it even seems plausible that micro-fractures will form before the level of minimum principal stress is reached. The process of gas-driven micro-fracturing leads to an increase of the pore space, which is accompanied by a detectable increase in intrinsic permeability and a change in the capillary pressure-saturation relationship. In the terminology of multiphase flow concepts, gas flow is still controlled by visco-capillary forces (phase interference between wetting and non-wetting fluid); the main difference with respect to conventional two-phase flow is that the transport properties of the solid phase (rock permeability, relative permeability, capillary pressure relationship) can no longer be viewed as invariants since they depend on the state of deformation of the rock.

(iv) Gas transport along macroscopic tensile fractures: a macroscopic tensile fracture (hydro-frac / gas-frac) develops when the gas pressure is larger than the sum of the minimum principal stress and the tensile strength of the rock. The macroscopic fracture is initiated quasi-instantaneously and propagates at about the velocity of a shear wave. Gas flow in such a macroscopic tensile fracture can be seen as a single-phase flow process. Successful hydro-fracs are characterised by a fracture transmissivity which increases the bulk permeability of the treated rock by many orders of magnitude. The conceptual, theoretical and experimental framework for fracture propagation is well documented in standard hydrocarbon exploration literature (Valkó & Economides 1997).

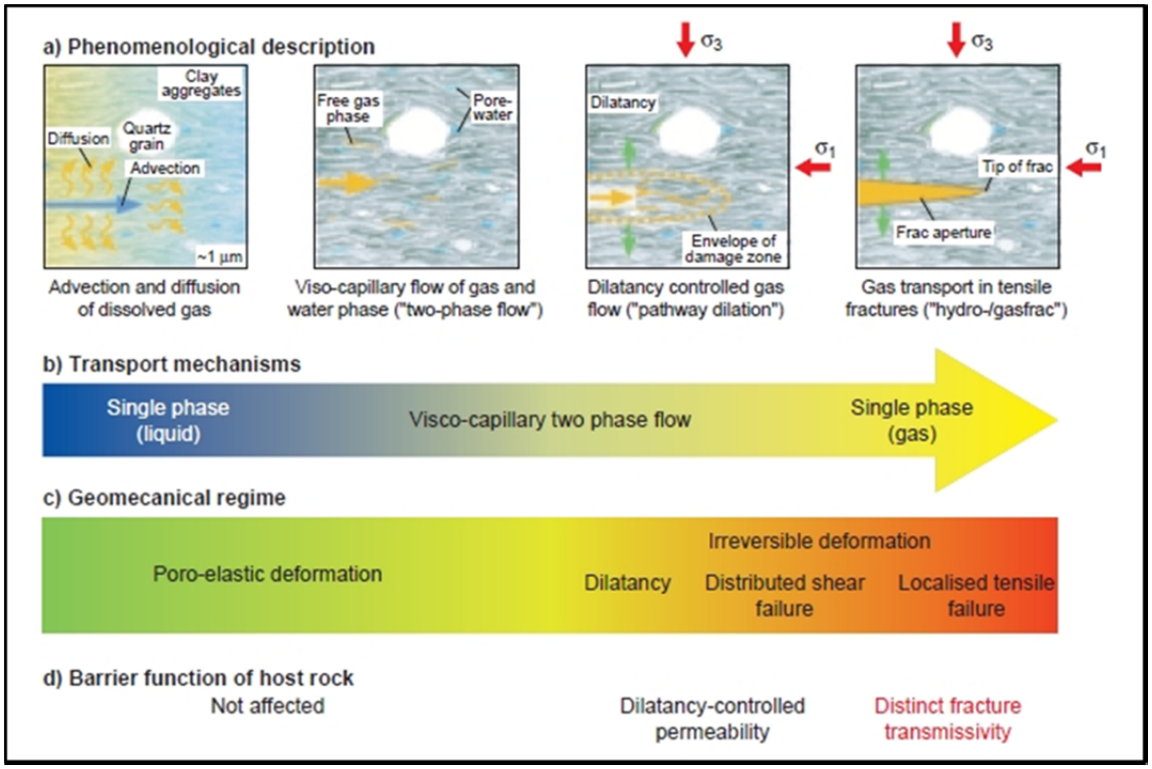

Figure 1-3. Classification and analysis of gas transport processes in Opalinus Clay (Marschall et al. 2005): (a) phenomenological description based on the microstructural model concept; (b) basic transport mechanisms; (c) geomechanical regime; (d) effect of gas transport on the barrier function of the host rock.

As seen in Figure 1-3a, the phenomenological description is inspired by the microstructural conceptualisation of the Opalinus Clay (Nagra 2002). The complex hydro-mechanical processes are decomposed into a problem of transport of immiscible fluids (Figure 1-3b) and a geomechanical problem (Figure 1-3c). The effect of gas transport on the hydraulic barrier function of the rock is highlighted for each of the transport mechanisms (Figure 1-3d), and thus, most interest is focused on

understanding the process and mechanisms governing the advective transport of gas before a macroscopic tensile fracture will develop (mechanisms ii and iii).

1.2. Motivation

There is now a growing body of evidence (Shaw 2013) that in the case of saturated plastic clays with low diffusion coefficients and subjected to high gas pressures, classic concepts of porous-medium two-phase flow are inappropriate to explain the gas transport processes. Migration of gas in low permeability rock formations is a rather complex phenomenon, governed by different coupled mechanical and hydraulic processes which are not fully understood, especially referred to flow through dilatant pathways. Therefore, coupled hydro-mechanical experimental tests in which gas migration is investigated as well as robust numerical analysis are mandatory to adequately evaluate the long-term safety of the disposal system. The motivation to perform this Thesis arises from the need to present a set of well-posed experimental data, in which the stress state, the orientation of the bedding planes, the deformation of the material during gas injection, the evolution of the microstructure and the paths followed by gas, are key issues to be addressed.

1.3. Objectives

In the long-term of the repositories, gas migration processes, strongly coupled with the hydro-mechanical conditions, will affect the host rocks. This thesis was motivated by the challenging task of better understanding and modelling the gas migration behaviour of argillaceous materials, particularly, Boom Clay, Opalinus Clay and 'Brauner Dogger'. More specifically, the objectives of the PhD research included:

- the exploration and identification of the conditions, main features and significant aspects to be considered in gas migration processes in argillaceous rocks;
- the development of robust test protocols able to reproduce the behaviour of the materials under repository conditions;
- the performance of a set of gas injection/dissipation tests which enables to evaluate the air permeability in nearly saturated materials;
- the investigation of the volume change behaviour during gas injection and dissipation (changes in gas and liquid pressures and their impact on gas permeability);
- the evaluation of the role played by the orientations of the bedding planes of rock in the gas transport process;

- the study of the influence of the gas injection rate in the transport process;
- the analysis of the microstructural changes during the gas injection and dissipation and how it affects the intrinsic permeability due to the formation of preferential pathways;
- the study of the pressurization mechanisms which occur during the gas injection and dissipation through numerical simulations of the experimental results with a coupled thermo-hydro-mechanical code in which an embedded fracture permeability model is included.

1.4. Methodology

This Thesis is fundamentally experimental; nonetheless, also numerical simulations have been performed to complement the experimental information.

To study of deep argillaceous materials a special focus was given to reproducing the *in situ* conditions in order to obtain profitable results. Different hydro-mechanical paths under oedometer and isotropic conditions were performed before gas injection and dissipation experiments with the aim of accounting for the influence of the stress state. Furthermore, different injection rates and orientation of the bedding planes were used and the role played by them in the gas transport process was analysed. Major significance was placed in measuring volume changes during the gas injection and dissipation stages. Also, the evolution of the pore network was followed by means of microstructural techniques such as mercury intrusion porosimetry, micro-focus tomography and field emission scanning electron microscopy. All these experimental data facilitated knowing key properties about gas migration and were used in a numerical analysis to provide a further insight into the local processes, fluxes and pressure evolution, and thus, complement the understanding of gas migration in deep clayey rocks.

1.5. Layout of the Thesis

The manuscript consists of 8 chapters covering the developments achieved during the PhD research. The chapters are organised in a logical sequence, starting with the basic properties of the studied materials followed by a description of their hydro-mechanical behaviour, and progressively addressing the problem of the gas migration, from the laboratory results, through its consequences in the evolution of microstructure to the numerical analysis.

In Chapter 2, the studied materials are characterized. It contains the geological origin of clays, the main geotechnical properties and initial conditions; as well as their *in situ* location and stress state. Also, the pore size distribution and the water retention curves of the intact materials are presented.

Chapter 3 introduces the experimental equipment and protocols used in the tests including an explanation of the selected stress and boundary conditions applied in each test.

Chapter 4 is dedicated to the hydro-mechanical behaviour of the three studied materials. Mechanical properties on loading and unloading are presented together with water permeability measurements.

Chapter 5 is devoted to gas migration experiments showing the results of gas injection and dissipation stages for different protocols. Volume change behaviour during this process is examined in detail. Air permeability evolution, the role played by the bedding orientation and the influence of the injection rate are also addressed.

In Chapter 6, the evolution of the pore network induced by air migration is tracked by using different microscopic experimental techniques. Qualitative and quantitative analysis of the developed fissures is accounted for, together with the effects on the transport properties.

Chapter 7 extends the experimental results to a numerical analysis. The code and basic physic equations are explained in brief. Fissures induced by air passage are taken into account by means of the embedded fracture permeability model (Olivella & Alonso 2008). Initially, a simulation with a pre-defined zone of fracture development is presented. Subsequently, the introduction of heterogeneity using a random porosity filed allows fractures to develop automatically, without the need of a pre-defined zone.

Finally, Chapter 8 contains the main conclusions of the study and outlooks for future works.

1.6. Research activities performed along the PhD Thesis

The research activities carried out during the PhD period are listed chronologically:

- PhD Thesis Proposal defence: “Laboratory investigation of gas transport processes in Boom Clay” within the Doctoral Programme of Geotechnical Engineering, Barcelona, September 26th, 2013.

- Report: Gonzalez-Blanco, L. & Romero, E. Laboratory investigation of gas transport process in Boom Clay. PhD collaboration agreement with ONDRAF/NIRAS (2013-2016). Annual report 1, October, 2013.
- Progress meeting: between ONDRAF/NIRAS and EURIDICE (X. Sillen and X. Li) and CIMNE/UPC (E. Romero and L. Gonzalez-Blanco) in Barcelona, November 8th, 2013.
- Progress meeting: between ONDRAF/NIRAS and EURIDICE (X. Sillen and X. Li) and CIMNE/UPC (E. Romero) in Mol, Belgium, May 16th, 2014.
- Poster: Gonzalez-Blanco, L., Romero, E., Li, X. & Sillen, X. Importance of stress state and material degradation on gas transport processes in Boom Clay. *IGD-TP Geodisposal Conference*, Manchester, UK, June 24th - 26th, 2014.
- Conference paper and oral presentation: Gonzalez-Blanco, L., Romero, E., Li, X. & Sillen, X. Importance of sample volume changes and material degradation on gas transport properties in Boom Clay. *7th International Congress on Environmental Geotechnics*, Melbourne, Australia, November 10th - 14th, 2014. (Speaker: E. Romero)
- Report: Gonzalez-Blanco, L. & Romero, E. Laboratory investigation of gas transport process in Boom Clay. PhD collaboration agreement with ONDRAF/NIRAS (2013-2016). Annual report 2, October, 2014.
- Progress meeting: between ONDRAF/NIRAS and EURIDICE (X. Sillen, X. Li, S. Levasseur and H. Van Baelen) and CIMNE/UPC (E. Romero and L. Gonzalez-Blanco) in Brussels, Belgium, January 16th, 2015.
- Research seminary: Gonzalez-Blanco, L. & Romero, E. Laboratory investigation of gas transport process in Boom Clay. Department of Geotechnical Engineering and Geosciences, Universitat Politècnica de Catalunya, Barcelona, January 22th, 2015. (Speaker: L. Gonzalez-Blanco).
- Oral presentation: Gonzalez-Blanco, L., Romero, E., Li, X. & Sillen, X. Volume change behaviour of Boom Clay during gas injection and dissipation experiments. *6th International Conference in Clays in Naturals and Engineered Barriers for Radioactive Waste Confinement*, Brussels, Belgium, March 23th - 26th, 2015. (Speaker: L. Gonzalez-Blanco).
- Oral presentation: Gonzalez-Blanco, L., Romero, E., Li, X., Sillen, X., Marschall, P. & Senger, R. Gas (air) tests on medium and deep clay formations. *Special Exchange Meeting on Geomechanical Issues. 6th International Conference in Clays in Naturals and Engineered Barriers for Radioactive Waste Confinement*, Brussels, Belgium, March 26th - 27th, 2015. (Speaker: E. Romero).
- Poster: Romero, E., Marschall, P., Gonzalez-Blanco, L. & Gómez, R. Compressibility properties on loading and on air injection of two deep claystone formations. *6th International Conference in Clays in Naturals and Engineered Barriers for Radioactive Waste Confinement*, Brussels, Belgium, March 23th - 26th, 2015.
- Report: Romero, E. & Gonzalez-Blanco L. Nagra Technical Report: Arbeitsbericht NAB 15-06: Complementary water and air permeability tests on core samples from Schlattingen SLA-1 borehole. May 2015.
- Research stay: in Delft University of Technology supervised by Prof. C. Jommi, Delft, The Netherlands, May 1st - July 30th, 2015.

- Oral presentation: Gas migration process in deformable clay formations. *International Symposium on Energy Geotechnics*, Barcelona, Spain, June 2nd - 4th, 2015. (Speaker: E. Romero)
- Report: Gonzalez-Blanco, L. & Romero, E. Laboratory investigation of gas transport process in Boom Clay. PhD collaboration agreement with ONDRAF/NIRAS (2013-2016). Annual report 3 (2015). September, 2015.
- Oral presentation: Romero, E., Gonzalez-Blanco, L., Li, X., Sillen, X., Marschall, P. & Segner, R. Gas Migration and Coupled Hydro-Mechanical Issues in Claystones and Plastic Clay for Radioactive Waste Disposal at Great Depth. *Second EAGE Workshop on Geomechanics and Energy - The ground as energy source and storage*, Celle, Germany, October 13th -15th, 2015. (Speaker: E. Romero)
- Progress meeting: between ONDRAF/NIRAS and EURIDICE (X. Sillen, X. Li, S, Levasseur, H. Van Baelen and C. Guangjing) and CIMNE/UPC (L. Gonzalez-Blanco and E. Romero) in Brussels, Belgium, February 26th, 2016.
- Oral presentation: Romero, E. & Gonzalez-Blanco, L. Exploring air migration in argillaceous formations: experimental results and numerical modelling. *IV International Workshop of Modern Trends in Geomechanics*, Assisi, Italy, May 16th - 18th, 2016. (Speaker: E. Romero)
- Conference paper: Romero, E. & Gonzalez-Blanco, L. Exploring air migration in argillaceous formations: experimental results and numerical modelling. *IV International Workshop of Modern Trends in Geomechanics, G. Viggiani, D. Salciarini, F. Silvestri, C. Tamagnini, G.M.B. Viggiani (Eds)*, Assisi, Italy, May 16th - 18th, 2016.
- Oral presentation and conference paper: Gonzalez-Blanco, L., Romero, E. & Jommi, C. Hydro-Mechanical Modelling of Gas Injection Experiments in Boom Clay. *8th Workshop of CODE_BRIGHT users*, Barcelona, Spain, May 19th, 2016. (Speaker: L. Gonzalez-Blanco).
- Journal paper: Gonzalez-Blanco, L., Romero, E., Jommi, C., Li, X. & Sillen, X. Gas migration in a Cenozoic clay: Experimental results and numerical modelling. *Geomechanics for Energy and the Environment*, 6: 81-100, 2016, DOI: 10.1016/j.gete.2016.04.002.
- Book chapter: Gonzalez-Blanco, L., Romero, E., Li, X., Sillen, X., Marschall, P. & Jommi, C. Air injection tests in two argillaceous rock formations: experimental results and modelling. *Energy Geotechnics. F. Wuttke, S. Bauer & M. Sanchez (Eds)*. Chapter 97: 715-721, 2016 Taylor & Francis Group, London ISBN: 978-1-315-31524-9.
- Oral presentation: Gonzalez-Blanco, L., Romero, E., Li, X., Sillen, X., Marschall, P. & Jommi, C. Air injection tests in two argillaceous rock formations: experimental results and modelling. *1st International Conference on Energy Geotechnics, ICEGT*, Kiel, Germany, August 29th -31st, 2016. (Speaker: L. Gonzalez-Blanco).
- Report: Gonzalez-Blanco, L. & Romero, E. Laboratory investigation of gas transport process in Boom Clay. PhD collaboration agreement with ONDRAF/NIRAS (2013-2016). Annual report 4 (2016). October, 2016.
- Oral presentation: Gonzalez-Blanco, L., Romero, E., Jommi, C. Li, X. & Sillen, X. Exploring fissure opening and its connectivity in a Cenozoic clay induced by gas injection. *International workshop on Advances in Laboratory Testing and Modelling of Soils and Shales*, Villars-sur-Ollon, Switzerland, January 18th -20th, 2017. (Speaker: L. Gonzalez-Blanco).

- Book Chapter: Gonzalez-Blanco, L., Romero, E., Jommi, C. Li, X. & Sillen, X. Exploring fissure opening and its connectivity in a Cenozoic clay during gas injection. Chapter in Springer Series in Geomechanics and Geoengineering, January, 2017 In book*: Advances in Laboratory Testing and Modelling of Soils and Shales (ATMSS)*, 288-295, DOI: 10.1007/978-3-319-52773-4_33.

2
MATERIALS USED IN THE RESEARCH

2.1. Background

The argillaceous rocks are a broad and often complex group of detrital sedimentary deposits which may be generally classified as clays, shales, mudstones, siltstones and marls. They are of interest as potential host rocks for geological disposal of high level waste and spent fuel not only in Europe but also in countries as Japan or United States of America, mainly because of their relatively low permeability, good sorptive characteristics, low solubility and their ability to act in a plastic manner, which makes them self-sealing in certain circumstances.

Currently, within several projects of the European Commission, there are three argillaceous formations that are being studied in detail: The Boom Clay in Belgium, the Opalinus Clay in Switzerland and the Callovo-Oxfordian Clay in France. These clays formation represent a spectrum ranging from clays with a volumetric water content of 40% and relative high plasticity up to a highly consolidated stiff claystone with volumetric water content lower than 12% (Volckaert et al. 2005). This Thesis is mainly focused in Boom Clay; however, complementary studies on two indurated clays from Switzerland, the above mentioned Opalinus Clay and the so-called 'Brauner Dogger' are also included.

This chapter summarises the main properties of the materials used in the research which belong to three different argillaceous formations considered suitable for deep disposal of high-level and/or long-lived radioactive waste.

The chapter is organized in two parts, the first one dedicated to the Boom Clay and the second to the indurated clayey rocks, Opalinus Clay and 'Brauner Dogger'. Each part tackles the following issues: the geological origin of clays and their *in situ* location and stress state; the main geotechnical properties and initial conditions; an explanation about the protocols followed during sample preparation, storage of the samples and the

synthetic water used in the tests; followed by the determination of the pore size distribution and the water retention curves for their intact state.

2.2. Boom Clay

2.2.1. Geological origin of the material

The Boom Clay formation is a marine sediment of the Cenozoic, specifically of Rupelian age (30 My). At the Mol-Dessel nuclear site, the Boom Clay lies 190-290 m below ground level (Figure 2-1). The Boom Clay layer is almost horizontal (it dips 1-2% towards the NE) and water bearing sand layers are situated above and below it. The underground water level is situated more or less at the ground surface.

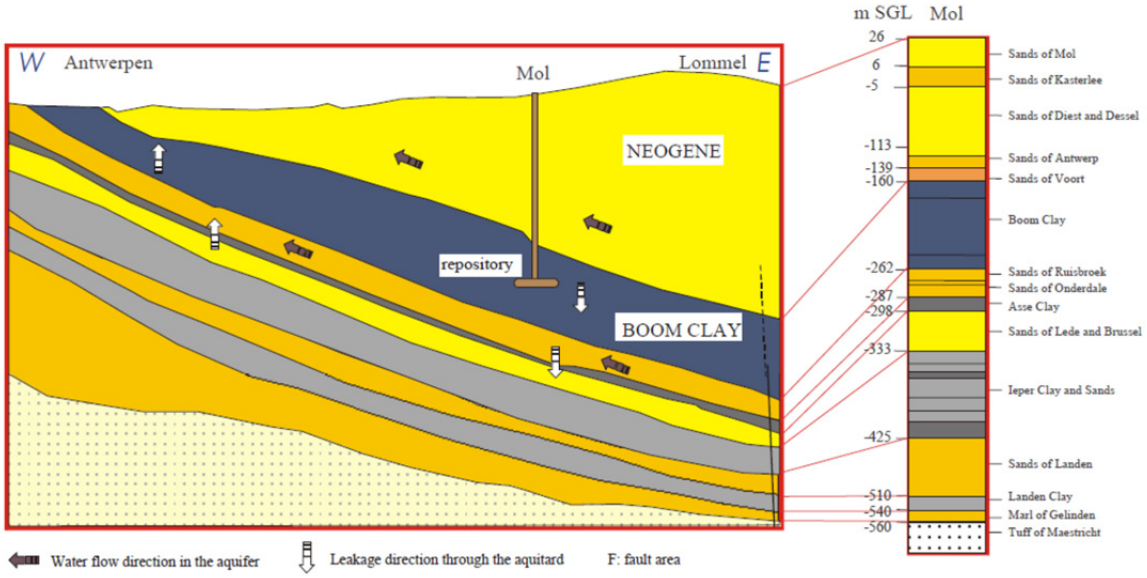

Figure 2-1. West-East geological section through Mol (Sillen & Marivoet 2007).

The mineralogical composition of the Boom Clay is very homogeneous in the vertical profile of the Boom Clay from a qualitative point of view. However, significant variations exist in the quantitative mineralogy, which is related to different grain-size distributions in silt-dominated and clay-dominated layers. It consists mainly of clay minerals dominated by illite, kaolinite and smectite. The complementary non-argillaceous fraction is mainly constituted by quartz and feldspar. In smaller quantities, the clay sequence is characterised by the presence of beds containing levels of carbonates (calcareous concretions of septarian limestone nodules) and also pyrite and marcasite concretions, as well as a fraction of organics (Romero 1999; Coll 2005; Li et al. 2007; Delage et al. 2008). Table 2-1 summarises the literature review of Boom clay mineralogy, in which slight differences between the authors can be detected.

Table 2-1. Literature review of Boom Clay mineralogy

Minerals (%)	ONDRAF/NIRAS 2001	DeCraen et al. 2004	Volckaert et al. 2005	Li et al. 2007	Zeelmaekers 2011
Clay minerals	30-70	30-60	55	23-59	66.4
Illite	50	10-45	28		7.2
Kaolinite	10	5-20	6	5-15	8.3
Smectite	30	10-30	16		
Chlorite	5	0-5		1-4	3.9
Glauconite	3				
Non clayey minerals					
Quartz	20	15-60		23-57	21
Calcite, dolomite		1-5			4.2
Pyrite	1-5	1-5		1-5	1.9
Feldspar	5-10	1-10		6-11	
Carbonates	1-5	1-5		1-5	
Organic material	1-3	1-5		1-5	

2.2.2. Sample location

Boom Clay samples were retrieved at the HADES underground research facility URL (Mol, Belgium). Figure 2-2 shows a scheme of the URL in the Boom Clay formation and the location of the retrieved samples. Afterwards, the cores were vacuum packed using reinforced aluminium foil and thermo-welded plastic. They were stored at room temperature ranging between 15 and 20°C and at an average relative humidity of 45% before being sent. These samples were received at the UPC Geotechnical Laboratory (Barcelona, Spain).

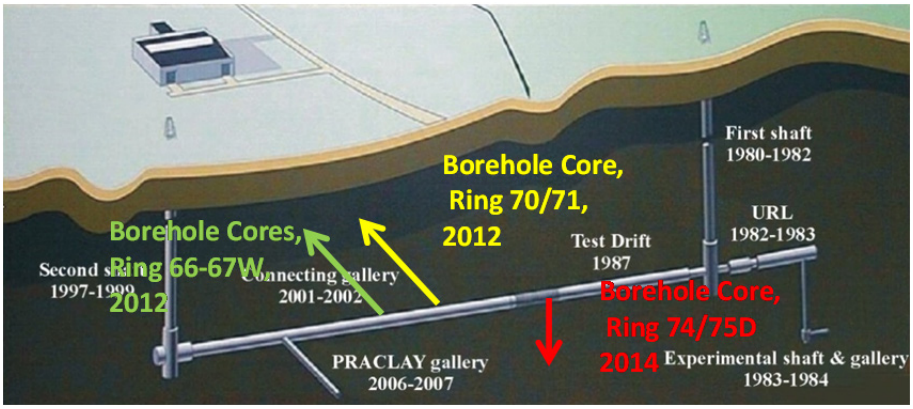

Figure 2-2. Scheme of the URL in the Boom Clay formation at Mol and locations of core-sample retrieval.

The first set of samples, which were received at the end of 2012, are identified as Core 8 (ID: CGR70_71W_Core8) and Core 7 (ID: CGR70-71W_Core7) (Figure 2-3). They were retrieved at a depth of 223 m in the borehole 2012/2 which was horizontally drilled in September 2012 in the Connecting Gallery at Ring 70-71 (horizontal borehole towards the West).

At the beginning of 2014, other Boom Clay samples were requested to SCK·CEN to continue the research. Two core samples were received at the UPC Geotechnical Laboratory in May 2014 (Figure 2-4). They are identified as Core 8 (ID: CGR66-67W_Core 8_Sectiona) and Core 9 (ID: CGR66-67W_Core 9_Sectionc) and were horizontally drilled from Ring 66-67 of the borehole 2012/6 at the HADES (horizontal borehole towards the West) at a depth of 223 m. Table 2-2 summarises the borehole samples properties.

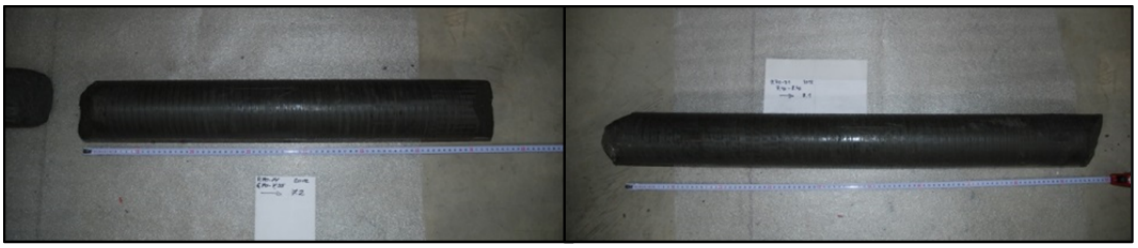

Figure 2-3. Boom clay samples: Core 8 (ID: CGR70_71W_Core8) and Core 7 (ID: CGR70-71W_Core7).

Figure 2-4. Boom clay samples: Core 8 (ID: CGR66-67W_Core 8_Sectiona) and Core 9 (ID: CGR66-67W_Core 9_Sectionc).

Table 2-2.Details of borehole samples of Boom Clay

Boring Nº	Core number	Piece (intrados)	Sample zone (m)	External diameter (mm)	Sample length (m)	Borehole direction
HADES 2012/2	8	#8.1	7.40-8.40	100	1.0	Horizontal
HADES 2012/2	7	#7.2	6.70-7.35	100	0.6	Horizontal
HADES 2012/6	8	#8	7.50-8.40	100	0.9	Horizontal
HADES 2012/6	9	#9.1	8.50-8.85	100	0.35	Horizontal

2.2.3. *In situ* stress state

The *in situ* stress state near the HADES underground research facility is briefly presented here to contextualize the results on the hydro-mechanical behaviour of Boom Clay and justify the pre-conditioning paths initially applied in each test.

At the depth of the HADES underground research facility, the lithostatic pressure, or total vertical stress, σ_v, imposed by the weight of the overlying material is about 4.5 MPa. The undisturbed pore pressure u_w at the depth of HADES URL (but measured at a sufficient distance from the galleries) is about 2.2 MPa and corresponds well to a hydrostatic distribution up to the water table which is close to the surface. The effective vertical stress is thus $\sigma'_v = \sigma_v - u_w = 2.3\ MPa$. The K_0 value (ratio of horizontal to vertical effective stresses) was determined by laboratory methods and *in situ* investigations. The *in situ* investigations from HADES by means of pressuremeter, dilatometer, self-boring pressuremeter (SBP), hydro-fracturing tests, borehole breakouts analysis and back-analysis of the stresses in the liner, gave some scattered K_0 values (0.3-0.9). Laboratory investigations indicated values for K_0 between 0.5 and 0.8 (Li et al. 2007).

More recently *in situ* campaigns (Cornet 2009) with self-boring pressuremeter tests (SBP) and hydro-fracturing tests were conducted at different distances (up to 40 metres) from the underground laboratory in three boreholes along different directions (horizontal, vertical downwards, and inclined at 45°) to map the 3D-stress state and also to delineate the damaged zone around the connecting galleries. The results of these tests confirm that the *in situ* stress state in the far field of HADES URL is transverse isotropic, with the major stress component being vertical. The interpretation of the tests yields values for the coefficient of earth pressure at rest in the range 0.7–0.8 and a horizontal effective stress (σ'_h) of about 1.9 MPa. It should be noted,

however, that the interpretation of SBP tests and hydro-fracturing tests in a medium that may also present anisotropic material properties is delicate, so, these values of K_0 and σ'_h might undergo revisions. The latest laboratory results related to K_0 conditions in Boom Clay were published by Dao (2015). Different tests were performed under oedometer conditions (controlled rate strain or controlled rate stress) with lateral stress measurement and also under triaxial conditions preventing lateral deformation. K_0 values yielded between 0.78 and 0.85 respectively.

2.2.4. Geotechnical characterization and initial conditions

The basic geotechnical and hydraulic properties of the studied core-samples in their intact state are summarised in Table 2-3. For the main characterisation, material from Core 8.1 (at a distance of 7.40-7.51 m from the intrados of the connecting gallery) was used.

The particle size distribution of Boom clay was obtained using two methods: sieve analysis and sedimentation process (ASTM D422). The sieve analysis allows the classification from gravel size to a particle size of 0.075 mm and with the sedimentation analysis can separate soil fractions from 0.075mm down to a size of about $2 \cdot 10^{-4}$ to $5 \cdot 10^{-4}$ mm. Figure 2-5 shows the results of Boom clay particle size distribution compared with different studies and methods (conventional and laser). Moreover, the values of the coefficient of uniformity depend on the selected method, being $C_u \approx 7$ for laser methodology and 22 for the conventional one; whereas the coefficient of curvature, C_c, is around 1 in all the cases.

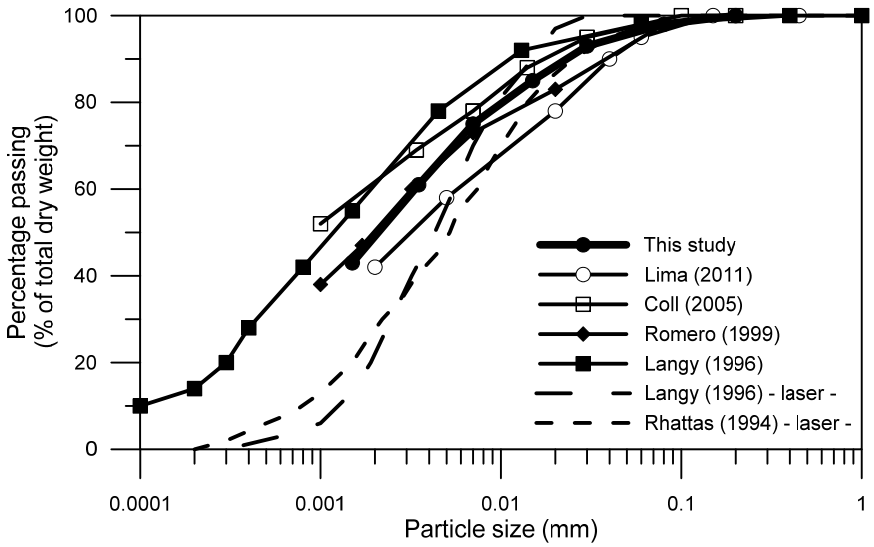

Figure 2-5. Particle size distribution (after Lima 2011).

The specific gravity of the soil grains (G_s) at 20 ºC is 2.67 for Boom Clay, determined according to ASTM D854. Other values reported in the literature varied between 2.65 and 2.70 (Horseman et al. 1987; Romero 1999; Coll 2005).

Consistency limits were also investigated for Boom Clay (ASTM D4318). A limit liquid (w_L) of 67% and a plastic limit (w_P) of 29% were measured, resulting in a value of plasticity index of 38%. Figure 2-6 shows the plasticity chart, which also includes consistent results reported by different authors. Boom Clay can be classified according to the plasticity chart as high-medium plastic inorganic clay (CH) (Unified Soil Classification System, ASTM D2487).

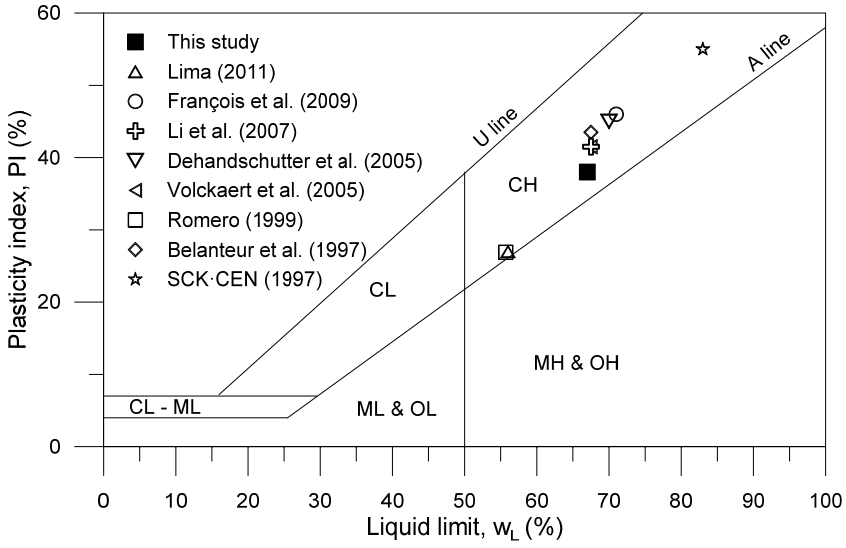

Figure 2-6. Plasticity chart (after Lima 2011).

The main geotechnical properties are summarized in Table 2-3 and compared with those reported by Li et al. (2007) and Lima (2011). This table also indicates an important initial total suction due to the retrieval of a quasi-saturated soil. The measured suction, 2.45 MPa, is consistent but slightly higher (possibly due to some desiccation during storage) than the theoretical value obtained if the stress relief (undrained unloading) is assigned to the pore pressure according to the *in situ* stress state.

Table 2-3. Boom Clay characterization.

Parameter	This study	Li et al. 2007	Lima 2011
Geotechnical properties			
Density of solids, ρ_s (Mg/m^3)	2.67		2.67
Dry density, ρ_d (Mg/m^3)	1.63-1.69	1.61-1.78	1.65-1.71
Plastic limit w_P (%)	29	23-29	29
Liquid limit w_L (%)	67	55-80	56
Plasticity index, I_P(%)	38	32-51	27
Hydraulic properties			
Total suction, s (MPa)	2.45		2.5-4
Air-entry value from MIP (MPa)	4.8		
Dominant pore size from MIP (nm)	70		
Degree of saturation, S_r	1		0.91-1

Table 2-4 contains the initial conditions of samples used in each test and includes the nomenclature used to denominate each test. It consists of: *Test protocol* (P1, P2, P3 or P4: different protocols for oedometer tests; Spl: Splitting test, Dif: Diffusion test) - *Type of air injection* (FI: fast injection; SI: slow injection; NI: non-injection) - *Orientation of bedding planes* (N: normal to flow; P: parallel to flow) - *Execution order* (Order followed for each type of test: 1, 2…). More details are given in Chapter 3. The table also includes the location of the samples referred to the core, indicating the distance from the gallery intrados.

Figure 2-7 to Figure 2-9 depict the schemes of the different cores, enclosing the water content and the bulk density profiles along them. In the picture, the circles represent samples with the bedding normal to the axis, while rectangles indicate samples trimmed with bedding parallel to the axis. Some of the samples were used in Romero et al. (2016) and are indicated as 'Thermal research'; as well as the failed samples which correspond with those that broke during the trimming process due to internal discontinuities or the presence of pyrite concentrations.

Table 2-4. Initial conditions for samples used in each test.

Reference	Core	Distance from gallery intrados (m)	Bulk density (Mg/m^3)	Void ratio	Water content (%)
Material characterization	CGR70_71W_Core8	7.4 - 7.51	2.04	0.61	23.80
Failed sample	CGR70_71W_Core8	7.51 - 7.67	2.04	0.60	23.00
P1_FI_P	CGR70-71W_Core8	7.67 - 7.72	2.06	0.58	22.63
Failed sample	CGR70-71W_Core8	7.72 - 7.77	2.04	0.61	22.90
P3_FI_N_1	CGR70-71W_Core8	7.77 - 7.84	2.06	0.58	22.90
P2_FI_P	CGR70-71W_Core8	7.84 - 7.94	2.03	0.63	23.81
P1_FI_N	CGR70-71W_Core8	7.94 - 8.07	2.02	0.64	23.18
Failed sample	CGR70-71W_Core8	8.07 - 8.23	-	-	23.39
Spl_1_N	CGR70-71W_Core8	8.23 - 8.31	-	-	23.90
Spl_2_P	CGR70-71W_Core8	8.31 - 8.40	-	-	23.90
P4_NI_N_1	CGR70-71W_Core7	6.70 - 6.75	2.05	0.59	23.12
P4_NI_N_2	CGR70-71W_Core7	6.75 - 6.80	2.03	0.62	22.67
P4_NI_N_3	CGR70-71W_Core7	6.80 - 6.85	2.04	0.60	23.12
Suct_1_N	CGR70-71W_Core7	6.82 - 7.00	2.02	0.63	23.19
P3_FI_P_1	CGR70-71W_Core7	7.00 - 7.05	2.06	0.58	23.25
P3_SI_N_1	CGR70-71W_Core7	7.05 - 7.17	2.04	0.61	23.52
P3_SI_P	CGR70-71W_Core7	7.17 - 7.23	2.05	0.59	22.81
Dif_1_N	CGR70-71W_Core7	7.23 - 7.35	2.04	0.60	22.64
Failed sample	CGR66-67W_Core8_Section_a	7.59 - 7.66	2.05	0.59	23.71
Thermal test 1*	CGR66-67W_Core8_Section_a	7.66 - 7.95	2.00	0.67	22.75
P3_FI_P_2	CGR66-67W_Core8_Section_a	7.95 - 8.03	2.05	0.59	23.44
Thermal test 2*	CGR66-67W_Core8_Section_a	8.03 - 8.12	2.04	0.61	22.70
P3_SI_N_2	CGR66-67W_Core8_Section_a	8.12 - 8.18	2.06	0.58	23.65
P3_FI_N_2	CGR66-67W_Core8_Section_a	8.19 - 8.27	2.06	0.58	22.70

*Thermal research: Romero et al. 2016

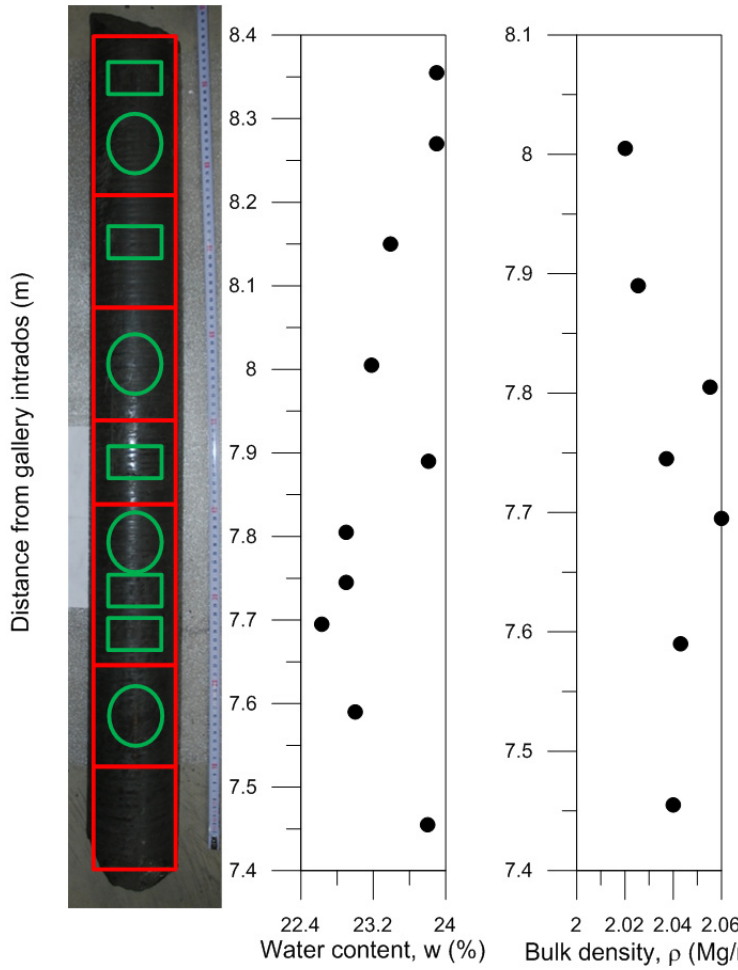

Figure 2-7. Profiles of water content and bulk density along the core CGR70_71W_Core8.

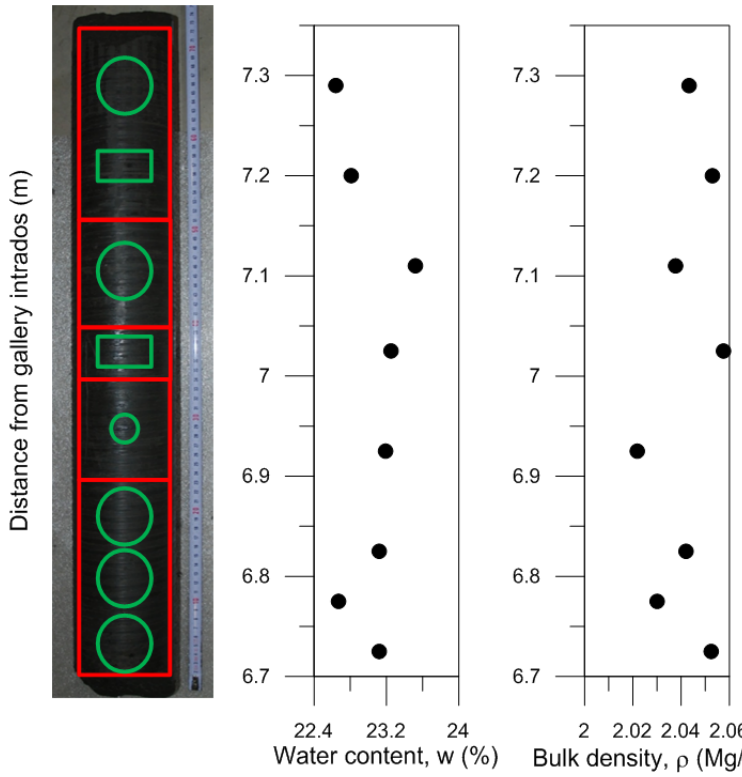

Figure 2-8. Profiles of water content and bulk density along the core CGR70_71W_Core7.

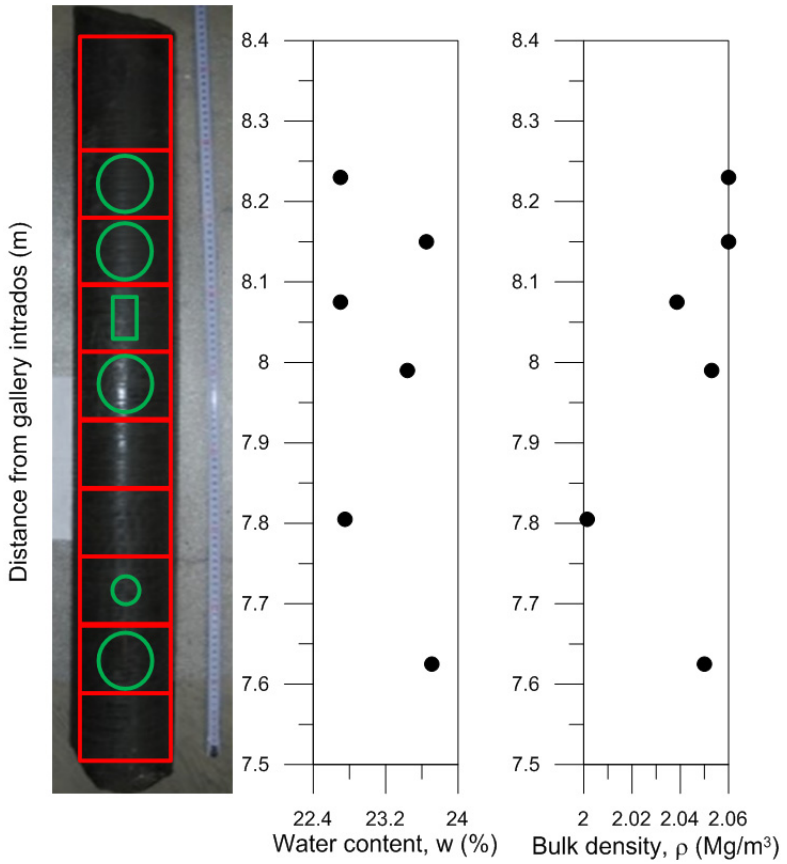

Figure 2-9. Profiles of water content and bulk density along the core CGR66-67W_Core8_Section_a.

2.2.5. Specimen and synthetic water preparation

Initially, the borehole samples were opened and divided into several pieces by trimming using a hand-operated lathe and cutting hand tools (trimming knife, scraper and wire saw). After trimming, the pieces were carefully stored to maintain the initial water content. To this aim, the samples were wrapped with high-density vacuum storage bags with a vapour water permeability of 1.8 g/m^2/24h at 23°C/85% of relative humidity, and then, vacuum packed. A commercial vacuum packer was used to apply a fast vacuum to the sample, as shown in Figure 2-10. Afterwards, the pieces were classified and stored in a sealed humidity chamber at a temperature of 20°C and a relative humidity about 99%.

Figure 2-10. Vacuum equipment and vacuum packed samples.

The samples for oedometer tests were trimmed using a hand-operated lathe and cutting hand tools (trimming knife, scraper and wire saw) with special care in the bedding direction, in order to obtain samples with the bedding planes orientated parallel and orthogonal to the core axis. The samples were installed in metal ring of internal diameter D_{int} = 50 mm and height H = 20 mm. (Figure 2-11).

During the preparation of the samples, some of them broke (Figure 2-12) due to existing discontinuities or the presence of burrows and hard pyrite concentrations (De Craen 1998).

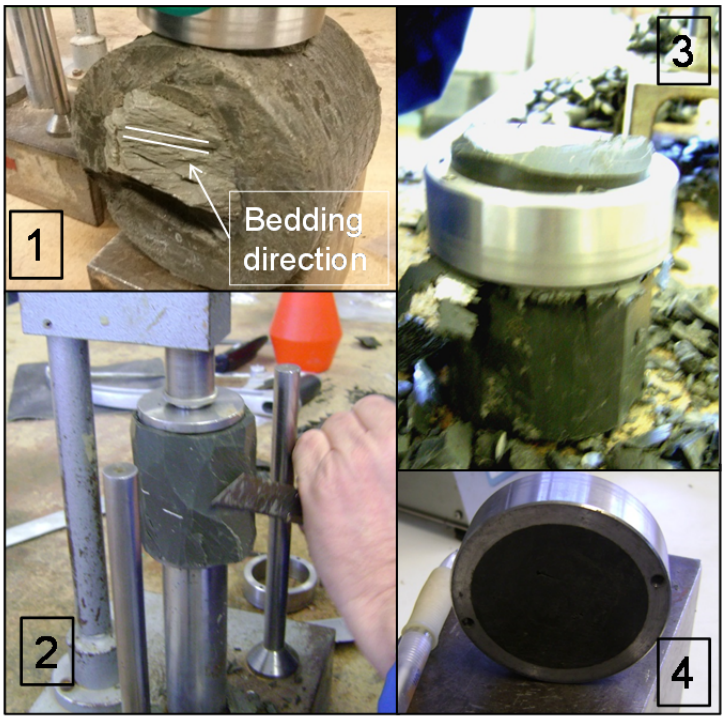

Figure 2-11. Preparation of oedometer samples.

Figure 2-12. Failed samples due to the breakage during the preparation.

Due to the fact that Boom Clay was formed in marine deposit, the *in situ* pore water is dominated by sodium bicarbonate. Therefore, the water used in the tests was

synthetically prepared in the laboratory with a similar composition to the *in situ* one. According to De Craen et al. (2004), the Synthetic Boom Clay Water (SBCW) was prepared as follows:

• firstly, a specified amount of salts $NaHCO_3$ (1170 mg/L), H_3BO_3 (43 mg/L), KCl (25 mg/L), $MgCl_2 \cdot 6H_2O$ (22 mg/L), NaF (11 mg/L), NaCl (10 mg/L), Na_2SO_4 (0.3 mg/L) were dissolved in 1 L of distilled water (7.5 to 7.1 µS/cm of water electrical conductivity) leaving for a few minutes until complete dissolution (TDS 1281.3 mg/L);

• secondly, 5 g of $CaCO_3$ were poured in the dilute saline solution, followed by 72 h of stirring.

The osmotic suction measured with WP4 psychrometer was below 0.5 MPa.

2.2.6. Pore size distribution

Mercury Intrusion Porosimetry (MIP) tests were performed to characterise the porosity network on an 'AutoPore IV 9500 – Micrometrics Instrument Corp' porosimeter. Cubical samples of Boom Clay were trimmed with 10 mm in dimension and freeze-dried before the MIP tests. Details of the technique and the sample preparation can be found in Chapter 6.

The pore network description was complemented by nitrogen adsorption tests carried out on an 'ASAP 2020 – Micrometrics Instrument Corp' equipment (Figure 2-13). The pore size distribution was estimated following the Barrett, Joyner and Halenda (BJH) method using the desorption information (Webb & Orr 1997). A wider range of pore sizes is covered when using this complementary information.

Figure 2-13. Equipment used for nitrogen adsorption tests.

Figure 2-14 shows the cumulative intruded pore volume normalised by solid volume (intruded void ratio) plotted against the entrance pore size for Boom Clay intact samples. There is some deviation from the initial void ratio in MIP data (refer to Table 2-4), due to the limited capacity of the porosimeter to enter the smallest pores (non-intruded porosity with pores size below 6 nm). However, data from nitrogen adsorption method almost reach the initial void ratio.

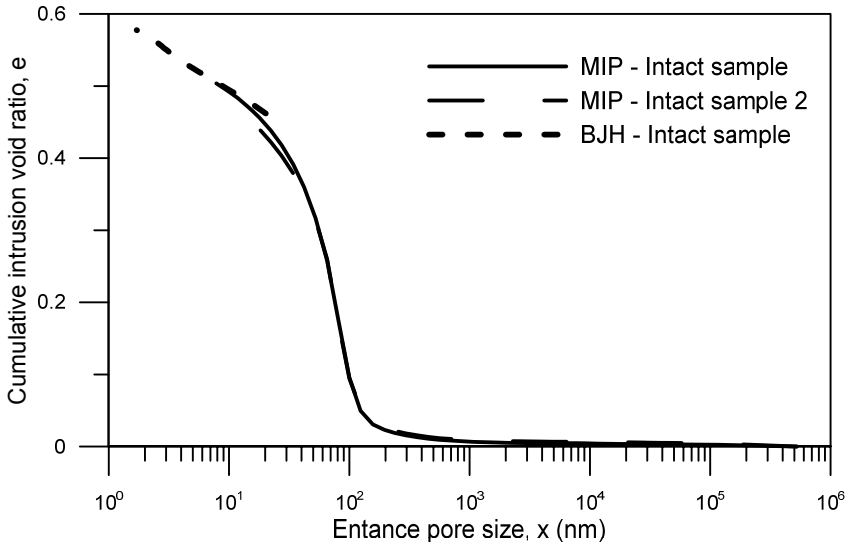

Figure 2-14. Cumulated intruded void ratio obtained with MIP and BJH techniques.

Other useful information that can be obtained from the MIP and BJH tests is the pore size density function (PSD), defined as:

$$PSD = f(logx) = -de/d(logx) \quad (2.1)$$

where x represents the entrance pore size. The PSD function obtained from MIP displays one dominant pore size at intra-aggregate scale, as expected for a matrix type microstructure, being around 70 nm. Regarding BJH data, a less important smaller peak is observed around 3 nm (Figure 2-15).

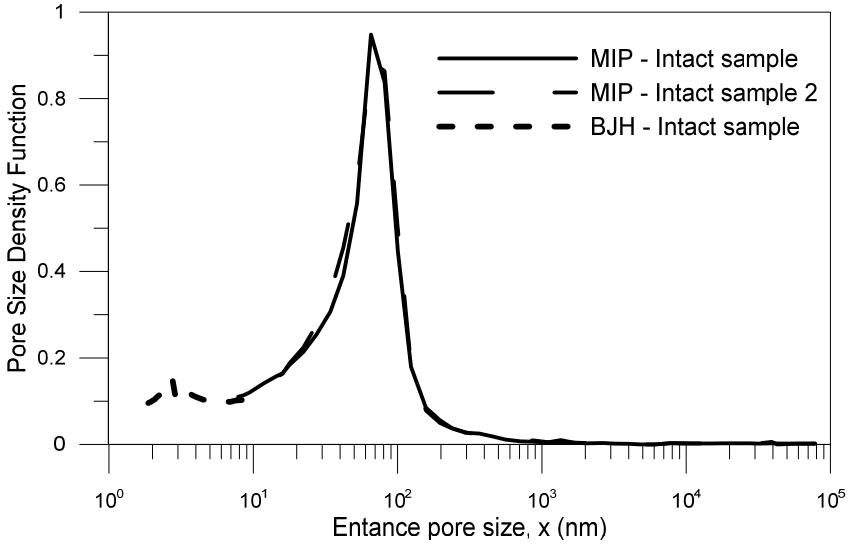

Figure 2-15. PSD function of intact Boom Clay.

2.2.7. Water retention curve

A dew point psychrometer (Cardoso et al. 2007) was used to obtain the water retention curve in the total suction range from 1 to 100 MPa. The specimens were dried in steps starting from the initial total suction, stored for one day for equalization, weighed and then, total suction was measured. Afterwards, from the dry state, samples were wetted in steps following identical procedure until saturation (Figure 2-16). Data obtained with the same method by Le et al. (2008) are included in Figure 2-17 for comparison.

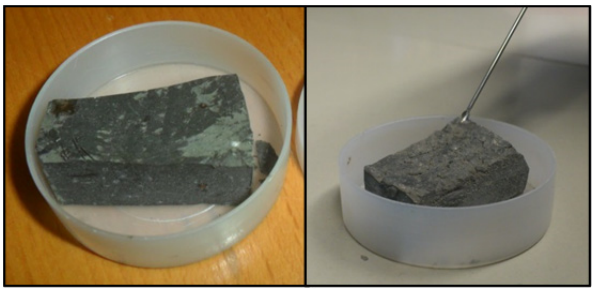

Figure 2-16. Sample for water retention curve determination. Photo on the left: drying process; on the right: wetting process.

Pore size distribution results from MIP tests were also used to determine the relationship between matric suction and degree of saturation, as well as the air entry value corresponding to the dominant pore mode (see Chapter 6 Section 6.2.1 for the procedure).

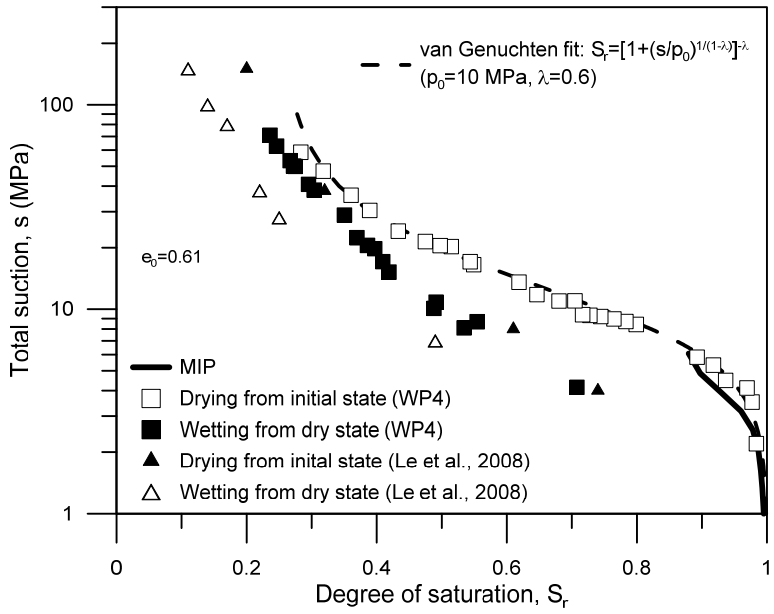

Figure 2-17. Water retention curve.

Suction (s) and degree of saturation (S_r) data in the drying branch were fitted to van Genuchten's equation (2.2).

$$S_r = \left[1 + (s/p_0)^{(1/(1-\lambda))}\right]^{-\lambda} \quad (2.2)$$

Fitted parameters λ and p_0, the latter associated with the air entry value, are included in the figure.

Figure 2-17 shows the estimated water retention curve which includes curves based on MIP data together with psychrometer measurements and the fitted van Genuchten's equation. The air entry value (AEV), corresponding to the dominant pore mode

detected from MIP data, was determined using Laplace's equation and is reported in Table 2-3.

2.3. Indurated clays

2.3.1. Sample location

Two core samples were recovered by Nagra from the geothermal well Schlattingen-1 (SLA-1) at two different depths (781.55 m depth 'Brauner Dogger' (BD) and 936.26 m deep Opalinus Clay (OPA)). The geothermal well SLA-1 is located on the road between Basadingen, Schlattingen and Diessenhofen (Canton Thurgau) about 10 km south-east of the town of Schaffhausen in the North-eastern part of the Swiss Molasse Basin (Figure 2-18). The borehole reached a final depth of 1508 m, passed through the Quaternary, Tertiary, Jurassic and Triassic sediment sequence, and finally reached the crystalline basement (Albert et al. 2012). The stratigraphic profile of borehole Schlattingen-1 is shown in Figure 2-19, and technical borehole data are summarised in Table 2-5.

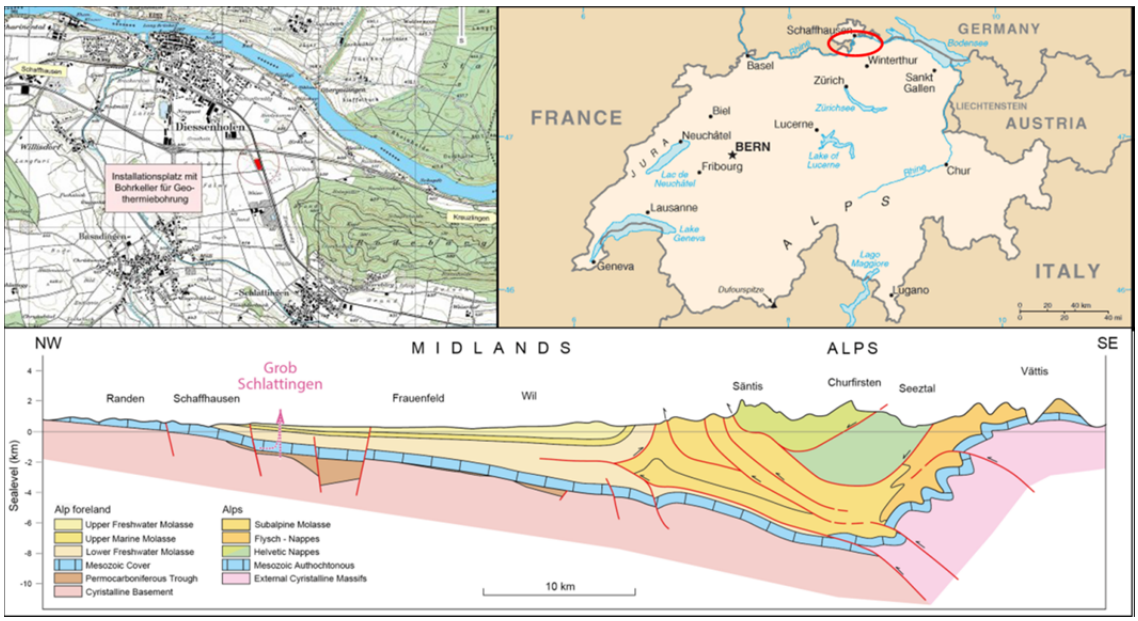

Figure 2-18. Location of the Schlattingen borehole and schematic cross section of Northern Switzerland (Frieg et al. 2015).

Table 2-5. Technical borehole information about the geothermal well Schlattingen 1.

Geothermal Well Schlattingen 1 (SLA-1)		
Location	Village of Schlattingen, around 10 km south-east of Schaffhausen	
Coordinates	N 47°40'41.7", E8°45'42"	
Elevation	416.6 m above sea level	
Max. depth	1508.0 m bg.	
Drilling techniques	Percussion drilling, cuttings	0 – 725 m 989-1116 m bg. bg. 1185 – 1508 m bg.
	Single barrel core drilling	725 – 989 m bg. 1116 – 1185 m bg.

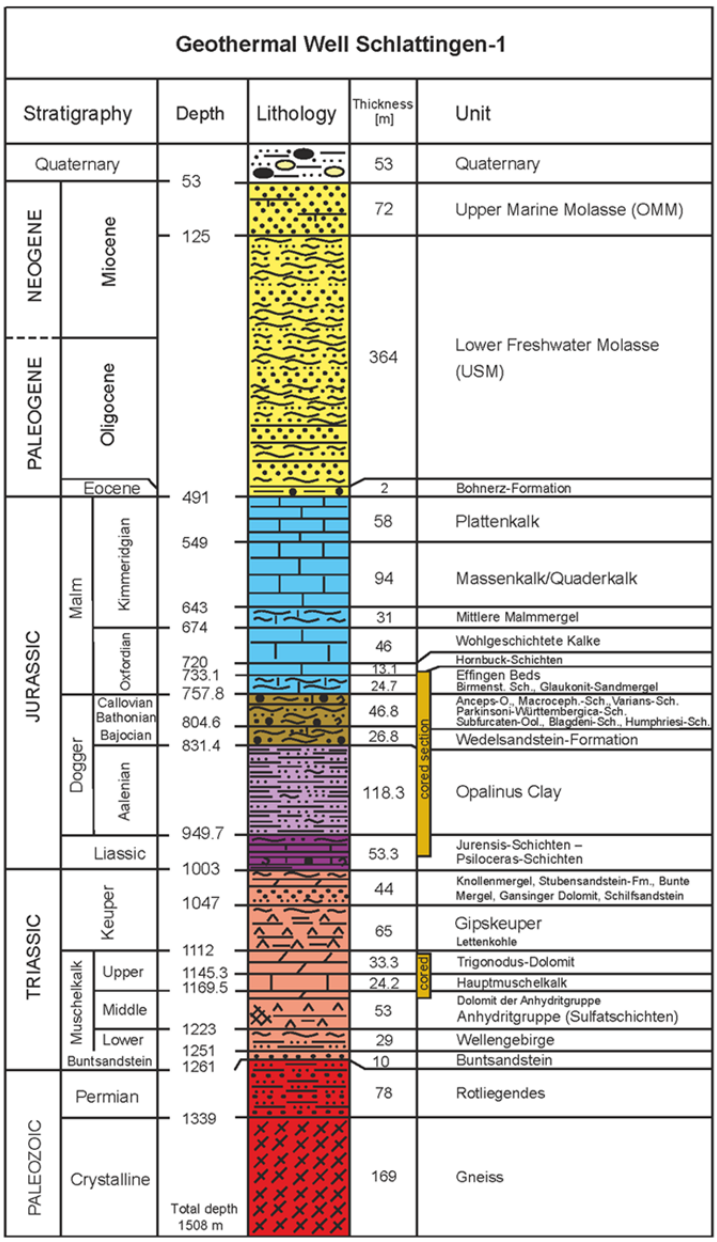

Figure 2-19. Stratigraphy of the geothermal well Schlattingen 1 (SLA-1) (Albert et al. 2012).

2.3.2. *In situ* stress state

Extensive geomechanical testing programmes were conducted by Nagra on core samples from the Mont Terri underground laboratory (URL MT) in North-western Switzerland and with core samples from the boreholes of Benken and Schlattingen-1 in North-eastern Switzerland (Figure 2-20).

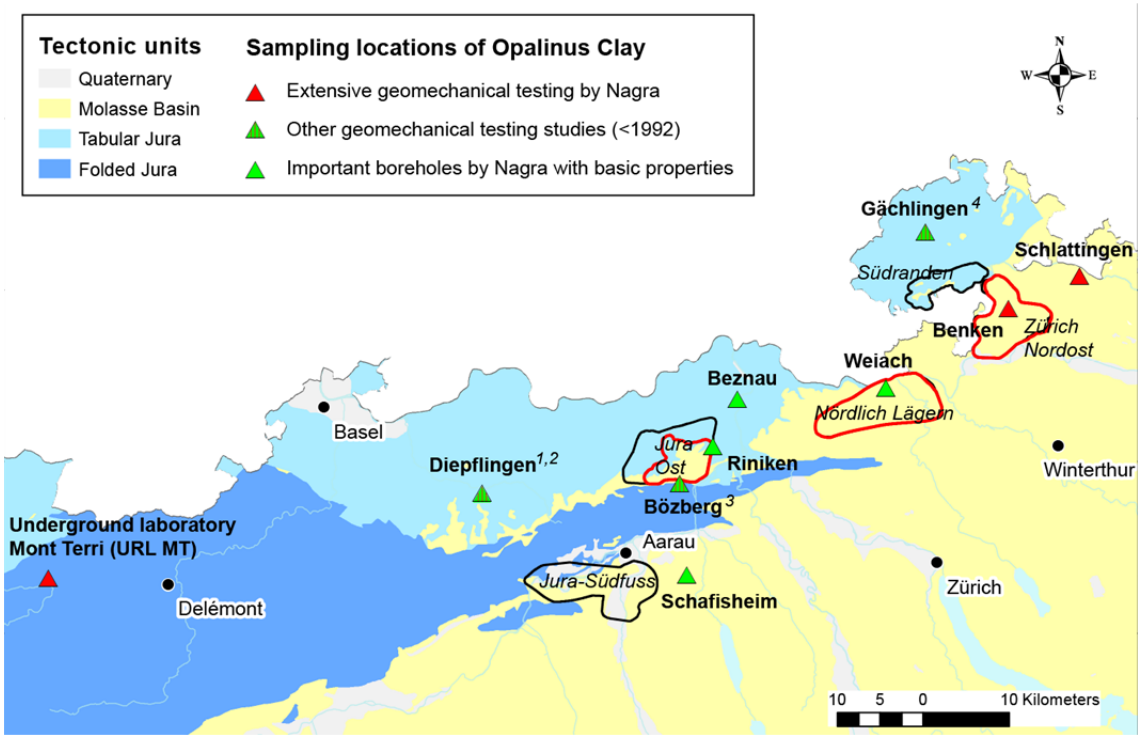

Figure 2-20. Regional tectonic map of Northern Switzerland with source localities of Opalinus Clay used for characterization and geomechanical testing (Giger & Marschall 2014).

The stress measurements in the borehole SLA-1 (Vietor et al. 2012) were performed in the open hole by minifrac tests. The measurements yielded a stress profile reaching from 592 m to 1455 m depth. It straddled in several rock units and included the top of the crystaline basement. The minimum horizontal stress was directly determined from the shut-off pressure of the data logs. The vertical profile is shown in Figure 2-21. It was assumed that one of the principal stresses was vertical and the vertical stress component was calculated from the overburden using an average density value of 2500 kg/m^3. Data from the 'Brauner Dogger' formation can be directly obtained from that figure, but due to the lack of information, stress state at the depth of Opalinus Clay should be estimated based on data published in Giger & Marschall (2014).

Stress data from SLA-1 borehole at the depth of BD samples (782 m) yielded values of minimum and maximun horizontal stress of $\sigma_h = 15\ MPa$ and $\sigma_H = 21\ MPa$, while the calculated vertical stress was $\sigma_v = 19.55\ MPa$, given a value of total mean stress

$p = 18.5\ MPa$. Hydrostatic water pressure was assumed $u_w = 7.82\ MPa$, and therefore, vertical effective stress resulted in $\sigma'_v = 11.75\ MPa$, whereas the effective mean stress is $p' = 10.7\ MPa$.

In the case of the stress state at the OPA samples (936 m), the vertical stress was calculated using the same overburden, resulting in $\sigma_v = 23.4\ MPa$. Giger & Marschall (2014) reported a value of K-ratio (σ_h/σ_v) of 0.82 for a depth of 900 m, which implies a horizontal stress $\sigma_h = 19.2\ MPa$. Hydraulic head distributions in Opalinus Clay were discussed for the boreholes of Benken, Riniken and Schafisheim. To a first approximation, pore fluid pressure in Opalinus Clay can be considered hydrostatic (Giger & Marschall 2014). Therefore, the water pressure for OPA samples was $u_w = 9.36\ MPa$ given an effective mean stress (p') of 11.24 MPa and in terms of effective vertical stress, 14.01 MPa.

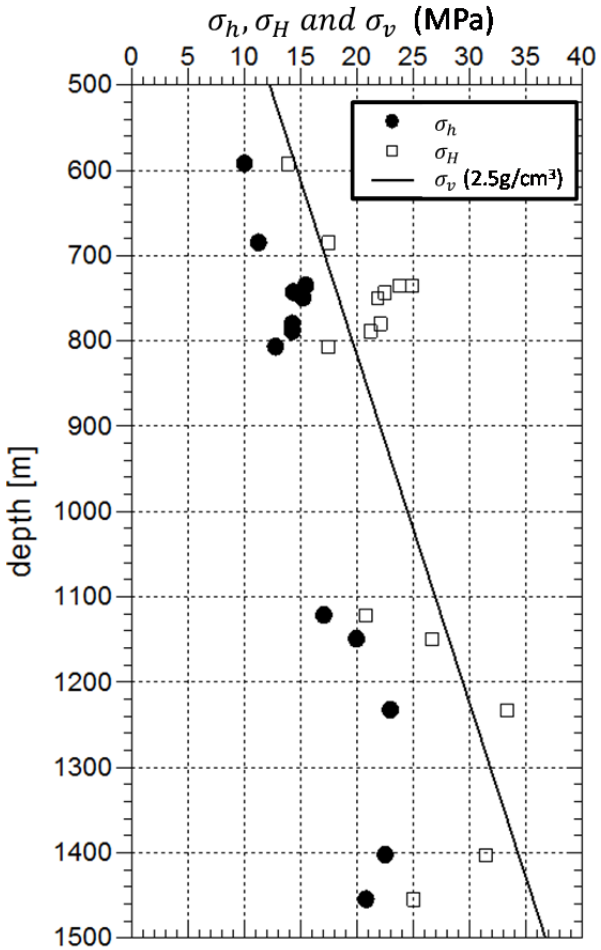

Figure 2-21. Stress magnitude data from hydraulic fracturing in the borehole SLA-1 (Giger & Marschall 2014).

2.3.3. General characterization and initial conditions

Cores from two different stratigraphic sequences were tested in the Geotechnical Laboratory of UPC. One of them corresponds to a clay-rich sequence from the 'Brauner Dogger' (BD) (781.55 – 781.85 m depth, from Upper Dogger unit: Bathonian/Bajocian age), and consisting of silty to clay-rich marls with clay content of 25–45%, 30–50% of carbonate and 20–25% of quartz (Ferrari & Laloui 2013; Ferrari et al. 2014). The other tested material was retrieved from the deeper Opalinus Clay (OPA) formation (936.26 – 936.49 m) and consists mainly of claystone with a carbonate content of 10–20% and a quartz content of 15–32% (Ferrari et al. 2014). The OPA sequence starts at 831 m bg (Figure 2-19). The cores were recovered with a double core barrel using NaCl drilling mud. After on-site core documentation, the 100 mm diameter samples were cast immediately in epoxy resin and placed inside PVC tubes for safe preservation during shipment. A total of four core–samples were received at the Geotechnical Laboratory. A published report NAB 13-51 (Romero & Gómez 2013) described the information regarding two of these core-samples (Table 2-6).

Table 2-6. Samples received at the Geotechnical Laboratory (UPC)

Sequence and core-sample reference	Depth bg (m)	Date (core preservation)	Observations
'Brauner Dogger' OED 20/Harz	776.51 – 776.72	21/03/2011	Romero & Gómez (2013)
'Brauner Dogger' EMPA SLA	781.55 – 781.85	21/03/2011	This study
Opalinus Clay OED	879.79 – 880.01	17/04/2011	Romero & Gómez (2013)
Opalinus Clay OED 1/1	936.26 – 936.49	10/06/2011	This study

The main geotechnical properties of the studied samples are summarised in Table 2-7. This information is complemented with the initial suction measured with dew point mirror psychrometer (Cardoso et al. 2007) and the dominant entrance pore size determined by mercury intrusion porosimetry and nitrogen adsorption/desorption tests (BJH method, Webb & Orr 1997).

Table 2-8 shows the comparison between the initial conditions of ‘Brauner Dogger’ samples: OED 20/Harz (776.51 - 776.72 m) and EMPA SLA (781.55 - 781.85 m), together with results reported by Ferrari & Laloui (2013) for ‘Brauner Dogger’ (767 – 778 m). A good agreement is observed between the results reported in the table, in which the new sample presented slightly lower porosity. A higher initial total suction was observed in the new BD, which is more consistent with the expected initial suction

in these deep materials. If the initial suction is due to stress relief during the extraction of the cores and assuming that the upper layers were saturated, then the total initial suction of the BD OED 20/Harz should approximately be 10 MPa at least. In addition, some drying of the samples during the extraction and storage would have enlarged this value.

Table 2-9 shows a comparison between Opalinus Clay samples: OED (879.79 - 880.01 m) and OED 1/1 (936.26 - 936.49 m), as well as OPA results reported by Ferrari et al. (2014). Despite their different depths, the geotechnical properties are very consistent, which indicate the homogeneity of the Opalinus Clay formation. Again, the initial suction values are not consistent being underestimated for the OPA OED sample.

Table 2-7. Initial conditions of tested samples

Sequence / formation	'Brauner Dogger'	Opalinus Clay
Core-sample reference	EMPA SLA (781.55 – 781.85 m)	OED 1/1 (936.26 – 936.49 m)
Bulk density, ρ (Mg/m^3)	2.55	2.53
Water content, w (%)	4.78	4.79
Density of solids, ρ_s (Mg/m^3)	2.69	2.69
Dry density, ρ_d (Mg/m^3)	2.48	2.43
Void ratio, e	0.09-0.11	0.11
Porosity, n	0.08-0.10	0.10
Degree of saturation, S_r (ρ_w= 1 Mg/m^3)	0.95 – 1.0	0.98 – 1.0
Total suction, s (MPa)	37	44
Dominant pore mode from MIP (nm)	22	< 8
Air-entry value from MIP (MPa)	13	> 37
Dominant pore mode from BJH (nm)	2.7	2.7
Air-entry value from BJH (MPa)	118	118
Liquid limit, w_L (%)	24	29
Plastic limit, w_P (%)	17	18

Table 2-8. Comparison of initial conditions of 'Brauner Dogger' samples

Sequence / formation	'Brauner Dogger'		
Core-sample reference	OED 20/Harz (776.51 – 776.72 m)	EMPA SLA (781.55 – 781.85 m)	Ferrari & Laloui 2013 (767 – 778 m)
Bulk density, ρ (Mg/m^3)	2.51	2.55	2.55
Water content, w (%)	4.34 – 5.43	4.78	2.70 – 3.50
Density of solids, ρ_s (Mg/m^3)	2.69	2.69	2.72
Dry density, ρ_d (Mg/m^3)	2.38 – 2.41	2.48	2.46 – 2.48
Void ratio, e	0.116 – 0.130	0.09 - 0.11	0.09 – 0.11
Porosity, n	0.104 – 0.115	0.08 - 0.10	0.08 – 0.10
Degree of saturation, S_r	around 1.0	0.95 – 1.0	0.78 – 0.92
Total suction, s (MPa)	5	37	45 MPa at Sr = 0.89
Dominant pore mode from MIP (nm)	20	22	16
Air-entry value from MIP (MPa)	14	13	18
Liquid limit, w_L (%)	28	24	25 – 29
Plastic limit, w_P (%)	18	17	23

Table 2-9. Comparison of initial conditions of OPA samples.

Sequence / formation	Opalinus Clay		
Core-sample reference	OED (879.79 – 880.01 m)	OED 1/1 (936.26 – 936.49 m)	Ferrari et al. 2014 (855 – 891 m)
Bulk density, ρ (Mg/m^3)	2.53	2.53	2.54 – 2.55
Water content, w (%)	4.30 – 4.70	4.79	3.3 – 3.6
Density of solids, ρ_s (Mg/m^3)	2.69	2.69	2.71
Dry density, ρ_d (Mg/m^3)	2.42 – 2.43	2.43	2.45 – 2.47
Void ratio, e	0.107 – 0.112	0.11	0.10 – 0.11
Porosity, n	0.097 – 0.101	0.10	0.09 – 0.10
Degree of saturation, S_r	1.0	0.98 – 1.0	0.93 – 0.96
Total suction, s (MPa)	4	44	67 MPa at S_r = 0.73
Dominant pore mode from MIP (nm)	16	< 8	7
Air-entry value from MIP (MPa)	18	> 37	42
Liquid limit, w_L (%)	- -	29	29 – 33
Plastic limit, w_P (%)	- -	18	19 – 22

2.3.4. Specimen and synthetic water preparation

The protocol followed to prepare the samples is summarised in Figure 2-22 and Figure 2-23. A band saw was first used to pre-cut the PVC tube and core sample under dry conditions at two different lengths, around 25 mm for oedometer tests and around 30 mm for isotropic tests. The samples were then sub-cored under dry conditions with a

lathe to obtain a cross-section with 50 mm in diameter. Afterwards, cores were prepared to match a final height of 20 mm for oedometer tests and 25 mm for isotropic tests. Cores were then packed in plastic bags under vacuum (Figure 2-24). Finally, samples with adequate size for mercury porosimeter tests (1 cm^3) and psychrometer tests were also cut with the band saw and are shown in Figure 2-25.

Figure 2-22. Pre-cutting a slice of the core sample under dry conditions with a band saw.

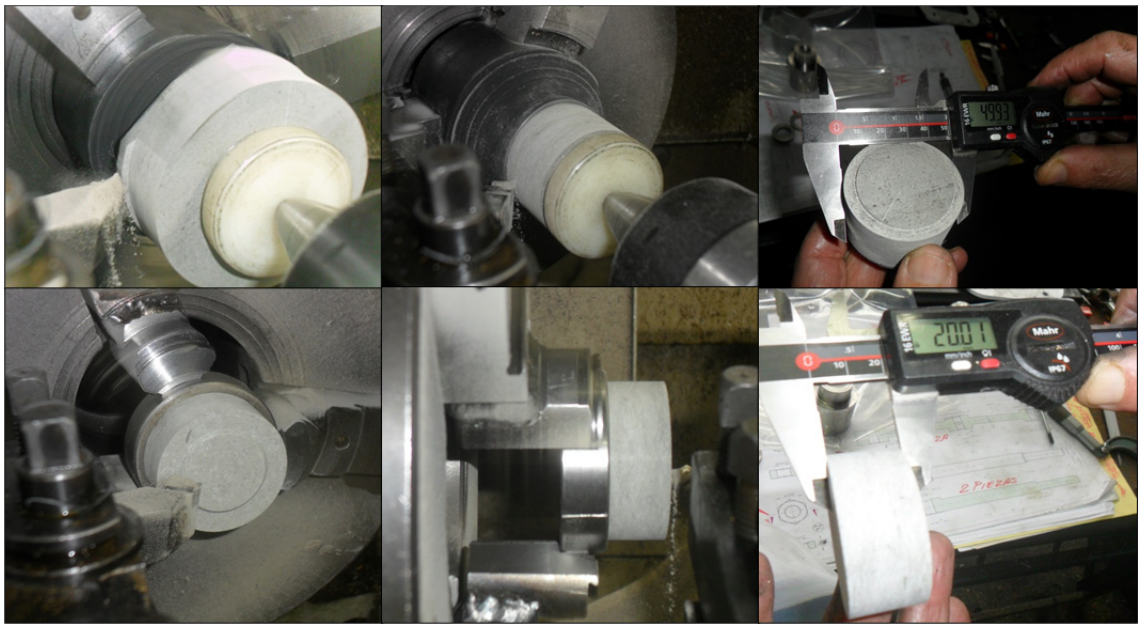

Figure 2-23. Final size of the samples (diameter and height) obtained under dry conditions with a lathe.

Figure 2-24. Sealing under vacuum of the samples ready for testing.

Figure 2-25. Samples for MIP and psychrometer tests cut under dry conditions with a band saw.

Synthetic water for Opalinus and 'Brauner Dogger' is considered to be the same. Therefore, approximately 3 kg of Artificial Pore Water (APW) were prepared following

instructions given by Mäder (2011). After preparation, the APW solution was stirred for 5 days. Osmotic suction was measured using psychrometer readings (WP4 dew point psychrometer) and estimated from electrical conductivity measurements (Romero 1999). Table 2-10 summarises the main properties, where π is the measured osmotic suction, EC is the measured electrical conductivity and a_L is the estimated liquid activity (equivalent to the relative humidity RH of the air in contact with APW). An equivalent osmotic suction (0.98 MPa) of the pore fluid has been measured by Ferrari et al. 2014.

Table 2-10. Properties of Artificial Pore Water.

	π (MPa)	EC (mS/cm)	a_L (-)
APW	1.04 – 1.10	19.30 – 19.42	0.9919 – 0.9923

2.3.5. Pore size distribution tests

Mercury intrusion porosimetry tests were carried out on freeze-dried samples to characterise their porosity network jointly with nitrogen adsorption tests following the same methods described above.

Figure 2-26 shows the cumulative intruded pore volume normalised by solid volume (intruded void ratio e) plotted against the entrance pore size for 'BD' sample. There is some deviation from the initial void ratio (e=0.11) due to the limited capacity of the porosimeter to enter the smallest pores (non-intruded porosity) but the total porosity was covered with the BJH method. Its PSD function displays two dominant pore modes, one at approximately 22 nm and the other at 2.7 nm (Figure 2-27).

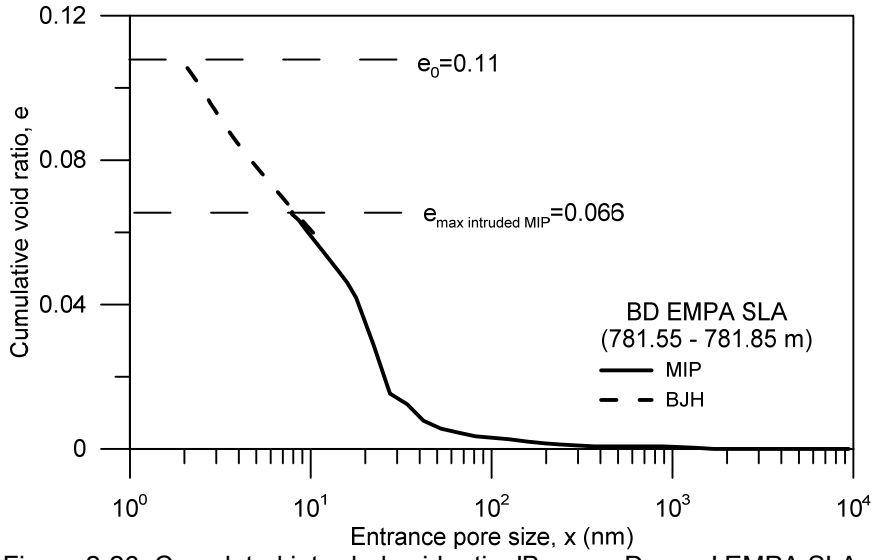

Figure 2-26. Cumulated intruded void ratio. 'Brauner Dogger' EMPA SLA.

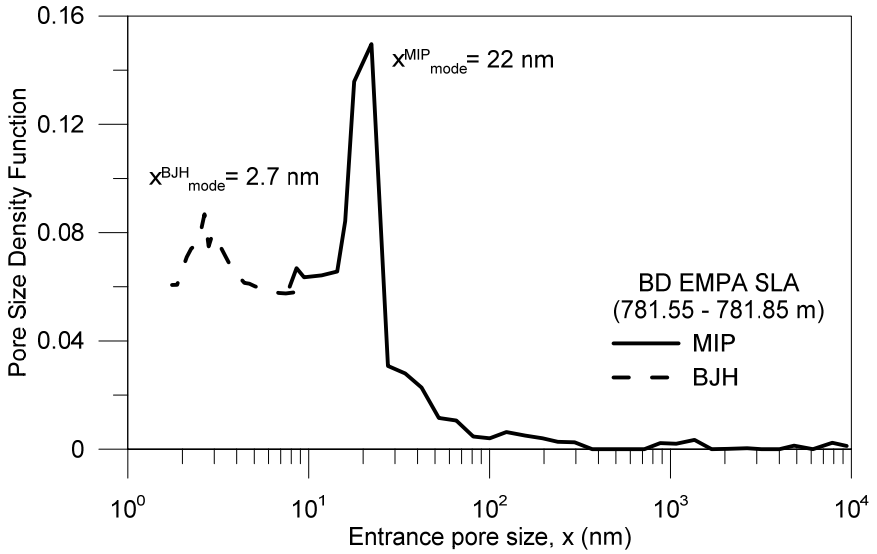

Figure 2-27. PSD Function with dominant pore mode. 'Brauner Dogger' EMPA SLA.

Figure 2-28 shows the equivalent cumulative intruded pore volume normalised by solid volume (intruded void ratio) plotted against the entrance pore size for the Opalinus Clay sample (OED 1/1 936.26 – 936.49 m). There is again deviation from the initial void ratio (e=0.110) due to the non-intruded porosity. In this case, the total porosity is slightly higher than the range covered by the BJH method. The PSD function for this material is plotted in Figure 2-29. With the MIP technique, no dominant peak was detected (< 8 nm) and for this reason, the test on this sample was repeated given the same results. With the BJH method, a pore mode of 2.7 nm was obtained.

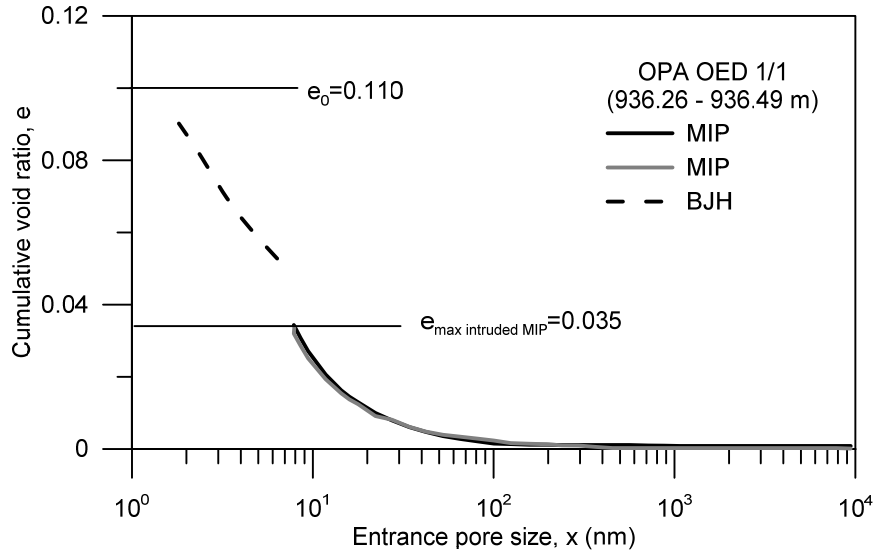

Figure 2-28. Cumulated intruded void ratio. OPA OED 1/1.

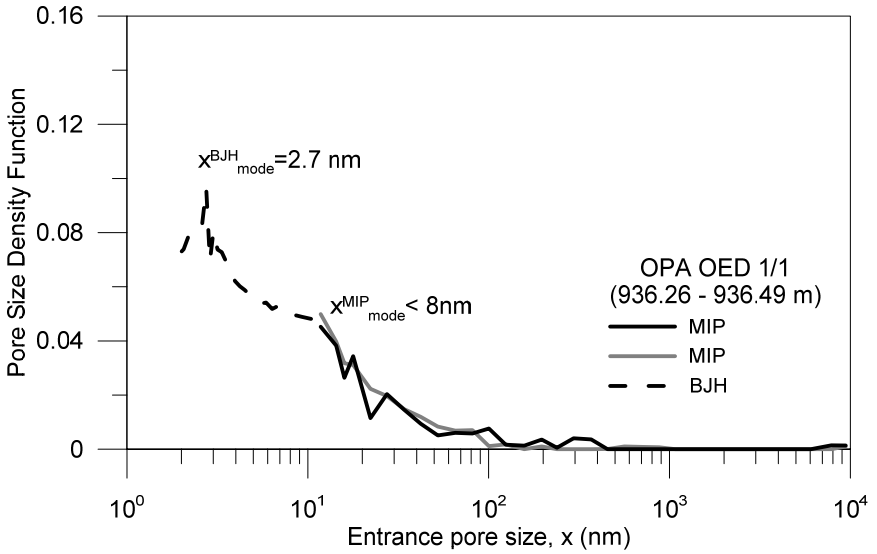

Figure 2-29. PSD Function with dominant pore mode. OPA OED 1/1.

Figure 2-30 and Figure 2-31 show a comparison of the cumulative void ratio and PSD function between samples belonging to the 'BD' sequence at different depths: EMPA SLA (781.55 – 781.85 m) and OED 20/Harz (776.51 – 776.72 m). In Figure 2-32 and Figure 2-33, a comparison between Opalinus sequence samples is shown: OED (879.79 – 880.01 m) and OED 1/1 (936.26 – 936.49 m). In both cases, the deepest samples display a smaller entrance pore size. Data of samples OPA OED and BD OED 20/Harz were published in Romero & Gómez (2013).

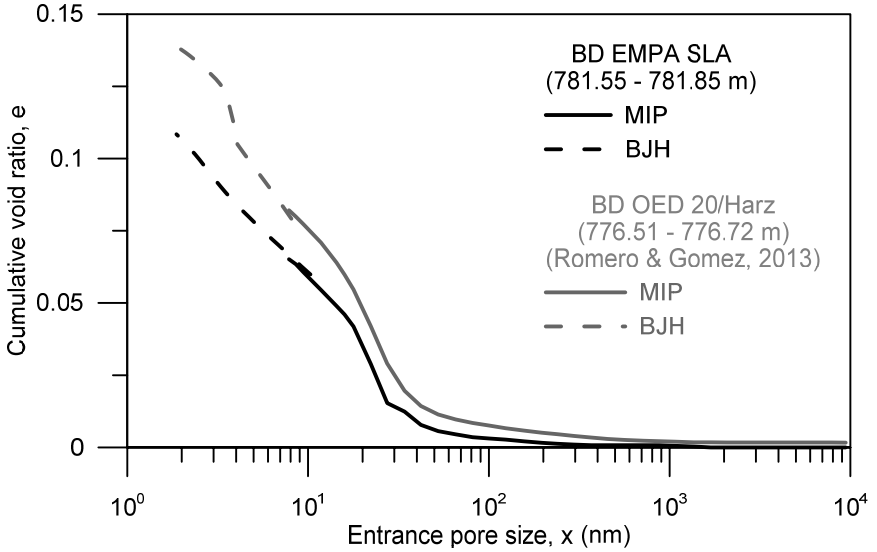

Figure 2-30. Cumulative intruded void ratio comparison between 'Brauner Dogger' samples EMPA SLA and OED 20/Harz.

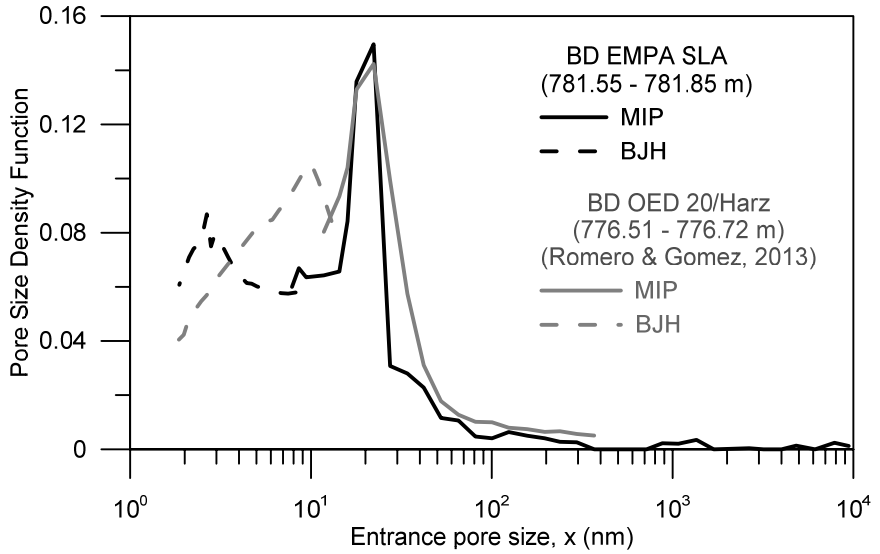

Figure 2-31. PSD function comparison between 'Brauner Dogger' samples EMPA SLA and OED 20/Harz.

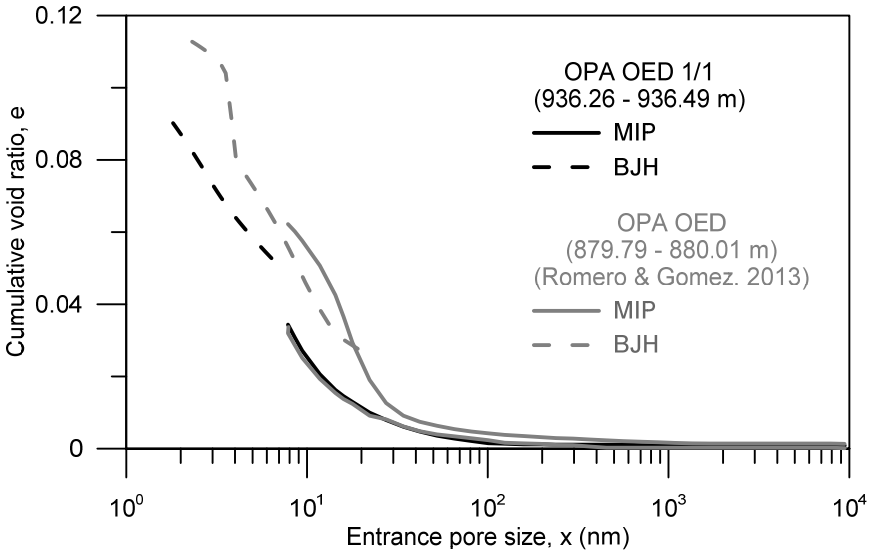

Figure 2-32. Cumulative void ratio comparison between Opalinus Clay samples OED 1/1 and OED.

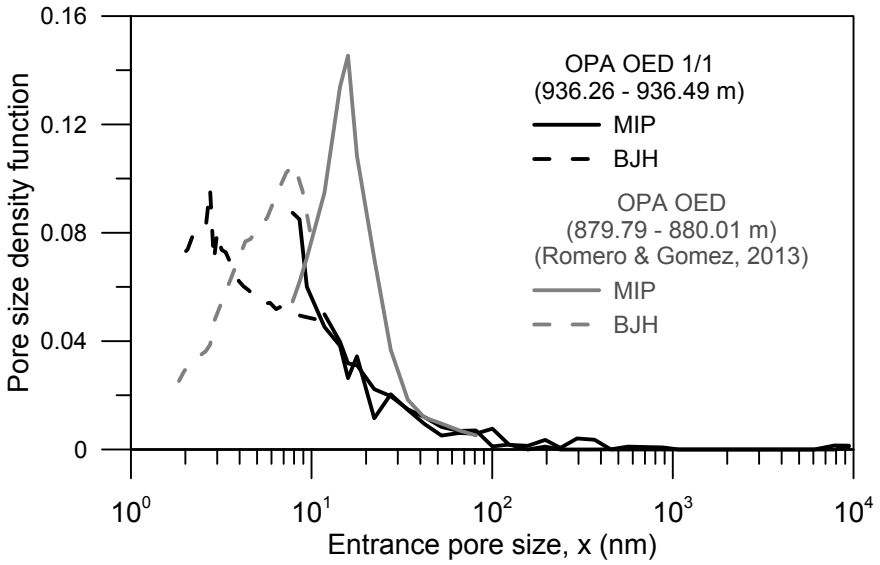

Figure 2-33. PSD function comparison between Opalinus Clay samples OED 1/1 and OED.

2.3.6. Water retention curves

A dew point psychrometer (Cardoso et al. 2007) was used to obtain the water retention curves in the total suction range from 1 to 100 MPa. Figure 2-34 and Figure 2-35 show the estimate water retention curves for EMPA SLA 'Brauner Dogger' (781.55 – 781.85 m) and OED 1/1 Opalinus Clay (936.26 – 936.49 m) samples. The specimens were dried in steps starting from the initial total suction, stored for one day for equalisation, weighed and the total suction was measured with the psychrometer. Then, from the dry state, samples were wetted in steps following identical procedure until saturation. Data obtained with the same method by Ferrari & Laloui (2013) and Ferrari et al. (2014) are included in the figures for comparison showing a good agreement. These figures also include a fitted curve published by Ferrari et al. (2014) with a Van Genuchten´s type expression:

$$S_r = [1 + (s/P_0)^n]^{(-\lambda)} \quad (2.3)$$

The values of fitting parameters are presented in the figures. The fitted curve for OPA samples presented by Ferrari et al. (2014) underestimates the curve for the deeper OED 1/1, so Figure 2-35 also includes a new curve with a high P_0 parameter, showing to this case a larger air entry value (AEV), consistently obtained for the deeper OED 1/1 (936.26 – 936.49 m).

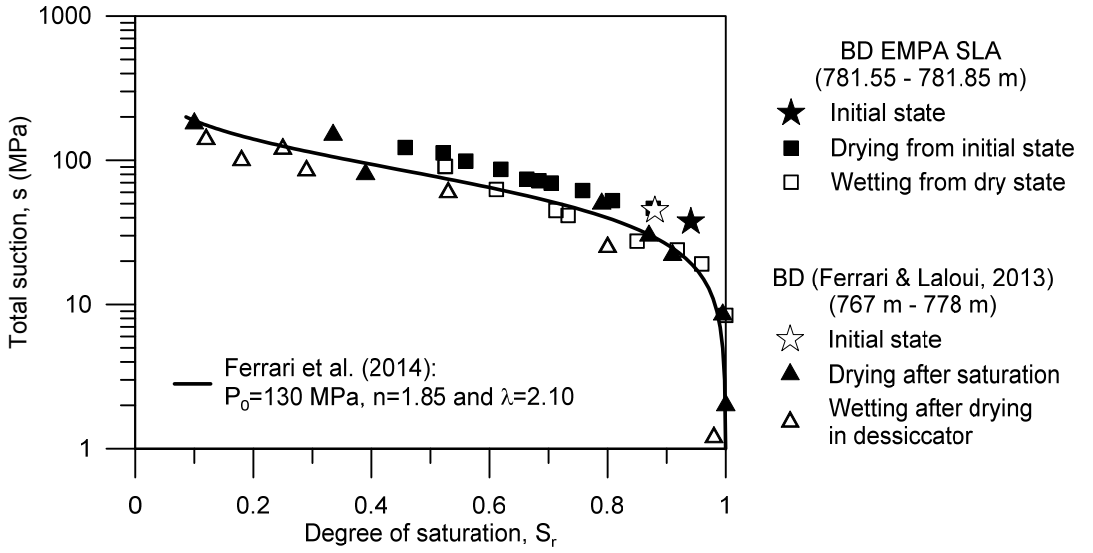

Figure 2-34. Water retention curve of 'Brauner Dogger'.

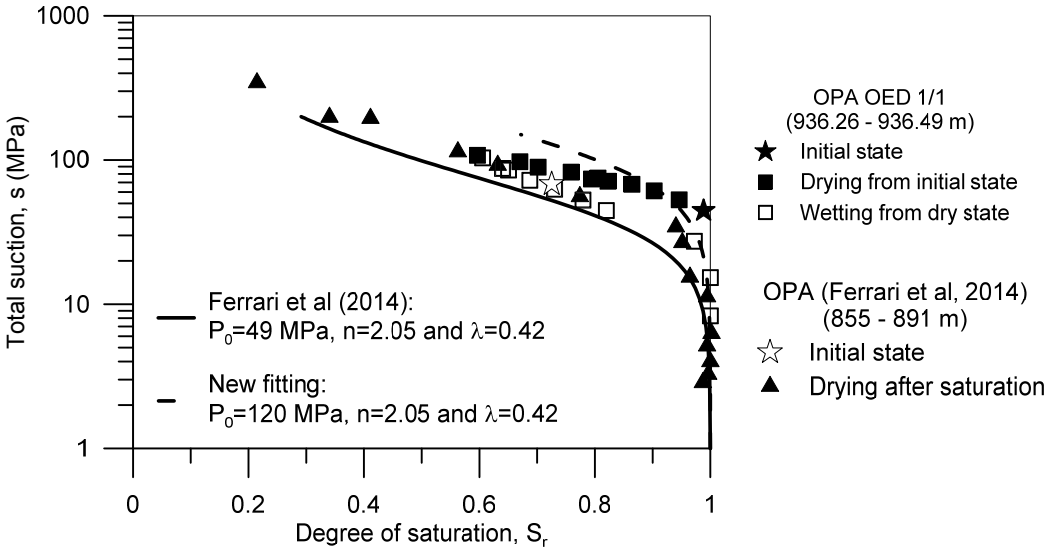

Figure 2-35. Water retention curve. of Opalinus Clay.

The following figures show the comparison between samples of the same sequence at different depths. In the 'Brauner Dogger' case (Figure 2-36), in which the depth is very similar, it can be observed some variations around the saturation state but the same behaviour at higher suction. The highest initial suction of EMPA SLA was due to the lower void ratio value that increased the capillarity pressure.

Figure 2-37 shows the water retention curves of both Opalinus Clay samples. Highest suction values were consistently obtained for the deeper sample.

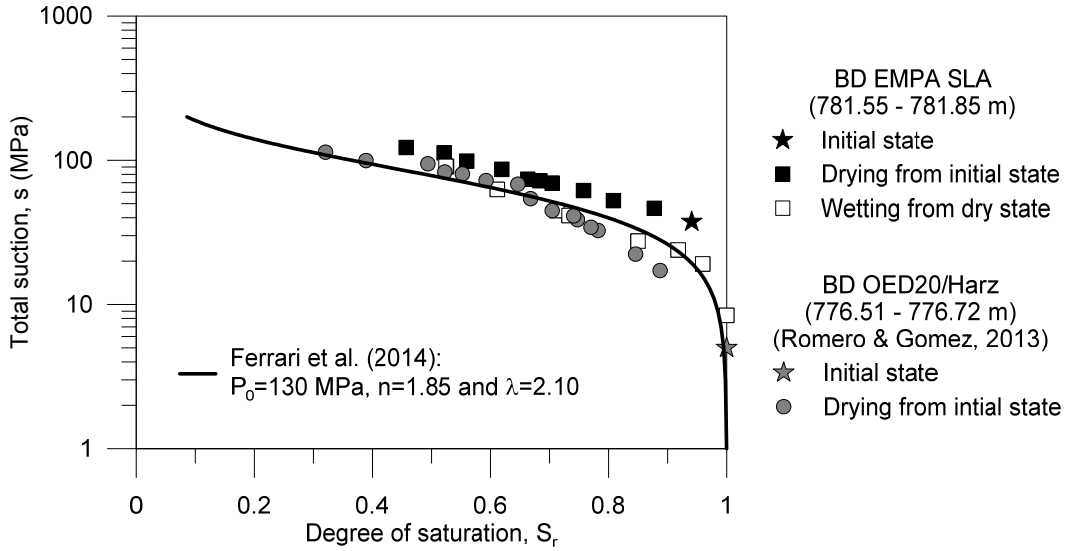

Figure 2-36. Comparison of water retention behaviour of 'Brauner Dogger' samples.

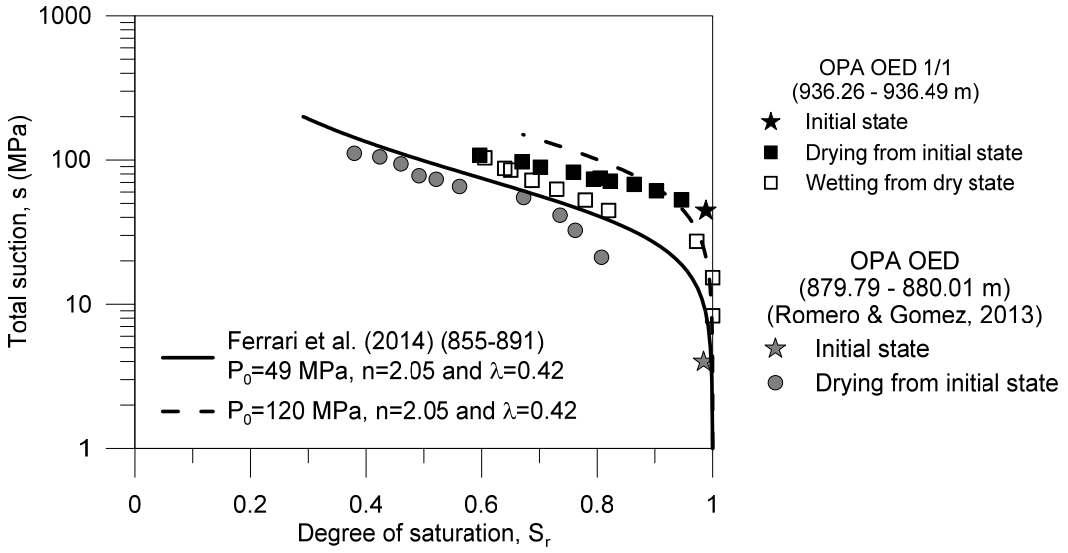

Figure 2-37 Comparison of water retention behaviour of Opalinus Clay samples.

3
EXPERIMENTAL EQUIPMENT AND PROTOCOLS

3.1. Background

Testing very low permeability materials used in the multi-barrier systems for nuclear waste disposal turns out to be an extremely demanding task with respect to the experimental setup and the test duration, typically in the order of several months for a single core sample. The equipment should be designed to match the expected *in situ* stress conditions of the materials, which means that stiff cells are necessary to bear the required high pressures. Moreover, ensuring the gas tightness to prevent leakages is mandatory and can affect the possible installation of sensors and transducers.

Gas migration experiments have been carried out in an extensive range of setups and protocols. The first publications dealing with gas migration were mostly in bentonites and focused on breakthrough experiments in which the gas pressure overpassed the minor principal stress (Pusch & Forsberg 1983; Gallé 2000; Horseman et al. 1999; Tanai & Yamamoto 2003). Swelling pressure oedometer cell and constant volume cell were commonly used in this kind of experiments in order to establish relationships between the dry density of the bentonite and the gas breakthrough pressures.

More recently, laboratory investigations on gas transport processes have been expanded to cover not only the bentonite materials but also the host rocks. Experimental procedures on sedimentary formations (Opalinus Clay, Callovo-Oxfordian claystone or Boom Clay among others), of interest in this study, comprise a wide variety. One of the main aspects to obtain suitable results is to reproduce the *in situ* stress state in the laboratory. As important as the *in situ* state is the pre-conditioning of the rock before testing, which also means reaching the degree of saturation of the natural conditions (Marschall et al. 2005; Romero & Gómez 2013; Harrington et al. 2013; Cuss et al. 2014). Although triaxial and isotropic cells are the most frequently used because its better control of isotropic or anisotropic stresses, studies under constant volume conditions or oedometer conditions have also been carried out since they present some advantages such as better control of injected fluids or deformations

(Villar, Martín, et al. 2012; Villar, Gutiérrez-Rodrigo, et al. 2012; Harrington et al. 2013). Regarding this last issue, the measurements of the deformational behaviour of the samples during the gas migration has been rarely tackled until recently (Romero et al. 2012; Shaw 2013; Cuss et al. 2014; Gonzalez-Blanco et al. 2014). Knowing the volume change behaviour of the materials along the gas injection and dissipation appears to be essential in order to establish the mechanisms of the gas passage.

Other issues that concern the selection of the equipment for studying gas migration are the method to inject the gas, the flow direction and the boundary conditions of the test. Generally, the inlet filter covers the entire area of the sample and the gas flow is applied in the axial direction; however, in some experiments, point-like inlet filters or needles are used to inject the gas (Arnedo et al. 2008; Shaw 2013; Wiseall et al. 2015). The advantage of the first method arises in a more homogeneous propagation of the fluid pressure through the samples, while in the second, it might be difficult to predict the pore pressure distribution, but it easily facilitates imposing radial flow (Volckaert et al. 1995; Harrington & Horseman 2003; Shaw 2013; Harrington et al. 2013). Regarding the way the gas pressure is applied, four different methods can be found in the literature: instantaneous pressure gradient (Hildenbrand et al. 2002; Hildenbrand et al. 2004), constant pressure ramp (Cuss et al. 2014), gas pressure increased stepwise (Shaw 2013) or volumetric rate (Volckaert et al. 1995; Horseman et al. 1999; Tanai & Yamamoto 2003; Harrington & Horseman 2003; Arnedo et al. 2008; Wiseall et al. 2015) being the last two types the most common.

Regarding all these issues, one of the first objectives of this study was to establish robust test protocols to perform the gas injection tests. Great importance was given to measure the deformational response of the materials during gas injection tests, which was rarely tackled when this study began. Another significant subject was to achieve equivalent stress level to the *in situ* one of each material in order to obtain representative results which could be exploitable for the safety assessment of radioactive waste disposal. Therefore, tests protocols were carefully chosen and adapted according to the analysis of the existing results and the requirements of ONDRAF/NIRAS and Nagra. Experimental equipment used in this research was selected based on its stiffness to bear high pressures and the possibility to measure sample displacements. Two cells which were available in the Geotechnical Laboratory of UPC were then selected and updated to fulfil these requirements. Moreover, inlet and outlet lines to allow water and gas flow were required as well as a significant number of external devices to apply boundary conditions. The selection of the boundary conditions during the gas injection tests - initial air pressure, maximum air

pressure, injection rate, etc. - was done based on previous experiments and in the initial set of test performed in Boom Clay which gave a proper justification of them according to experimental evidence.

This chapter addresses all these aspects. Firstly, the experimental equipment is described in detail, including the cells and the external devices. In the second part, a thorough explanation of the protocols followed is presented.

3.2. Experimental equipment

In this section, the experimental equipment used in gas injection tests, oedometer and isotropic cells, is described. Calibration of dead volumes in the cells is included here but axial displacement calibration of both apparatus can be found in Appendix A.

3.2.1. Oedometer setup

3.2.1.1. Equipment description

The main experimental work developed in this research was carried out in an unconventional oedometer. The setup for the oedometer tests (Figure 3-1), which consists of the oedometer cell, the boundary condition controllers and the data acquisition system, is described in detail below.

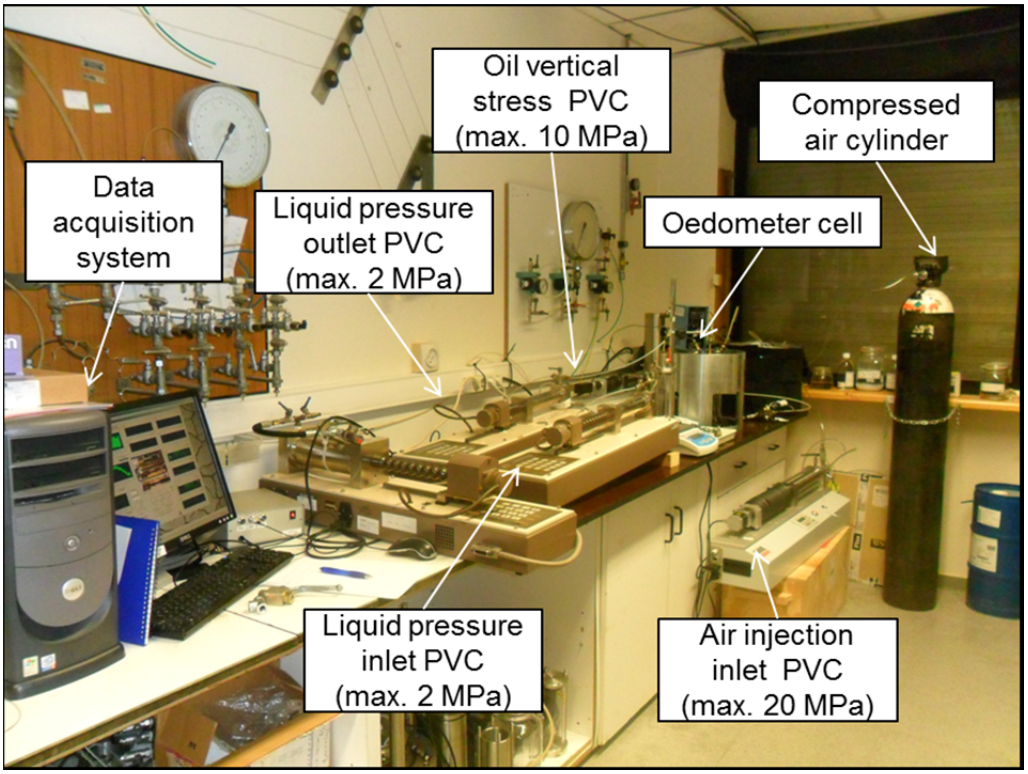

Figure 3-1. Setup for oedometer tests.

❖ *Oedometer cell*

A high capacity oedometer cell was updated to perform the current study. Initially, this equipment was designed to measure and apply temperature and suction. Therefore, it consists of an oedometer cell placed inside a thermal bath with a system for controlling suction which was specifically constructed for vapour and water transfer (Lima 2011). Figure 3-2 depicts a drawing of the equipment before its updating.

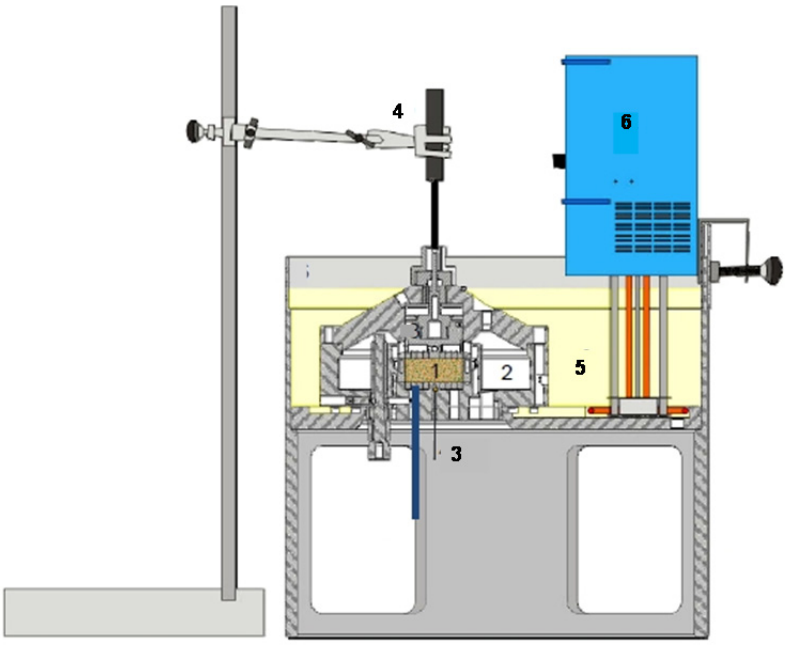

Figure 3-2. Setup of the temperature and suction controlled oedometer cell (Lima 2011): (1) soil sample; (2) annular vessel for saline solution; (3) thermocouple; (4) LVDT to monitor vertical displacements; (5) thermal bath filled with silicone oil and (6) thermostat.

To perform gas tests on saturated samples, a steel ring was designed to isolate and seal the sample from the vapour transfer chamber by two o-rings (Figure 3-3a). In this way, isolation ring also served to reduce the dead volume in the system. Additionally, several steel and brass parts were built to ensure separation of the inlet and outlet lines at each cap of the sample, prepared for gas and liquid connections (Figure 3-3b). A pneumatic axial loading piston (blocking system – number 3 in Figure 3-4), which supports a vertical stress capacity of more than 20 MPa, is used to apply vertical load.

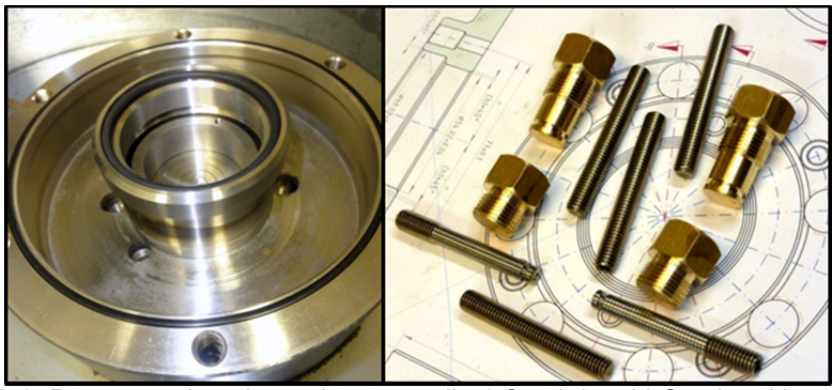

Figure 3-3. Parts to update the oedometer cell. a) Steel ring; b) Steel and brass parts.

The soil samples (height of 20 mm in a 50 mm diameter ring) were placed between the top and bottom caps made of concentric stainless steel rings (number 1 in Figure 3-2 and Figure 3-4), which operate as coarse porous stones allowing the injection and recovery, as well as the proper distribution of the injected fluids (water and air).

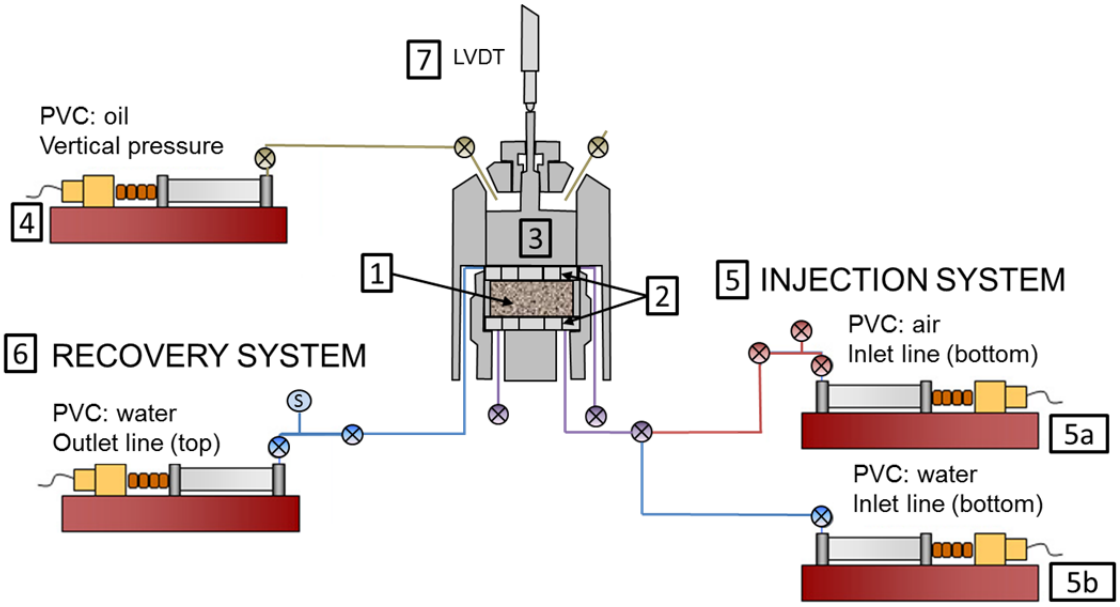

Figure 3-4. Scheme of oedometer setup: 1) Sample; 2) Coarse porous rings; 3) Hydraulic piston; 4) Oil PVC; 5) Injection system: a) water PVC, b) air PVC; 6) Recovery system: water PVC; 7) LVDT.

❖ *Boundary condition controllers*

Silicone oil (WACKER AK5) was chosen to apply vertical load through an automatic pressure/volume controller (PVC) from Wille Geotechnik (Germany). This controller has a maximum range of 10 MPa (volume 250 mL) with a resolution of 0.1 kPa and 0.05 mL. It is connected to the axial piston with a high strength steel tube to ensure proper transmission of the load and to prevent leakages. This controller was replaced by a higher capacity one (from GDS Instruments Ltd., United Kingdom) when the stress

level of the test required it. Its maximum range of pressure is 64 MPa with a resolution of 64 kPa.

The equipment uses other three automatic PVCs, two for water (injection and recovery at the downstream point), and one for gas (injection at the upstream point), which can be used in combination (for example, air injection and water pressure at downstream or water pressure at both sides). The gas injection PVC from Wille Geotechnik, that was specifically acquired for this research, has a maximum range of 20 MPa (volume 500 mL) and is able to control volume rates between 10^{-4} mL/min and 100 mL/min (volume resolution 1 mm^3). It is connected to a compressed air cylinder to achieve high pressures. The other two controllers are from GDS Instruments, with a maximum range of 2 MPa (volume 200 mL) and a resolution of 1 kPa (1 mm^3). The controller located at downstream was protected with a safety valve of 2 MPa of maximum pressure. All of these controllers have volume change gauges for the precise regulation and measurement of fluid pressure and volume changes.

Vertical displacements are measured with a calibrated external linear variable differential transformer (LVDT) from Solartron Metrology with a range of measurement of ±0.5 mm and a resolution of 0.001 mm.

Figure 3-4 depicts a scheme of the controllers' configuration and the connection lines with the oedometer cell.

- *Data acquisition system*

The data acquisition software was developed in Visual Basic (Microsoft) in order to monitor the pressures and volumes of controllers and the vertical displacements.

3.2.1.2. Dead volume determination of bottom and top lines

To determine the dead volume of the inlet and outlet lines, the equipment was mounted with a fake steel sample and loaded to ensure the proper contact between the porous disc and the steel piece.

The inlet line consists of: the air controller; five high pressure ball valves (three of them connected with a 'T' adaptor); approximately 2.1 m of metal tubing of 1.4 mm of inner diameter; and, the gaps inside the cell. Its volume (Figure 3-5), including the porous disc at the bottom, was measured using the air pressure decay method in each stretch, assuming that $P \cdot V = const$. The air PVC was filled with air at the beginning of every injection test (Stretch 1 in the figure). The results are shown in Table 3-1.

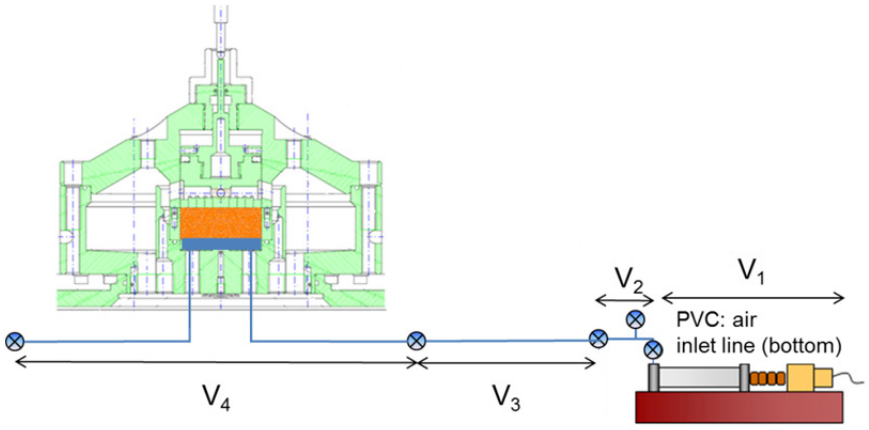

Figure 3-5. Scheme of inlet line in the oedometer cell.

Table 3-1. Volume of each stretch in the inlet line in the oedometer cell.

Stretch	Pressure (kPa)	Accumulated volume (mL)	Volume (mL)
1 (PVC)	1920.08	500	
2	1889.20	508.1728	8.1728
3	1859.92	516.1727	7.9999
4	1799.92	533.3793	17.2065
Total volume of inlet lines			33.3793

The outlet line consists of: the water controller; two high pressure ball valves; one low pressure valve; a safety valve to protect the controller; approximately 2.2 m of metal tubing of 1.4 mm of inner diameter; and, the gaps inside the cell. Its volume (Figure 3-6) was determined with direct measured of water volume to the second stretch and using the air pressure decay method inside the cell (third stretch), including the porous disc at the top. The water PVC in the outflow line was partially filled with water during the injection tests (around 34 mL). The approximate volume of the outlet lines was 88.5 mL. The results are shown in Table 3-2.

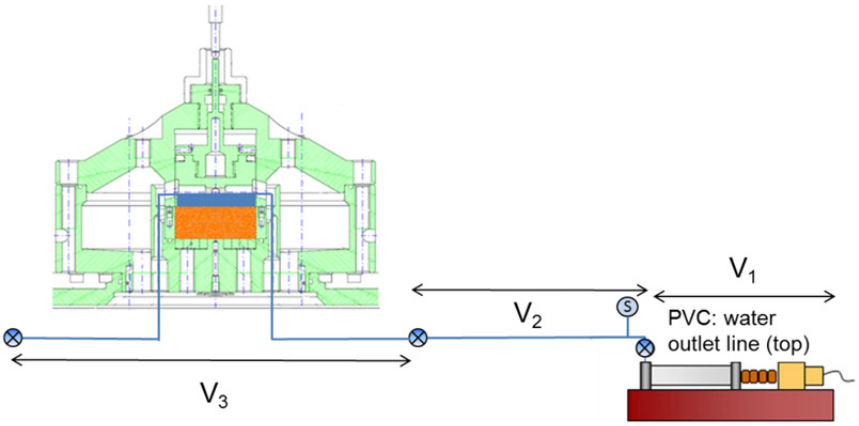

Figure 3-6. Scheme of outlet line in the oedometer cell.

Table 3-2. Volume of each stretch in the outlet line in the oedometer cell.

Stretch	Volume (mL)
1 (PVC)	34.189
2	10.611
3	43.668
Total volume of outflow lines	88.468

3.2.2. Isotropic setup

3.2.2.1. Equipment description

The isotropic cell was used to carry out air injection tests in deep indurated clays: Opalinus Clay and 'Brauner Dogger'. The setup for the oedometer tests (Figure 3-7), which consists of the isotropic cell, the boundary condition controllers and the data acquisition system, is described in detail below.

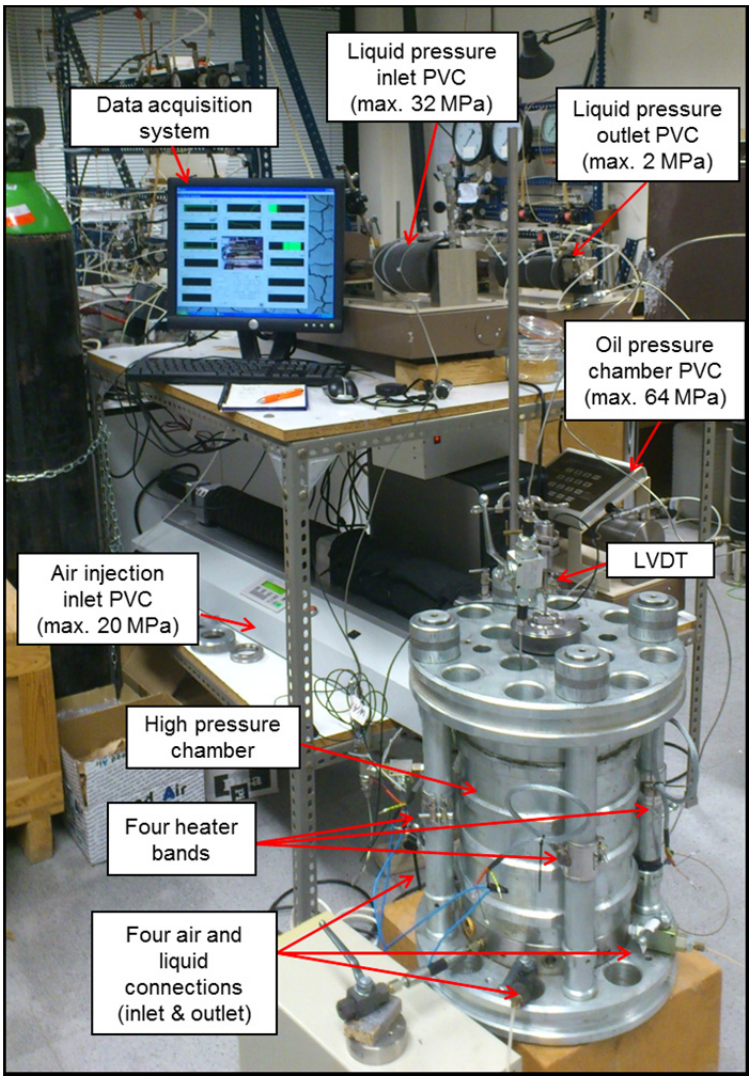

Figure 3-7. Setup for isotropic tests.

❖ *Isotropic cell*

The instrumented high-pressure isotropic cell was developed by Pineda et al. (2014). The cell was specifically designed to apply isotropic/anisotropic stress states up to a maximum of 40 MPa and was updated for injecting air at a controlled volume rate. Figure 3-8 shows a scheme of the isotropic cell jointly with the test setup. Each cap of the isotropic cell has inlet and outlet lines, prepared for air and water connections.

In order to preload the system and avoid leakage from the chamber, four heater bands were installed in each lateral rod (see the photo of the setup in Figure 3-7). Once the equipment was mounting and before tightening the locking thread, bands heated the steel rods and these dilated. Then the threads were tightened and taking advantage of compression due to cooling, the preload was achieved.

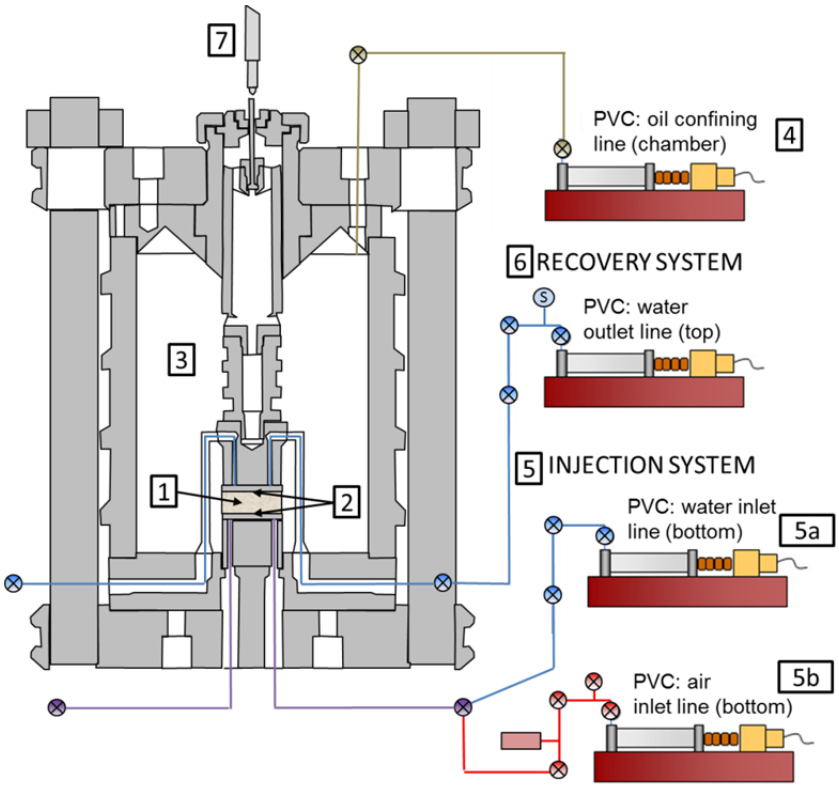

Figure 3-8. Scheme of the isotropic setup. 1) Sample; 2) Coarse porous rings; 3) Chamber; 4) Oil PVC; 5) Injection system: a) water PVC, b) air PVC; 6) Recovery system: water PVC; 7) LVDT.

To carry out the isotropic tests, a protocol to specimen mounting was developed (Figure 3-9). Samples 50.0 mm in diameter and 25.0 mm high were installed in the isotropic cell using three 1 mm thick neoprene membranes. Aluminium foils stuck with silicone grease were placed between membranes. Two o-rings and a metallic clamp were used at each end. In this way, air migration from the sample to the chamber was prevented.

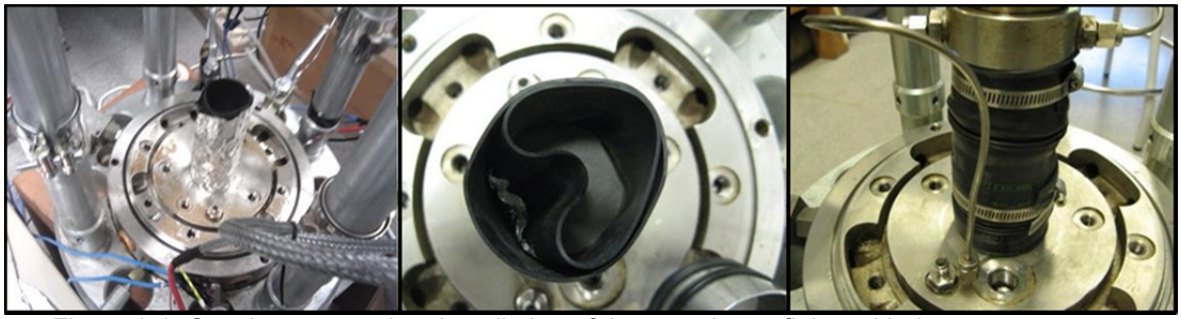

Figure 3-9. Specimen mounting: installation of the sample confining with three neoprene membranes and two aluminium foils.

❖ *Boundary condition controllers*

The equipment uses the same automatic pressure/volume controllers presented above: one to apply confining stress with oil pressure up to 64 MPa, one for gas (injection at the upstream point), and two for water (injection at upstream point and extraction at the downstream point).

The axial deformation of low-height specimens –confined by several neoprene membranes and aluminium foils– is registered with an external linear variable differential transformer (LVDT in Figure 3-8) from Solartron Metrology with a range of measurement of ±0.5 mm and a resolution of 0.001 mm.

❖ *Data acquisition system*

The data acquisition software was developed in Visual Basic (Microsoft) in order to monitor the pressures and volumes of controllers and the vertical displacements.

3.2.2.2. Dead volume determination of bottom and top lines

To determine the volume of the inlet and outlet lines, the equipment was mounted with a fake steel sample and loaded to ensure the proper contact between the porous disc and the steel piece.

The inlet line consists of: the air controller; six high pressure ball valves (three of them connected with a 'T' adaptor); approximately 0.97 m of metal tubing of 1.4 mm of inner diameter; and, the gaps inside the cell. Its volume (Figure 3-10), including the porous disc at the bottom, was measured using the air pressure decay method in each stretch, assuming that $P \cdot V = const$. The air pressure/volume controller (PVC) was filled with air at the beginning of every injection test (Stretch 1 in the figure). The results are shown in Table 3-3.

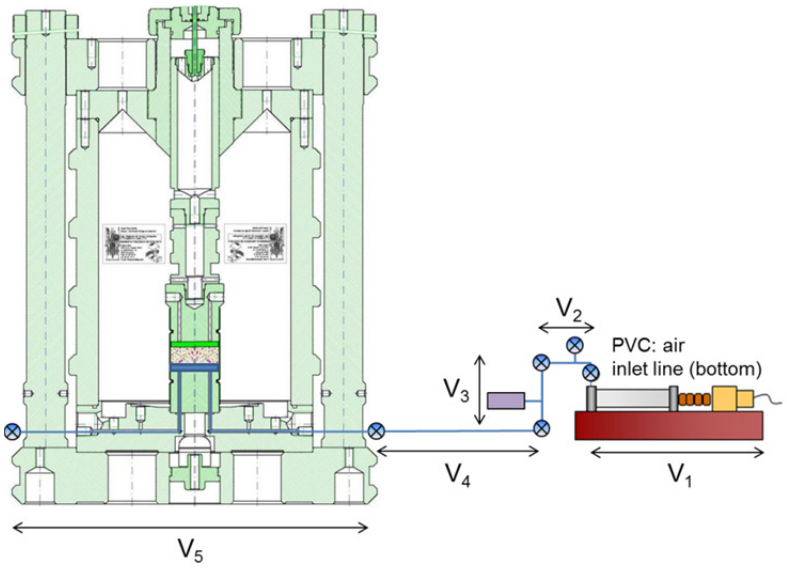

Figure 3-10. Scheme of inlet line in the isotropic cell.

Table 3-3. Volume of each stretch in the inlet line in the isotropic cell.

Stretch	Pressure (kPa)	Accumulated volume (mL)	Volume (mL)
1 (PVC)	2800.25	500	
2	2729.72	512.9189	12.9189
3	2659.72	526.4182	13.4993
4	2599.72	538.5676	12.1494
5	2519.72	555.6669	17.0993
Total volume of inlet lines			55.6669

The outlet line consists of: the water controller; four high pressure ball valves; one low pressure valve; a safety valve to protect the controller; approximately 2 m of metal tubing of 1.4 mm of inner diameter; and, the gaps inside the cell. Its volume (Figure 3-11) was determined with direct measured of water volume to the second stretch and using the air pressure decay method inside the cell (third stretch), including the porous disc at the top. The water PVC in the outflow line was partially filled with water during the injection tests (approximately volume of 22 mL). The results are shown in Table 3-4.

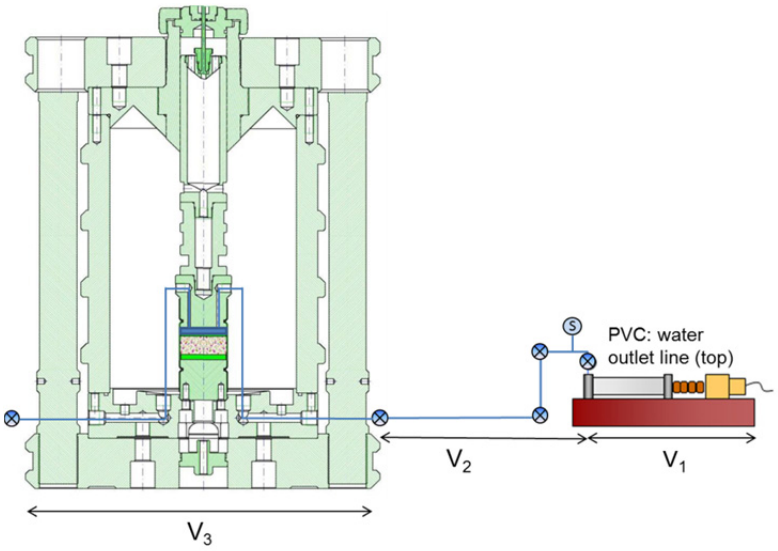

Figure 3-11. Scheme of outlet line in the isotropic cell.

Table 3-4. Volume of each stretch in the outlet line

Stretch	Accumulated volume (mL)	Volume (mL)
1 (PVC)	22.3973	
2	34.3373	11.9400
3	45.9343	11.5970
Total volume of outflow lines		23.5370

For both cases, relatively high volumes were obtained. Although the tubing is as thinnest as possible (1.54 mL/m), the ball valves contain large volume. These volumes were not the same as the used ones in Romero & Gómez (2013) whose results were used in this research for comparison since the equipment setup was updated for the new tests. However, it was expected that there were very similar.

3.3. Test protocols

During the research, innovative test protocols were used. As the investigation progressed, the protocols were modified to adapt to new needs and/or ONDRAF/NIRAS and Nagra requirements.

One of the greatest concerns at the beginning of the research was to select suitable boundary conditions during the gas injection. Results from previous experiments on Opalinus Clay (Romero et al. 2010) with air boundary condition at both sides of the sample reflected that this fact affected the degree of saturation, showing an important reduction. As a consequence, the air diffusion increased, the air injection pressure

decayed and the breakthrough did not occur (Figure 3-12). Moreover, it is known that the breakthrough pressure depends on the degree of saturation of the material (Graham et al. 2002). In order to keep the specimens close to the full saturation, water was selected for the downstream boundary condition in all the gas tests.

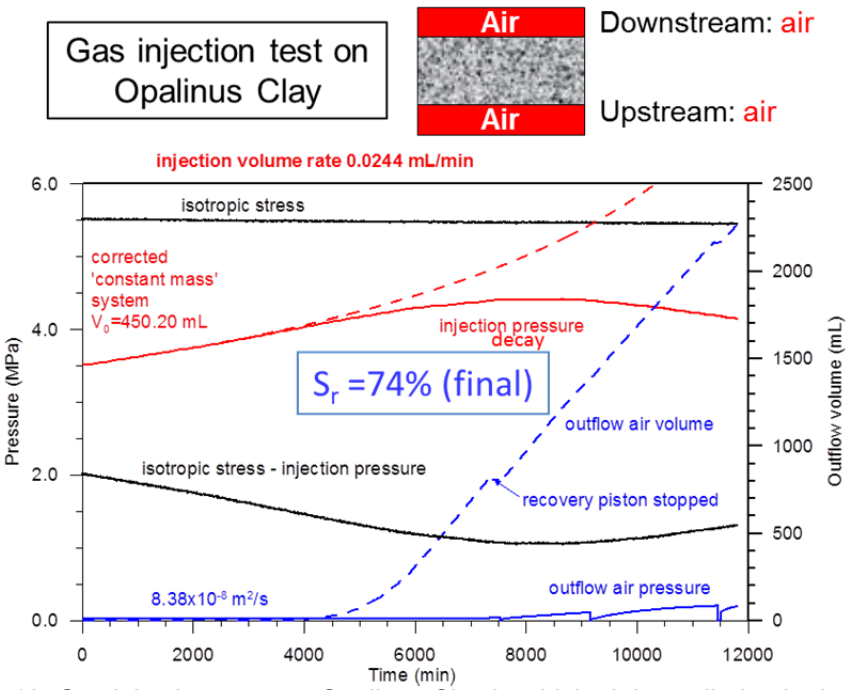

Figure 3-12. Gas injection tests on Opalinus Clay in which air is applied at both sides of the sample (after Romero et al. 2010).

Regarding the gas injection rate, there are still some uncertainties about the repository behaviour. It is assumed that if the gas production rate exceeds the rate of diffusion of gas in the host rock, the pore-water pressure will increase and gas will migrate through the matrix. It could be partially displacing water and entailing two-phase flow conditions, and/or through preferential gas pathways that may develop, possibly taking advantage of the material heterogeneity and anisotropy (bedding planes), previously sealed discontinuities in the EDZ (Excavation Damaged Zone) or along EBS (Engineered Barrier System)/EDZ interfaces. Gas flow through preferential pathways, under consideration of this study, implies relatively high gas injection rates to minimize the diffusion phenomenon. Initially, a fast injection rate of 100 mL/min was used. This rate was reduced fifty times (2 mL/min) to study the influence of the injection rate in the material behaviour along the gas injection process. In the case of the 'Brauner Dogger', the rate was reduced again fifty times (0.04 mL/min) because of no significant differences were found with the previous rates.

The strategies with respect to the stress level presented some differences between Boom Clay tests and tests on the indurated rocks.

In terms of the stress level during Boom Clay experiments, two different approaches were employed. Initially, high stress levels were used towards determining the threshold values of the minimum and maximum gas pressure in relation to the stress level. These test protocol has been classified as “High stress tests on Boom Clay”. Afterwards, it was decided to reduce the stress levels in order to be closer to the *in situ* one, so that, a second series of tests “Low stress tests on Boom Clay” was launched.

The stress levels along tests on the indurated rocks were higher than in Boom Clay in order to be similar to the *in situ* conditions. In these materials, two setups were used: the oedometer cell to determine the compressibility properties; and the isotropic cell for gas injection tests. For the isotropic tests, a simplified protocol of the one presented in Romero & Gómez (2013) was employed so that a comparison of the results could be made. Moreover, two injections were performed in each sample at different stress state or different injection rate. Equivalent stress path was followed in the oedometer tests.

The established protocols for each group of tests and material are described in detail in this section. Table 3-5 summarizes the protocols and boundary conditions of Boom Clay experiments, while Table 3-6 deals with tests performed on indurated clays.

Table 3-5. Test protocols and main boundary conditions for Boom Clay experiments.

Protocols for Boom Clay		Maximum vertical stress, $\sigma_{v\,max}$ (MPa)	Minimum air pressure, $u_{a\,min}$ (MPa)	Maximum air pressure, $u_{a\,max}$ (MPa)	Injection rate, r (mL/min)	Bedding plane orientation	Test label
High stress protocols	Protocol 1	9	3 6	8.5	100	Orthogonal	P1_FI_N
						Parallel	P1_FI_P
	Protocol 2	14	3	8.5	100	Parallel	P2_FI_P
Low stress protocols	Protocol 3	6	0.5	4	100	Orthogonal	P3_FI_N_1
							P3_FI_N_2
						Parallel	P3_FI_P_1
							P3_FI_P_2
					2	Orthogonal	P3_SI_N_1
							P3_SI_N_2
						Parallel	P3_SI_P
	Protocol 4	6	-	-	-	Orthogonal	P4_NI_N_1
							P4_NI_N_2
							P4_NI_N_3

Table 3-6. Test protocols and main boundary conditions for indurated rock experiments.

Protocols for Opalinus Clay and 'Brauner Dogger'		Maximum vertical stress, $\sigma_{v\,max}$ (MPa)	Minimum air pressure, $u_{a\,min}$ (MPa)	Maximum air pressure, $u_{a\,max}$ (MPa)	Injection rate, r (mL/min)	Bedding plane orientation	Test label
Oedometer tests	Opalinus Clay	25	-	-	-	Orthogonal	OPA_Oed-
	'Brauner Dogger'	25	-	-	-	Orthogonal	BD_Oed
Isotropic tests	Opalinus Clay	15	3	14	100	Orthogonal	OPA_Iso
		19		18			
	'Brauner Dogger'	15	3	14	2	Orthogonal	BD_Iso
					0.04		

3.3.1. Test protocols for Boom Clay

Four different protocols were defined for Boom Clay experiments. As the first stage of all of them is the same, it is initially explained in detail and afterwards, each protocol is described.

3.3.1.1. Pre-conditioning paths

The pre-conditioning paths are mandatory to reach the geostatic conditions of the material in the *in situ* state which will be the starting point of any oedometer test, ensuring the most similar stress state. These paths mainly consist in loading the samples up to a pre-defined stress level at constant water content reducing the initial suction and afterwards, saturating the sample with synthetic water. Through this process, it is achieved that the effective vertical stress, when the water pressure is applied, is close to the *in situ* one. Therefore, the first stage of all test protocols corresponds to this pre-conditioning path.

Boom Clay displays a high initial suction (around 2.5 MPa, see Table 2-3 in Chapter 2), due to the important stress relief, despite being saturated. The samples can undergo expansion and degradation as a clear consequence of suction reduction effects due to water contact at low stress levels (Lima 2011). To minimise these effects, the samples were always loaded at a target total stress and only then put in contact with water under atmospheric pressure to avoid any damage on the samples. Therefore, at the moment of applying the water pressure, the effective stress state will be equivalent to the *in situ* one.

At oedometer conditions, a total vertical stress of 3 MPa was considered to be the initial total vertical stress. On the one hand, 3 MPa is enough high to avoid a large swelling during saturation. On the other hand, it enables to reach the *in situ* effective stress after imposing water pressure and at the same time, keeping the stress level within the working range of the equipment. This first stage was carried out at a relatively fast rate of 15 kPa/min and at constant water content. During this path, it was expected to reduce the initial suction down to zero, since total stress will be transmitted to the pore pressure (initially with a total suction around 2.5 MPa). Therefore, small deformations due to suction changes are predicted.

Once a total stress of 3 MPa was reached, the samples were put in contact with SBCW at atmospheric pressure at the top and bottom sides in order to ensure full saturation. After reaching steady state conditions, water pressure at the downstream and

upstream boundaries was increased up to 0.5 MPa and hence, once the pore pressure was equalized, vertical effective stress compared with the *in situ* one.

3.3.1.2. High pressure test protocols for Boom Clay

These tests were performed with the objective of establishing threshold air pressures. Initial air pressure was targeted below and above the air entry value determined by MIP, while maximum air pressure was slightly inferior to the vertical stress and similar to the estimated horizontal stress (Protocol 1). This way, gas flow through the sample-ring interface was expected since the minor principal stress may be exceeded. This protocol also enabled to obtain the K_0 value but in terms of total stresses, and thus to settle the minimum difference between the maximum air pressure and the vertical / horizontal stresses in order to avoid gas flow through the interface for further experiments. Moreover, a demonstration test (Protocol 2) was performed reaching a higher difference between the maximum air pressure and the vertical stress to check the validity of this initial hypothesis.

❖ *Protocol 1: Gas flow though interface*

Two tests following this protocol were performed with bedding planes oriented parallel and orthogonal to flow. The different stages followed along the gas flow through interface protocol are summarised below and schematically represented in Figure 3-13:

- Stage 1 - Pre-conditioning path: as explained above a loading stage at constant water content was carried out before putting the sample in contact with SBCW to prevent damage as a consequence of suction reduction. After flooding, water pressure was increased to reach effective stress level equivalent to the *in situ* one. Therefore, this stage can be divided into three sub-stages and it was followed in all the Boom Clay protocols:
    - Loading at constant water content: vertical load from 0.1 to 3 MPa is applied without contact with SBCW at a constant and relatively fast rate of 15 kPa/min. The fast rate is justified since water is not being displaced (initial suction is only reduced). Suction reduction and the high stress applied prevent soil swelling during saturation which may modify the soil microstructure, and as consequence, the soil mechanical properties (Delage, Le, et al. 2008; Lima 2011).
    - At constant vertical stress of 3 MPa, samples were put in contact with SBCW at both sides of the sample and at atmospheric pressure to ensure full saturation. This process was run until the deformational response of the material was steady over time.

- - Water pressures at upstream (bottom cap) and downstream (top cap) points were increased from 0 (atmospheric pressure) to 0.5 MPa.

- Stage 2 - Water permeability determination: water pressure at the bottom side was increased from 0.5 to 0.6 MPa to induce flow of water through the sample. Downstream pressure remained constant (0.5 MPa, this top cap pressure was maintained constant along the different stages of the test) Axial deformation was monitored along this hydraulic process. Water permeability was measured under steady state conditions. After that, the backpressure was reduced to 0.5 MPa.
- Stage 3 - Drained loading: Vertical load from 3 MPa to 9 MPa was applied at a rate of 0.5 kPa/min ensuring drainage conditions (Lima 2011). Water pressures in both top and bottom caps were maintained constants and axial displacement was monitored along this mechanical process.
- Stage 4 - Water permeability determination: At a constant vertical stress of 9 MPa, water pressure at upstream was increased to 1.5 MPa and water permeability was measured under steady state conditions. Axial deformation was monitored along this hydraulic process.
- Stage 5 - Drainage of bottom cap: Water pressure in the upstream vessel was reduced to atmospheric conditions to allow for its fast replacement by air. Air pressure at the upstream point was rapidly increased from atmospheric conditions to a value 3 MPa.
- Stage 6 - Air injection below AEV: Fast air injection from 3 to 8.5 MPa at constant flow rate of 100 mL/min (constant vertical stress of 9 MPa) was applied, followed by a shut-off and recovery phase at constant air volume. Initial air pressure was below the air entry value (AEV). Evolutions of upstream and downstream pressures, as well as outflow volume and sample axial deformation, were measured during the injection and dissipation stages. Air permeability was determined at this step.
- Stage 7 - Re-saturation: Air pressure in the upstream vessel was reduced to atmospheric conditions to allow for its fast replacement by water. Upstream water pressure was then increased to 0.6 MPa to allow for sample re-saturation and water pore pressure equalisation and then water permeability was measured under steady state conditions.
- Stage 8 - Drainage of bottom cap: Water pressure in the upstream vessel was reduced to atmospheric conditions to allow for its fast replacement by air. Air pressure at the upstream point was rapidly increased from atmospheric conditions to a value 6 MPa.

- Stage 9 - Air injection above AEV: Fast air injection from 6 to 8.5 MPa at constant flow rate of 100 mL/min (constant vertical stress of 9 MPa) was imposed, followed by a shut-off and recovery phase at constant air volume. Initial air pressure was above the air entry value (AEV). Evolutions of upstream and downstream pressures, as well as outflow volume and sample axial deformation, were measured during the injection and dissipation stages. Air permeability was determined at this step.
- Stage 10 - Re-saturation: Air pressure in the upstream vessel was reduced to atmospheric conditions to allow for its fast replacement by water. Upstream water pressure was then increased to 0.6 MPa to allow for sample re-saturation and water pore pressure equalisation and then water permeability was measured under steady state conditions.
- Stage 11 - Drained unloading: Vertical stress was decreased from 9 to 0.5 MPa at a rate of 1 kPa/min and simultaneously, both upstream and downstream pressures were reduced to 0.

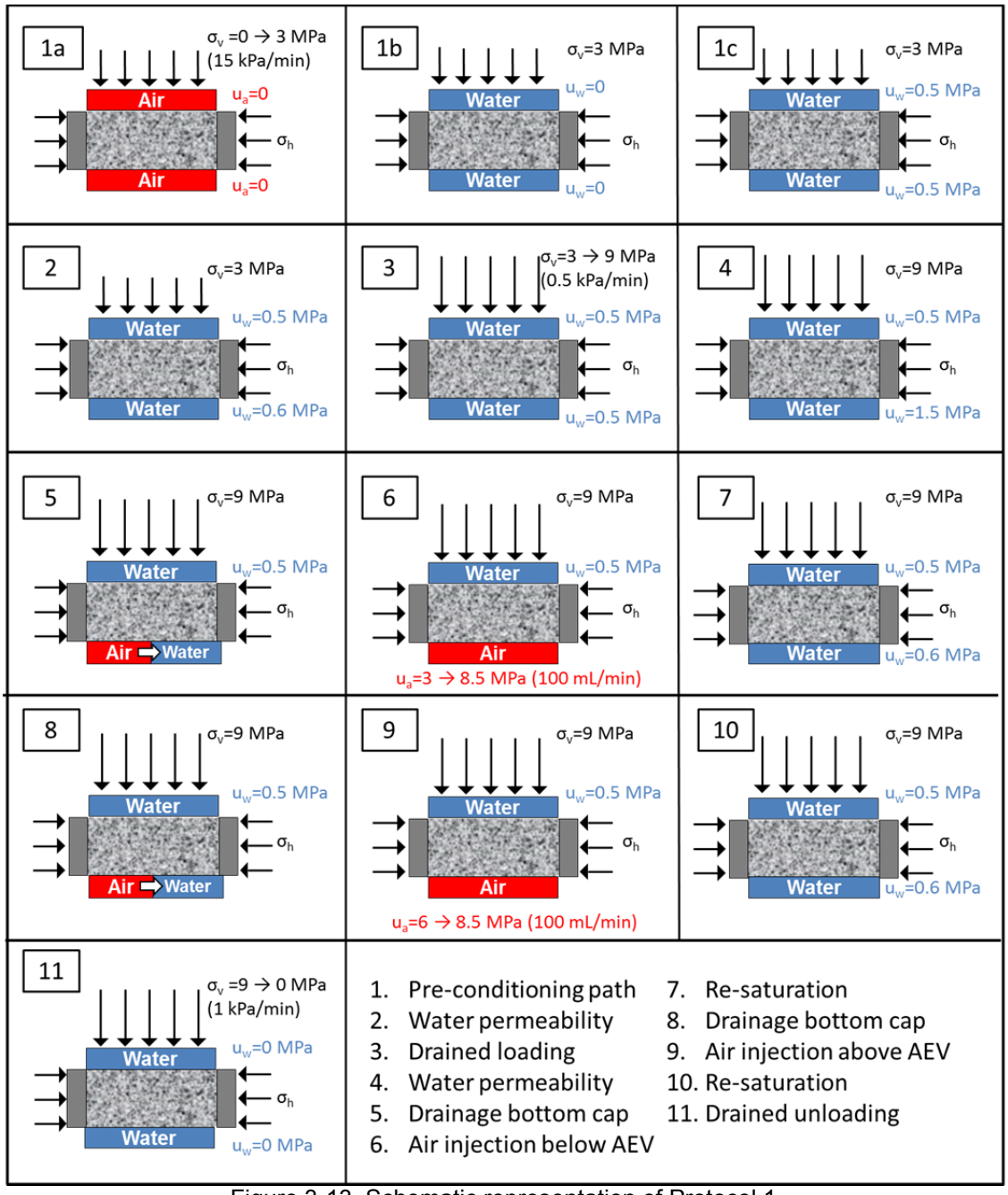

Figure 3-13. Schematic representation of Protocol 1.

❖ *Protocol 2: Gas flow through sample matrix*

A demonstration test was carried out injecting gas at a higher constant vertical stress (14 MPa) so that the maximum air pressure was much lower than the horizontal stress and gas flow through the sample could be ensured. In this way, the initial hypothesis of gas flow through the ring-sample interface (Protocol 1) could be validated. The followed stages are depicted in Figure 3-14. Only one demonstration test was performed using this protocol. The sample was orientated with the bedding planes parallel to the air flow.

- Stage 1 - Pre-conditioning path: exactly equal to Protocol 1.
- Stage 2 - Water permeability determination: exactly equal to Protocol 1.
- Stage 3 - Drained loading: Vertical load from 3 MPa to 14 MPa was applied at a rate of 0.5 kPa/min ensuring drainage conditions (Lima 2011). Water pressures in both top and bottom caps were maintained constants and axial displacement was monitored along this mechanical process.
- Stage 4 - Water permeability determination: At a constant vertical stress of 14 MPa, water pressure at upstream was increased to 1.5 MPa and water permeability was measured under steady state conditions. Axial deformation was monitored along this hydraulic process.
- Stage 5 - Drainage of bottom cap: Water pressure in the upstream vessel was reduced to atmospheric conditions to allow for its fast replacement by air. Air pressure at the upstream point was rapidly increased from atmospheric conditions to a value 3 MPa.
- Stage 6 - Air injection below AEV: Fast air injection from 3 to 8.5 MPa at constant flow rate of 100 mL/min (constant vertical stress of 14 MPa) was applied, followed by a shut-off and recovery phase at constant air volume. Initial air pressure was below the air entry value (AEV). Evolutions of upstream and downstream pressures, as well as outflow volume and sample axial deformation, were measured during the injection and dissipation stages. Air permeability was determined at this step.
- Stage 7 - Re-saturation: Air pressure in the upstream vessel was reduced to atmospheric conditions to allow for its fast replacement by water. Upstream water pressure was then increased to 0.6 MPa to allow for sample re-saturation and water pore pressure equalisation and then water permeability was measured under steady state conditions.
- Stage 8 - Drained unloading: Vertical stress was decreased from 14 to 0.5 MPa at a rate of 1 kPa/min and simultaneously, both upstream and downstream pressures were reduced to 0.
- MIP test was performed in the post-mortem sample after freeze-drying.

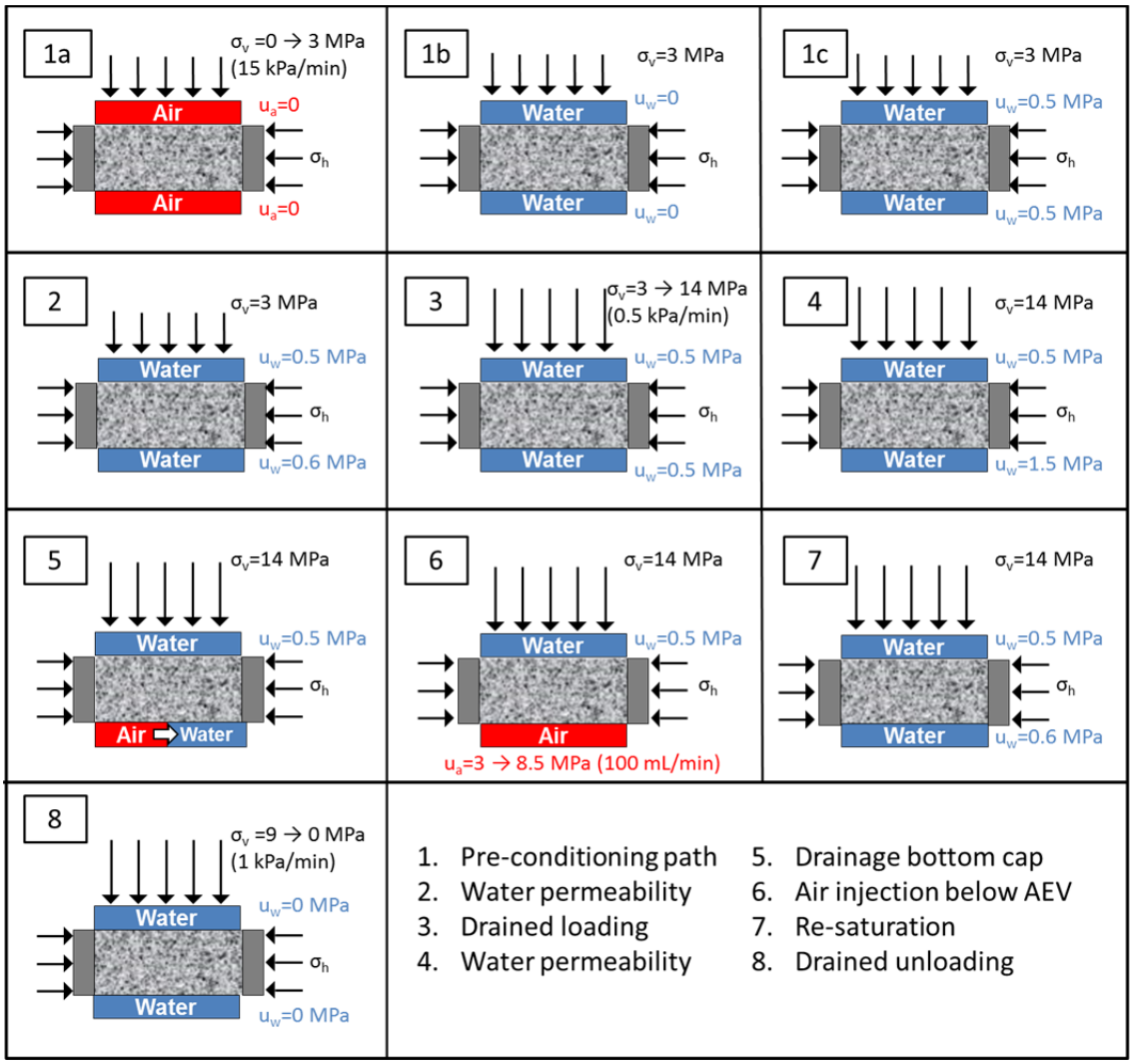

Figure 3-14. Schematic representation of Protocol 2.

3.3.1.3. Low pressure test protocol for Boom Clay

This series of tests on Boom Clay samples was launched after a progress meeting with ONDRAF/NIRAS. It was decided to move towards lower vertical stresses and air pressures in order to be closer to the *in situ* conditions of the repository and thus, to obtain more representative data of the Boom Clay behaviour against gas flow. To study more fundamental issues about the gas transport properties, gas flow through the sample was ensure maintaining more than 1 MPa of difference between maximum air pressure and the vertical stress, whilst, in view of the results of tests performed with Protocol 1, the initial air pressure was decided to be lower than the AEV. Boom Clay samples were tested at two orientations (bedding planes parallel and orthogonal to flow) and at two different injection rates: fast (100 mL/min) and slow (2 mL/min). Protocol 3 followed during these tests is explained below.

❖ *Protocol 3: Injection experiments*

In these experiments, water permeability determination stage after air injection was not carried out to prevent some possible closure of the microstructure aperture induced by the air injection. For the same reason, the unloading was carried out under undrained conditions in order to preserve the samples and track possible damage due to air passage with MIP technique. Furthermore, after two of these tests, micro-focus X-ray computed tomography (μ-CT) technique was also carried out to complement the information of the microstructure changes. Also, images of one post-mortem sample were taken from filed-emission scanning electron microscopy (FESEM).

The stages followed in this protocol are schematised in Figure 3-15 and explained below:

- Stage 1 - Pre-conditioning path: exactly equal to Protocol 1.
- Stage 2 - Water permeability determination: exactly equal to Protocol 1.
- Stage 3 - Drained loading: Vertical load from 3 MPa to 6 MPa was applied at a rate of 0.5 kPa/min ensuring drainage. Water pressures in both top and bottom caps were maintained constants and axial displacement was monitored along this mechanical process.
- Stage 4 - Water permeability determination: At a constant vertical stress of 6 MPa, water pressure at upstream was increased to 0.6 MPa and water permeability was measured under steady state conditions. Axial deformation was monitored along this hydraulic process.
- Stage 5 - Drainage of bottom cap: Water pressure in the upstream vessel was reduced to atmospheric conditions to allow for its fast replacement by air. Air pressure at the upstream point was rapidly increased from atmospheric conditions to a value 0.5 MPa.
- Stage 6 - Air injection: Air injection from 0.5 to 4.0 MPa at two different constant flow rates: fast (100 mL/min) or slow (2 mL/min) (constant vertical stress of 6 MPa) was applied, followed by a shut-off and recovery phase at constant air volume. Evolutions of upstream and downstream pressures, as well as outflow volume and sample axial deformation, were measured during the injection and dissipation stages. Air permeability was determined at this step.
- Stage 7 - Undrained unloading: Air pressure in the upstream vessel was reduced to atmospheric conditions as well as fluid pressure in the downstream

vessel. Simultaneously, vertical stress was decreased from 6 to 0 MPa under undrained conditions.

- MIP tests on all post-mortem samples.
- μ-CT on two post-mortem samples.
- FESEM on one post-mortem sample.

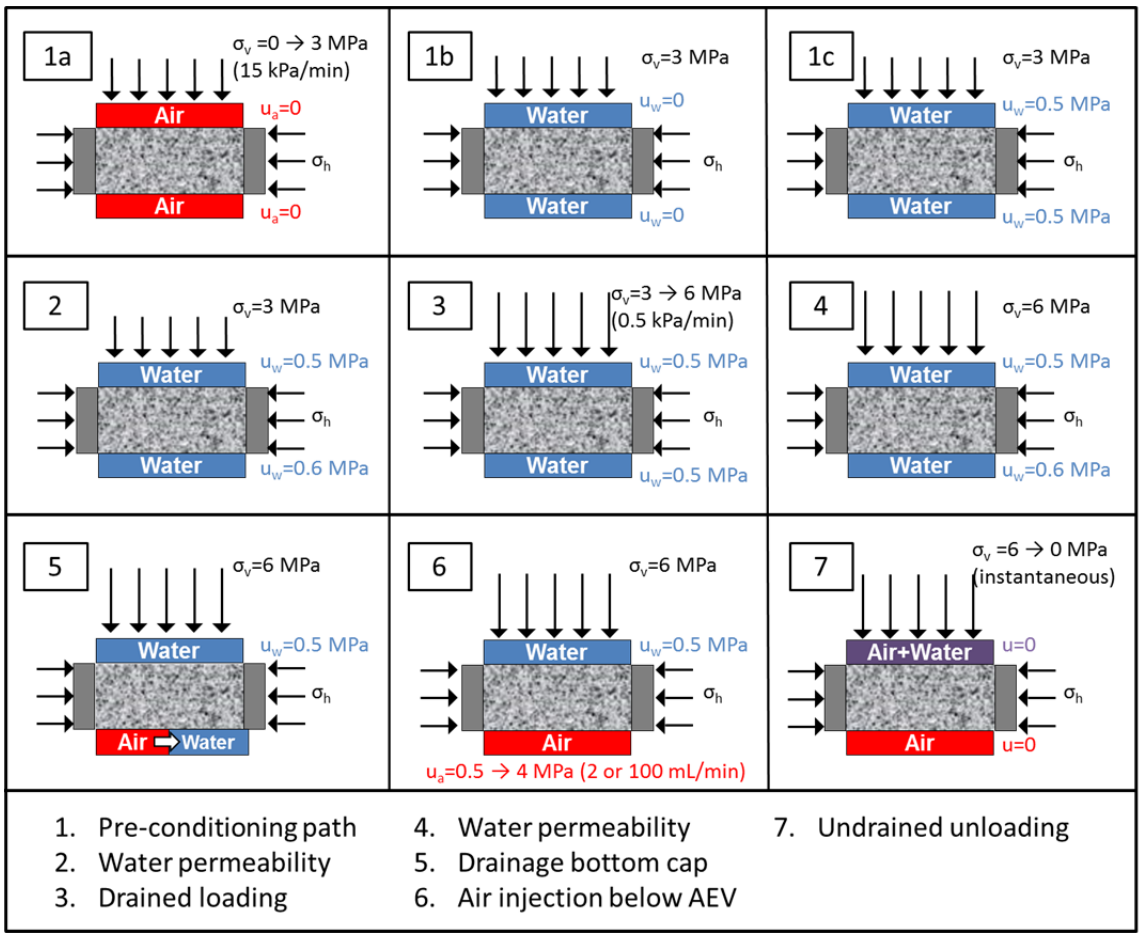

Figure 3-15. Schematic representation of Protocol 3.

❖ *Protocol 4: Non-injection experiments*

Three tests were carried out at the same stress level than the injection experiments (Protocol 3), but in these tests, air injection was not performed to clearly separate effects of the air injection and dissipation from the unloading ones. The unloading stage was different for each one to analyse the microstructural changes due to mechanical unloading. Figure 3-16 shows the test protocol followed for these tests.

- Stage 1 - Pre-conditioning path: exactly equal to Protocol 3.
- Stage 2 - Water permeability determination: exactly equal to Protocol 3.
- Stage 3 - Drained loading: exactly equal to Protocol 3.
- Stage 4 - Water permeability determination: exactly equal to Protocol 3.

- Stage 5 - Unloading: three different unloading paths were selected (Figure 3-17):
  - A drained unloading was performed at a rate of 0.9 kPa/min allowing the sample to absorb water.
  - A quasi-drained unloading was carried out. A faster unloading rate was chosen (30 kPa/min) but the sample was still able to absorb some water.
  - An undrained unloading was performed since the vertical stress was reduced instantaneously.
- MIP tests on post-mortem samples.

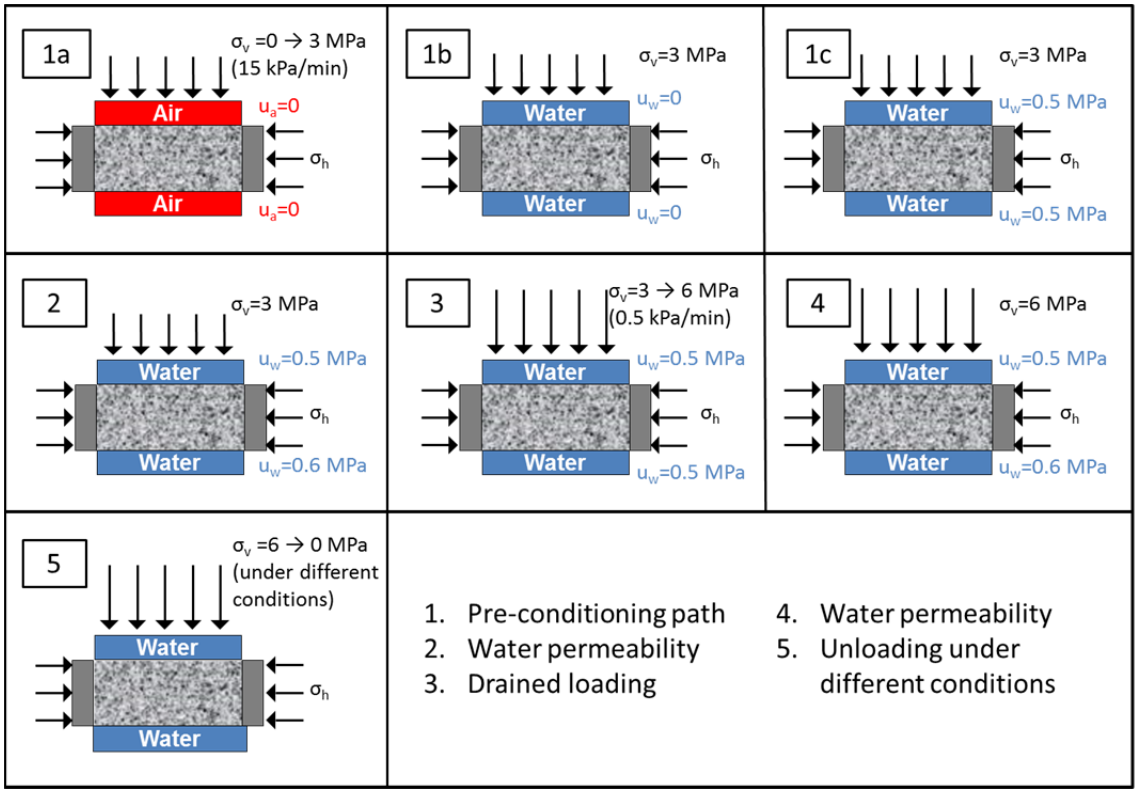

Figure 3-16. Schematic representation of Protocol 4.

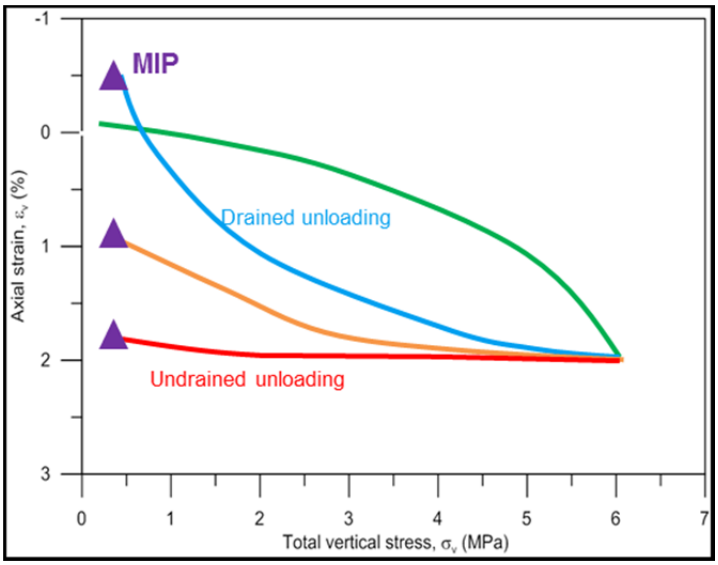

Figure 3-17. Different unloading paths followed in Protocol 4.

3.3.1.4. Complementary tests

Some tests were performed in order to obtain complementary experimental information as the tensile strength or the diffusion coefficient of dissolved air in water. The protocols and results are explained in Appendix B.

3.3.2. Test protocols for indurated clays

Two test protocols were established for indurated rocks, as shown in Table 3-6, one for the oedometer cell and other for the isotropic cell

Isotropic test protocols were adapted from the one proposed in Romero & Gómez (2013) to allow its further comparison. Regarding the oedometer tests, it was initially intended to perform gas injections, however, problems with the closure between the sample and the oedometer ring prevented from carried out permeability measurements and thus, air injection tests were only performed under isotropic conditions.

As well as in Boom Clay, a pre-conditioning path was firstly performed in both protocols in order to reach a stress level similar to the *in situ* one and it is initially explained. Since the stress conditions differ under oedometer or isotropic conditions, this stage is slightly different in each protocol.

3.3.2.1. Pre-conditioning paths

The pre-conditioning paths in the indurated rocks are also thought to prevent possible damage on the samples due to the saturation process. In this way, contact with synthetic water was only allowed when the samples were loaded up to a certain level. Regarding that the *in situ* conditions of OPA and BD are pretty similar (Chapter 2

Section 2.3.2) the same stress level was selected for both materials which simplified the protocols and the further comparison of the results but was still similar to the *in situ* effective stress.

These indurated samples display a very high initial suction due to the important stress relief, despite being almost saturated (see Chapter 2 Table 2-7). The samples can undergo degradation as a clear consequence of suction reduction effects due to water contact at low stress levels. To minimise these effects, the samples were always loaded at a target total stress and only then put in contact with water under atmospheric pressure to avoid any damage on the samples. Therefore, at the moment of applying the water pressure, the effective stress state will be equivalent to the *in situ* one.

At oedometer conditions, a total vertical stress of 12 MPa was considered to be the initial total vertical stress for both samples, BD and OPA. On the one hand, 12 MPa is enough high to avoid a large swelling during saturation. On the other hand, it enables to reach the *in situ* effective stress after imposing water pressure keeping the stress level within the working range of the equipment. This first stage was carried out at a relatively fast rate of 30 kPa/min and at constant water content. During this path, it was expected to reduce the initial suction, since total stress will be transmitted to the pore pressure and therefore small deformations due to suction changes are predicted.

Regarding the isotropic conditions, samples were loaded up to a total mean stress of 10 MP before water contact, following the same procedure as in the oedometer tests. Once a water pressure of 0.5 MPa was applied, the effective mean stress was close but slightly lower than the *in situ* one.

3.3.2.2. Test protocol for oedometer tests

The oedometer cell was initially intended to perform gas injection tests, however, the existing gap between the sample and the oedometer ring forced to modify the oedometer test protocol, since water and gas flows could not be performed. Then, oedometer test protocol turned out as followed:

- Stage 1 - Pre-conditioning path: as explained above a loading stage at constant water content was carried out before putting the sample in contact with water to prevent damage as a consequence of suction reduction. After that, water pressure was increased to reach effective stress level equivalent to the *in situ* one. This stage can be divided into two sub-stages:

- Vertical loading from 0.1 to 12 MPa at constant water content. A constant rate of 30 kPa/min was used followed by a day for equalisation.
- Flooding of the samples by the application of water pressure of 0.5 MPa at upstream (bottom cap) and downstream (top cap) points, allowing a period of time to stationary conditions and swelling stabilisation.

- Stage 2 - Drained loading: Vertical loading from 12 to 25 MPa with constant water pressure of 0.5 MPa in both top and bottom caps was performed at a rate of 30 kPa/min.
- Stage 3 - Quasi-undrained unloading: Vertical stress was reduced from 25 to 1 MPa at a rate of 60 kPa/min with constant water pressure of 0.5 MPa in both top and bottom caps. Finally, vertical stress and water pressure were rapidly reduced to atmospheric conditions.
- MIP tests on post-mortem samples.

3.3.2.3. Test protocol for isotropic tests

Gas injection tests on indurated rock were performed in an isotropic cell. As explained above, the protocols were adapted from the one used in Romero & Gómez (2013) by simplifying them in order to have a better comprehension of the results and optimize the test duration since several moths are required to each test, besides achieving comparable results with samples for the same borehole at different depths. In these experiments, two different injections were performed. In the case of Opalinus Clay, injections at the same rate (100 mL/min) but at different stress levels (isotropic stress of 15 and 19 MPa) were performed, while injection tests on 'Brauner Dogger' were carried out at the same stress level (15 MPa) and at two different rates (2 and 0.04 mL/min). Stages 1 to 6 are common for both materials, but from stage 7 onwards the protocols are different. The different stages that were followed in the isotropic cell for each material are summarised below.

❖ *Test protocol for Opalinus Clay*

A schematic representation of the followed protocol is depicted in Figure 3-18.

- Stage 1 - Pre-conditioning path: as explained in above a loading stage at constant water content was carried out before putting the sample in contact with water to prevent damage as a consequence of suction reduction. After that, water pressure was increased to reach effective stress level equivalent to the *in situ* one. This stage can be divided into two sub-stages:

  - Isotropic loading from 0.1 to 10 MPa at constant water content. A constant stress rate of 30 kPa/min was used followed by an equalisation period of 1 day.
  - Application of water pressure at upstream (bottom cap) and downstream (top cap) points to induce flow of water through the sample. The upstream pressure was increased from 0 to 2 MPa and downstream pressure from 0 and 0.5 MPa (this top cap pressure was maintained constant along the different stages of the test). Axial deformation was monitored along this hydraulic process. Water permeability was measured under steady state conditions.

- Stage 2 - Loading: Isotropic loading from 10 to 15 MPa at 30 kPa/min, maintaining downstream water pressure at 2 MPa and upstream water pressure at 0.5 MPa. Axial deformation was monitored along this hydro-mechanical process.
- Stage 3 - Water permeability determination: Water permeability was measured under steady state conditions. This stage lasted a minimum of two weeks to allow for pore pressure equalisation.
- Stage 4 - Drainage of bottom cap: Water pressure in the upstream vessel was reduced to atmospheric conditions for its fast replacement by air. Air pressure at the upstream point was rapidly increased from atmospheric conditions to 3 MPa. Isotropic stress was kept constant at 15 MPa.
- Stage 5 - First air injection: Air injection test from 3 to 14 MPa at constant flow rate of 100 mL/min was performed (constant isotropic stress of 15 MPa), followed by a shut-off and recovery phase at constant volume. Measurement of the evolution of upstream and downstream pressures as well as outflow volume and sample axial deformation during the injection and dissipation stages. This stage lasted a minimum of three weeks.
- Stage 6 - Re-saturation: Air pressure in the upstream vessel was reduced to atmospheric conditions for its fast replacement by water. Upstream water pressure was then increased to 0.5 MPa to allow for sample re-saturation and water pore pressure equalisation. This stage was maintained for one / two weeks.
- Stage 7- Loading: Isotropic loading from 15 to 19 MPa maintaining water pressure at 0.5 MPa in both caps following one day for equalisation.
- Stage 8 - Water permeability determination: Downstream water pressure was increased to 2 MPa to determine water permeability at a constant isotropic stress of 19 MPa. Axial deformation was monitored along this process. Water

permeability was measured under steady state conditions. This stage lasted a minimum of two weeks to allow for pore pressure equalisation.

- Stage 9 - Drainage of bottom cap: Water pressure in the upstream vessel was reduced to atmospheric conditions for its fast replacement by air. Air pressure at the upstream point was rapidly increased from atmospheric conditions to 3 MPa. Isotropic stress was kept constant at 19 MPa.
- Stage 10 - Second air injection: Fast injection test from 3 to 18 MPa at constant flow rate of 100 mL/min was performed (constant isotropic stress of 19 MPa), followed by a shut-off and recovery phase at constant volume. Measurement of the evolution of upstream and downstream pressures as well as outflow volume and sample axial deformation during the injection and dissipation stages. This stage lasted a minimum of three weeks.
- Stage 11 - Undrained unloading: Fast unloading from 19 MPa to 0. Simultaneously, both upstream and downstream pressures were reduced atmospheric conditions.
- MIP tests on the post mortem sample.

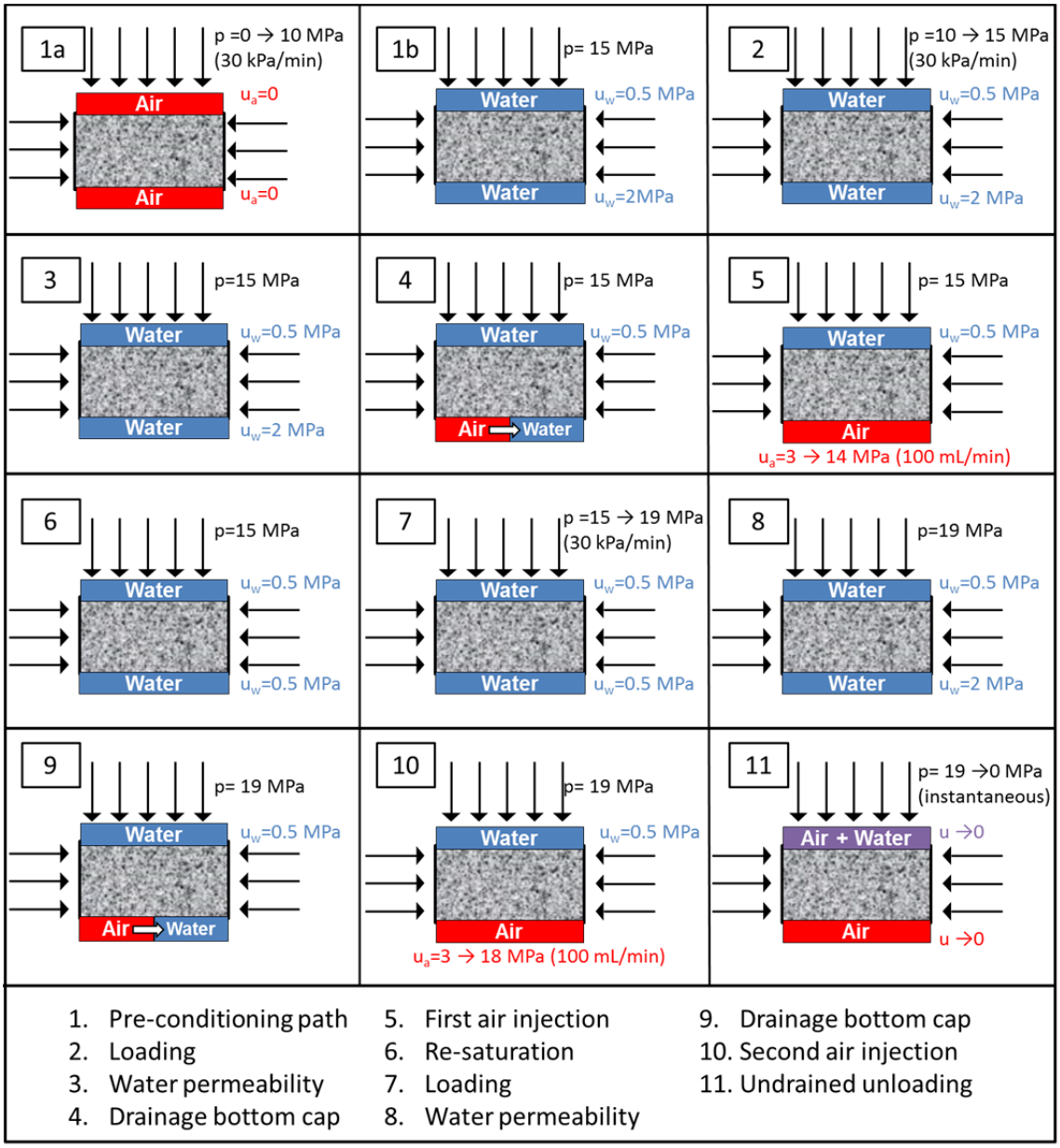

Figure 3-18. Schematic representation of protocol for isotropic test on Opalinus Clay

❖ *Test protocol for 'Brauner Dogger'*

A schematic representation of the followed protocol is depicted in Figure 3-19

- Stage 1 - Pre-conditioning path: exactly equal to protocol for Opalinus Clay
- Stage 2 - Loading: exactly equal to protocol for Opalinus Clay
- Stage 3 - Water permeability determination: exactly equal to protocol for Opalinus Clay
- Stage 4 - Drainage of bottom cap: exactly equal to protocol for Opalinus Clay
- Stage 5 - First air injection: equal to the protocol for Opalinus Clay with the exception of the injection rate, in this case, a constant flow rate of 2 mL/min was used.

- Stage 6 - Re-saturation exactly equal to protocol for Opalinus Clay
- Stage 7- Water permeability determination: Downstream water pressure was increased to 2 MPa to determine water permeability at a constant isotropic stress of 15 MPa after the air injection. Axial deformation was monitored along this process. Water permeability was measured under steady state conditions. This stage lasted a minimum of two weeks to allow for pore pressure equalisation.
- Stage 8 - Drainage of bottom cap: Water pressure in the upstream vessel was reduced to atmospheric conditions for its fast replacement by air. Air pressure at the upstream point was rapidly increased from atmospheric conditions to 3 MPa. Isotropic stress was kept constant at 15 MPa.
- Stage 9 - Second air injection: Fast injection test from 3 to 14 MPa at constant flow rate of 0.04 mL/min was performed (constant isotropic stress of 15 MPa), followed by a shut-off and recovery phase at constant volume. Measurement of the evolution of upstream and downstream pressures as well as outflow volume and sample axial deformation during the injection and dissipation stages. This stage lasted a minimum of three weeks.
- Stage 10 - Undrained unloading: Fast unloading from 15 MPa to 0. Simultaneously, both upstream and downstream pressures were reduced atmospheric conditions.

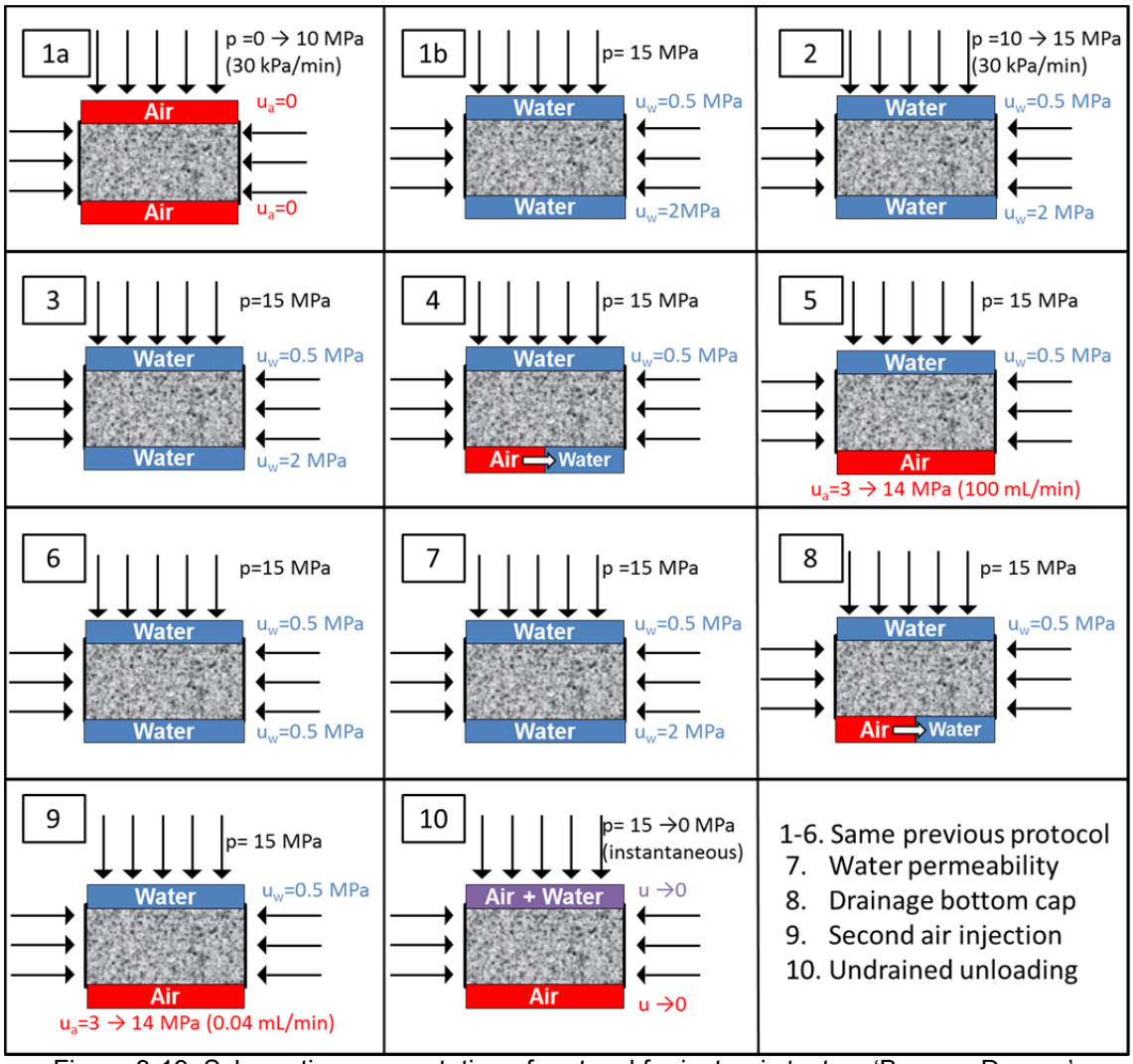

Figure 3-19. Schematic representation of protocol for isotropic test on 'Brauner Dogger'.

4
HYDRO-MECHANICAL BEHAVIOUR

4.1. Boom Clay

4.1.1. Background on Boom Clay behaviour

From 1975 onwards, extensive hydraulic, geochemical and geomechanical research has been carried out on Boom Clay at the HADES underground research laboratory in Mol, Belgium. An important set of data about the geomechanical behaviour of the rock mass has been collected both from *in situ* and from laboratory tests. Within the later, of interest in this research, data highlight the strong thermo-hydro-mechanical (THM) coupling and a great time dependency of Boom Clay. Therefore, the vast majority of laboratory tests campaigns in Boom Clay were piloted in two main directions (Li et al. 2007): a) Short term THM behaviour: elastoplastic hydro-mechanical behaviour in "saturated" condition and ambient temperature, jointly with the thermal effects on the hydro-mechanical behaviour at saturated state (Delage, Le, et al. 2008; Le 2008; Lima 2011; Bésuelle et al. 2014; Cui & Tang 2013; Nguyen 2013; ONDRAF/NIRAS 2013; Deng et al. 2011); and b) the time-related behaviour at ambient and elevated temperature in "saturated" condition (Cui et al. 2009; Blümling et al. 2007).

Recently, more attention was paid to the evaluation of both mechanical and transport properties in the Excavation Disturbed Zone around the underground storage gallery as well as the porosity evolution during different THM paths regarding the self-sealing properties of Boom Clay (Monfared et al. 2012; Prime et al. 2016; Dao 2015).

Here, the hydro-mechanical behaviour of Boom Clay is presented as a necessary complement of the main topic, the gas migration, and thus, hydro-mechanical paths are analysed and compare with previous results, given confidence to the selected experimental procedures. Moreover, hydro-mechanical results presented in this chapter provided a solid base for calibrating the required parameters in the numerical hydro-mechanical coupled analysis.

4.1.2. Compressibility properties on loading and unloading

As explained in Chapter 3, the pre-conditioning paths are mandatory to reach the geostatic conditions of the material in the *in situ* state which will be the starting point of any oedometer test, ensuring the most similar stress state. These paths mainly consist in loading the samples up to a pre-defined stress level at constant water content reducing the initial suction and afterwards, saturating the sample with synthetic water. Through this process, effective vertical stress is achieved when the water pressure is applied coming out very close to the *in situ* one.

At oedometer conditions, a total vertical stress of 3 MPa was considered to be the initial total vertical stress. On the one hand, 3 MPa is enough high to avoid a large swelling during saturation since the samples can undergo expansion and degradation as a clear consequence of suction reduction effects due to water contact at low stress levels. On the other hand, it enables to reach the *in situ* effective stress after imposing water pressure keeping the stress level within the working range of the equipment. This first stage was carried out at a relatively fast rate of 15 kPa/min and at constant water content. During this path, it was expected to reduce the initial suction down to zero, since total stress will be transmitted to the pore pressure (initially with a total suction around 2.5 MPa). Therefore, small deformations due to suction changes are predicted.

Figure 4-1 shows the continuous loading results at controlled stress rate in terms of axial strain (positive in compression) as a function of the vertical stress for samples tested with bedding planes orthogonal and parallel to the loading axis. Some differences can be observed in this initial stage: samples tested with bedding planes parallel to axis presented higher stiffness. This behaviour was attributed to the anisotropy of the elastic regimen besides a possible closure of the discontinuities and/or bedding planes in the sample in which they were orientated normal to the axis.

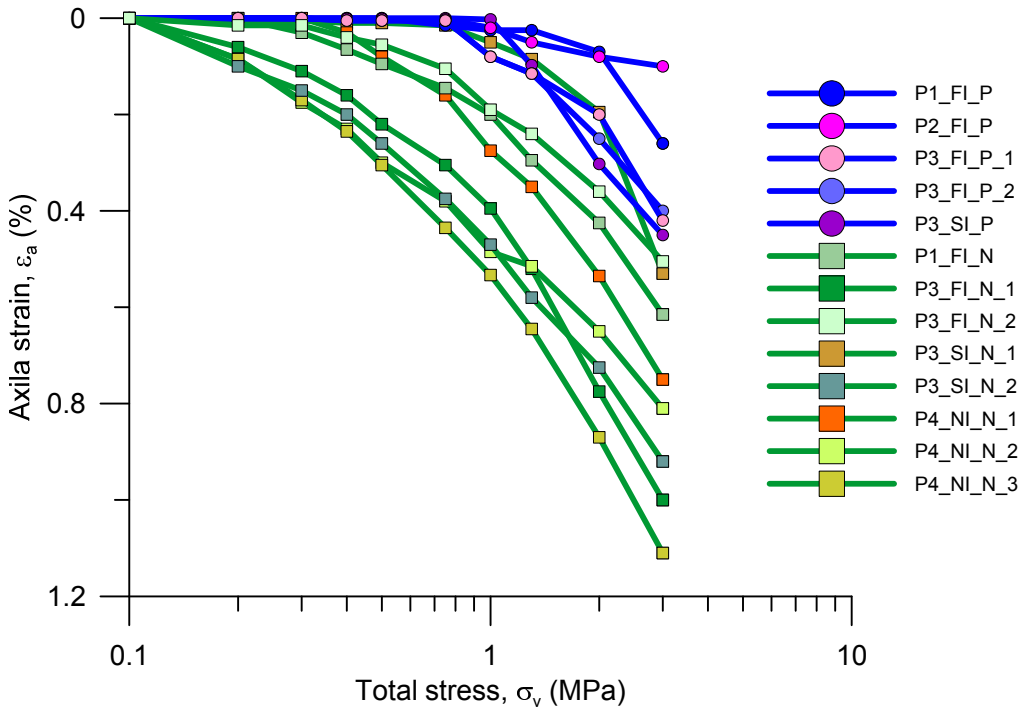

Figure 4-1. Axial strain against total stress during fast loading at constant water content.

Once a total stress of 3 MPa was reached, the samples were put in contact with SBCW at atmospheric pressure at the top and bottom sides in order to ensure full saturation. All samples underwent some swelling during this process, being lower for samples with bedding planes parallel to axis which were constrained to expand by oedometer conditions. Initially, it was expected that no deformation occurred during this process, since the Skempton's theoretical variation of the pore pressure (Eq. 4.1) resulted in an increase of the pore pressure during the loading higher than the initial suction, assuming elastic behaviour and the following parameters: $A = 1/3$; $B = 1$ and $K_0 = 0.84$)

$$\Delta u = B[\Delta\sigma_3 + A(\Delta\sigma_1 - \Delta\sigma_3)] = 2.68\ MPa \quad (4.1)$$

After a deepening in the question, a new hypothesis turned out. The expansion underwent during flooding was then thought to be due to a remained suction in the samples, considering that changes in suction imply deformational response. Although the pore pressure inside the samples was not measured, the simulations of these stage presented in Chapter 7 confirm this hypothesis.

Figure 4-2 and Figure 4-3 present the swelling behaviour of the samples during the flooding until its stabilization with time. Clearly, samples with bedding planes normal to flow which are less constrained to expand underwent a higher swelling besides its

anisotropy features. Table 4-1 compiles the maximum values of the axial deformation (negative values correspond to swelling) for each test.

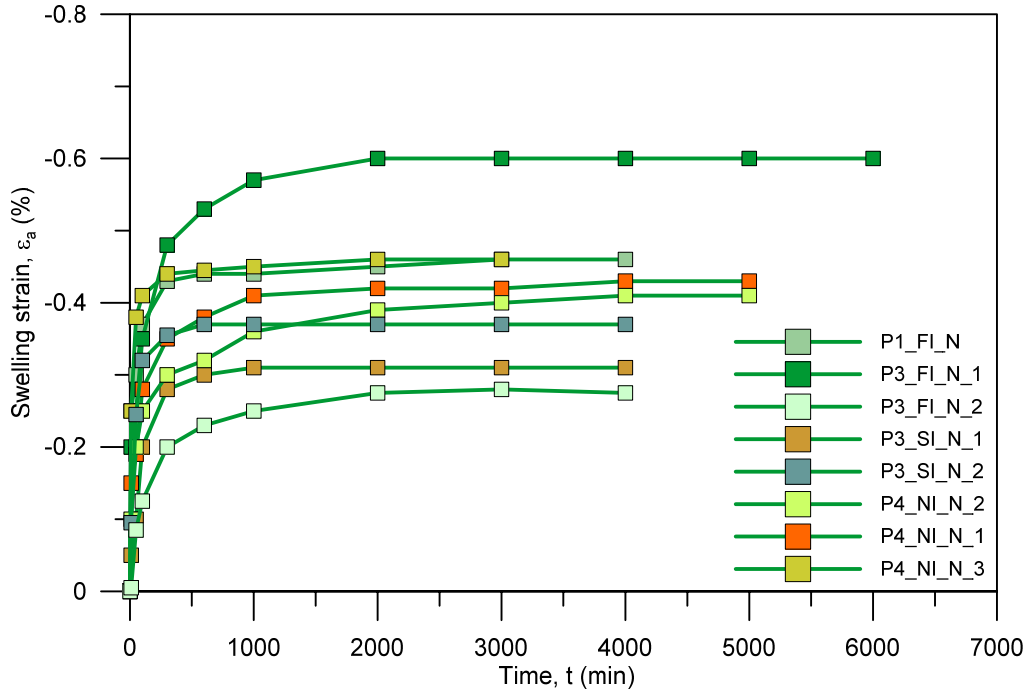

Figure 4-2. Swelling during flooding at constant total stress of samples with bedding planes normal to flow.

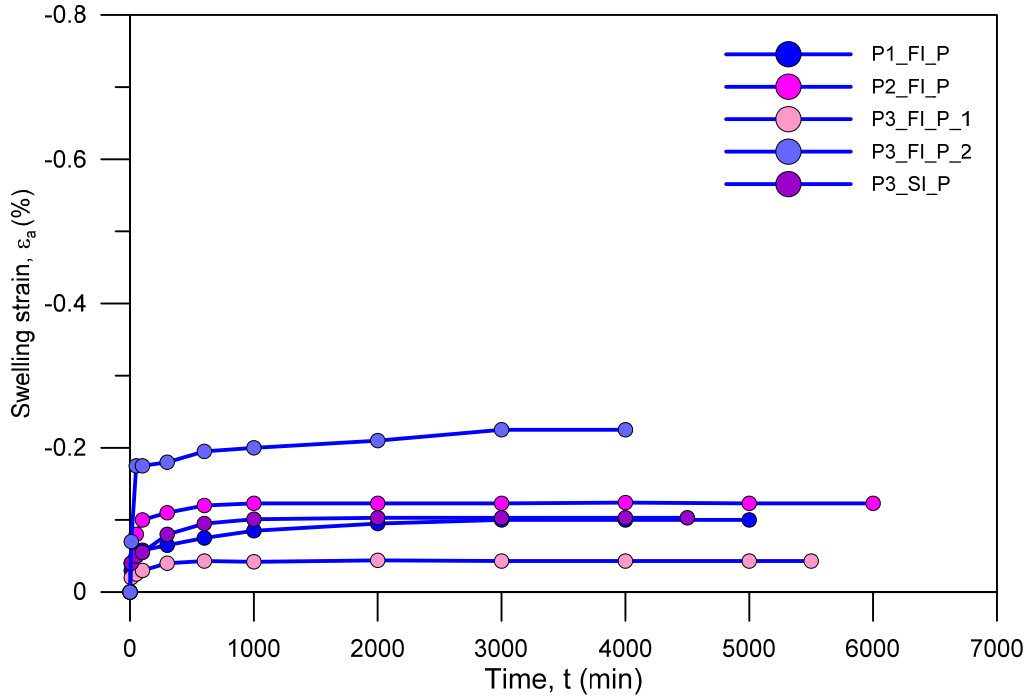

Figure 4-3. Swelling during flooding at constant total stress of samples with bedding planes parallel to flow.

Table 4-1. Swelling values

Sample orientation	Test	Swelling value (ε_a (%))
Normal to flow	P1_FI_N	-0.46
	P3_FI_N_1	-0.60
	P3_FI_N_2	-0.28
	P3_SI_N_1	-0.31
	P3_SI_N_2	-0.37
	P4_NI_N_1	-0.43
	P4_NI_N_2	-0.41
	P4_NI_N_3	-0.46
Parallel to flow	P1_FI_P	-0.01
	P2_FI_P	-0.12
	P3_FI_P_1	-0.04
	P3_FI_P_2	-0.22
	P3_SI_P	-0.10

After full saturation of the samples, a drained continuous loading was carried out in all the oedometer tests at a slow stress rate of 0.5 kPa/min in order to ensure drained conditions. This rate allowed water to be expelled during the process. Figure 4-4 shows the compressibility curves for both samples with bedding planes normal and parallel to the axis. Despite being natural samples, good consistency was achieved during this hydro-mechanical loading. Anisotropy behaviour during this stage was not as evident as in the pre-conditioning stage. However, samples with bedding planes normal to flow still presented a slightly higher compressibility, except for test P3_FI_P_1. Table 4-2 gathers the compressibility parameter which was calculated as the variation of the axial strain with the logarithm of the total vertical stress ($\delta\varepsilon_a/\delta\ln(\sigma_v)$).

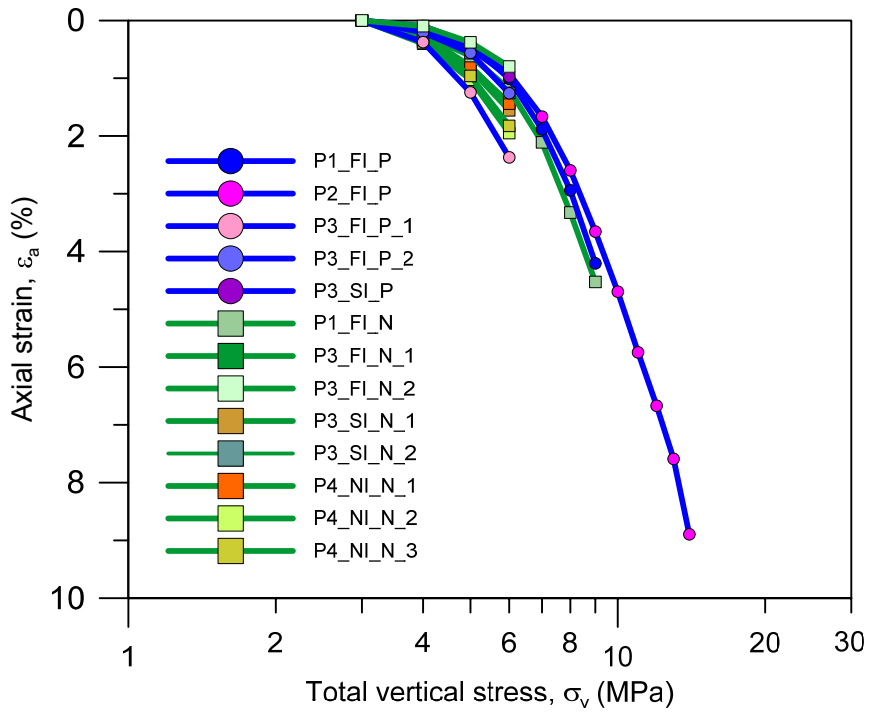

Figure 4-4. Compressibility curves after saturation under continuous loading at drained conditions for samples at both orientations.

Table 4-2. Compressibility parameter after saturation.

Sample orientation	Test	Pre-yield $(\sigma_v < 6\ MPa)$ $(\delta\varepsilon_a/\delta\ln(\sigma_v))$	Post-yield $(\sigma_v > 6\ MPa)$ $(\delta\varepsilon_a/\delta\ln(\sigma_v))$
Normal to flow	P1_FI_N	0.017	0.083
	P3_FI_N_1	0.020	
	P3_FI_N_2	0.012	
	P3_SI_N_1	0.022	
	P3_SI_N_2	0.017	
	P4_NI_1	0.021	
	P4_NI_2	0.027	
	P4_NI_3	0.026	
Parallel to flow	P1_FI_P	0.014	0.078
	P2_FI_P	0.013	0.102
	P3_FI_P_1	0.033	
	P3_FI_P_2	0.017	
	P3_SI_P_1	0.014	

Figure 4-5 and Figure 4-6 show the complete continuous loading results at controlled stress rate in terms of axial strain (positive in compression) as a function of the vertical stress in the oedometer tests for samples with bedding planes normal and parallel to flow respectively, where the SBCW was placed in contact with the sample at a vertical stress of 3 MPa. The as-retrieved samples showed high stiffness at the beginning, due to the high initial suction, while the stiffness decreased after contact with the SBCW.

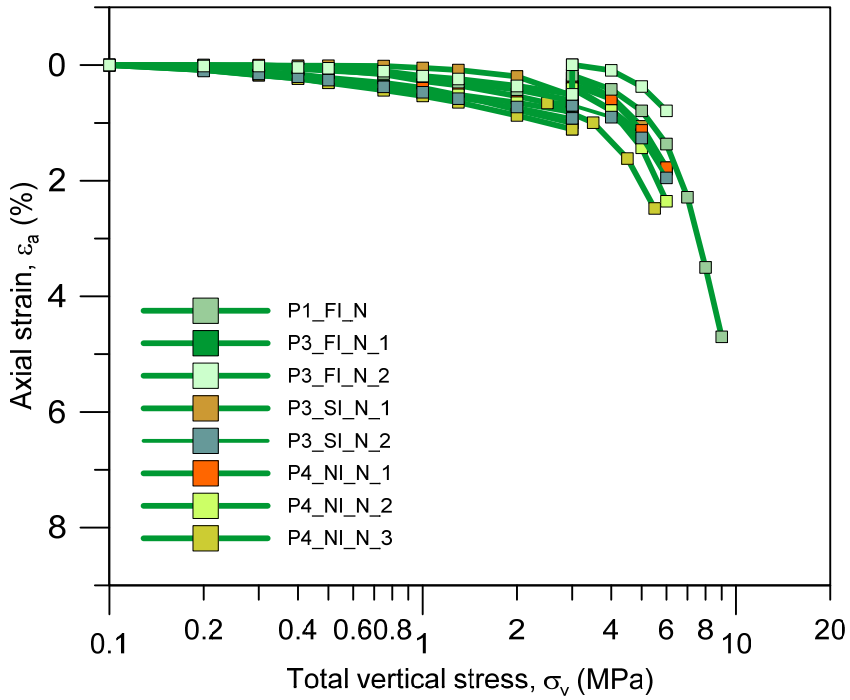

Figure 4-5. Complete hydro-mechanical paths (including loading at constant water content, saturation, water pressurization and drained loading) for samples tested with bedding normal to flow.

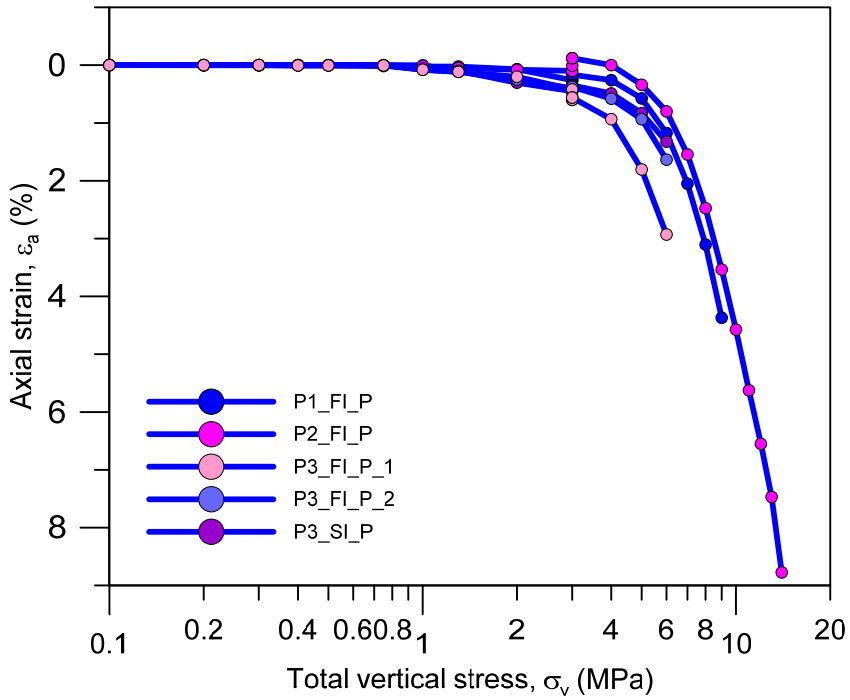

Figure 4-6. Complete hydro-mechanical paths (including loading at constant water content, saturation, water pressurization and drained loading) for samples tested with bedding parallel to flow.

Tests performed with Protocol 1 and Protocol 2, at higher stress than the estimated yield stress, facilitated evaluating the slope of the virgin compression curve and determining the yield stress, around 6 MPa for both orientations (Figure 4-7 and Figure

4-8). The slope of the post-yield compression line (over 6 MPa) is very similar for both samples (Compressibility parameter after saturation).

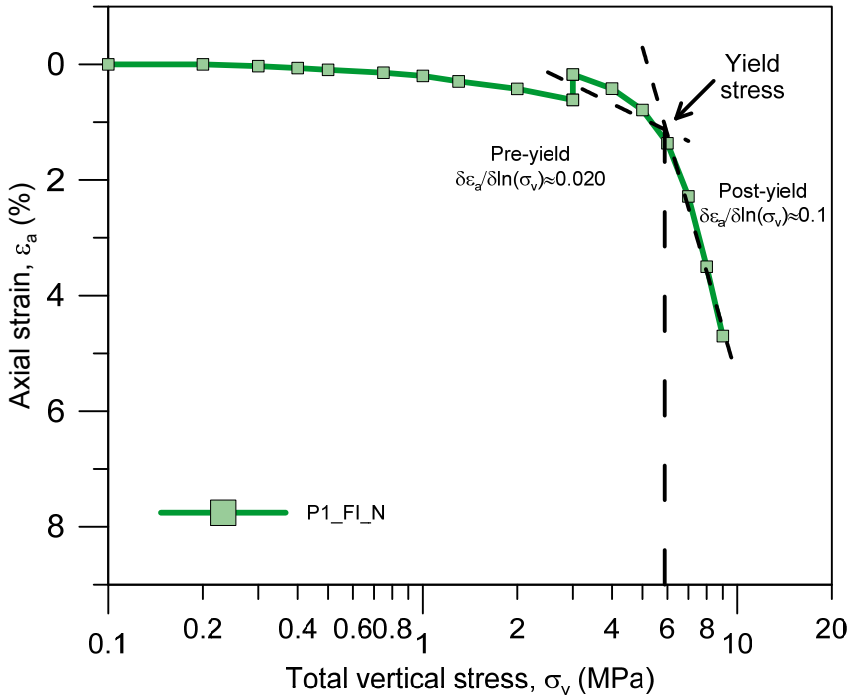

Figure 4-7. Pre-yield and post-yield compressibility parameters for the samples with bedding planes normal to flow.

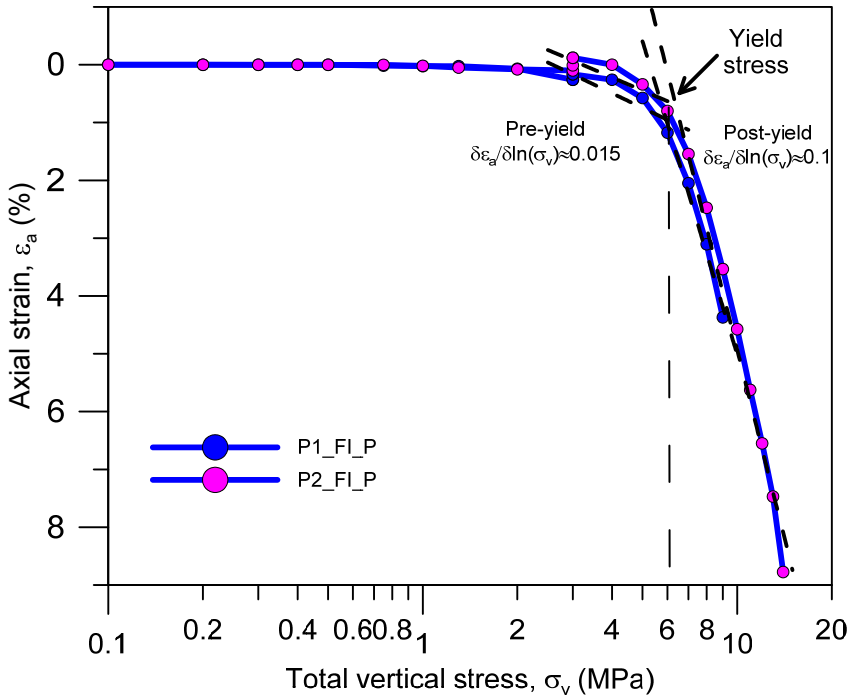

Figure 4-8. Pre-yield and post-yield compressibility parameters for the samples with bedding planes parallel to flow.

The overall pattern of the variation of post-yield compressibility parameters (λ_{oed} slope of the virgin loading in $e: ln(\sigma'_v)$ plane where e is the void ratio) with stress is

presented in Figure 4-9. Comparison with data reported by Lima (2011) is shown in the figure. Note that in the test T1 (E1-P1) from Lima (2011) the sample was put in contact with water at low stress so it underwent higher compression. Samples in this study present somewhat lower compressibility but follow the same trend. As observed on loading, the compressibility parameter continuously increases with increasing stress, evidencing that the transition towards yielded states is a gradual process. Constant value at the end of the curve has been taken as plasticity parameter in the simulation.

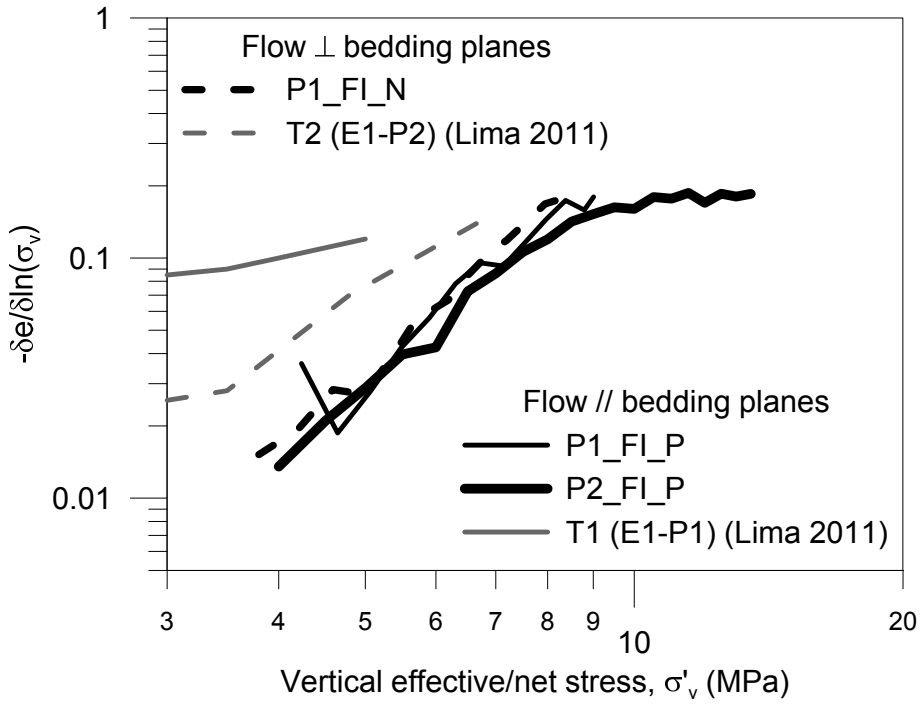

Figure 4-9. Post-yield (virgin loading) compressibility parameters for changes in net stress. Comparison with data reported by Lima (2011).

The different unloading paths followed in tests performed with Protocol 4 are shown in Figure 4-10. In test P4_NI_N_1, a drained unloading was performed at a rate of 0.9 kPa/min, allowing the sample to absorb water. In test P4_NI_N_2 a quasi-drained unloading was carried out. A faster unloading rate was chosen (30 kPa/min) but the sample was able to absorb some water, whereas in test P4_NI_N_3 an undrained unloading was performed since the vertical stress was reduced instantaneously. Deep differences between the drained and undrained paths were clearly obtained. It is known that the void ratio after unloading is highly dependent on the stress level and the stress path (Cui et al. 2009). Drained unloading paths produced a marked change in the structure of the sample, even increasing the porosity of the initial state. This fact is also observed through porosimetry tests as is explained in Chapter 6. For the purpose of this study, the preservation of sample structure after the gas injection was mandatory in order to analyse the changes that it induced. Therefore, undrained unloading paths as

in test P4_NI_N_3, ensured good quality of the sample structure, since almost null deformation was recorded.

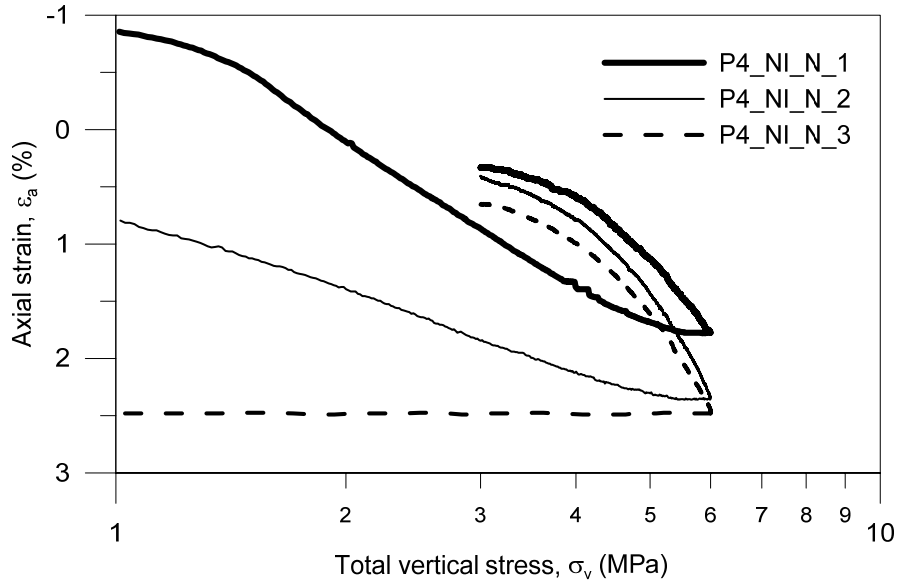

Figure 4-10. Compressibility curves following different unloading paths (samples with bedding planes normal to flow).

4.1.3. Water permeability

The water permeability was determined at several stages of the oedometer tests with the constant-head method (Deng et al. 2011) based on the water outflow volume under steady-state conditions at different stress states and pressure gradients in order to establish a correlation with the porosity of the clay. Nonetheless, in this section, only a representative stage of water permeability determination is explained. The rest of plots used in water permeability determination are gathered in Appendix C.

When applying the constant-head method in the oedometer cell, constant vertical stress was maintained along the stage. The specimens were fully saturated at the beginning of the measurements. The water pressure of the bottom cap (upstream) was applied using a pressure/volume controller (PVC) at different pressures depending on the test and the stage; the downstream cap was kept constant at a pressure of 0.5 MPa in all cases. The hydraulic conductivity of the samples was calculated from the water volume change recorded by the PVC with Darcy's law.

$$\frac{\Delta V_w}{\Delta t} = k_w \cdot A \cdot i \qquad (4.2)$$

In Figure 4-11, the results obtained from one of the stages of test P1_FI_N using the constant-head method are shown. The volume of SBCW passing through the soil

specimen (around 20 mm high) under a pressure gradient of 0.1 MPa is plotted versus time. An outflow velocity ($\Delta V_w/\Delta t$) at steady-state conditions of $2.5 \cdot 10^{-12}$ m^3/s can be determined being the hydraulic gradient, i, 512 (water head divided by sample height); hence, the hydraulic conductivity, k_w, is $2.5 \cdot 10^{-12}$ m/s is obtained (at a void ratio of 0.605).

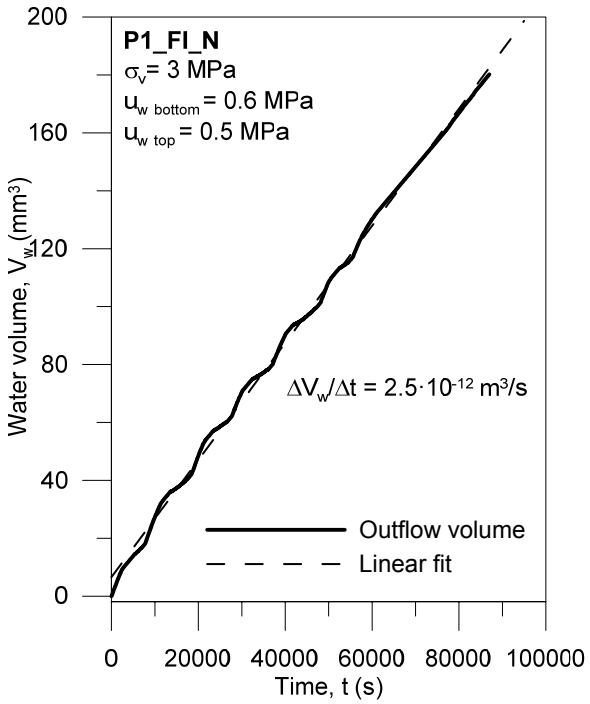

Figure 4-11. Time evolution of water outflow volume during the first stage of water injection, test P1_FI_N.

In Table 4-3 a summary of the water permeability values on Boom Clay samples is presented, where σ_v is the vertical total stress, i the hydraulic gradient applied, e_{av} the average void ratio and k_w the hydraulic conductivity. It also includes the intrinsic permeability, K_w, considering a water property factor of $\rho_w g/\mu_w = 9.744 \cdot 10^6 (m \cdot s)^{-1}$ at 20ºC (water density $\rho_w = 998.2\, kg/m^3$ and water dynamic viscosity $\mu_w = 1.005 \cdot 10^{-3} N \cdot s/m^2$).

Table 4-3. Results of water permeability at different stages of the oedometer tests.

Sample orientation	Test	Vertical stress	Hydraulic gradient	Average void ratio	Water permeability,	
		σ_v (MPa)	i	e_{av}	k_w (m/s)	K_w (m^2)
Normal to flow	P1_FI_N	3	513	0.605	$2.5\cdot10^{-12}$	$2.6\cdot10^{-19}$
		9	5361	0.534	$9.5\cdot10^{-13}$	$9.7\cdot10^{-20}$
		9	539	0.524	$5.7\cdot10^{-13}$	$5.8\cdot10^{-20}$
		9	540	0.519	$5.2\cdot10^{-13}$	$5.3\cdot10^{-20}$
	P3_FI_N_1	3	516	0.568	$2.6\cdot10^{-12}$	$2.7\cdot10^{-19}$
		6	2601	0.551	$1.2\cdot10^{-12}$	$1.2\cdot10^{-19}$
		6	523	0.543	$1.9\cdot10^{-12}$	$2.0\cdot10^{-19}$
	P3_FI_N_2	3	512	0.580	$2.1\cdot10^{-12}$	$2.2\cdot10^{-19}$
	P3_SI_N_1	3	514	0.603	$4.1\cdot10^{-12}$	$4.2\cdot10^{-19}$
		6	2628	0.565	$1.3\cdot10^{-12}$	$1.3\cdot10^{-19}$
		6	525	0.565	$1.2\cdot10^{-12}$	$1.2\cdot10^{-19}$
	P3_SI_N_2	3	515	0.573	$2.7\cdot10^{-12}$	$2.8\cdot10^{-19}$
	P4_NI_1	3	515	0.582	$2.9\cdot10^{-12}$	$3.0\cdot10^{-19}$
		6	520	0.561	$1.8\cdot10^{-12}$	$1.8\cdot10^{-19}$
	P4_NI_2	3	515	0.611	$2.0\cdot10^{-12}$	$2.1\cdot10^{-19}$
		6	523	0.579	$1.3\cdot10^{-12}$	$1.3\cdot10^{-19}$
	P4_NI_3	3	517	0.599	$3.6\cdot10^{-12}$	$3.7\cdot10^{-19}$
		6	524	0.569	$1.8\cdot10^{-12}$	$1.8\cdot10^{-19}$
Parallel to flow	P1_FI_P	3	512	0.576	$5.0\cdot10^{-12}$	$5.1\cdot10^{-19}$
		9	5344	0.510	$2.0\cdot10^{-12}$	$2.1\cdot10^{-19}$
		9	537	0.511	$2.8\cdot10^{-12}$	$2.9\cdot10^{-19}$
		9	563	0.497	$2.7\cdot10^{-12}$	$2.8\cdot10^{-19}$
	P2_FI_P	3	511	0.612	$5.0\cdot10^{-12}$	$5.1\cdot10^{-19}$
		14	5583	0.469	$4.6\cdot10^{-13}$	$4.7\cdot10^{-20}$
		14	560	0.450	$3.6\cdot10^{-13}$	$3.7\cdot10^{-20}$
	P3_FI_P_1	3	514	0.570	$2.3\cdot10^{-12}$	$2.4\cdot10^{-19}$
		6	2632	0.531	$2.9\cdot10^{-12}$	$3.0\cdot10^{-19}$
		6	531	0.518	$2.6\cdot10^{-12}$	$2.7\cdot10^{-19}$
	P3_FI_P_2	3	514	0.579	$9.9\cdot10^{-12}$	$0.1\cdot10^{-19}$
		6	519	0.558	$4.2\cdot10^{-12}$	$4.3\cdot10^{-19}$
	P3_SI_P	3	517	0.594	$6.1\cdot10^{-12}$	$6.3\cdot10^{-19}$
		6	2596	0.579	$3.7\cdot10^{-12}$	$3.8\cdot10^{-19}$
		6	519	0.575	$2.4\cdot10^{-12}$	$2.5\cdot10^{-19}$

Figure 4-12 shows the relation between water permeability and average void ratio for the different stages followed in all tests performed. The results highlighted the clear dependence of the water permeability with the porosity. Furthermore, slightly higher water permeability was observed with flow parallel to bedding planes as expected, which indicated marked anisotropic feature. The data were fitted with an exponential curve which enables to obtain an experimental equation to predict the hydraulic

conductivity by knowing the void ratio. The parameters are shown in the figure for each orientation.

$$k_w = a \cdot \exp(b \cdot e_{av}) \quad (4.3)$$

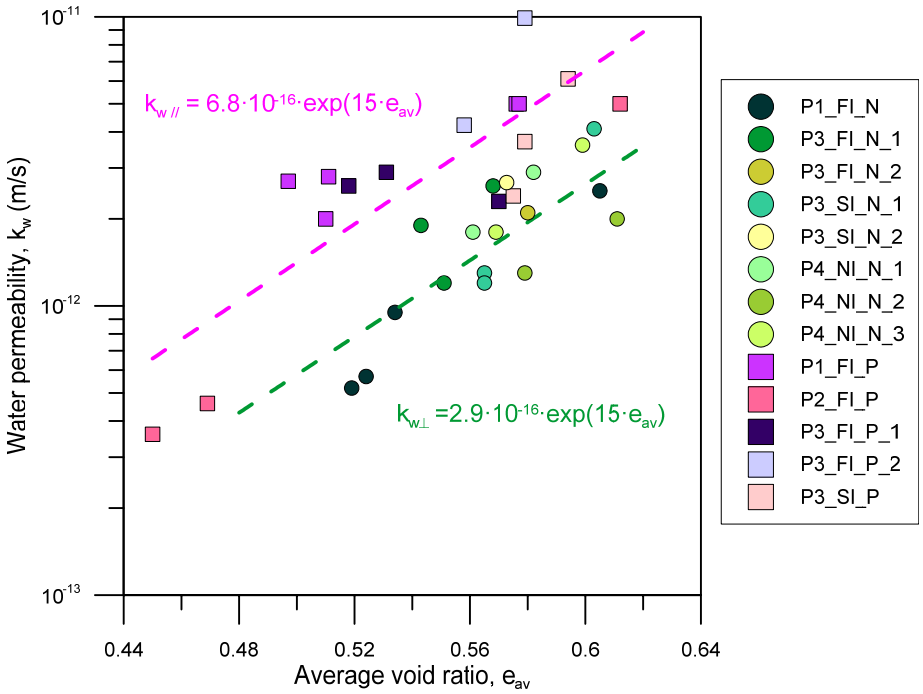

Figure 4-12. Water permeability results as a function of void ratio.

These results show a good agreement with permeability data reported by several authors (Nguyen 2013; Lima 2011; Le 2008) for Boom Clay samples recovered at Mol site and at the same depth (Figure 4-13).

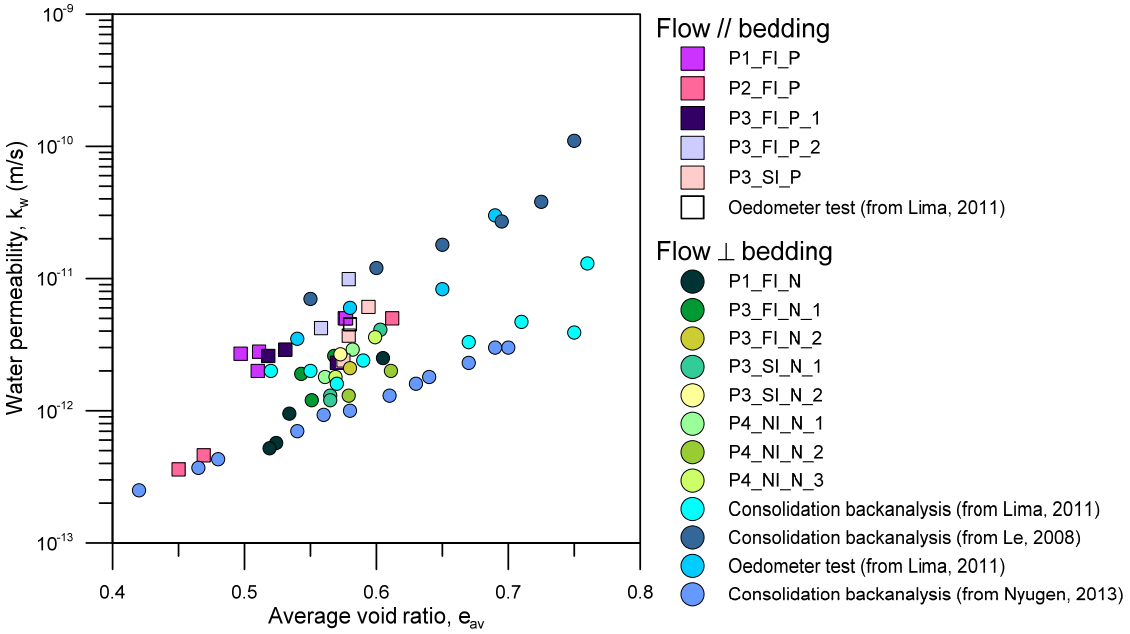

Figure 4-13. Water permeability data in terms of the average void ratio in comparison with data reported by several authors.

4.2. Indurated clays

4.2.1. Background on indurated clays behaviour

Although the hydro-mechanical behaviour of Opalinus Clay at the Mont Terri URL depth is well studied (Marschall et al. 2005; Amann & Vogelhuber 2015), information on deeper samples behaviour, of concern in this study, is quite limited. Still, the hydro-mechanical behaviour of deeper Opalinus Clay and 'Brauner Dogger' samples coming from the same borehole has been published by Romero & Gómez (2013); Ferrari & Laloui (2013); Ferrari et al. (2012). These publications deal with the compressibility properties of both materials under isotropic and oedometer conditions and also include water permeability values which are used for comparison with the results obtained here.

4.2.2. Compressibility properties on loading and unloading

The pre-conditioning paths in the indurated rocks are thought to prevent possible damage on the samples due to the saturation process. In this way, contact with water was only allowed when the samples were loaded up to a certain level. Regarding that the *in situ* conditions of OPA and BD are pretty similar (Chapter 2 Section 2.3.2) the same stress level was selected for both materials which simplified the protocols and the further comparison of the results but was still similar to the *in situ* effective stress.

4.2.2.1. Oedometer tests

Indurated samples display a very high initial suction due to the important stress relief, despite being almost saturated (see Chapter 2 Table 2-7). The samples can undergo degradation as a clear consequence of suction reduction effects due to water contact at low stress levels. To minimise these effects, the samples were always loaded at a target total stress and only then put in contact with water under atmospheric pressure to avoid any damage on the samples. Therefore, at the moment of applying the water pressure, the effective stress state will be equivalent to the *in situ* one.

At oedometer conditions, a total vertical stress of 12 MPa was considered to be the initial total vertical stress for both samples, BD and OPA. On the one hand, 12 MPa is enough high to avoid a large swelling during saturation. On the other hand, it enables to reach the *in situ* effective stress after imposing water pressure keeping the stress level within the working range of laboratory. This first stage was carried out at a relatively fast rate of 30 kPa/min and at constant water content. During this path, it was expected to reduce the initial suction, since total stress will be transmitted to the pore pressure and therefore small deformations due to suction changes are predicted.

Figure 4-14 and Figure 4-15 show the continuous loading results in terms of axial strain as a function of the net and effective vertical stress for the two tested materials (EMPA SLA 'Brauner Dogger' at 781.55 - 781.85 m and OED 1/1 Opalinus Clay 936.26 – 936.49 m depth). Initially, the samples were loaded up to 12 MPa (A-B in the figures) at constant water content at a rate of 30 kPa/min followed by a day for equalisation. Then, the samples were flooded at a constant total vertical stress of 12 MPa and afterwards a water pressure of 0.5 MPa was applied to both sides of the sample. In this way, the vertical effective stress after reaching equalization was 11.5 MPa, close to the *in situ* values (11.75 MPa for BD and 14.01 for OPA).

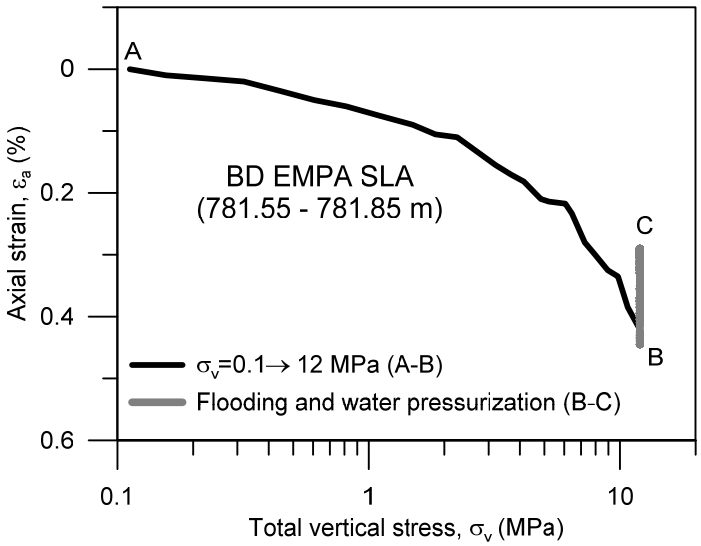

Figure 4-14. Compression curve during oedometer pre-conditioning path of EMPA SLA 'Brauner Dogger' in terms of total stress.

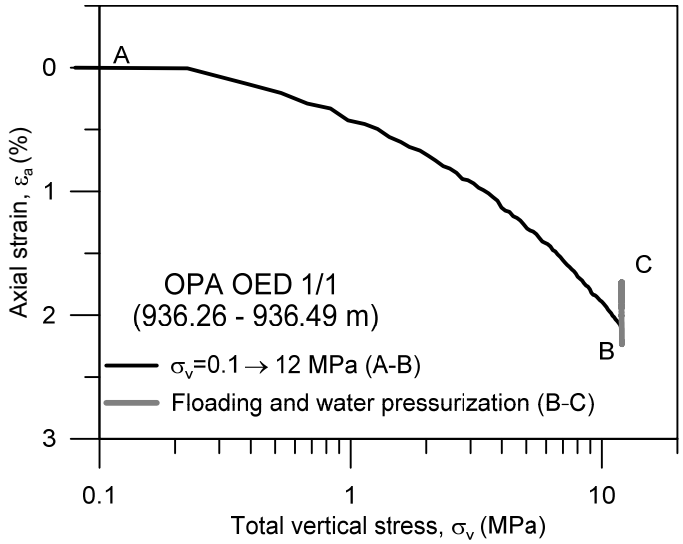

Figure 4-15.Compression curve during oedometer pre-conditioning path for OED 1/1 Opalinus Clay in terms of total stress.

Swelling strains (negative strains correspond to swelling) during water contact (flooding) and pressurization at constant $\sigma_v = 12\,MPa$ for BD EMPA SLA and OPA OED 1/1 are shown in Figure 4-16. The loading up to 12 MPa was not enough to reduce the initial suction (very high values indicated in Chapter 2 Table 2-7) to zero, therefore, when they were put in contact with water, some swelling occurred being higher in the Opalinus Clay sample which presents a higher initial suction.

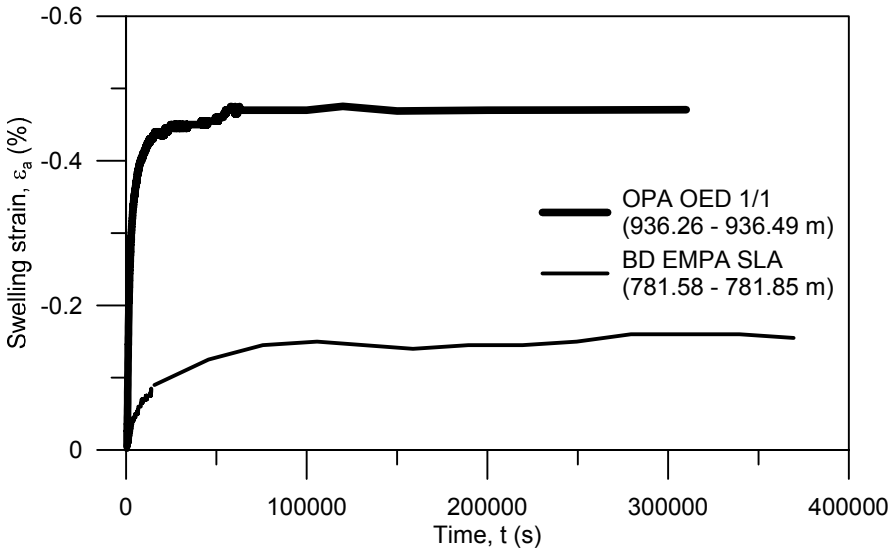

Figure 4-16. Swelling during flooding until steady-state conditions for OED 1/1 Opalinus Clay and EMPA SLA 'Brauner Dogger'.

Regarding the entire loading and unloading path, Figure 4-17 and Figure 4-18 show the continuous loading results in terms of axial strain as a function of the net and effective vertical stress for the two tested materials (EMPA SLA 'Brauner Dogger' at 781.55 - 781.85 m and OED 1/1 Opalinus Clay 936.26 – 936.49 m depth) including the pre-conditioning path explained above. After having increased the water pressure at the boundaries (point C in the figures), an attempt was made to measure permeability, increasing downstream water pressure to impose a gradient of 5 MPa. Nevertheless, the water pressure could not be able to rise because a large flux was detected in the downstream side since the gap between the sample and the oedometer ring remained open. Due to the impossibility to measure water permeability at this stress level, the samples were loading up to 18 MPa and permeability measurement was again tried with no success. The same occurred after loading the samples up to 25 MPa. The loading path from 12 to 25 MPa is depicted in terms of net stress in the figures (C-D). Finally, the samples were unloading from 25 MPa to 1 MPa of total stress at a rate of 30 kPa/min (D-E). In the end, vertical stress and water pressure were rapidly reduced to atmospheric conditions (E-F).

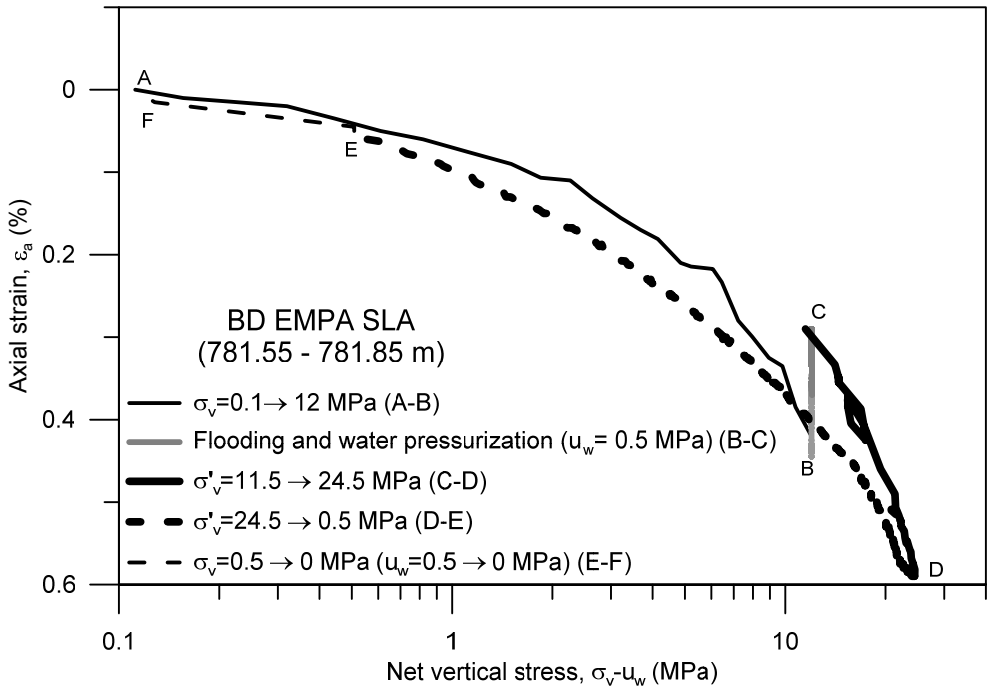

Figure 4-17. Compression curve during oedometer loading and unloading for EMPA SLA 'Brauner Dogger' in terms of net/effective stress.

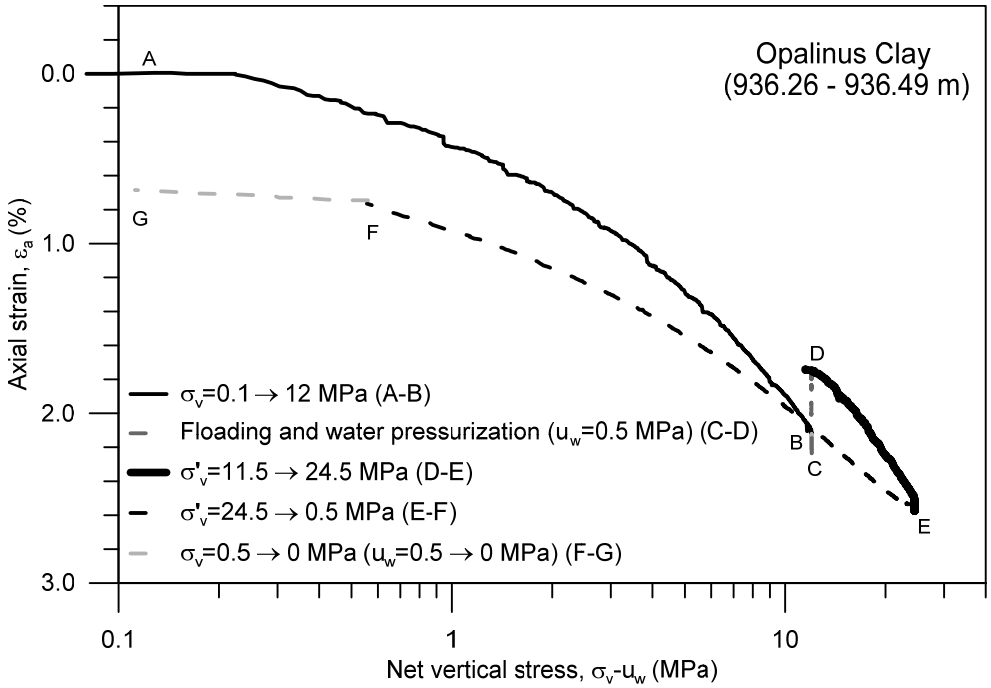

Figure 4-18. Compression curve during oedometer loading and unloading for OED 1/1 Opalinus Clay in terms of net/effective stress.

The compressibility curves were compared with the ones published by Ferrari & Laloui (2013). Axial strains reported for 'Brauner Dogger' samples (Figure 4-19) are very close to the ones presented here, whereas those corresponding to the Opalinus Clay sample are slightly higher due to the different initial void ratio (shallow sample), which is higher in that case (Figure 4-20).

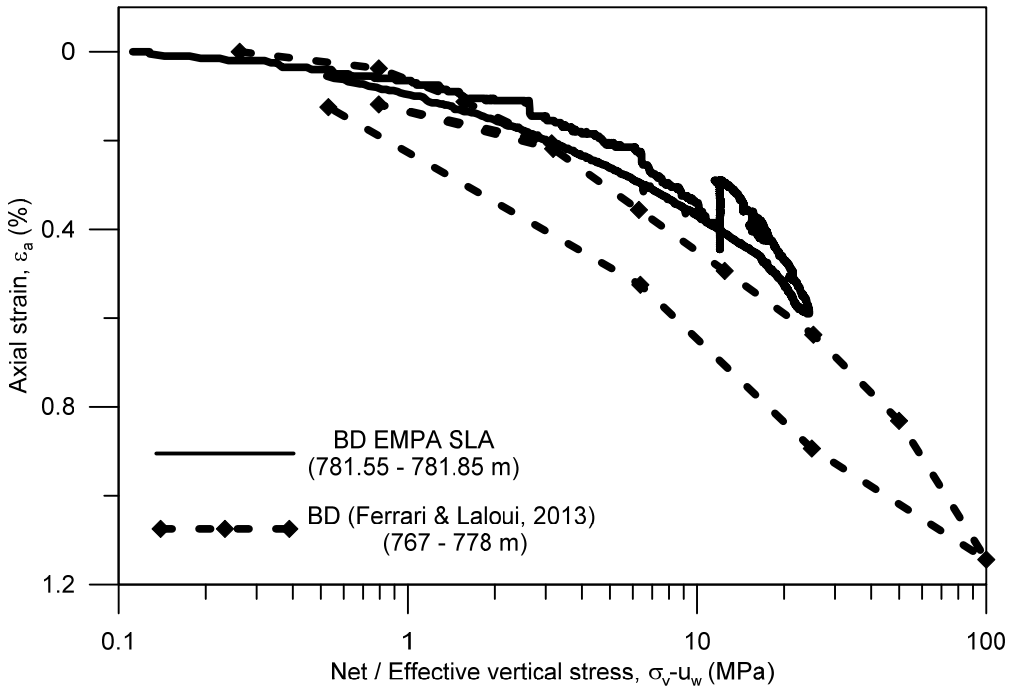

Figure 4-19. Comparison of compression curves for 'Brauner Dogger' samples: EMPA SLA (781.55 – 781.85 m) and 'Brauner Dogger' (767-778) from Ferrari & Laloui (2013).

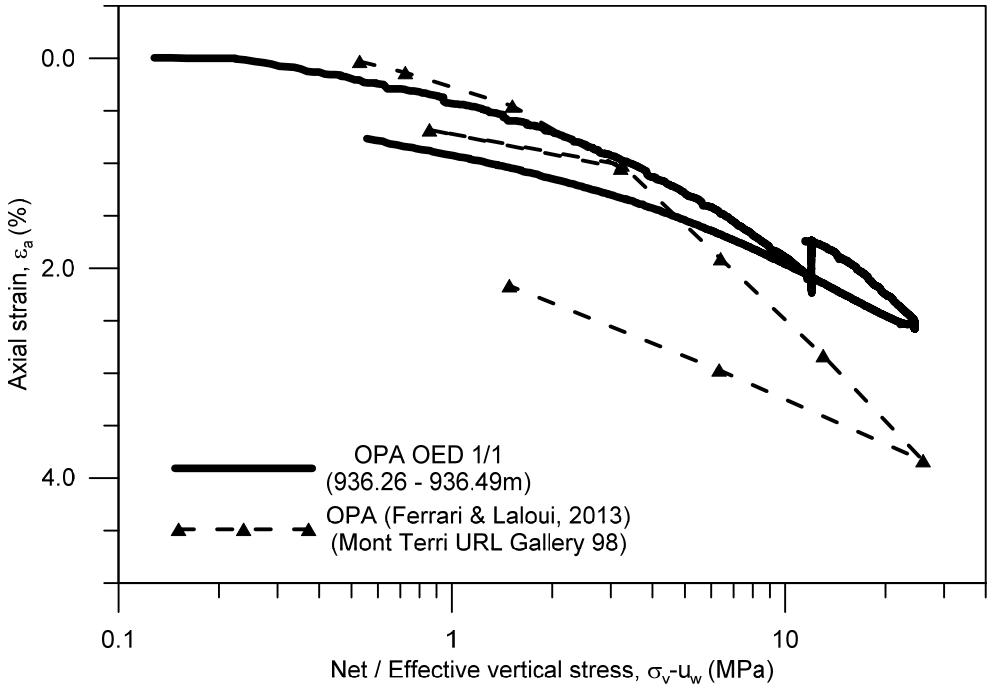

Figure 4-20. Comparison of compression curves for Opalinus Clay samples: OED 1/1 (936.26 – 936.49 m) and shaly facies (Mont Terri URL Gallery 98) from Ferrari & Laloui (2013).

The drained constrained modulus for the loading/unloading stages of each test can be estimated as $E'_k = (\delta\sigma_v - u_w)/\delta\varepsilon_a$ and the results of both samples are reported in Table 4-4 together with the axial strain and the void ratio at the end of the each stage. These values are shown in Figure 4-21 for both samples, where the vertical stress is in a linear scale. These oedometer results reveal that EMPA SLA 'Brauner Dogger' is

stiffer than OED 1/1 Opalinus Clay. The evolution of the modulus on the paths followed for both samples is shown in Figure 4-22. Figure 4-23 shows the 'Brauner Dogger' modulus together with Ferrari & Laloui (2013) results which are in good agreement.

Table 4-4. Different loading/unloading stages followed on both materials.

	EMPA SLA 'Brauner Dogger' (781.55 – 781.85 m)			OED 1/1 Opalinus Clay (936.26 – 936.49 m)		
Stage	E'_k (MPa)	ε_a(%)*	e*	E'_k (MPa)	ε_a (%)*	e*
Initial	--	--	0.09	--	--	0.11
σ_v=1 to 12 MPa at constant water content	--	0.39	0.085	--	2.21	0.085
σ_v=12 MPa u_w=0.5 MPa	--	0.29	0.087	--	1.74	0.091
σ_v=12 to 25 MPa u_w=0.5 MPa	4270	0.59	0.083	1615	2.58	0.081
σ_v=25 to 1 MPa u_w=0.5 MPa	6040	0.05	0.089	2660	0.78	0.101
After final unloading	--	0	0.09	--	0.59	0.103

*Void ratio at the end of the stage

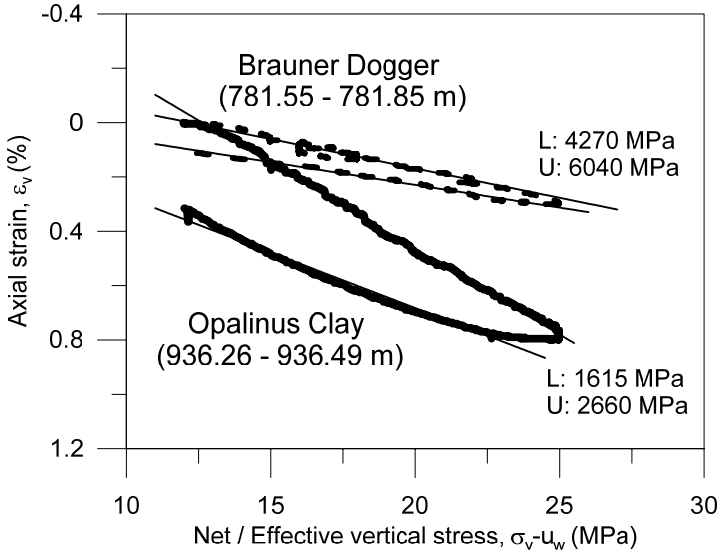

Figure 4-21. Compression curves during oedometer loading and unloading for EMPA SLA 'Brauner Dogger' and OED 1/1 Opalinus Clay with average drained constrained modulus values.

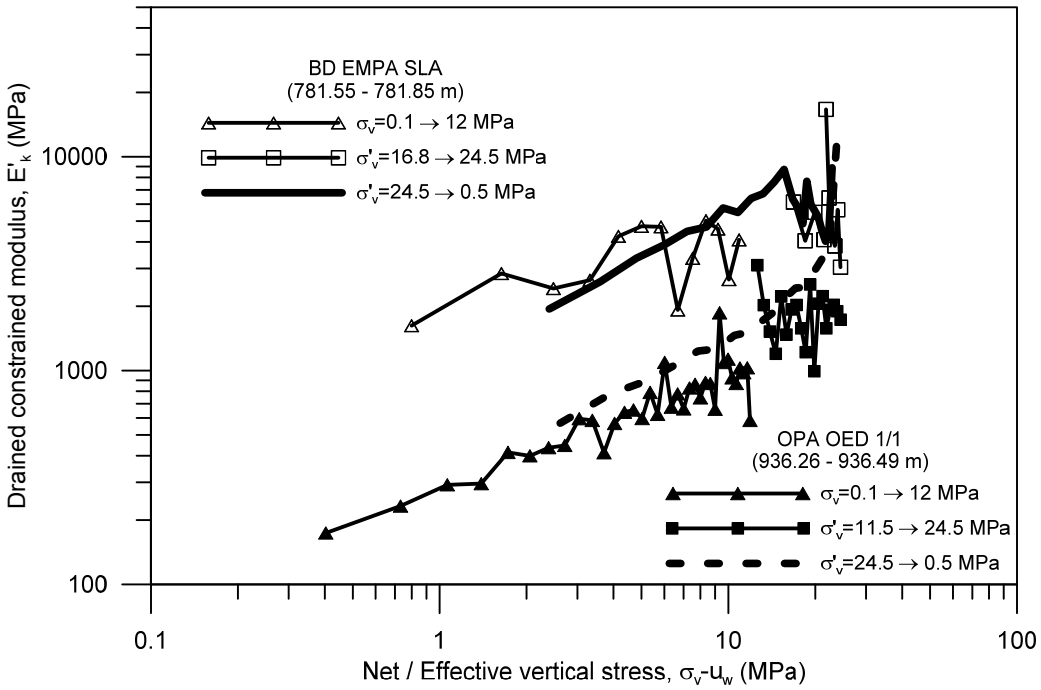

Figure 4-22. Drained constrained modulus during oedometer loading and unloading for EMPA SLA 'Brauner Dogger' and OED 1/1 Opalinus Clay in terms of net/effective stress.

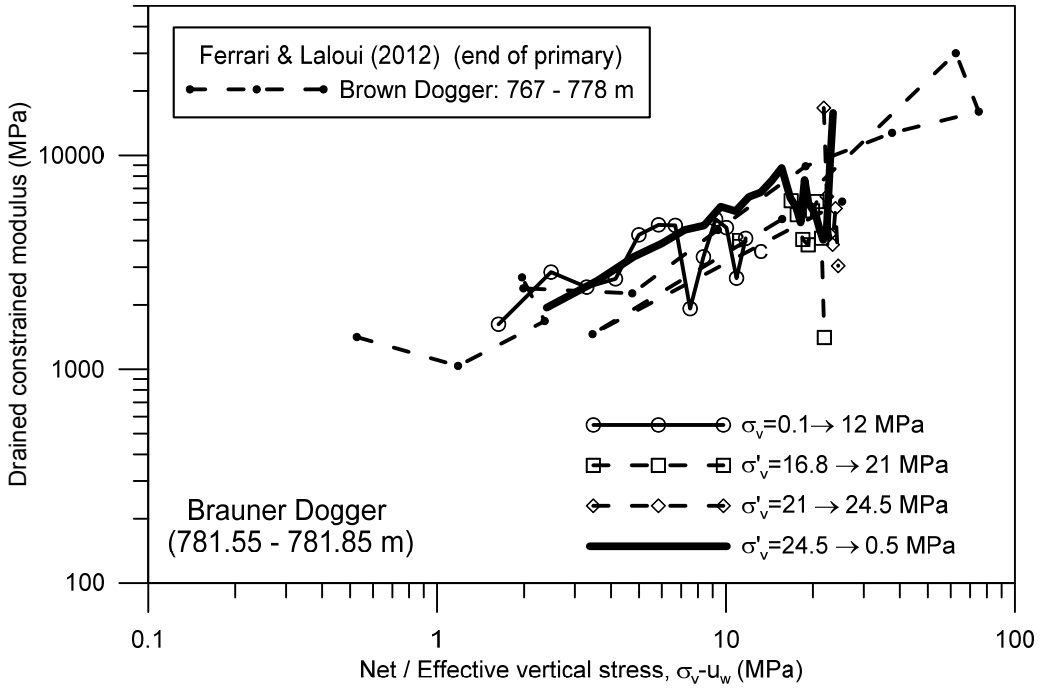

Figure 4-23.Drained constrained modulus during oedometer loading and unloading for EMPA SLA 'Brauner Dogger' (781.55 – 781.85 m) and 'Brauner Dogger' (767 - 778 m) from Ferrari & Laloui (2013) in terms of net/effective stress

4.2.2.2. Isotropic tests

In order to prevent the damage of the samples and to reach similar stress state than the *in situ* one, samples were loaded up to a total mean stress of 10 MP before water contact, following the same procedure as in the oedometer tests. Once a water

pressure of 0.5 MPa was applied, the effective mean stress was close but slightly lower than the *in situ* one.

Figure 4-24 shows the axial deformation on isotropic loading from 0.1 to 10 MPa at constant water content for the two tested materials (BD EMPA SLA and deep OPA OED 1/1) whereas Table 4-5 summaries the approximate values of axial strain and void ratio (radial strain was considered negligible during this process on the low-height specimens). These results are corrected by the equipment deformation presented in Appendix A as well as those reported by Romero & Gómez (2013) for BD OED 20/Harz (776.51 - 776.72 m depth) and OPA OED (879.79 - 880.01 m depth). A comparison of the compression curves between all these samples is also shown in Figure 4-25 which displays similar behaviour of the samples of each sequence during the loading.

These results (Figure 4-24 to Figure 4-27) suggest that BD EMPA SLA is slightly stiffer than deep OPA OED 1/1.

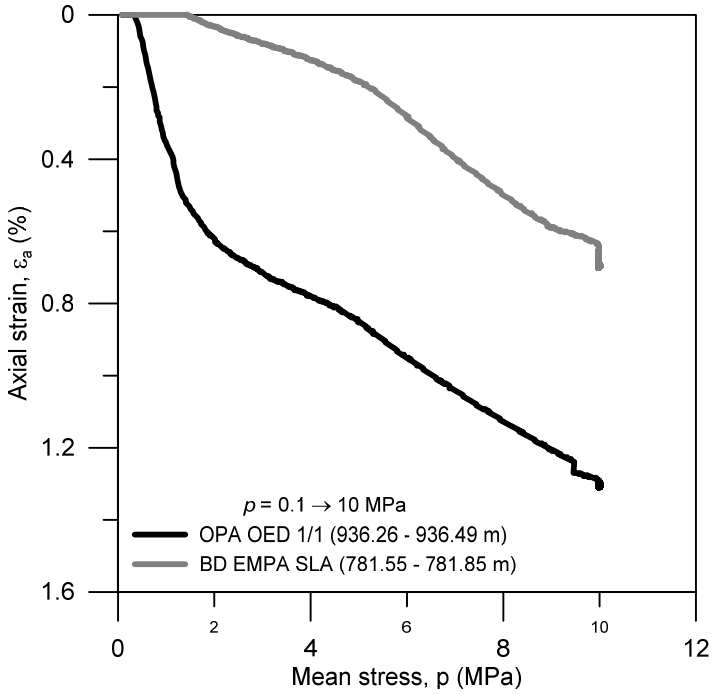

Figure 4-24. Preliminary compression curves during isotropic loading from 0.1 to 10 MPa at constant water content for EMPA SLA 'Brauner Dogger' and deep OED 1/1 Opalinus Clay.

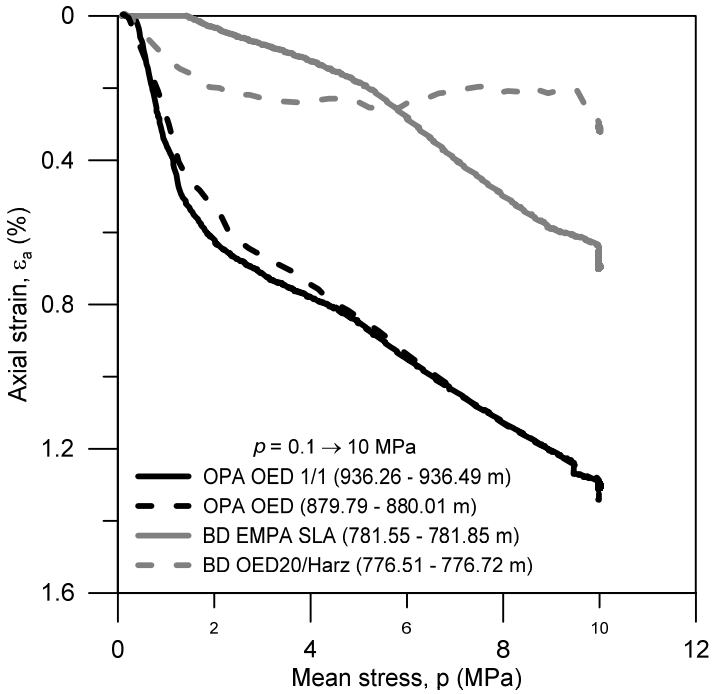

Figure 4-25. Comparison of preliminary compression curves during isotropic loading from 0.1 to 10 MPa at constant water content (OPA OED and BD OED20/Harz data from Romero & Gómez 2013).

Table 4-5. Comparison of axial strain and approximate void ratio obtained during isotropic loading (OPA OED and BD OED20/Harz data from Romero & Gómez 2013).

Isotropic loading from 0.1 to 10 MPa at constant water content			
Opalinus Clay	OED (879.79 - 880.01 m) (e_0=0.109)	ε_a(%)	1.34
		Approx. e	0.094
	OED 1/1 (936.26 - 936.49 m) (e_0=0.110)	ε_a(%)	1.3
		Approx. e	0.096
'Brauner Dogger'	OED 20/Harz (776.51 - 776.72 m) (e_0=0.130)	ε_a(%)	0.3
		Approx. e	0.113
	EMPA SLA (781.55 - 781.85 m) (e_0=0.090)	ε_a(%)	0.7
		Approx. e	0.092

Swelling strains (negative strains correspond to swelling) during water pressure application (flooding) at a constant mean stress of10 MPa for BD EMPA SLA and deep OPA OED 1/1 are shown in Figure 4-26. This swelling is associated with the reduction of the remained suction (loading to 10 MPa was not enough to reduce the initial suction to zero). Higher values of swelling were found for Opalinus Clay.

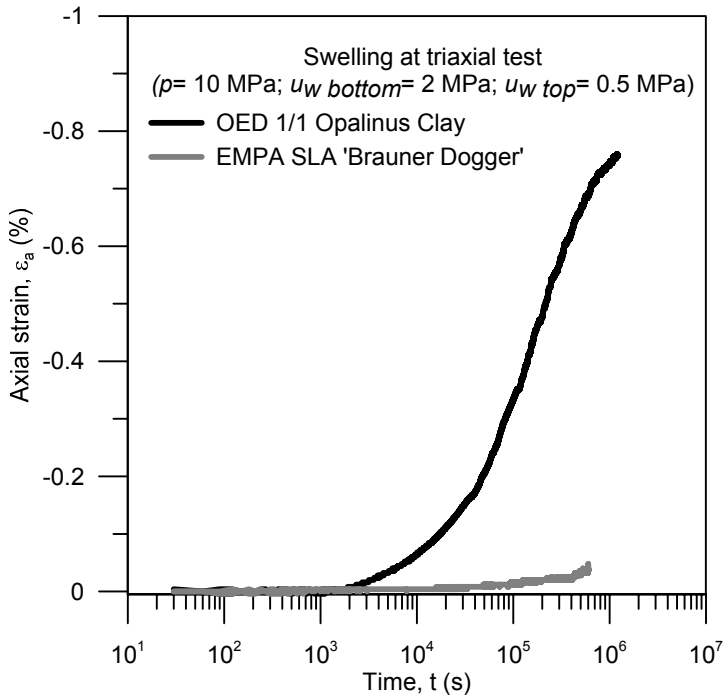

Figure 4-26. Swelling during water pressure application (flooding) at constant p=10 MPa for EMPA SLA 'Brauner Dogger' and deep OED 1/1 Opalinus Clay.

4.2.2.3. Comparison

Figure 4-27 shows the compressibility curves for both samples under oedometer and isotropic conditions and also the swelling results were compared with those obtained during the oedometer tests (Figure 4-28). Higher compressibility and swelling were found for Opalinus Clay in both tests.

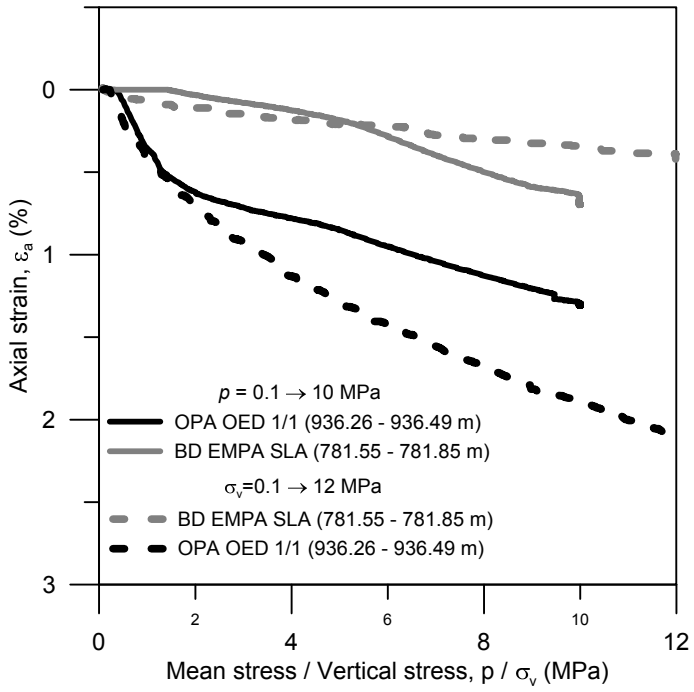

Figure 4-27. Compressibility under oedometric and isotropic conditions for OED 1/1 Opalinus Clay and EMPA SLA 'Brauner Dogger'.

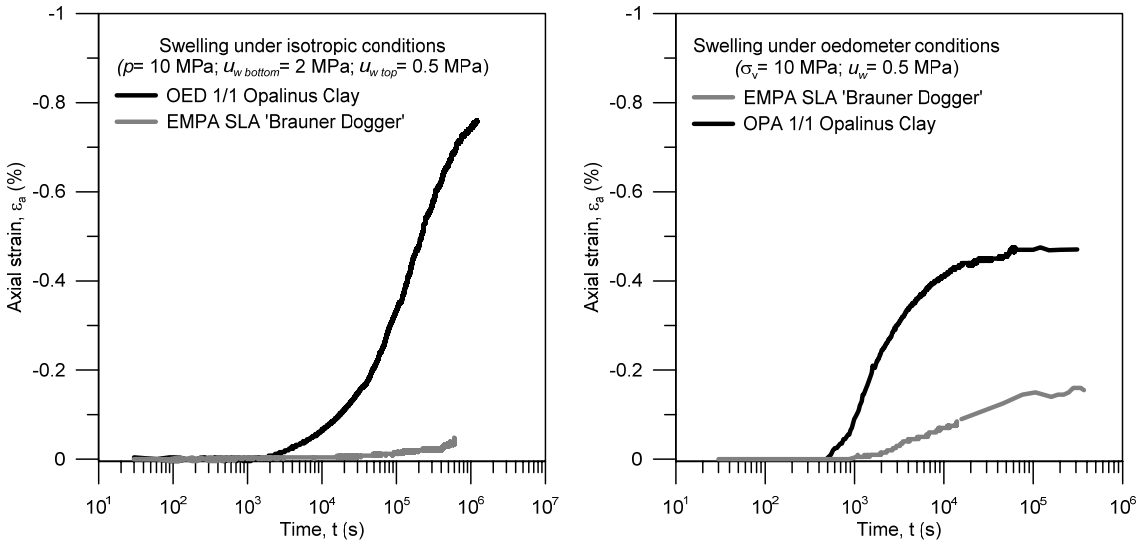

Figure 4-28. Comparison of swelling produced during isotropic and oedometer tests for EMPA SLA 'Brauner Dogger' and deep OED 1/1 Opalinus Clay.

4.2.3. Water permeability

Following the same procedure described for Boom Clay, water permeability in indurated samples was determined using the constant-head method but under isotropic conditions. Similarly, in this section, only a representative stage of water permeability determination is explained. The rest of plots corresponding to several stages of water permeability determination for both Opalinus Clay and 'Brauner Dogger' are presented in Appendix C.

Figure 4-29 shows time evolution in terms of outflow volume (V_w) and $\Delta V_w/(A \cdot i \cdot \Delta t)$ during one stage of water permeability determination stage, where A is the sample cross-section, i the hydraulic gradient applied, V_w the water volume flowing through the sample, and Δt the elapsed time. Changes in volume and time are referred to a fixed initial value under steady state conditions (under steady state conditions $\Delta V_w/(A \cdot i \cdot \Delta t)$ corresponds to hydraulic conductivity k_w shown in the figures and summarised in Table 4-6 and Table 4-7). The controller used for applying the bottom water pressure is less accurate in volume measurement than the one used at the top boundary, and so it regularly displayed higher values of inflow volume. Thus, the evolution of water volume outflow was used to determinate the volume flowing through the sample.

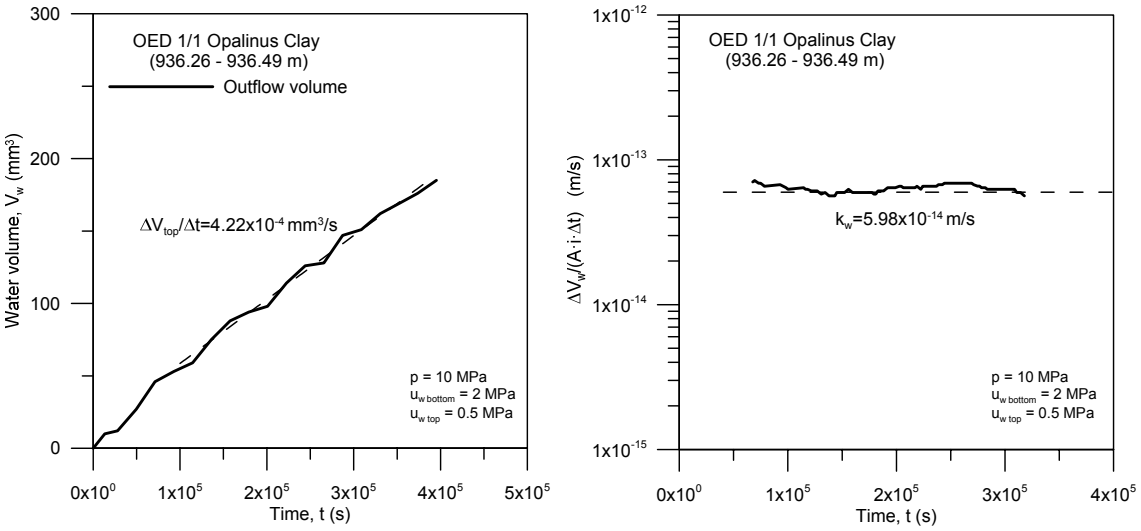

Figure 4-29. Time evolution of $\Delta V_w/(A \cdot i \cdot \Delta t)$. Stage at $p = 10\ MPa$; $u_{w\ bottom} = 2\ MPa$; $u_{w\ top} = 0.5\ MPa$. OED 1/1 Opalinus Clay sample.

Table 4-6 and Table 4-7 summarises the water permeability tests on OED 1/1 Opalinus Clay (936.26 – 936.49 m) and EMPA SLA 'Brauner Dogger' (781.55 – 781.85 m) samples, where p is the isotropic total stress, u_w the water back pressure applied on bottom and top caps, i the hydraulic gradient, e_{av} the average void ratio and k_w the hydraulic conductivity. It also includes the intrinsic permeability to water, K_w, considering a water property factor of $\rho_w g/\mu_w = 9.744 \cdot 10^6 (m \cdot s)^{-1}$ at 20ºC (water density $\rho_w = 998.2\ kg/m^3$ and water dynamic viscosity $\mu_w = 1.005 \cdot 10^{-3} N \cdot s/m^2$).

Table 4-6. Water permeability results of OED 1/1 Opalinus Clay.

Stage				OED 1/1 Opalinus Clay (936.26 – 936.49 m)		
p (MPa)	$u_{w\ bottom}$ (MPa)	$u_{w\ top}$ (MPa)	Hydraulic gradient i	Average void ratio e_{av}	k_w (m/s)	K_w (m^2)
10	2.0	0.5	6234	0.104	$5.98 \cdot 10^{-14}$	$6.14 \cdot 10^{-21}$
15	2.0	0.5	6243	0.103	$3.25 \cdot 10^{-14}$	$3.34 \cdot 10^{-21}$
19	2.0	0.5	6292	0.092	$2.67 \cdot 10^{-14}$	$2.74 \cdot 10^{-21}$

Table 4-7. Water permeability results of EMPA SLA 'Brauner Dogger'.

Stage				EMPA SLA 'Brauner Dogger' (781.55 – 781.85 m)		
p (MPa)	$u_{w\ bottom}$ (MPa)	$u_{w\ top}$ (MPa)	Hydraulic gradient i	Average void ratio e_{av}	k_w (m/s)	K_w (m^2)
10	2.0	0.5	6220	0.093	$1.20 \cdot 10^{-14}$	$1.23 \cdot 10^{-21}$
15	2.0	0.5	6308	0.091	$6.00 \cdot 10^{-15}$	$6.22 \cdot 10^{-22}$
15	5.0	0.5	19029	0.090	$5.98 \cdot 10^{-15}$	$6.14 \cdot 10^{-22}$

Results for Opalinus Clay clearly show the variation of water permeability with the stress state, or in other words, the lower the void ratio is, the lower the permeability. In this case of BD, two water injections at 15 MPa of isotropic pressure were performed before and after the first gas injection but two different pressure gradients were selected. Consistently, the water permeability results are almost equal.

The permeability values are represented in Figure 4-30 as a function of the average void ratio together with the corrected ones corresponding to OED 20/Harz ‘Brown Dogger’ (776.51 - 776.72m) and OED Opalinus Clay (879.79 - 880.01m) from Romero & Gómez (2013) - noticed that average void ratio of these results was corrected with the new calibration of the equipment, and thus are not exactly the same as in the original publication-. Surprisingly, very small change in void ratio resulted in quite large variations of permeability in these deep indurated clays.

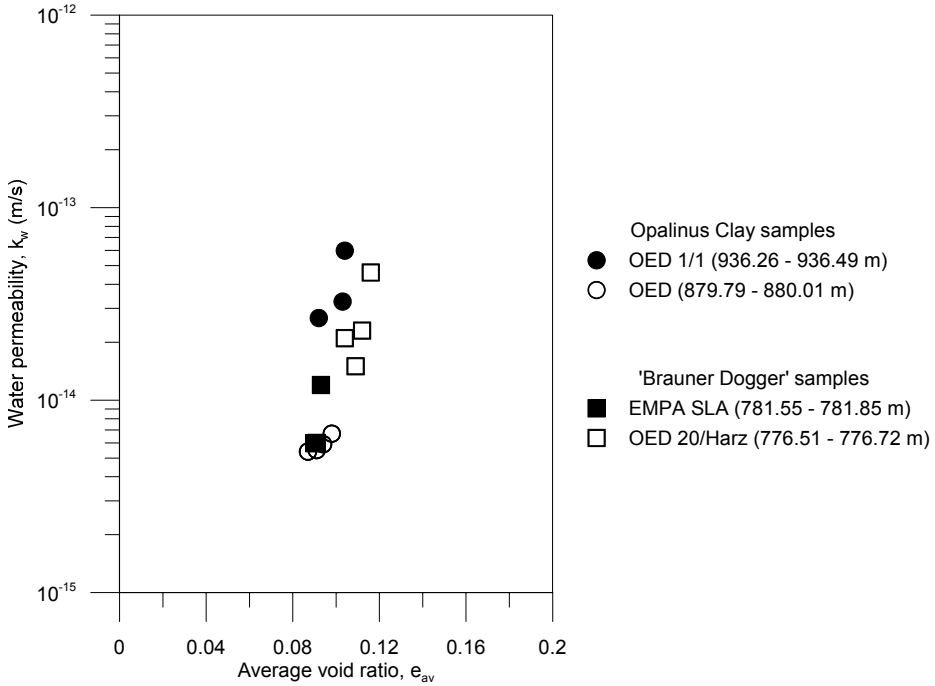

Figure 4-30. Water permeability as a function of the average void ratio.

In order to build up confidence in the results, also data reported by Ferrari & Laloui (2013): - BD (767 -778 m); OPA (Mont Terri URL Gallery 98) and shallow OPA samples (OPA BHA-8/1 in the shaly facies, MI-niche; approx. 300m depth) were included. Figure 4-32 and Figure 4-31 show the water permeability (flow perpendicular to bedding planes) as a function of average void ratio In the present study slightly higher values of water permeability were obtained for Opalinus Clay samples whereas values for ‘Brauner Dogger’ are in good agreement with the previous ones.

The clear measured dependency on void ratio has been fitted to the exponential equation indicated in both figures for both ‘Brauner Dogger’ and Opalinus Clay formations.

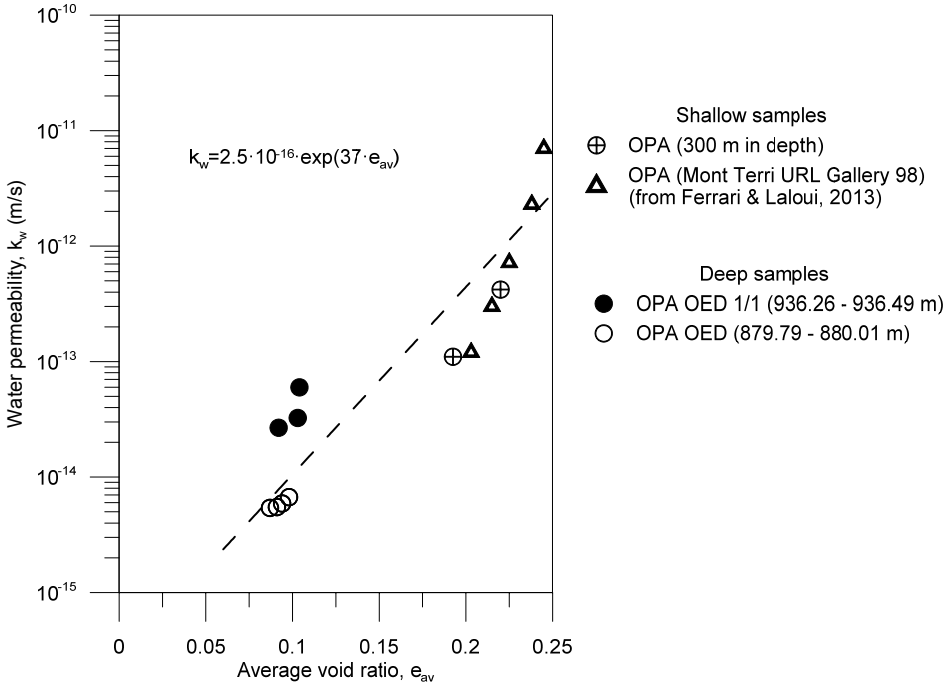

Figure 4-31. Water permeability as a function of the void ratio for Opalinus Clay formation. Exponential fitting.

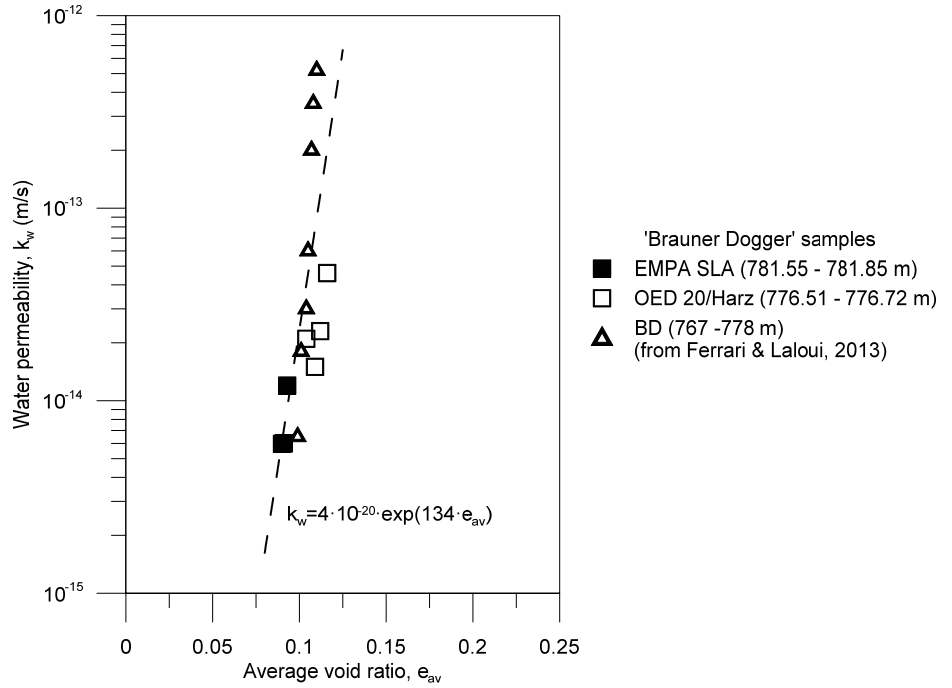

Figure 4-32. Water permeability as a function of the void ratio for ‘Brauner Dogger’ formation. Exponential fitting.

5
GAS INJECTION AND DISSIPATION EXPERIMENTS

5.1. Background

Migration of gas in rocks reveals some specific mechanisms that do not meet the multiphase flows. These mechanisms are complex, as they seem to be highly dependent on the heterogeneity and the microstructure of clayey materials.

Within the field of radioactive waste disposal, most of the research concerning gas migration process in the past decades has been focused on the bentonite-based engineering barrier materials. The earliest experimental papers on gas migration in clay relating to radioactive waste disposal were published by Pusch & Forsberg (1983). Saturated Mx-80 bentonite was tested in order to determine its gas permeability after gas breakthrough. These initial experiments highlighted that the degree of saturation of specimens after the passage of the gas through the clay was close to 100%, suggesting that the gas must have passed through a small number of discrete pathways.

The correlation between dry density and degree of saturation of different compacted bentonites with resulting breakthrough pressures has also been object of numerous studies (see for instance Tanai et al. 1996; Tanai & Yamamoto 2003; Graham et al. 2002; Gutiérrez-Rodrigo et al. 2015). Results showed that the breakthrough pressure increases with clay density and decreases with the degree of saturation.

Horseman et al. (1999) and Harrington & Horseman (1999) reported a series of controlled flow rate gas injection experiments on saturated compacted Mx-80 buffer bentonite. Perhaps the most relevant result was that no water displacement was observed to occur inside the specimen, despite the fact that the observed breakthrough pressure seems to be higher than the air entry pressure of compacted bentonite. The peaks observed in gas pressure and measured flows into and out of the specimen were also quite characteristic. The spontaneous decrease in pressure after the peak was taken as an indication of the aperture of a preferential path of high conductivity.

The absence of a marked peak during the second injection phase indicates that the initial path remained partially open. This interpretation was also consistent with the lower gas pressure reached during the second injection phase. It was also checked that the gas pressure at peak was equal to the swelling pressure plus the existing pore pressure. In others words, the gas pressure had to reach the total stress in a critical plane in order to develop a preferential path. However, there is not clear evidence the aperture of the preferential path was inside the specimen and not in the sample-cell interface. In fact, in subsequent publications of the same authors (Harrington & Horseman 2003) it was recognized that besides the development of preferential paths along compaction interfaces which were interpreted as the beginning of inflow of air into the sample, gas pathways between the sample and the cell wall contact was also observed.

In recent times, more attention is being given to the study of gas flow in the host rocks, mainly by means of full scale tests. Nonetheless, laboratory scale experiments are considered to be mandatories to better understand the complex mechanisms of gas transport through clays with well-controlled conditions, avoiding the uncertainties that field measurements may lead. However, in spite of the interest for the long term prediction of waste disposal barriers performance in sedimentary rocks, careful investigation of the coupled hydro-mechanical response of sedimentary formations in relation with gas migration has not received much attention, until recently (Romero et al. 2012; Romero & Gómez 2013; Senger et al. 2014; Cuss et al. 2014; Harrington et al. 2015; Z. B. Liu et al. 2016). The latter studies showed that migration of gas in low permeability rock formations is a rather complex phenomenon, governed by different coupled mechanical and hydraulic processes. Specifically, intrinsic permeability, porosity and water saturation, stress state and stress history, shear strength, strain level, and damage are all playing a role in the response, as well as the gas generation rate and the gas pressure in the near field. Therefore, coupled hydro-mechanical experimental tests are mandatory, in which gas migration is investigated to adequately evaluate the long-term safety of the disposal system.

Experimental data on Boom Clay are still poor, with the exception of the results from laboratory tests within the framework of the MEGAS project (Volckaert et al. 1995), two breakthrough tests (Hildenbrand et al. 2002; Hildenbrand et al. 2004) and recent gas diffusion experiments (Jacops et al. 2013; Jacops et al. 2015). To improve the knowledge on the response to gas migration and the predictive capabilities on the long term behaviour of Boom Clay as host formation, a comprehensive series of air injection tests under oedometer conditions has been performed. Relatively fast volume rate air

injections tests (air pulse tests) were performed to give priority to dominant single-phase air flow mechanisms associated with the opening of stress-dependent discontinuities, rather than on slower two-phase flow and air diffusion mechanisms through the matrix. The tests were specifically designed on samples with oriented bedding planes to investigate their effects on the coupled hydro-mechanical mechanisms dominating gas migration, pressurisation, and release in the clay. Contrarily to previous works (Volckaert et al. 1995; Hildenbrand et al. 2002; Hildenbrand et al. 2004; Arnedo et al. 2008; Arnedo et al. 2013a; Gutiérrez-Rodrigo et al. 2015), volume changes were allowed in the experimental setup, and the deformation response was analysed during air injection, air pressure increase and dissipation.

With regard to Opalinus Clay, experimental data on gas migration have been published for samples retrieved from Mont Terri URL (Hildenbrand et al. 2004; Marschall et al. 2005). However, there is a lack of data on deep Opalinus Clay and 'Brauner Dogger' with the exception of the technical report NAB 13-51 (Romero & Gómez 2013). As an extension of this study and in order to gain confidence on the results, air injection tests under isotropic conditions were performed at different injection rates in these two indurated clays, focusing in the volume change response during injection and dissipation stages.

On balance, experimental data on gas transport in argillaceous rocks are still limited. Therefore, more laboratory work is necessary to mainly understand the physics of the gas migration problem, but also to provide data for numerical analysis. According to these aims, this Chapter describes the experimental results of the air injection tests, initially on Boom Clay followed with results on indurated clays and ending with a comparison of the results and some concluding remarks.

5.2. Boom Clay

Initially, data recorded during air injection and dissipation stages are presented, followed by a deeper analysis of the results, including air permeability determination and the study of the volume change during the gas migration process.

5.2.1. Air injection tests at high stress level

These preliminary tests were performed with the objective to establish threshold air pressures (see Protocol 1 Chapter 3). Initial air pressure was targeted below and above the air entry value determined by MIP, while maximum air pressure was slightly inferior to the vertical stress and similar to the estimated horizontal stress. In this way,

gas flow through the sample-ring interface was expected since the minor principal stress may be exceeded. This protocol also enabled to obtain the K_0 value but in terms of total stresses (referred as K_0^*), and thus to settle the minimum difference between the maximum air pressure and the vertical / horizontal stresses in order to avoid gas flow through the interface for further experiments.

Two different air injections stages were carried out for each orientation following Protocol 1. The first injection was started with an air pressure of 3 MPa lower than the air entry value (around 4.5 MPa from MIP data of intact sample). After full saturation, the second injection with an initial air pressure of 6 MPa, higher than the air entry value, was performed.

The following figures (Figure 5-1 and Figure 5-2) show the time evolution of air inflow and outflow pressures during the fast controlled volume-rate tests (100 mL/min) at a constant vertical stress of 9 MPa, as well as the outflow air volume. Axial displacements are also plotted.

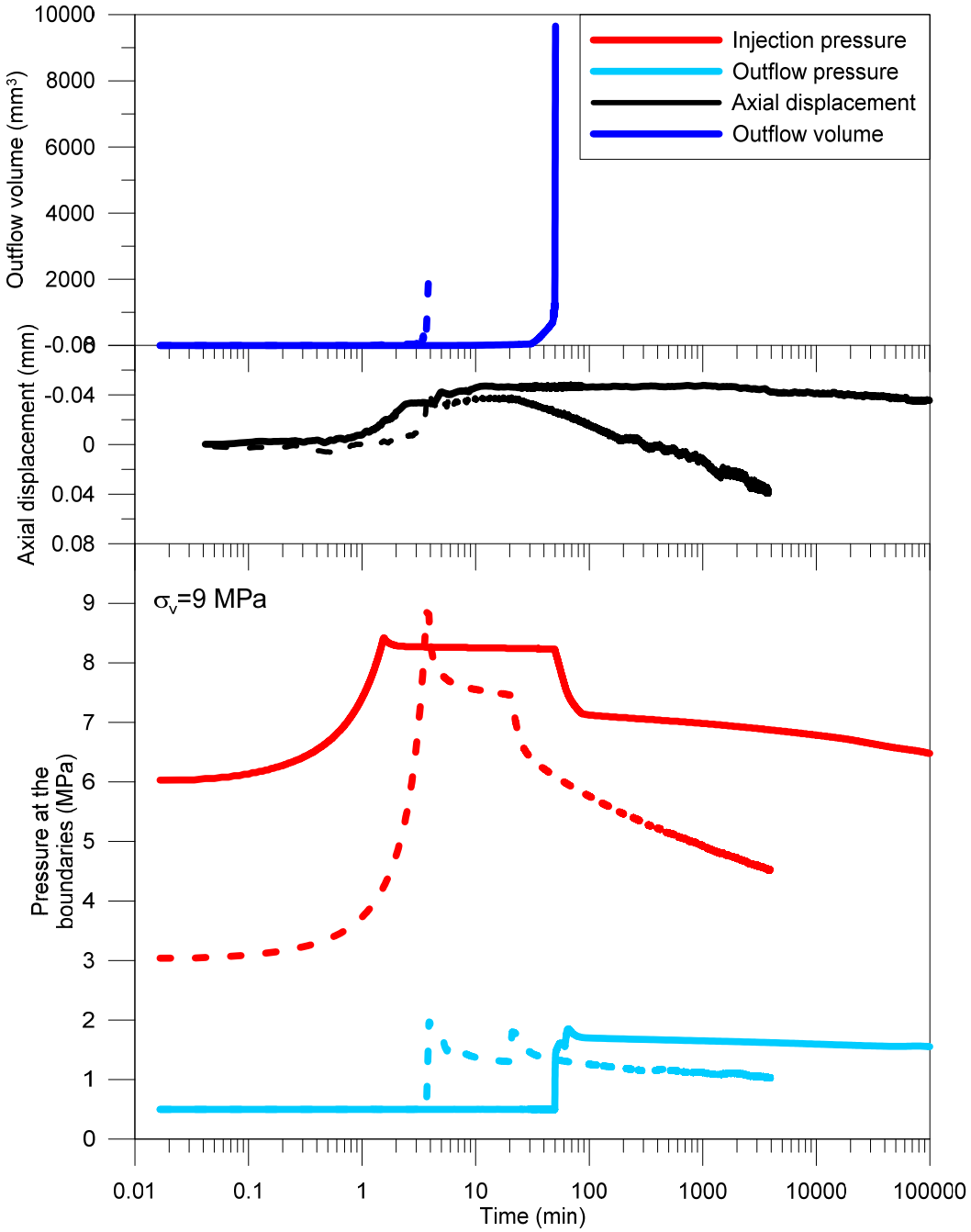

Figure 5-1. Measured time evolution of pressures at the boundaries and outflow volume, together with axial displacements at a constant vertical stress of 9 MPa. First injection with initial air pressure lower than AEV (lines in dash); second injection with initial air pressure higher than AEV (continuous lines). Boom Clay with bedding plane orientation normal to flow (P1_FI_N).

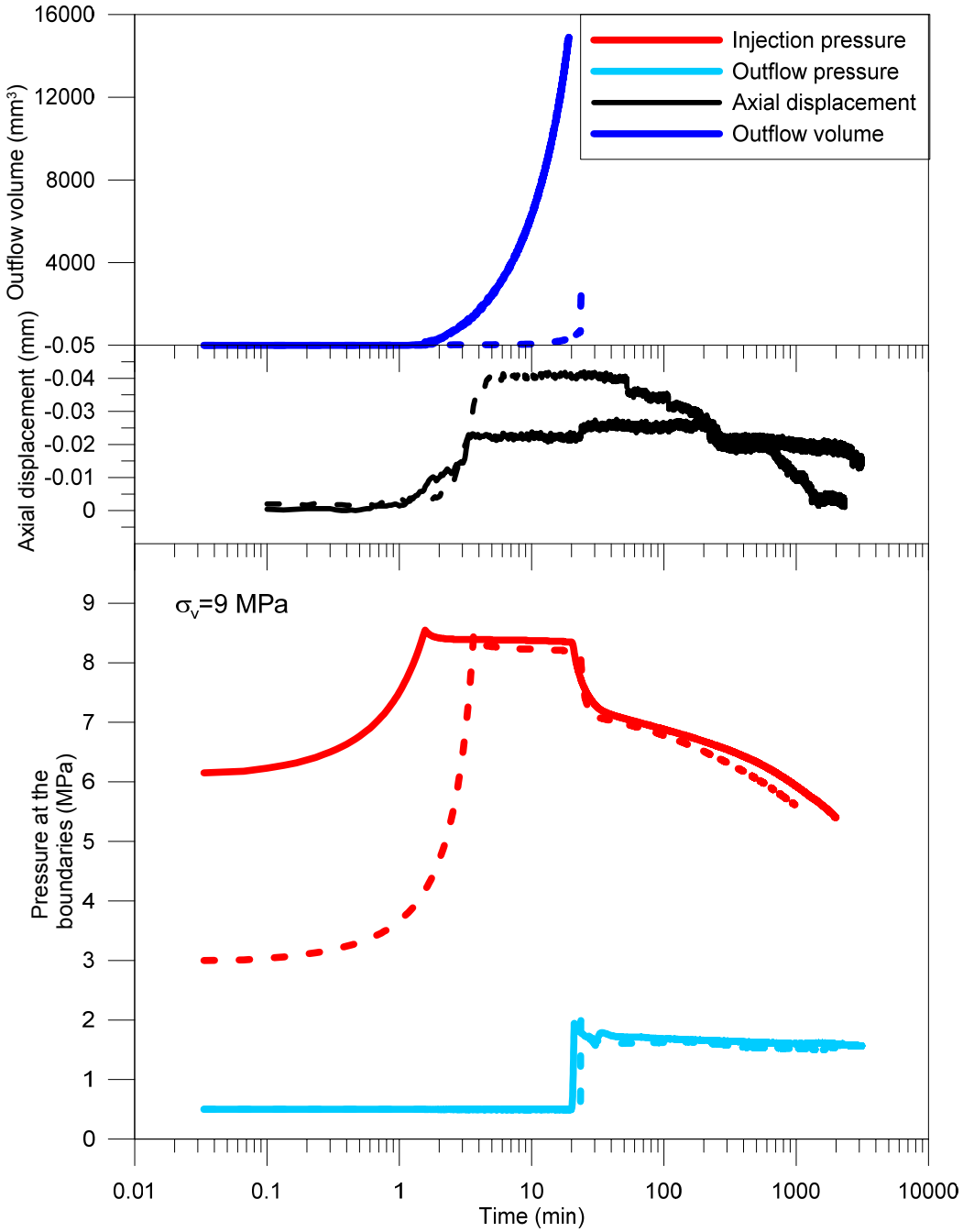

Figure 5-2. Measured time evolution of pressures at the boundaries and outflow volume, together with axial displacements at a constant vertical stress of 9 MPa. First injection with initial air pressure lower than AEV (lines in dash); second injection with initial air pressure higher than AEV (continuous lines). Boom Clay with bedding plane orientation normal to flow (P1_FI_P).

As observed in the figures, the injection pressure was able to increase to 8.5 MPa, followed by shut-off and recovery period at constant air injection volume in all the cases except for the first injection of test P1_FI_N (Figure 5-1). In this case, maximum gas pressure exceeded 8.5 MPa due to a problem with the air injection controller.

A common behaviour was found in all the injections (except for the mentioned). When the maximum air pressure of 8.5 MPa was reached, after shut-off, a small spike in the inflow pressure was recorded which was attributed to the inertia of the air pressure injection system. Afterwards, the inflow pressure remained initially flat, and then, the injection pressure showed a sharp decline coupled with a rise of the downstream pressure and a large outflow of gas. In most of the cases, the constant downstream pressure condition of 0.5 MPa was not possible to maintain due to the high outflow air volume rates detected (the downstream pressure increased until reaching 2 MPa, where a constant pressure was again prescribed by the pressure release valve). This behaviour appeared to be a consequence of the passage of air through the ring-sample interface where the radial total stress was applied.

With regard to the axial displacement response (negative axial displacements and strains correspond to expansion), the samples at constant vertical total stress displayed expansion at the early fast air injection stage (air pressure increase and effective stress decrease) and progressive compression on air pressure dissipation (air pressure decrease and effective stress increase).

For the first gas injection of Test P1_FI_N (flow normal to bedding planes) due to a problem with the controller, the target pressure of 8.5 MPa was surpassed and immediately there was a large amount of air outflow and a peak in vertical displacements (Figure 5-1). Most probably air pressure overpassed the lateral stress and a path between the sample and the ring wall was opened. However, the pressure dissipated quickly and then stabilised, which suggested that this path closed up. Nevertheless, at 7.5 MPa another sharp decline in the inflow pressure was observed, together with a rise in the outflow pressure, in the same way as in the other cases.

These experiments reveal that the behaviour of the material against an increase of the gas pressure does not depend on whatever the initial pressure was lower or higher than its air entry value. The mechanism that controls the air flow seems to be more related to the local heterogeneity and not to the classical invariant of the capillary air entry pressure. Consequently, in the following tests, the initial air pressure was set lower than the AEV so that the range of pressures was closer to the *in situ* one.

Now, focusing on the inflow pressure drop after the shut-off, the time evolution of inflow pressure and total vertical stress are plotted in Figure 5-3 for all the cases. Note that there is a lack of data regarding total lateral stress.

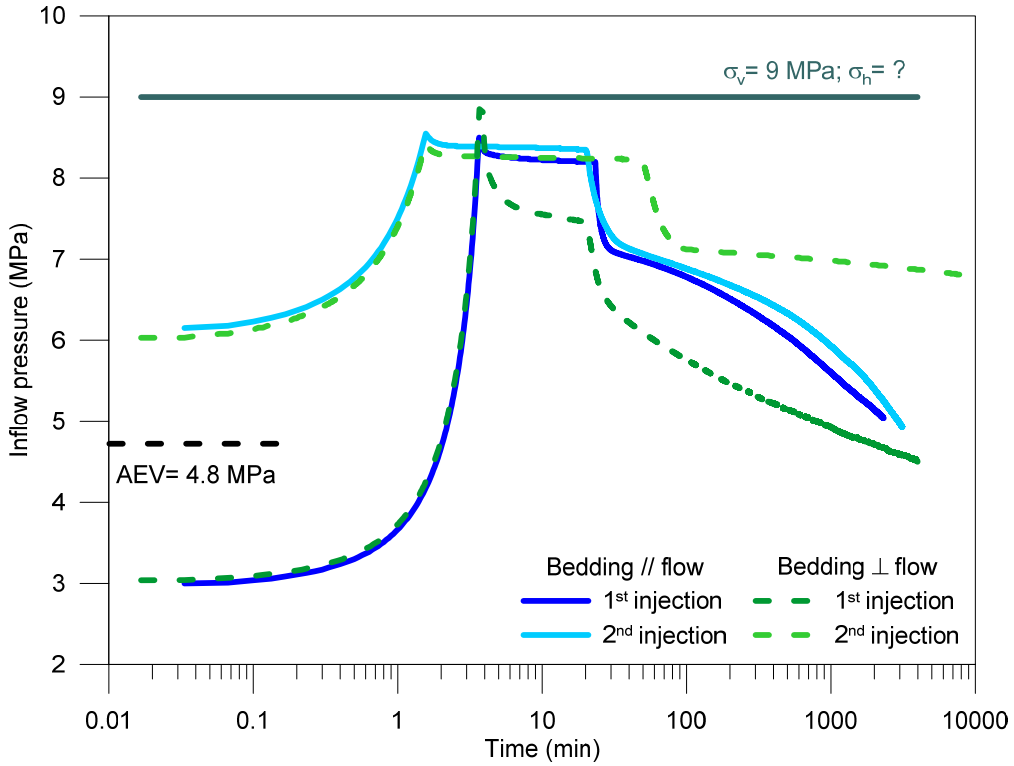

Figure 5-3. Comparison of the time evolution of air injection pressure for tests performed with Protocol 1.

This behaviour was interpreted in terms of the changes in overconsolidation ratio and K_0 value. At the beginning of the injections, the samples were normally consolidated (vertical stress of 9 MPa), and the estimate value of K_0 is around 0.74 (Horseman et al. 1987; Nguyen 2013). It was expected some increase of the lateral stress during air injection, since the samples tends to an overconsolidated state during effective stress decrease because the air injection acts as an unloading. Subsequently, K_0 increased (Figure 5-4). If not, a failure would have been observed when the injection pressure was between 6.4-6.1 MPa (calculations based in total stress using values of friction angle reported by Horseman et al. 1987; Nguyen 2013). However, the samples were still able to maintain the gas pressure up to 8.5 MPa, so it is thought that K_0 value rose up to $K_0^* = \sigma_h/\sigma_v = 0.94$ in terms of total stress. With time, a sharp decline of the inflow pressure took place in all samples, which could be due to the time-dependant effect (some lateral stress relaxation) or the effect of gas pressure front propagation. Hence, K_0 decreased and as a consequence, gas passage was produced through the interface. In that point, it is assumed that gas pressure was equal to lateral total stress. Afterwards, the gas pressure was reduced, but not the lateral stress, so the pathway through the interface closed up and the gas flux was forced to be through the sample. This fact can be detected in the change of the inflow pressure decline trend, which occurred upon 7 MPa approximately. Values of inflow pressures and K_0^* value in terms of total stress are listed in Table 5-1 for each injection. Nevertheless, despite this

closure, an important outflow was still occurring since outflow pressure was not able to stabilise to the target 0.5 MPa. This reasoning was done by examining the behaviour of previous air tests under isotropic stress conditions reported by Romero et al. (2012), where there was no abrupt drop of inflow pressure after shut-off.

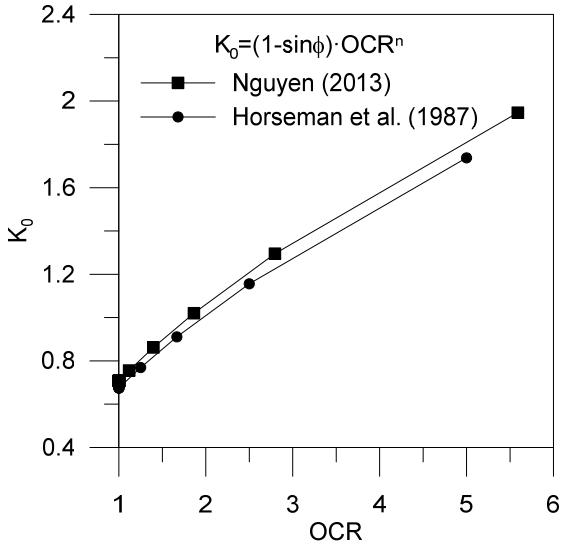

Figure 5-4. Increase of K_0 with overconsolidation ratio (data from Horseman et al. 1987; Nguyen 2013).

Table 5-1. Measured air injection pressures and calculated K_0^* before and after the drop.

Test		Before the drop		Pressure drop	After the drop	
		u_a (MPa)	K_0^*	Δu_a	u_a (MPa)	K_0^*
P1_FI_N	1st injection	7.48	0.83	0.94	6.54	0.73
	2nd injection	8.25	0.92	1.12	7.13	0.79
P1_FI_P	1st injection	8.21	0.91	1.14	7.07	0.78
	2nd injection	8.35	0.93	1.14	7.21	0.80

A simple test was carried out to study the possible lateral relaxation of stress with time. An oedometer sample with bedding planes parallel to the axisymmetric axis was trimmed and loaded in a press up to 3MPa. Afterwards, at constant volume, the time evolution of the vertical stress was recorded. This time evolution of the vertical stress is plotted in Figure 5-5, which shows a reduction of around 0.5 MPa at an early stage and then appears to stabilise at around 2.5 MPa. Extrapolation of this result to the previous air injection tests may explain the lateral stress relaxation (around 8.2 MPa) and thus the air passage through the sample-ring interface.

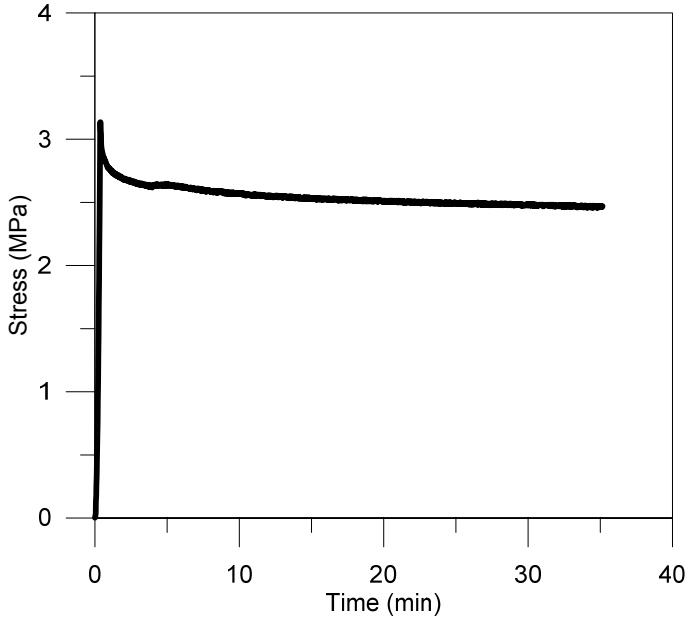

Figure 5-5. Vertical stress relaxation during a constant volume test under oedometer conditions.

Additionally, a demonstration test was carried out injecting gas at a higher constant vertical stress than in previous tests, so that the maximum air pressure was much lower than the lateral stress and gas flow through the sample could be ensured. In this way, the initial hypothesis of gas flow through the ring-sample interface (Protocol 1) could be validated. The sample was orientated with the bedding planes parallel to the air flow and Protocol 2 was followed.

Figure 5-6 shows the time evolution of air inflow and outflow pressures during the fast injection at a constant vertical stress of 14 MPa, as well as the outflow air volume for the sample with bedding planes parallel to flow at initial air pressures of 3 MPa. Axial displacements are also plotted.

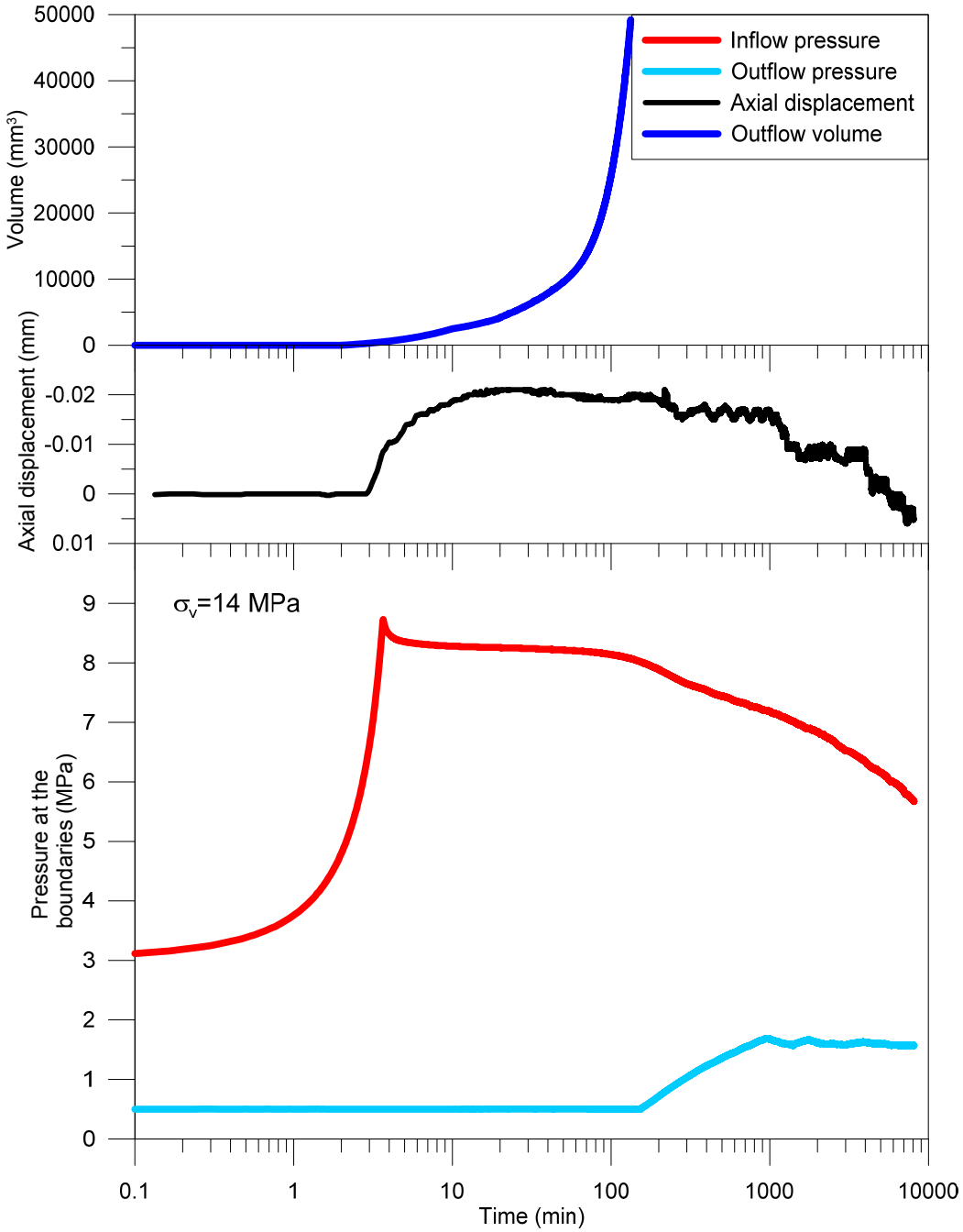

Figure 5-6. Measured time evolution of pressures at the boundaries and outflow volume, together with axial displacements at a constant vertical stress of 14 MPa. Initial air pressure lower than AEV. Boom Clay with bedding plane orientation parallel to flow (P2_FI_P).

As observed in the figure, the injection pressure was able to increase to 8.5 MPa, followed by shut-off and recovery period at constant air injection volume. When the maximum air pressure of 8.5 MPa was reached, after shut-off and after a small spike -due to the inertia of the air pressure system-, the pressure remained initially flat. In this stage, a slight outflow could be observed and then, the injection pressure showed a decrease coupled with a rise of the downstream pressure and a large outflow of gas. However, in this case, there was not a sharp drop in the injection pressure, as those obtained for the previous tests, indicating that the horizontal stress relaxation and the

resulting evolution of K_0 might be the cause of the air passage between the ring-sample interface (Figure 5-7). It was not a problem in the case because of the higher vertical stress that involved a higher horizontal stress.

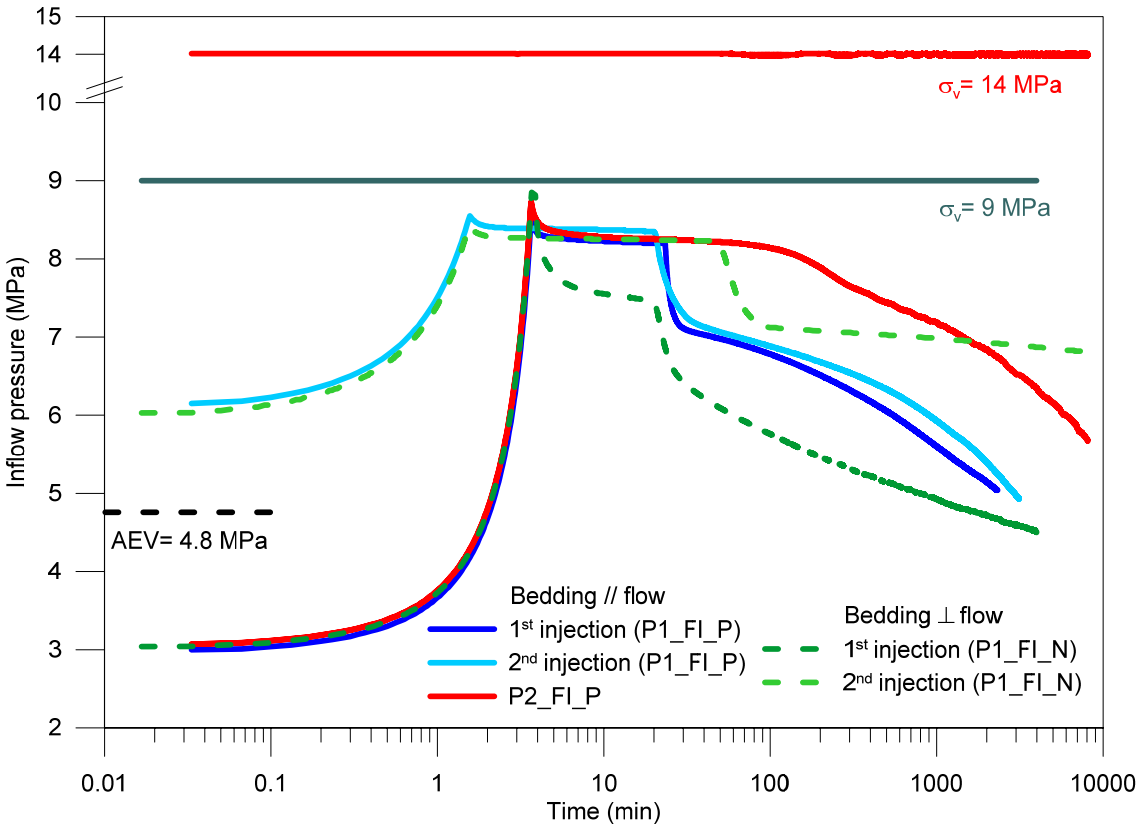

Figure 5-7. Comparison of the time evolution of air injection pressure for tests performed with Protocol 1 and 2.

More research is, indeed, needed regarding the gas migration through interfaces, whether between the canister and clay-based materials or different clays (bentonite/host rock), since they can represent a weakness in the repositories (Davy et al. 2009; J. Liu et al. 2016). However, it is out of the scope of this investigation.

5.2.2. Air injection tests at low stress level

These tests are devoted to studing the constitutive behaviour of the material along gas injection and dissipation avoiding the gas flow between the interfaces. In this regard, the difference between total vertical stress and maximum air pressure higher than 1 MPa must be imposed as explained in Chapter 3. At the same time, lower maximum vertical stresses were applied so that stress state was comparable to the *in situ* one.

A total of seven oedometer tests were performed using Protocol 3 in Boom Clay samples at two orientations (bedding parallel and normal to flow) and at two different injection rates (2 and 100 mL/min). Data recorded in the entire set of experiments are

collected in Appendix D, whereas here, only representative results are explained in detail.

Figure 5-8 and Figure 5-9 present the results from tests performed at two different air injection rates, fast (100 mL/min) and slow (2 mL/min), respectively. To allow comparison, each figure contains data of samples tested at both orientations (bedding parallel and normal to flow). In the figures, it is shown the time evolution of the air inflow pressure at the upstream boundary and outflow pressure at the downstream boundary, as well as the outflow volume (at a constant downstream water pressure of 0.5 MPa). Axial displacement along air injection and dissipation stages are also plotted (negative values correspond to expansion). The air pressure at the upstream boundary increased in time from 0.5 to 4 MPa (A–B in the figure) in all cases, followed by shut-off (point B) and dissipation at closed air injection line that means constant air injection volume (B–C).

A common behaviour was found in all oedometer tests: while air pressure increased, effective stress decreased and samples underwent some expansion until the outflow took place, at such time, upstream pressure decreased which directly implied an increase in effective stress and thus, samples displayed compression. Gas migration is, therefore, a highly coupled process.

Analysing these results in depth, some trends can be observed. Firstly, samples with bedding orientated normal to flow systematically showed larger expansions no matter the injection rate. Nonetheless, the first air outflow breakthrough depended on the injection rate. In samples tested at 100 mL/min, the first outflow was detected during the dissipation stage, whereas in samples tested at 2 mL/min it already occurred during the last phase of the injection stage (Table 5-2). The outflow volume rapidly increased indicating the breakthrough time until the downstream controller was filled. At this time the outflow pressure started to increase until the maximum of 1.8 MPa limited by release valve was reached. Another point to highlight is that during the fast injection very small displacement was recorded and samples underwent most of the expansion after the shut-off. On the contrary, expansion of the samples tested at slow rate occurred during the injection stage, reaching its maximum at the shut-off. This fact will be further studied in the following sections.

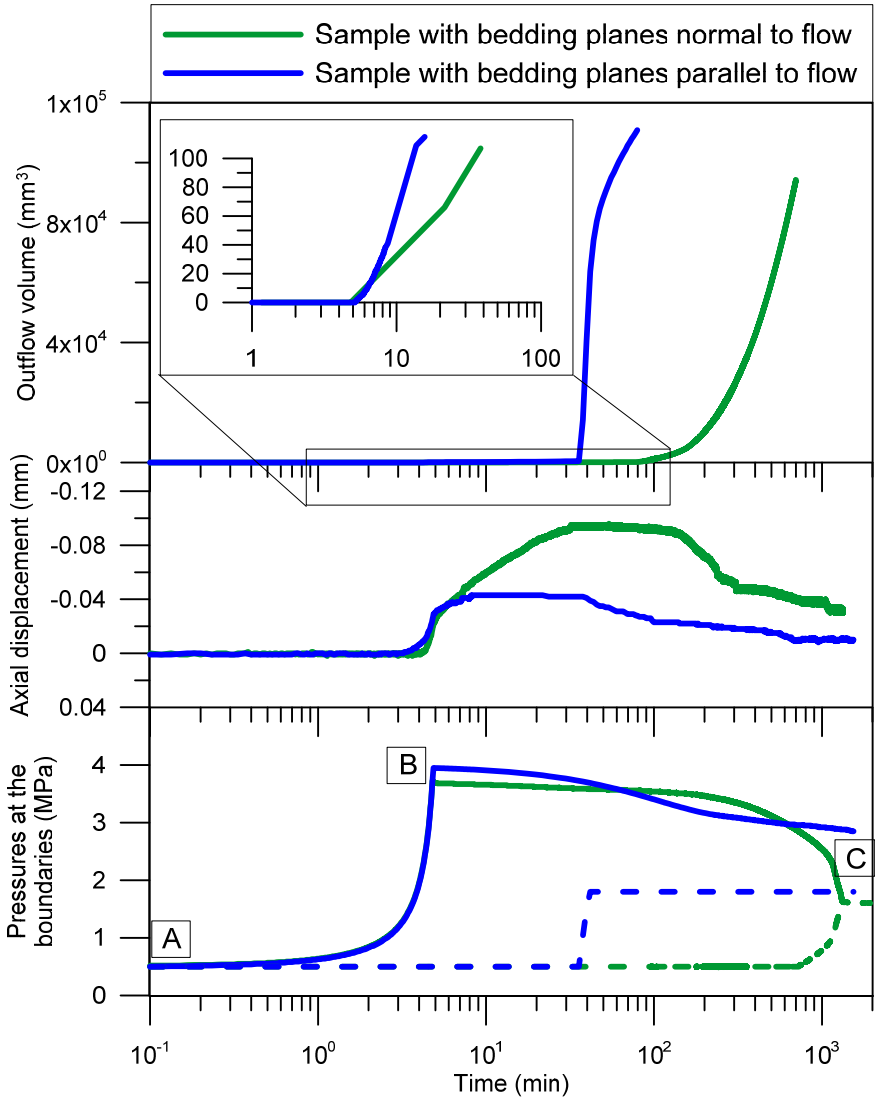

Figure 5-8. Measured time evolution of pressures at the boundaries and outflow volume, together with axial displacements at a constant vertical stress of 6 MPa. Fast injection on Boom Clay with bedding plane orientation parallel (blue) and normal (green) to flow (P3_FI_P_2 and P3_FI_N_1).

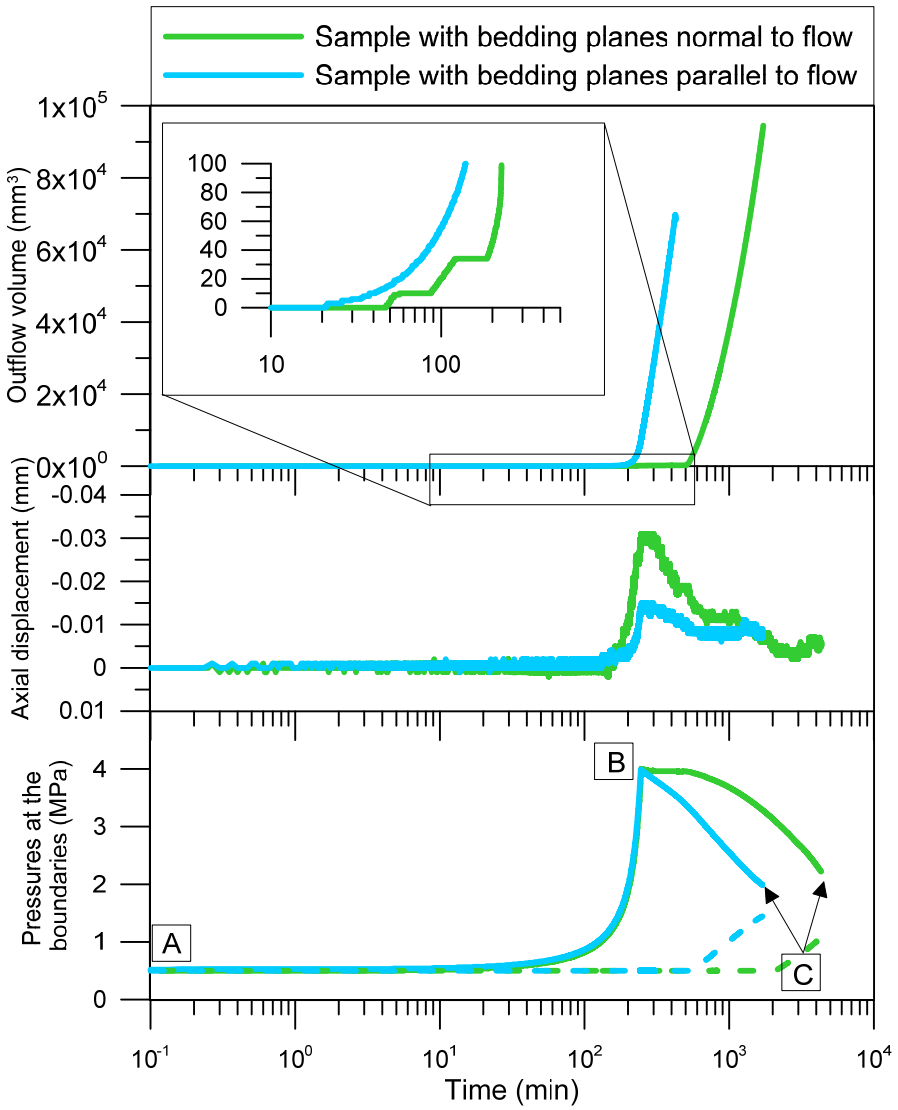

Figure 5-9. Measured time evolution of pressures at the boundaries and outflow volume, together with axial displacements at a constant vertical stress of 6 MPa. Slow injection on Boom Clay with bedding plane orientation parallel (blue) and normal (green) to flow (P3_SI_P and P3_SI_N_2).

Table 5-2. Time of first outflow detection

Injection rate	Test	Time of outflow breakthrough (min)
Fast injection r=100 mL/min ($t_{shut-off}$=4.8 min)	P3_FI_N_1	5.62
	P3_FI_N_2	4.92
	P3_FI_P_1	4.90
	P3_FI_P_2	5.20
Slow injection r=2 mL/min ($t_{shut-off}$=245 min)	P3_SI_N_1	11.60
	P3_SI_N_2	20.77
	P3_SI_P_1	47.43

Air pressure dissipation rate (ratio between inflow pressure during dissipation stage and time) are presented in Table 5-3. Data turned out to be quite erratic. Initially, it was expected a somewhat faster dissipation rate in samples with bedding planes orientated

parallel to the air flow, but expansion and aperture of pathways may have more impact in the dissipation process. Also, the filling of the controller in the downstream line could influence these results.

Table 5-3. Air dissipation rate obtained at the final stage of air injection experiments

Bedding orientation	Test	Dissipation rate $\Delta u_a/\Delta t$ (MPa/min)
Bedding normal to air flow	P3_FI_N_1	$-1.1\cdot10^{-3}$
	P3_FI_N_2	$-1.0\cdot10^{-4}$
	P3_SI_N_1	$-3.0\cdot10^{-5}$
	P3_SI_N_2	$-5.0\cdot10^{-4}$
Bedding parallel to air flow	P3_FI_P_1	$-5.0\cdot10^{-5}$
	P3_FI_P_2	$-6.0\cdot10^{-4}$
	P3_SI_P_1	$-1.4\cdot10^{-3}$

5.2.3. Intrinsic permeability

Air permeability calculations were performed using the gas pressure decay method. A pressurized tank of known volume V with an initial absolute pressure $\bar{u}_a$(upstream reservoir) was connected to the bottom cap, whereas the top cap was maintained under a pressure of $\bar{u}_{at}$. The time evolution of the absolute air pressure decay $\bar{u}_a$ inside the bottom tank was recorded, and was used to estimate the mass of air flowing through the sample assuming perfect gas law:

$$\frac{dn}{dt} = \frac{V}{RT}\frac{d\bar{u}_a}{dt} \tag{5.1}$$

where n corresponds to the mols of air flowing through the sample, R is the ideal gas constant and T the absolute temperature.

The mass inflow rate dn/dt can be also estimated using the generalized Darcy's law for compressible fluid and the perfect gas law:

$$\frac{dn}{dt} = -\frac{A}{2RT}\frac{k_{ia}}{\mu_a}\frac{\left(\bar{u}_a^2 - u_{atm}^2\right)}{L} \tag{5.2}$$

where k_{ia} the intrinsic air permeability, which depends on different properties of the solid matrix (void ratio, pore size distribution, shape of pores, tortuosity) and reflects the changes undergone during matrix degradation at standard temperature and pressure, respectively. A and L are the cross-sectional area and length of the specimen, and μ_a the air dynamic viscosity at standard temperature and pressure. By

using equations (5.1) and (5.2), the following expression is obtained for the air permeability K_a (see for instance, Yoshimi & Osterberg 1963)

$$K_a = \frac{k_{ia}\rho_a g}{\mu_a} = -\frac{2LV\mu_a}{A\left(P_a{}^2 - P_{at}{}^2\right)}\frac{dP_a}{dt} \tag{5.3}$$

where $\bar{u}_{at} = u_a - u_{atm}$ is the gauge air pressure just inside the specimen at the upstream end, $\rho_a$the density of air at standard temperature and pressure, and g the acceleration of gravity. More detailed calculations on air mass balance are presented in Appendix E.

Nevertheless, the use of this expression to calculate air intrinsic permeability presents some limitations that have to be taken into account. It considers that the fluid flow takes place on the whole area of the sample; however, it is expected, and afterwards proved (see Chapter 6), that air flows through preferential dilatant pathways. The expression was chosen since it was also used to obtain gas intrinsic permeability in several publications such as Arnedo et al. (2013) and Pineda et al. (2014). It is assumed that the air pathways are desaturated and that the relative permeability to air is maximum in these paths (relative permeability close to one), even though the matrix is saturated and the global degree of saturation is higher than 95%. This way, the expression allows obtaining intrinsic permeability values to air flow that can be compared to those obtained for water, which can be used to study the influence of sample deformation on air transport properties.

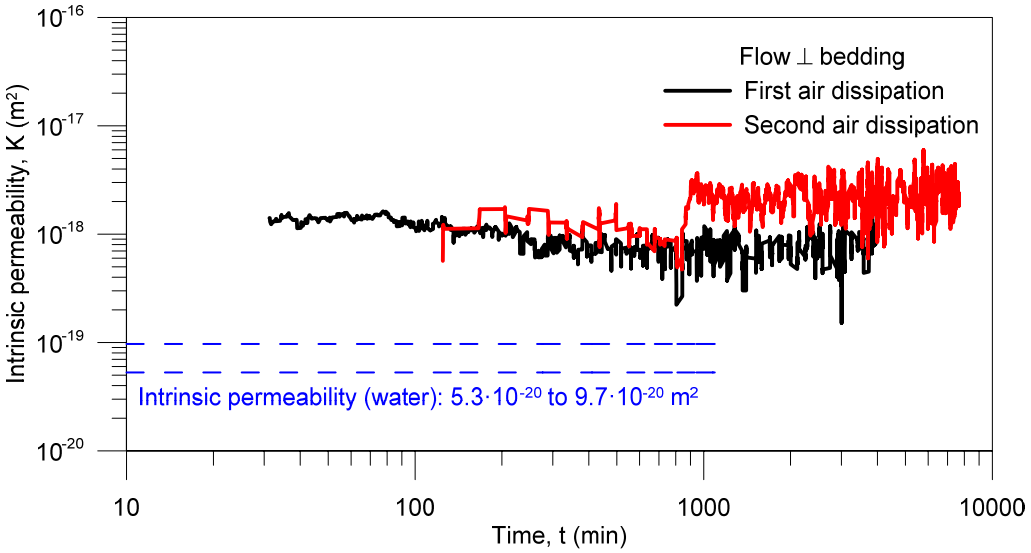

Figure 5-10 and Figure 5-11 present the time evolution of intrinsic permeability during air pressure dissipation after the pressure drop for the tests performed at high stresses (Protocol 1). Only the final part of the dissipation was considered for the permeability

calculation assuming quasi-steady state conditions. Intrinsic permeability values to water flow at the same stress level were also plotted for reference. As observed, a somewhat higher intrinsic permeability for air (around 10^{-18} m^2) was obtained compared to water.

Another highlight of these experiments is that intrinsic permeability to air in the second injection after full saturation of the sample was slightly higher in both tests. It could be considered an indicator of some damage of the sample after the first injection which persisted in the sample fabric despite the saturation. However, it is not a strong difference and in order to evaluate the sealing capacity of the Boom Clay and a large number of similar experiments are required.

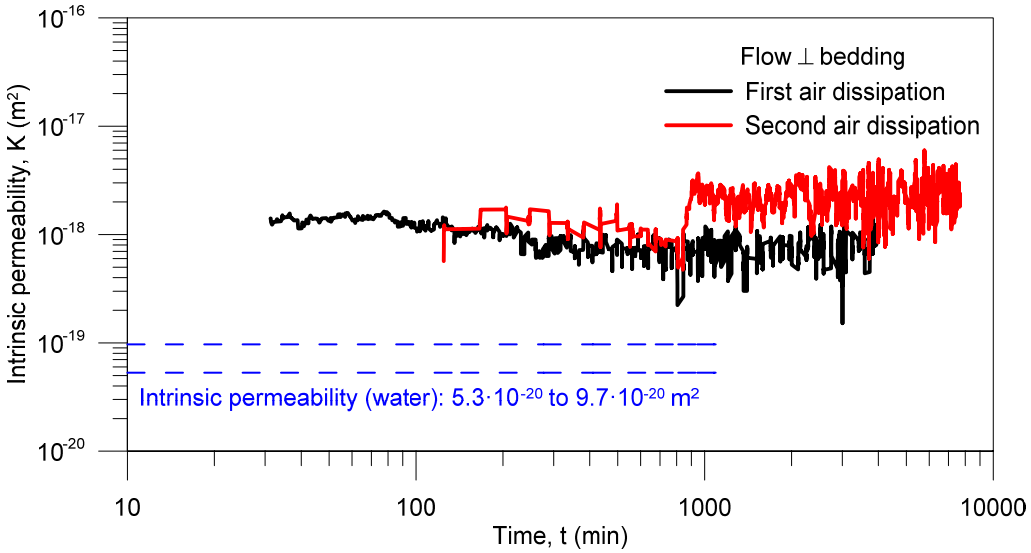

Figure 5-10. Evolution of intrinsic permeability (air) during air dissipation with flow normal to bedding planes (P1_FI_N).

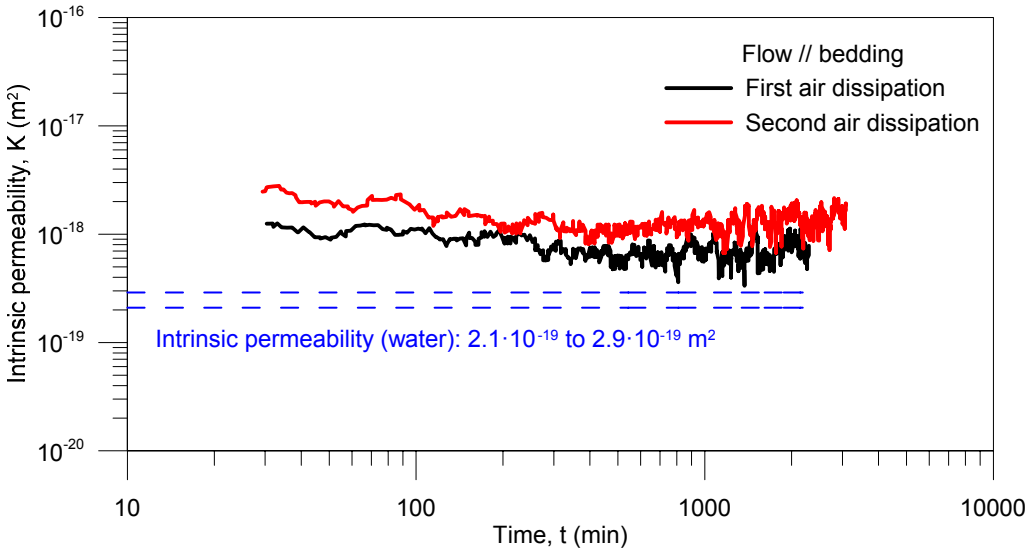

Figure 5-11. Evolution of intrinsic permeability (air) during air dissipation with flow parallel to bedding planes. (P1_FI_P)

Figure 5-12 presents the evolution of intrinsic permeability during air injection pressure dissipation for the test performed with Protocol 2. Intrinsic permeability values for water were also plotted for reference. As in the previous ones, intrinsic permeability to air turned out to be around one order of magnitude higher than intrinsic permeability to air. As expected, this sample presented a lower value than the previous ones (Figure 5-13) because of it was loaded to higher stress levels (up to 14 MPa).

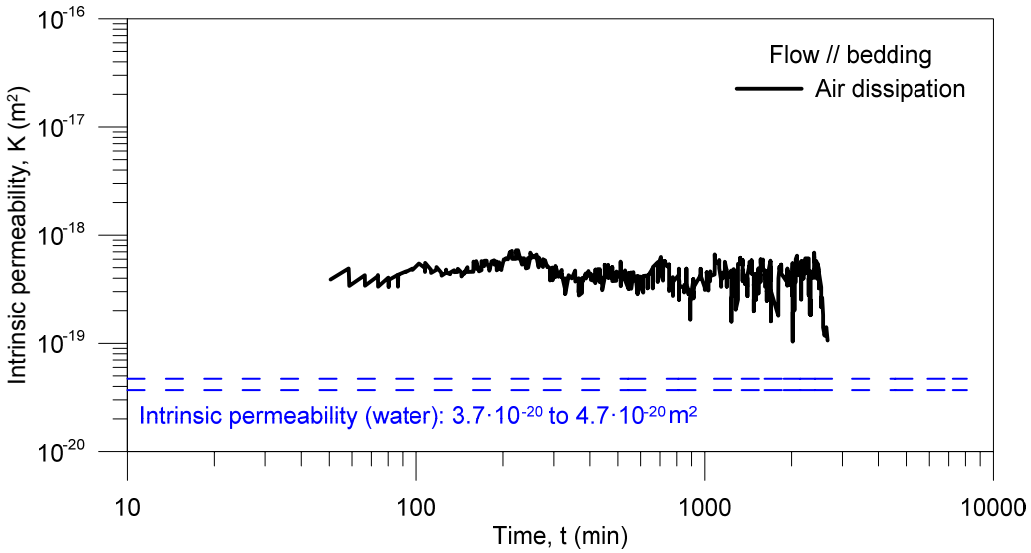

Figure 5-12. Evolution of intrinsic permeability (air) during air dissipation for the sample with bedding planes parallel to flow (P2_FI_P).

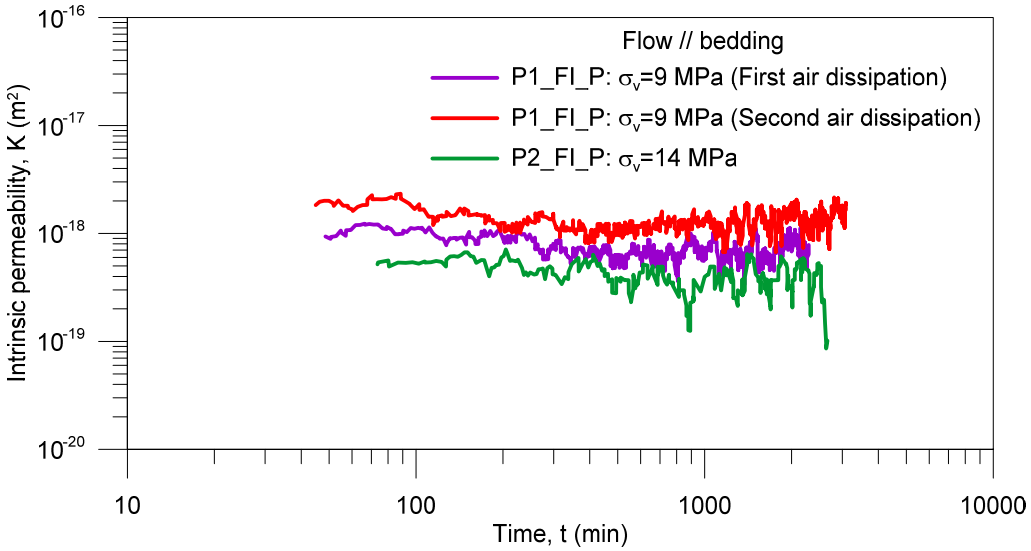

Figure 5-13. Comparison of intrinsic permeability values obtained for samples with bedding planes parallel to flow at high stress level.

Following the same procedure, the evolution of intrinsic permeability was also determined for tests carried out with Protocol 3. Figure 5-14 and Figure 5-15 display the results for samples with bedding planes normal and parallel to flow respectively.

Regarding the evolution of intrinsic permeability in samples with bedding planes normal to flow, a good agreement was obtained in samples under the same conditions and rates. It can be observed that the higher rate (100 mL/min) used, the higher the permeability resulted, which is consistent with the deformational behaviour found during the air injection and dissipation. However, in the case of samples tested with bedding planes oriented parallel to flow, this fact was not reflected.

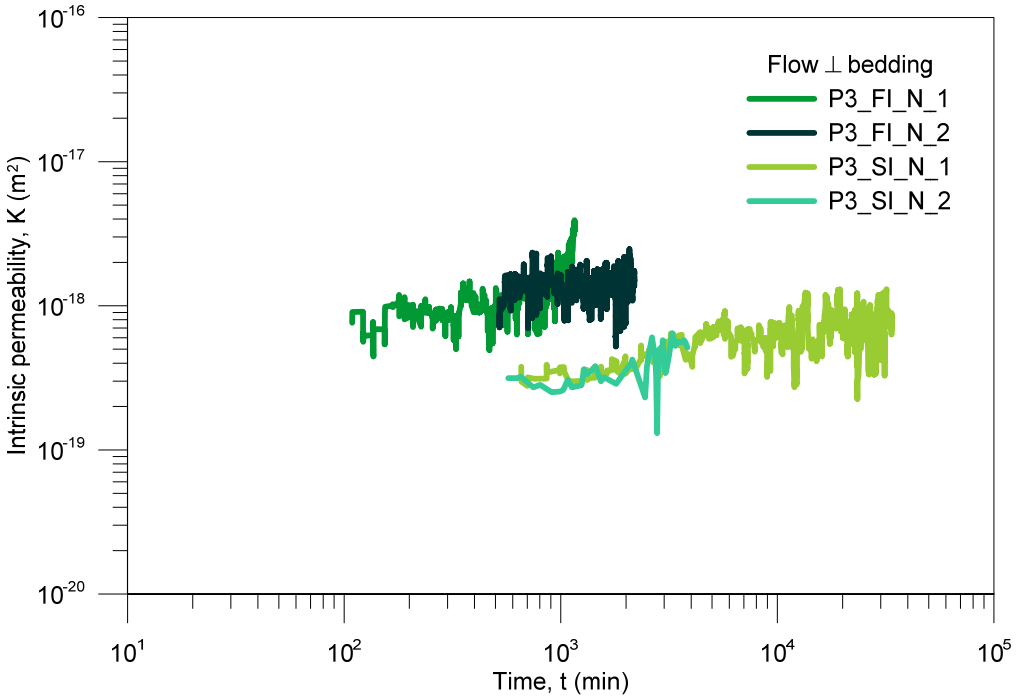

Figure 5-14. Evolution of intrinsic (air) permeability with time along the dissipation stages for tests performed following Protocol 3 with bedding planes normal to flow.

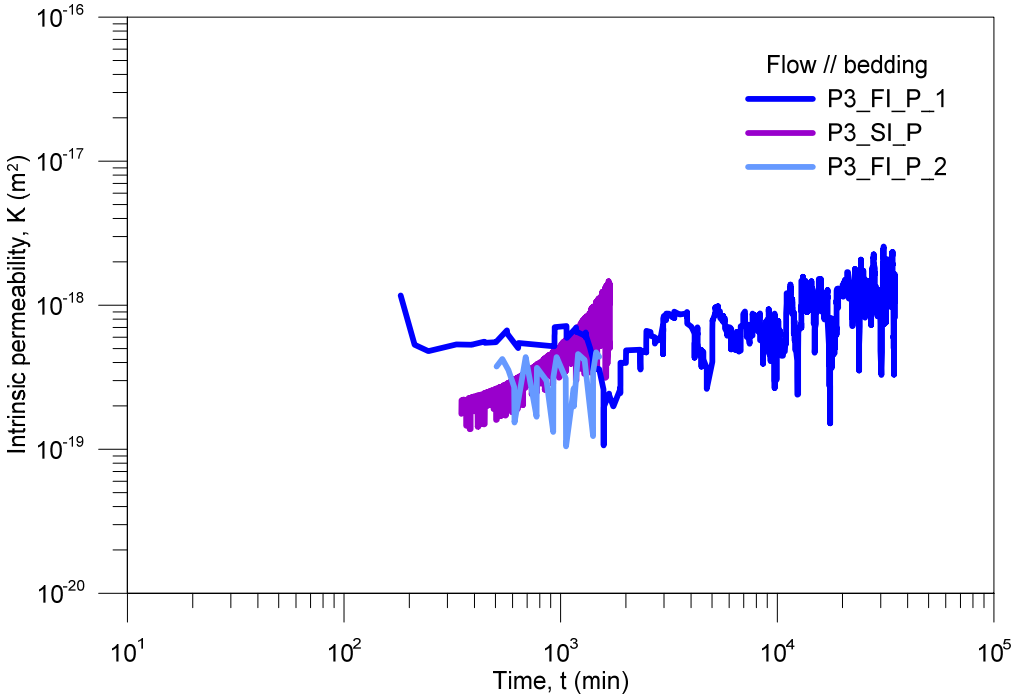

Figure 5-15. Evolution of intrinsic (air) permeability with time along the dissipation stages for tests performed following Protocol 3 with bedding planes parallel to flow.

To better understanding, Figure 5-16 shows the mean values for air and water intrinsic permeability versus the average void ratio for all tests. Water intrinsic permeability, which consistently displayed lower values compared to air intrinsic values, depended on sample orientation. Higher water intrinsic permeability values were observed when bedding planes were parallel to flow. This was not the case of the air intrinsic

permeability values, which highlights the role played by the deformation of the material along the injection and dissipation stages.

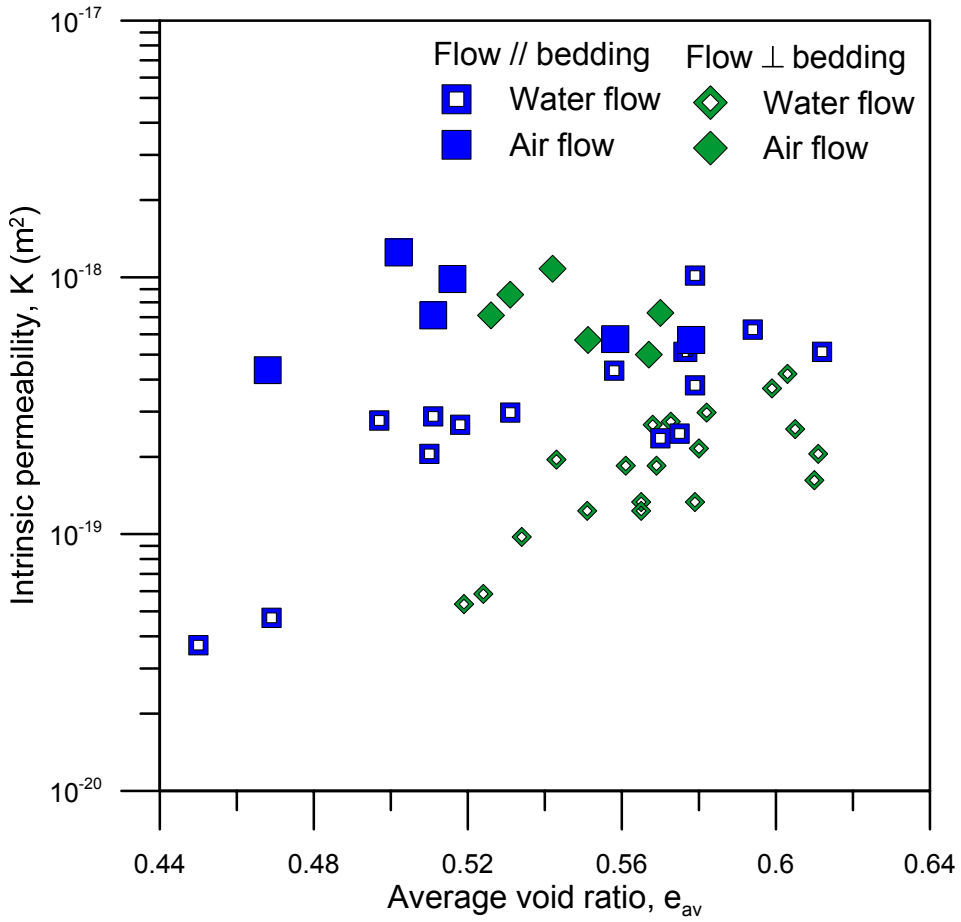

Figure 5-16. Intrinsic permeability from air and water injection stages of samples at both orientations.

5.2.4. Volume change behaviour during air injection and dissipation

As it has been pointed out in the previous section, intrinsic permeability to air flow seems to be very dependent on the deformational behaviour during the injection and dissipation stages, and thus, a deeper analysis is required.

Initially, air injection was considered as an unloading stage, and then pore pressure changes associated with it induce constitutive (effective) stress variations and volumetric deformations. Pore pressure, therefore, increases during the injection which induces mean effective stress to decrease and consequently expansion of the material. Of course, the pore pressure dissipation stage implies a compression due to the mean effective stress increase. Yet, to evaluate this behaviour, a new constitutive stress must be defined, since there is a lack of data related to the pore pressure and only pressures at the boundaries was recorded in the experiments. So, this point onwards, constitutive

stress will refer to the net vertical stress σ_v minus the air pressure at the injection point u_a.

The axial strain response during air tests at high stress state (Protocol 1) with flow orthogonal and parallel to bedding is plotted in terms of constitutive stress changes. Compression strains are positive. Three different stages are indicated in the figures for the evolution of the axial strains: a) an initial small expansion during the fast injection stage due to constitutive stress decrease (*AB* in the figures); b) an expansion after the shut-off (BC) followed by a flat phase which corresponds with the inflow pressure drop (*CC'*), and c) a final compression stage during the recovery period at increasing constitutive stress (*CD*). The stiffness of the last stage corresponding to air dissipations through the samples is indicated in the figure. A stiffer response on air dissipation was observed in the sample with bedding planes parallel to flow and in the second injections.

The same graph was plotted for the test performed at 14 MPa of constant vertical stress (P2_FI_P) indicating the different stages, but obviously, here there was not CC' stage since none pressure drop occurred during the tests.

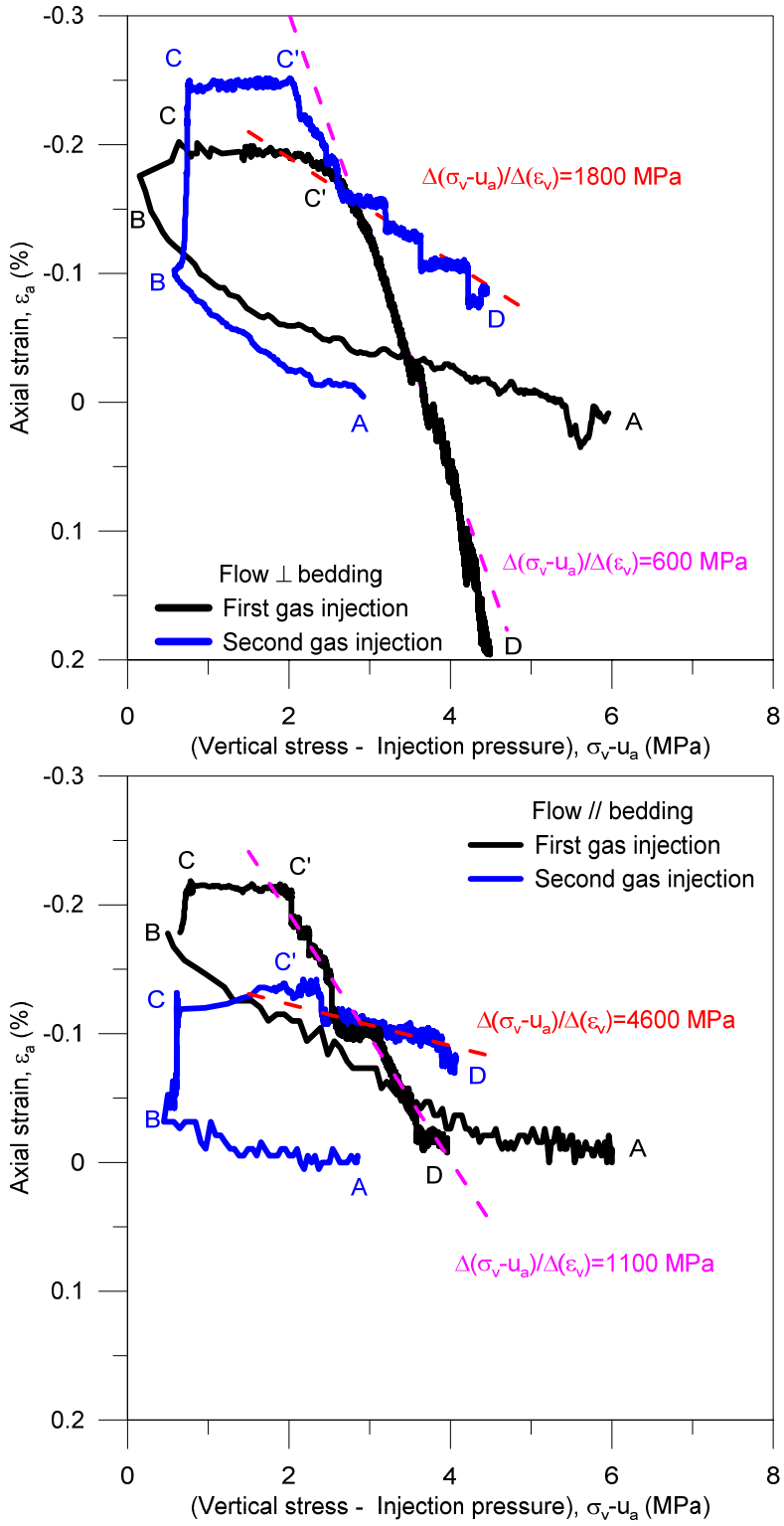

Figure 5-17. Comparison of axial strain changes associated with constitutive stress changes during air injection/dissipation stages: P1_FI_N (top) and P1_FI_P (bottom).

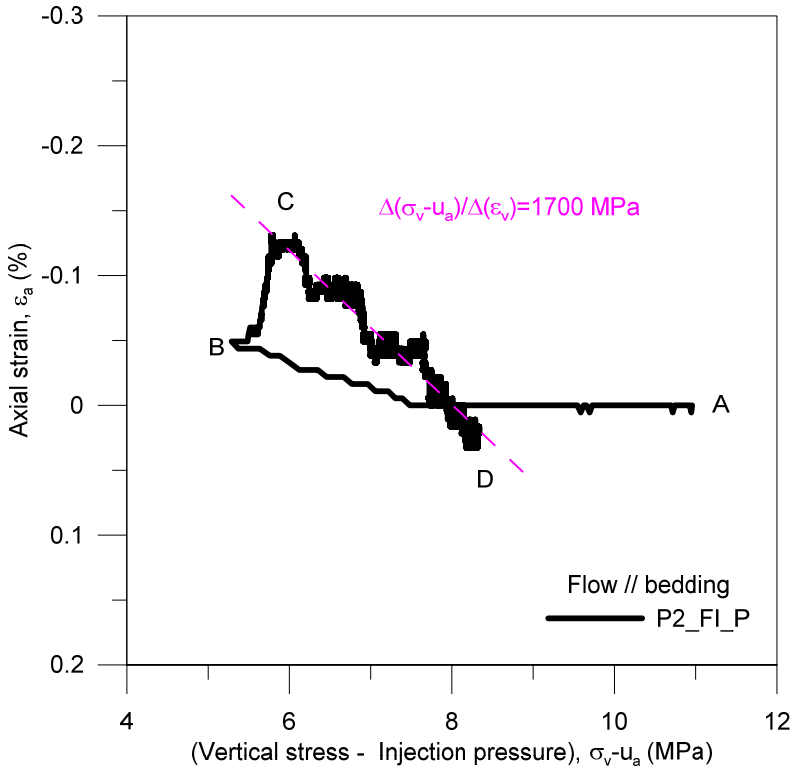

Figure 5-18. Axial strain changes associated with constitutive stress changes during air injection/dissipation stages for test P2_FI_P.

A comparison of the stiffness of the material with bedding planes parallel to flow during air pressure dissipation and loading/unloading stages was performed for this last test (Figure 5-19). It can be observed, a sifter response in the range of constitutive stress were air injection/dissipation occurred than during the loading stage, and softer but more similar than during the unloading stage. Although the air dissipation was considered a loading stage since constitutive stress increased during the process, the sample was normally consolidated during mechanical loading while in both, air dissipation and unloading stage, sample presented an overconsolidated state.

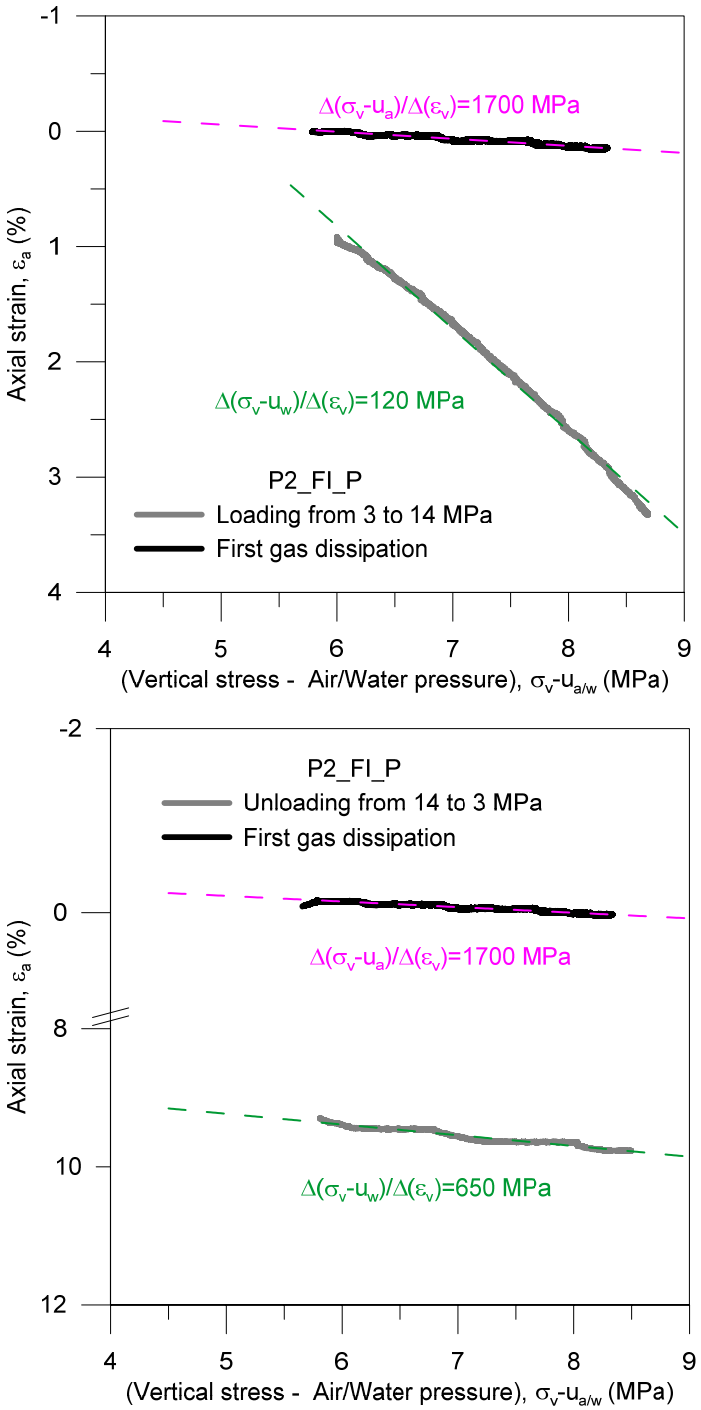

Figure 5-19. Comparison of axial strain changes associated with constitutive stress changes during air injection/dissipation and loading/unloading stages for test P2_FI_P.

Evaluating now the evolution of volumetric strain with constitutive stress changes along the air injection and dissipation for the tests performed at low stress state (Protocol 3), two different situations were found. For samples tested at fast injection rate (Figure 5-20), the axial strain presents the three different stages before defined: a) an initial small expansion during the fast injection stage due to constitutive stress decrease (*AB* in the figures); b) an expansion after the shut-off (BC) and c) a final compression stage during the recovery period at increasing constitutive stress (*CD*). However, for samples

tested at slow injection rate (Figure 5-21), the second stage did not take place because all the expansion occurred during the injection stage (AB), and therefore, during the dissipation (BC) only compression was recorded.

With regard to the results of the fast injection tests, samples at constant vertical stress displayed some small expansion at the early fast air injection stage (A to B) which was slightly larger at the slower air injection rate and when bedding planes were not confined by the oedometer condition (bedding planes orthogonal to flow). After shut-off (point B), expansion continued in the samples subjected to fast air injection (B to C) as the air pressure front propagated into the sample, inducing the fluid pressure to increase and the constitutive stress to decrease. Again, the expansion was larger in the case of flow orthogonal to bedding planes, where the material was less constrained to expand. Some elapsed time later after shut-off, the air injection pressure started to decline along the dissipation stage towards point D. This dissipation stage induced the constitutive stress to increase leading to the progressive compression of the material.

In contrast, when the injection rate was slowly enough, samples expanded during the injection stage, reaching its maximum at the maximum air pressure (minimum constitutive stress). Hence, expansion after shut-off was not observed. In this case, the injection rate allowed pore pressure to be nearly equilibrated during air injection and there was not a pressure front propagation after the shut-off. In fact, the first outflow detection in the slow injection tests occurred during the injection stage, indicating that the pressure front reached the top of the sample. These samples subjected to slow injection rate showed a quasi-reversible volume change response along the dissipation stage.

Comparing the two figures, it can be clearly observed that the faster the injection rate, the larger the expansion undergone by the samples. Moreover, samples with bedding planes orthogonal to flow consistently underwent the largest expansions during air injection or dissipation and also, larger compressions on air dissipation because of oedometer conditions.

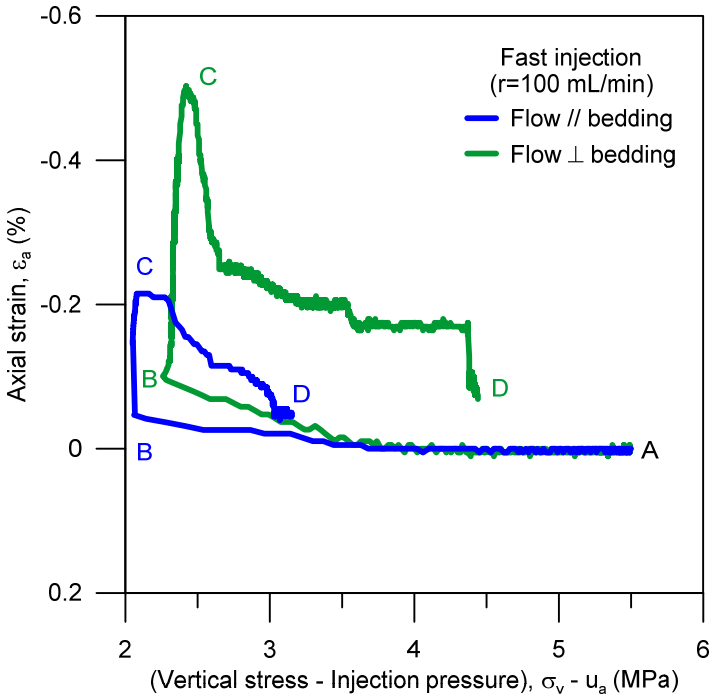

Figure 5-20. Evolution of volumetric strain with constitutive stress during air injection/dissipation stages in fast injection experiments.

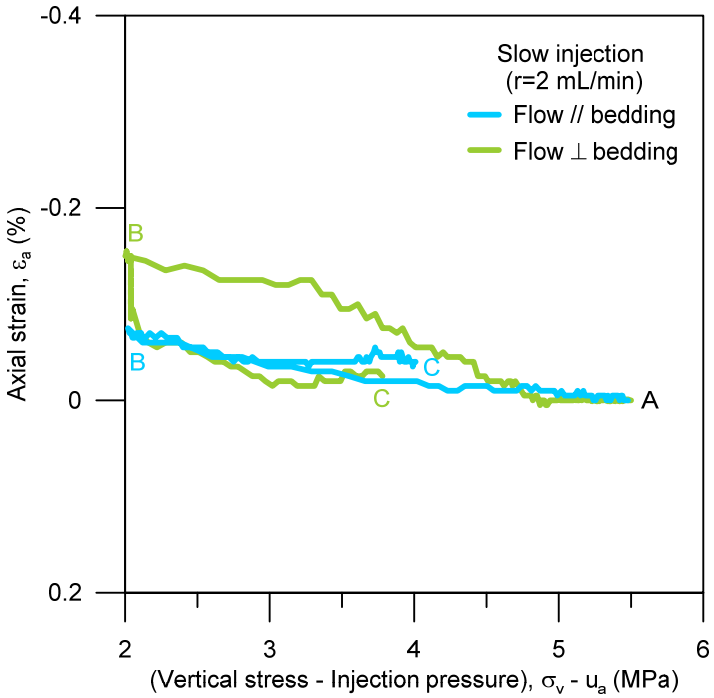

Figure 5-21. Evolution of volumetric strain with constitutive stress during air injection/dissipation stages in slow injection experiments.

Thus far, analysis of volume change in terms of constitutive stress change has been performed. However, if these volumetric strain changes (around 0.20-0.30%) are solely interpreted as changes in pore volume, then changes in intrinsic permeability are expected to be small referred to water permeability results accordingly to predictions of classic two-phase flow models. Nonetheless, intrinsic permeability values are greater

than the corresponding water permeability for the same void ratio (see Figure 5-16). This fact gain relevance if normalized values of the intrinsic permeability are plotted against the change in the void ratio (Figure 5-22). To normalized it, a value of $4.2 \cdot 10^{-19}$ m^2 was selected for both orientations as the intrinsic permeability of the intact material, taken as average from the water permeability measurements at the *in situ* stress state. Now, it is proved that two-phase flow concepts just apply to water flow in compression -changes of void ratio are negatives-. In contrast, changes in permeability to air flow in expansion - void ratio variations are positives- are very large with a very small porosity variation, and thus, other mechanisms, such as the opening of discontinuities suggested by, for instance, Olivella & Alonso 2008, have to take place to enhance intrinsic permeability changes.

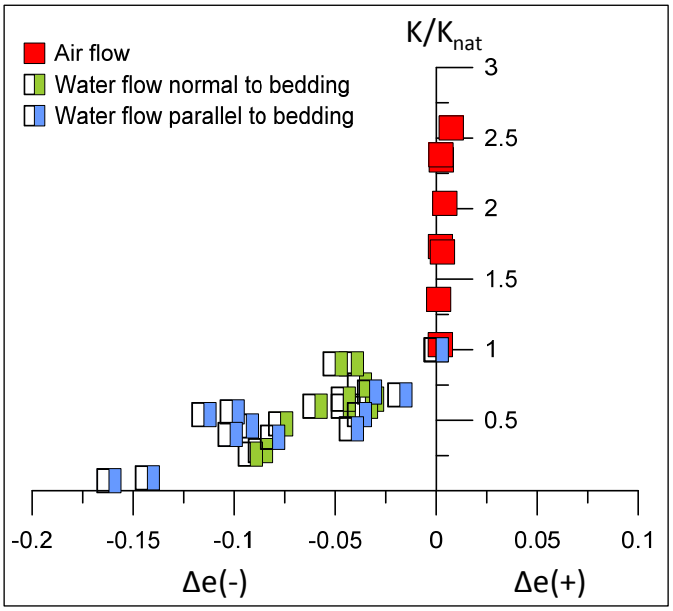

Figure 5-22. Normalized intrinsic permeability against changes of void ratio during water injection (compression: negative change of void ratio) and air injection (expansion: positive change of void ratio).

So, intrinsic permeability to air is possibly affected by the maximum expansion reached in the injection process (Figure 5-23) which could produce the opening of fissures in the material. Higher permeability values were detected at larger expansions, which suggest the role played by clay deformation on gas transport processes is significant. In order to evaluate it, Chapter 6 of this Thesis is devoted to tracking the changes in the pore network after injection tests which will provide valuable information in this regard.

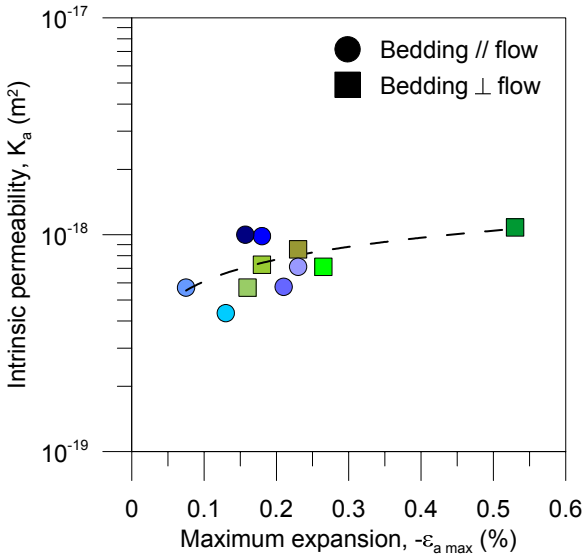

Figure 5-23. Intrinsic permeability to air plotted versus the maximum expansion during air injection/dissipation tests.

5.3. Indurated clays

In this section results obtained from air injection and dissipation tests on indurated clays are presented. Intrinsic permeability to air is analysed as well as the volume change behaviour during gas migration.

5.3.1. Air injection tests on OED 1/1 Opalinus Clay

Figure 5-24 presents the air injection results for the low-permeability OED 1/1 Opalinus Clay sample at a constant isotropic confining stress of 15 MPa when air injection pressure was increased to 14 MPa at a rate of 100 mL/min.

As observed in the figure, the injection pressure was able to increase to 14 MPa followed by a shut-off and recovery period at constant volume. The injection pressure essentially remained flat in the recovery stage at constant volume without appreciable outflow volume detected (the outflow pressure remained at 0.5 MPa). The outflow volume slightly increased after 1000 min, when a steeper decline was recorded for the air pressure in the recovery stage. The evolution of the axial deformation is also presented in the figure.

Figure 5-25 shows the equivalent time evolution of air injection pressure, axial displacement, as well as outflow volume and pressure at downstream under a higher isotropic stress of 19 MPa on the same material. In this case, the injection air pressure increased to a value slightly larger (18 MPa) than before. The injection pressure followed a linear decay but after 4000 min approximately, presented a sharp change, with a faster dissipation. The outflow volume slightly increased after 400 min but the

outflow pressure was able to be maintained at 0.5 MPa. The evolution of the axial deformation is also presented in the figure (negative axial displacement corresponds to expansion), which indicates that important injection pressure decay occurred when the sample underwent maximum expansion. This experiment had to be stopped before the air pressure dissipated more because a leakage of the fluid in the chamber (mean stress) was detected (only a decay of 0.2 MPa in isotropic stress occurred due to this leakage).

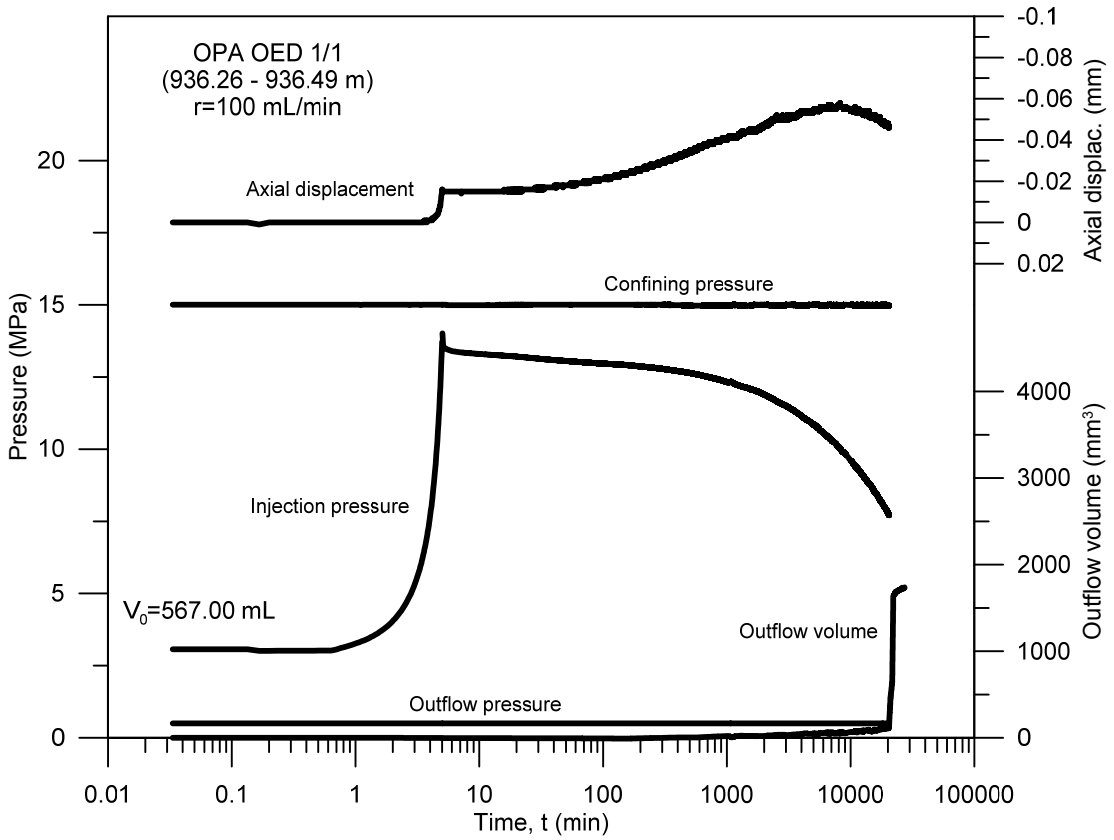

Figure 5-24. Measured time evolution of pressures at injection and outflow sides together with outflow volume and axial displacement at *p*=15 MPa. OED 1/1 Opalinus Clay sample.

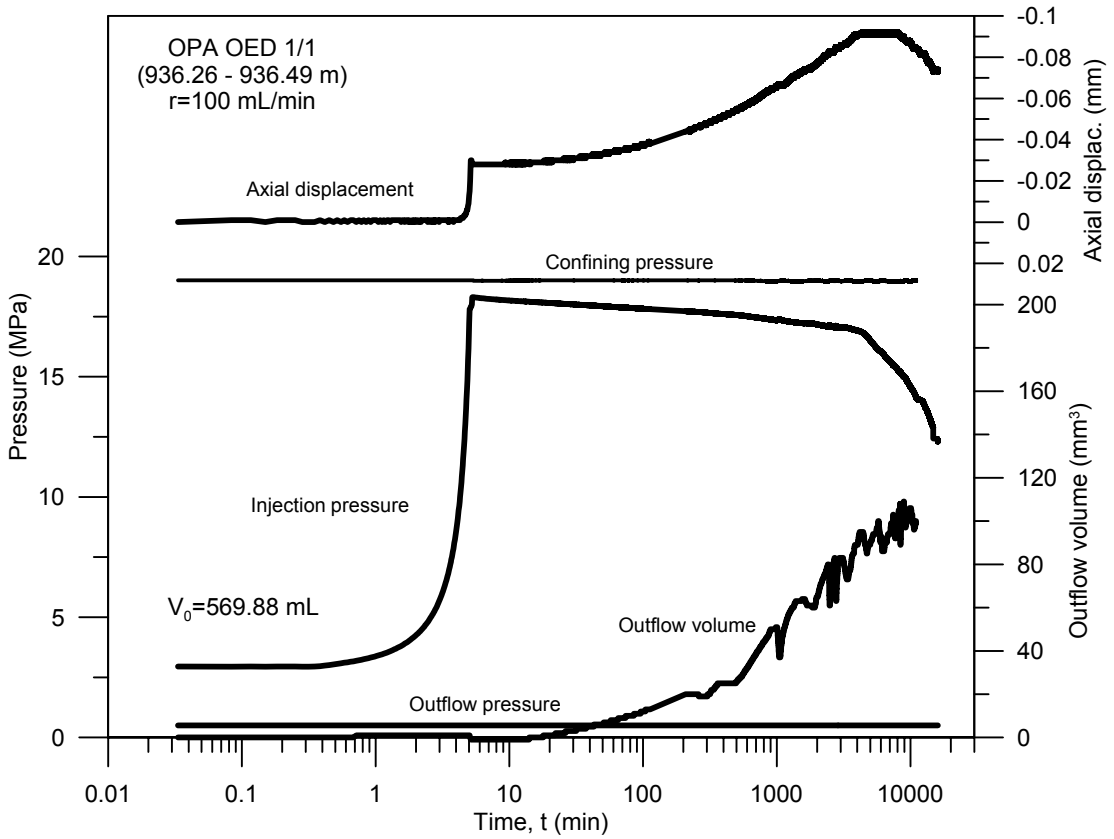

Figure 5-25. Measured time evolution of pressures at injection and outflow sides together with outflow volume and axial displacement at *p*=19 MPa. OED 1/1 Opalinus Clay sample.

5.3.2. Air injection tests on EMPA SLA 'Brauner Dogger'

Figure 5-26 and Figure 5-27 present the air injections for the low-permeability EMPA SLA 'Brauner Dogger' (781.55 - 781.85 m) sample at isotropic confining stress of 15 MPa. In the first one, the air injection pressure was increased to 14 MPa at a rate of 2 mL/min. The second injection was decided to be a slower one at the same mean stress (*p* =15 MPa) instead of an injection at the same rate at higher mean stress, with the aim of studying its influence on the gas transport properties. In this case, since the control volume injection rate was slower (0.04 mL/min), some difference could be appreciated, such the detection of outflow volume even before the shut-off stage. The injection pressure underwent a faster dissipation in the recovery stage at constant volume. The evolution of the axial deformation is also presented in the figure.

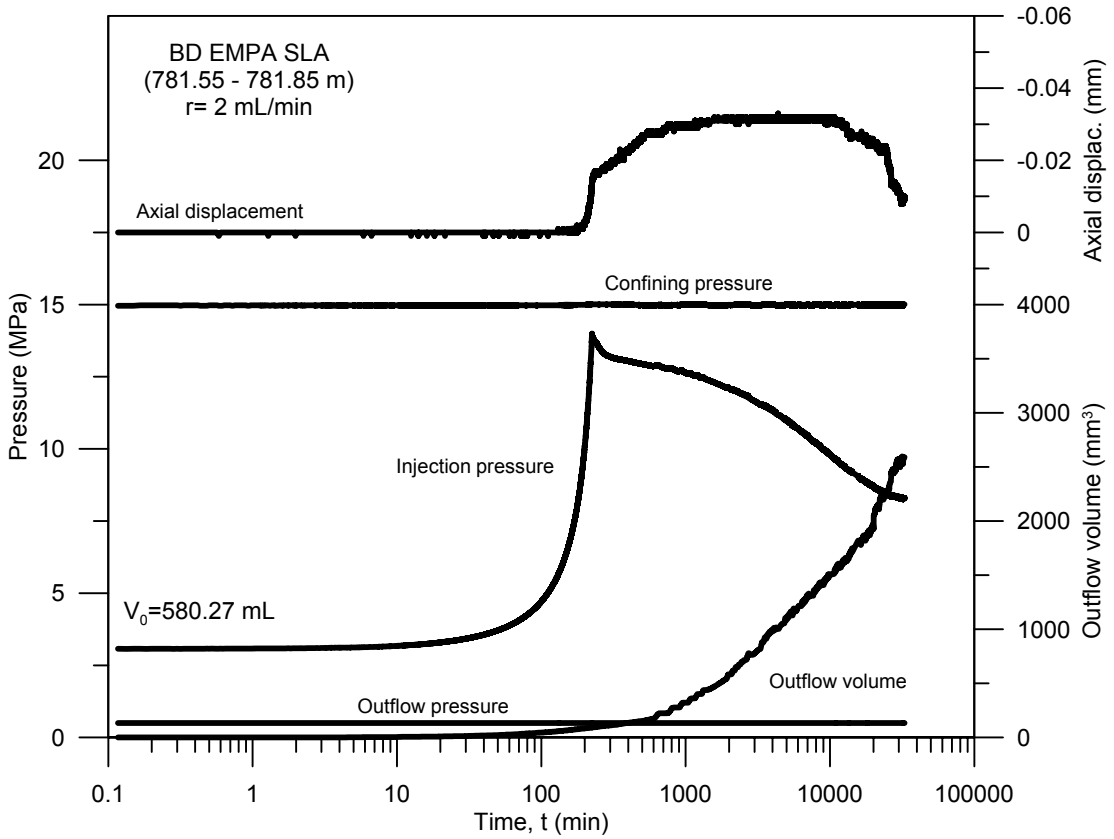

Figure 5-26. Measured time evolution of pressures at injection (r=2 mL/min) and outflow sides together with outflow volume and axial displacement at *p*=15 MPa. EMPA SLA 'Brauner Dogger' sample.

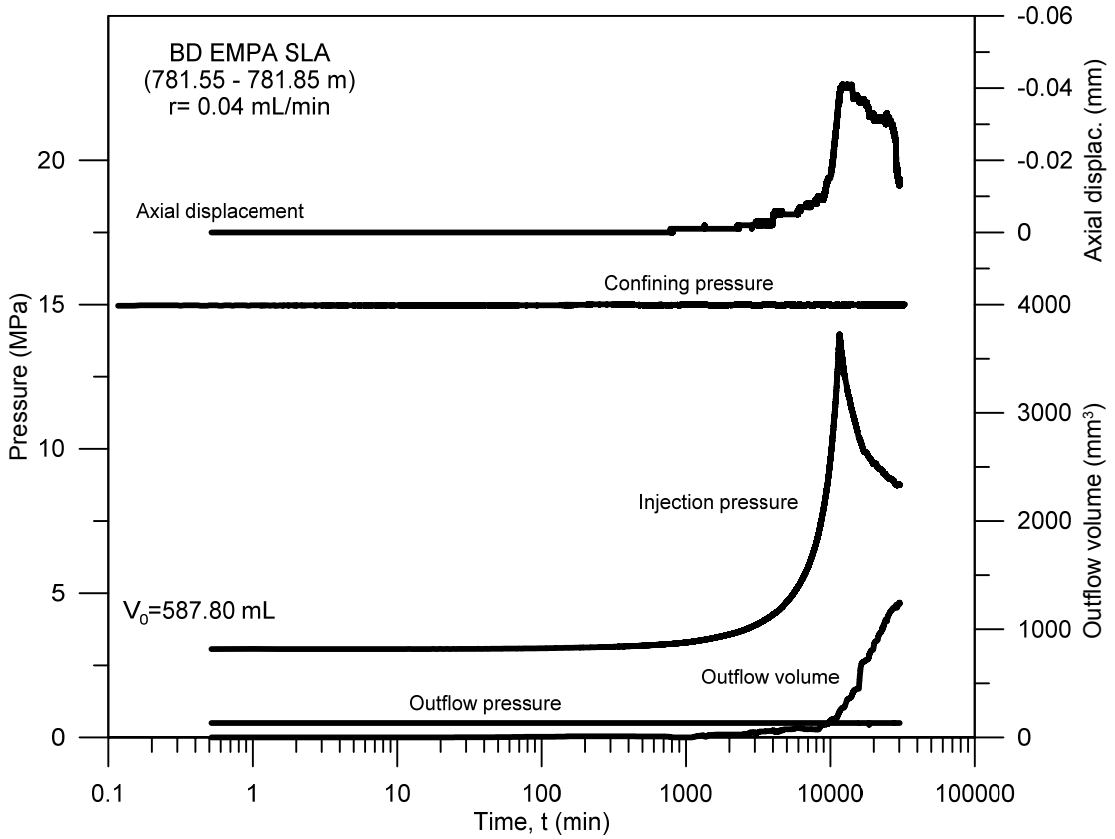

Figure 5-27. Measured time evolution of pressures at injection (r=0.04 mL/min) and outflow sides together with outflow volume and axial displacement at p=15 MPa. EMPA SLA 'Brauner Dogger' sample.

5.3.3. Comparative analysis of the results

The following figures depict the different injection tests for both formations in comparison with data reported by Romero & Gómez (2013) in NAB 13-51.

In Figure 5-28, the evolution of pressures, volumes, and displacements during the injection stage at p=15 MPa for Opalinus Clay samples is shown. Both samples were tested at a volume injection rate of 100 mL/min. The behaviour is very similar despite being samples at relatively different depths. The new sample, OED 1/1 OPA, presents a slightly higher displacement and a sharp increase in the outflow volume that was not detected in the previous test.

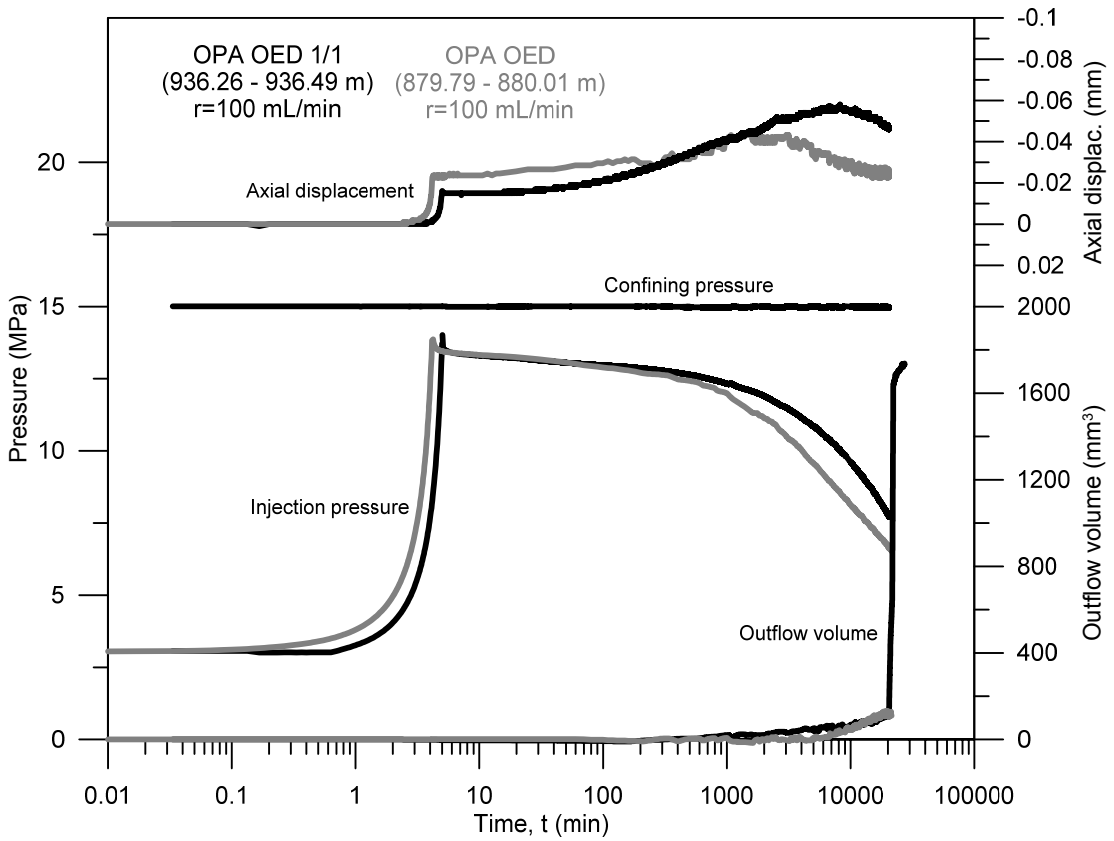

Figure 5-28. Comparison of the time evolution of pressures at injection and outflow sides together with outflow volume and axial displacement at *p*=15 MPa between OED 1/1 Opalinus Clay and OED Opalinus Clay samples.

Regarding the injections at an isotropic stress of 19 MPa, (Figure 5-29) some great differences could be observed. OED 1/1 Opalinus Clay sample displayed a flatter air pressure behaviour at the first stage of air dissipation jointly with a higher expansion, until an increase in the air dissipation rate which produced the compression of the material. In contrast, during the dissipation stage, OED Opalinus Clay sample presented a continuous decay of air pressure and a flat deformational response.

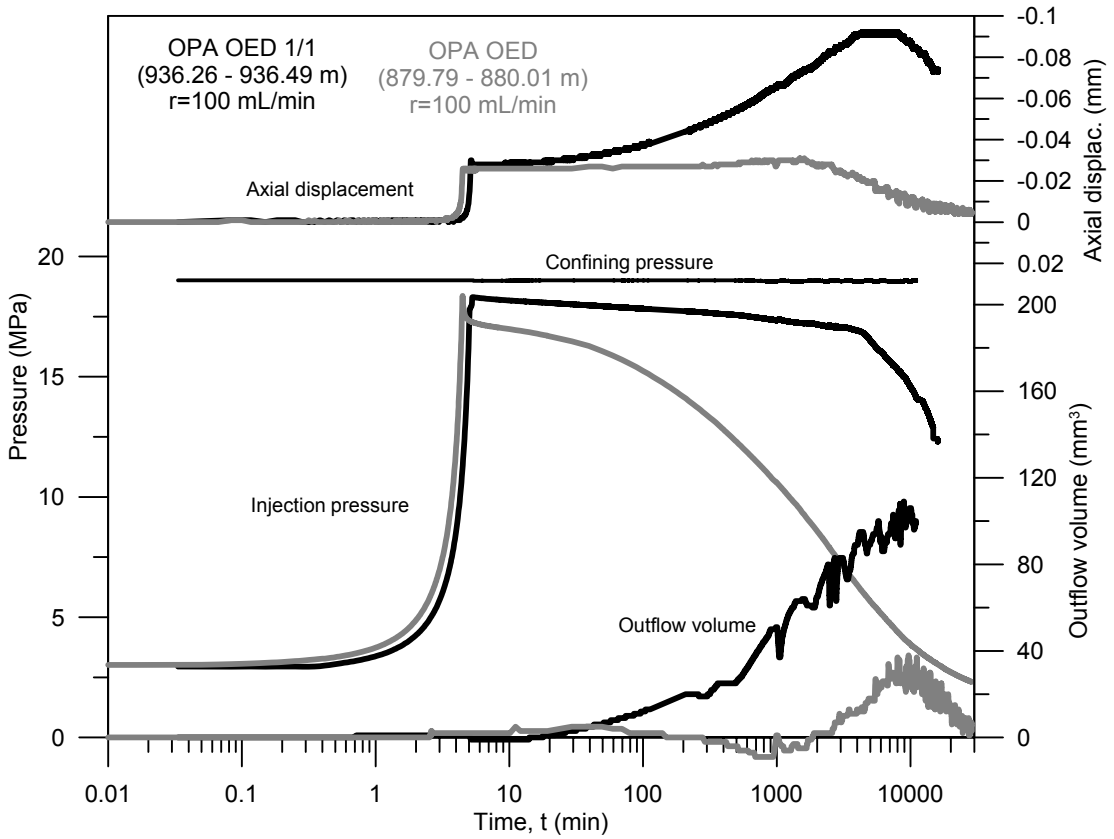

Figure 5-29. Comparison of the time evolution of pressures at injection and outflow sides together with outflow volume and axial displacement at *p*=19 MPa between OED 1/1 Opalinus Clay and OED Opalinus Clay samples.

The comparison of the behaviour along the air injection and dissipation stages for 'Brauner Dogger' samples is shown in Figure 5-30. In this case, different injection rates were used at the same isotropic stress (p=15 MPa) on samples retrieved at approximately the same depth. With regard the axial displacements, the injection rate plays an important role. Meanwhile, at fast and medium rates (100 and 2 mL/min), the expansion of the materials occurred with some delay in the dissipation stage, and after some time, the samples underwent compression; the expansion at slow rate (0.04 mL/min) occurred during the injection and in the dissipation stage the sample only underwent compression.

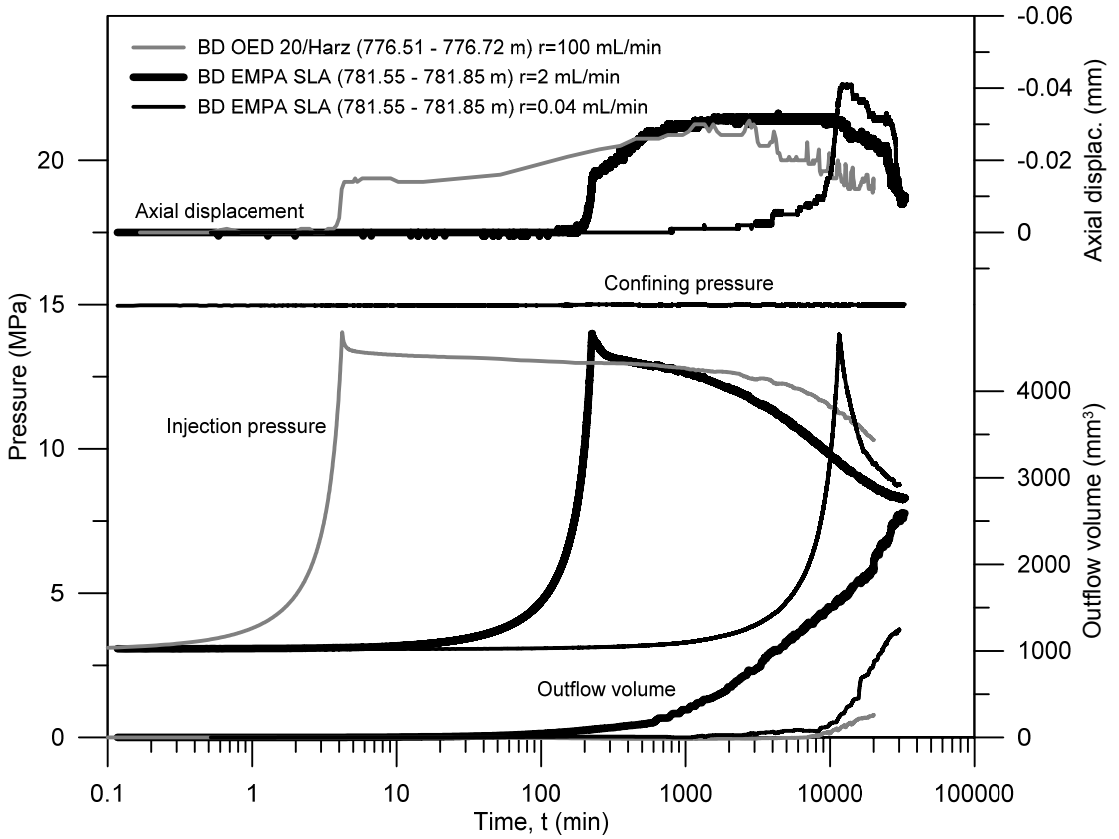

Figure 5-30. Comparison of the time evolution of pressures at injection and outflow sides together with outflow volume and axial displacement at *p*=15 MPa and different injection rates between EMPA SLA 'Brauner Dogger' and OED 20/Harz 'Brauner Dogger' samples.

5.3.4. Intrinsic permeability

The evolution of the intrinsic (air) permeability, K, was calculated from upstream and downstream pressure records during the air dissipation stages at constant air injection volume using the same methodology described for Boom Clay (see Section 5.3.2).

Figure 5-31 shows the intrinsic permeability values obtained for OED 1/1 Opalinus Clay sample at two different constant isotropic stresses (15 and 19 MPa) and the same injection rate (100 mL/min). It presents a slightly lower value of air permeability at higher isotropic stress state.

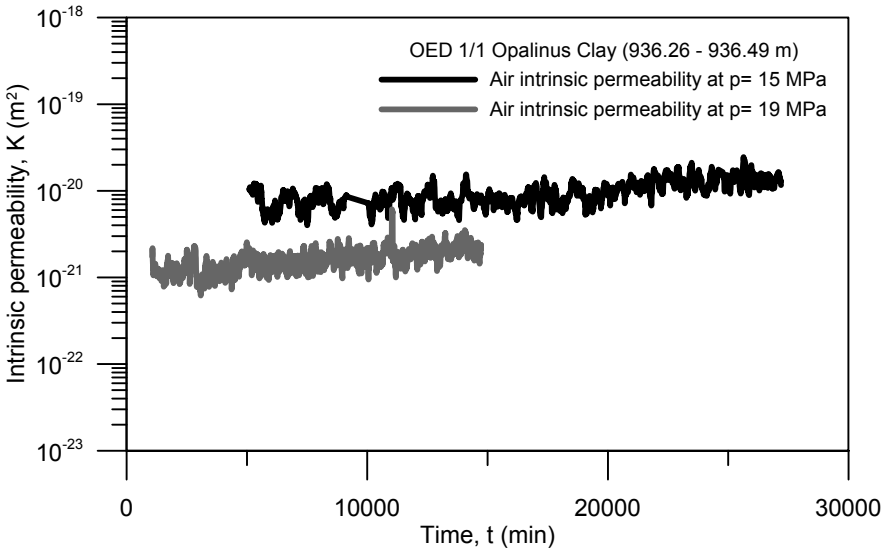

Figure 5-31. Evolution of intrinsic (air) permeability with time along the dissipation stages for injection tests performed at constant isotropic stresses of 15 and 19 MPa of OED 1/1 Opalinus Clay sample.

Figure 5-32 shows the intrinsic (air) permeability (K) obtained for EMPA SLA 'Brauner Dogger' sample tested at the same isotropic stress (15 MPa) and different injection rates (2 and 0.04 mL/min). They result to be quite similar, being slightly higher the one tested at the slower rate. Note that these injections were performed in the same sample, so some damage could persist after the first injection despite its subsequent saturation.

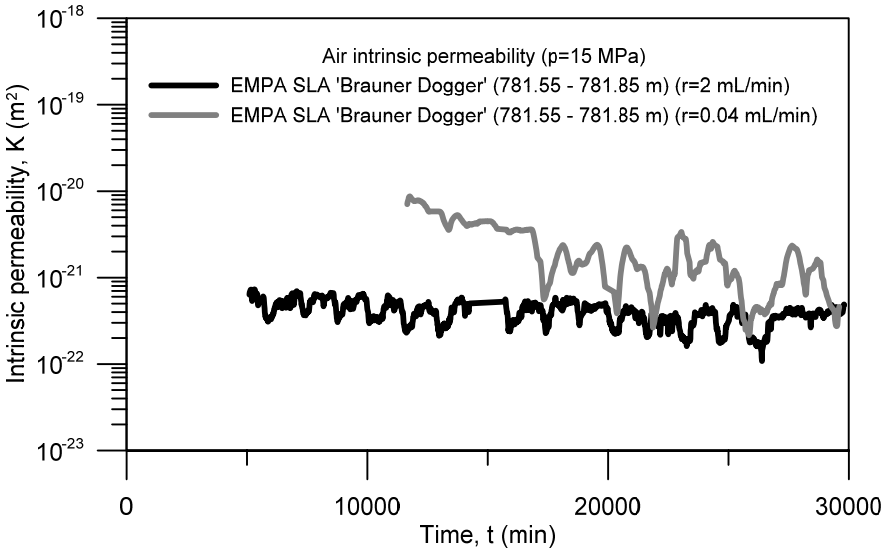

Figure 5-32. Evolution of intrinsic (air) permeability with time along the dissipation stage for the injection tests performed at different rates at a constant isotropic stress of 15 MPa of EMPA SLA 'Brauner Dogger' sample.

Data reported in Romero & Gómez (2013) were used to calculate the intrinsic permeability to air flow of samples OED Opalinus Clay and OED 20/Harz 'Brauner

Dogger' in order to stablish a comparison. Both Opalinus Clay samples at a constant isotropic stress of 15 MPa showed an identical evolution of intrinsic (air) permeability (Figure 5-33). OED 20/Harz 'Brauner Dogger' sample, tested at higher injection rate (100 mL/min) presented a somewhat higher intrinsic permeability than when was tested at slower rates (Figure 5-34).

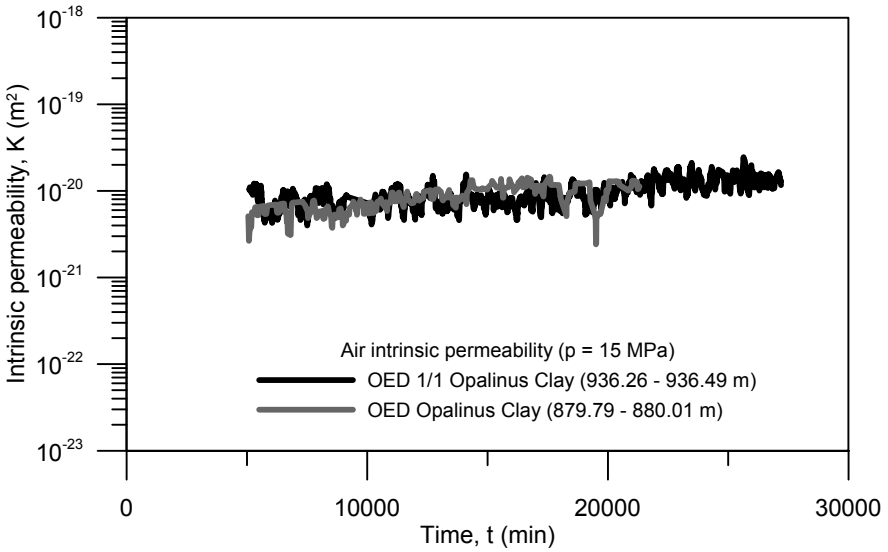

Figure 5-33. Comparison of the evolution of intrinsic (air) permeability between OED 1/1 and OED Opalinus Clay samples.

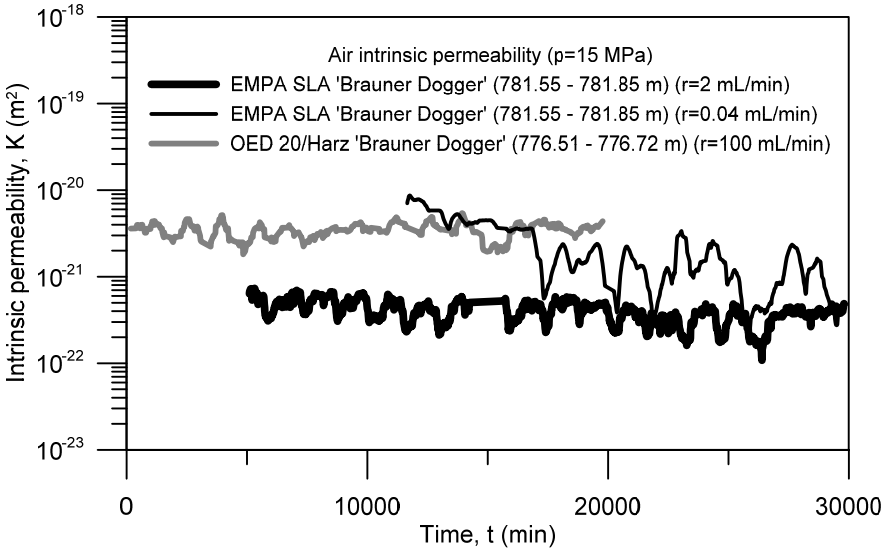

Figure 5-34. Comparison of the evolution of intrinsic (air) permeability between EMPA SLA and OED 20/Harz 'Brauner Dogger' samples.

All average values of intrinsic permeability (air and water) are depicted in Figure 5-35 as a function of the void ratio for both samples (OED 1/1 Opalinus Clay and EMPA SLA 'Brauner Dogger'). Similar values for both fluids are found on contrary as happens with Boom Clay in which higher intrinsic permeability values to air were obtained. The

comparison with previous results is shown in Figure 5-36. The indurated rocks present relatively large change in intrinsic permeability with very small changes in porosity.

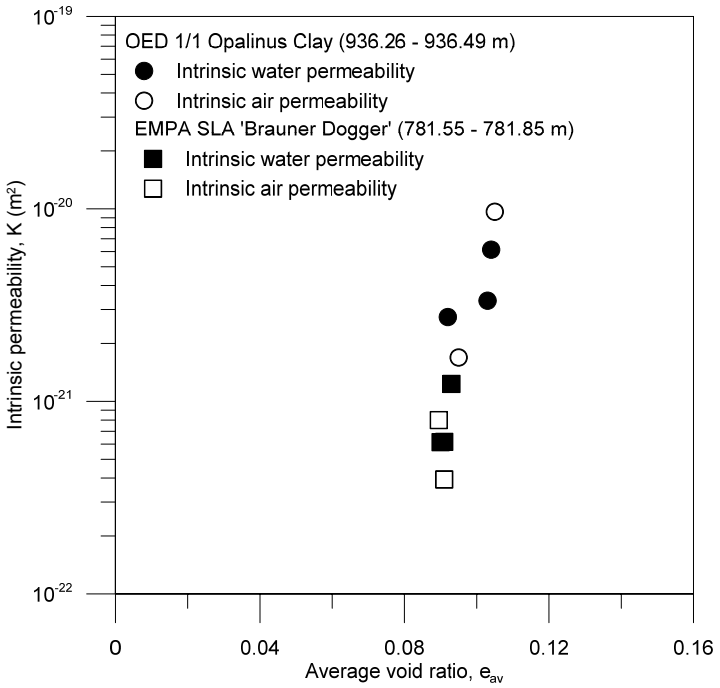

Figure 5-35. Intrinsic permeability for EMPA SLA 'Brauner Dogger' and OED 1/1 Opalinus Clay samples for both air and water injection tests as a function of the void ratio.

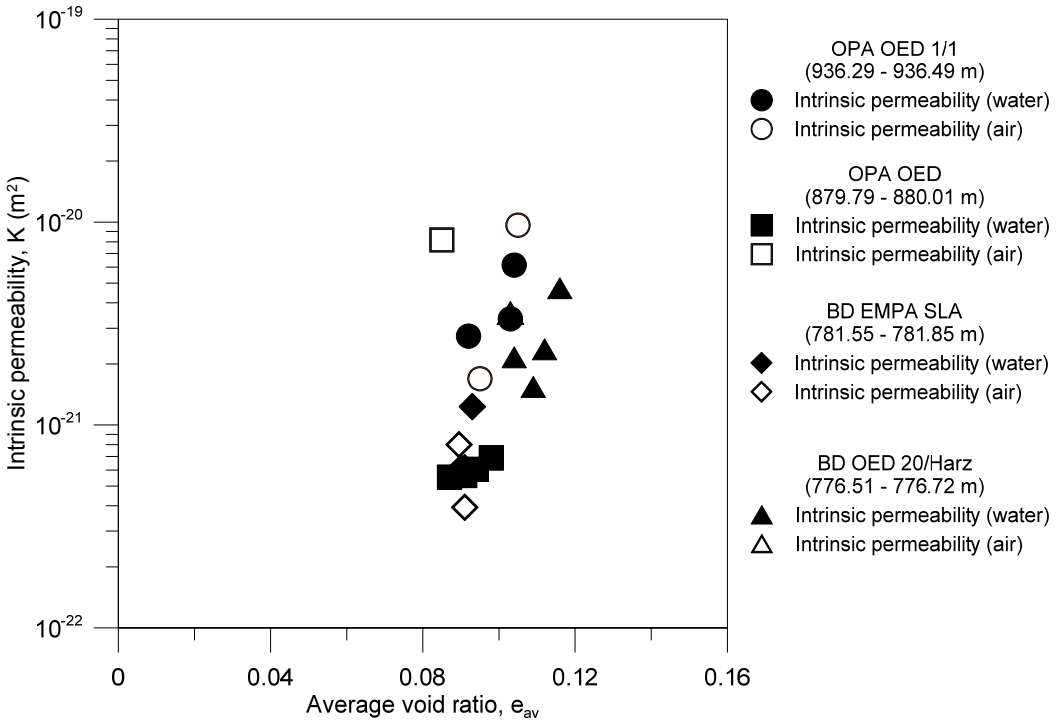

Figure 5-36. Water and air intrinsic permeability values of both 'Brauner Dogger' and Opalinus Clay formations as a function of the void ratio.

5.3.5. Volume change behaviour

Figure 5-37 shows the strain evolution (radial strain was considered negligible during this process on the low-height specimens) during the air injection tests on OED 1/1 Opalinus Clay sample at $p = 15\ MPa$ and $p = 19\ MPa$. The axial strains are plotted in terms of constitutive stress changes (this time defined as the isotropic stress p minus the air pressure at the injection point u_a). In these cases, changes in porosity are a consequence of changes in fluid pressure, since tests were carried out at constant *p*. The examination of the axial strains revealed different deformational stages. During the air injection stage (A to B in the figure); the sample underwent approximately the same small expansion. After shut-off (B in the figure), expansion continued as a consequence of the air pressure front propagation into the sample (B to C), which induced the fluid pressure to increase and the constitutive stress to decrease. Expansions on pore pressure increase were consistent with compressibility results on loading/unloading obtained in oedometer test. Some elapsed time after shut-off, the air injection pressure started to decrease along the dissipation stage towards point D, which induced sample compression during constitutive stress increase. Axial stiffness values $\Delta(p - u_a)/\Delta\varepsilon_a$ in the figure are in agreement with loading/unloading results.

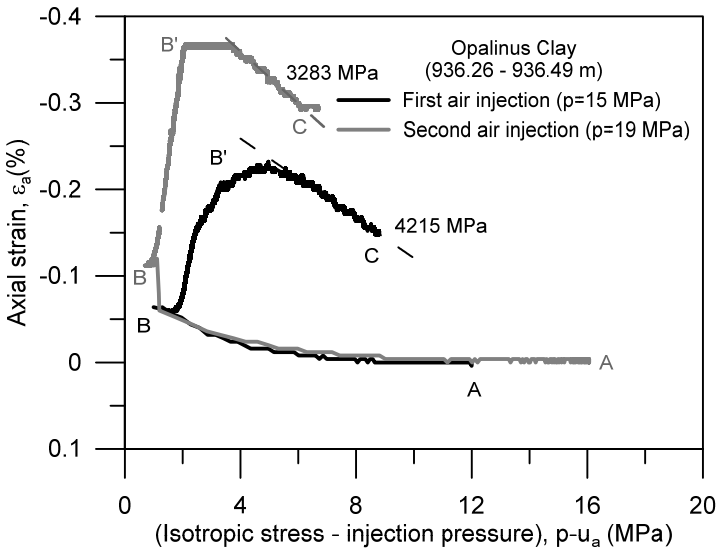

Figure 5-37. Axial strain changes associated with constitutive (effective) stress changes during air tests of OED 1/1 Opalinus Clay sample.

A comparison of axial strains in terms of constitutive stress changes between Opalinus Clay samples recovered at different depths is shown in Figure 5-38. Similar behaviour was obtained in injections performed at the same fast rate. Although the deeper sample underwent slightly higher expansion,

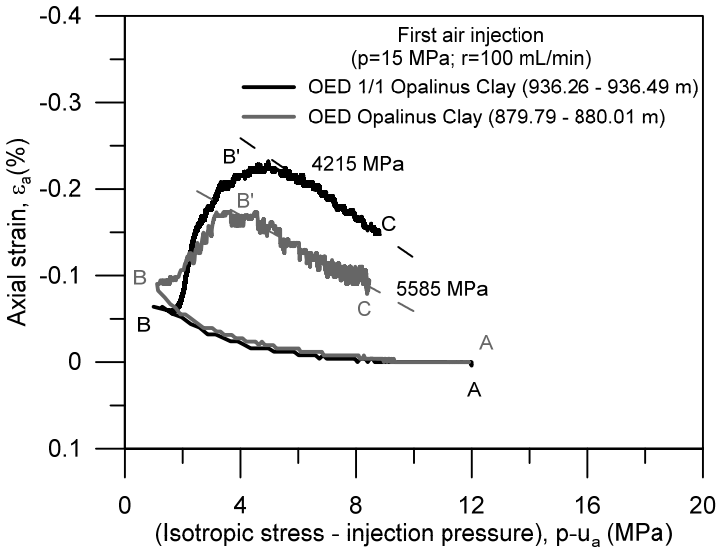

Figure 5-38. Comparison of axial strain changes associated with constitutive (effective) stress changes during air tests at *p* = 15 MPa between OED 1/1 and OED Opalinus Clay samples.

Figure 5-39 compare the behaviour of 'Brauner Dogger' samples recovered at a similar depth and tested at the same isotropic stress (15 MPa) but at different air injection rate (100, 2 and 0.04 mL/min). Samples tested at 100 and 2 mL/min underwent approximately the same small expansion at the early fast air injection stage (A to B), in which no appreciable differences were observed despite different volume injection rates. After shut-off (point B), expansion continued in the samples subjected to fast and medium air injection (B to C) as the air pressure front propagated into the sample, inducing the fluid pressure to increase and the constitutive stress to decrease. This expansion after shut-off was not observed on sample subjected to slow air injection rate (0.04 mL/min) since pore pressure was nearly equilibrated during air injection (all the expansion occurred during the injection stage). Some elapsed time later after shut-off, the air injection pressure started to decline along the dissipation stage towards point D. This dissipation stage induced the constitutive stress to increase leading to the progressive compression of the material. Axial stiffness values $\Delta(p - u_a)/\Delta\varepsilon_a$ are in agreement with oedometric loading/unloading results.

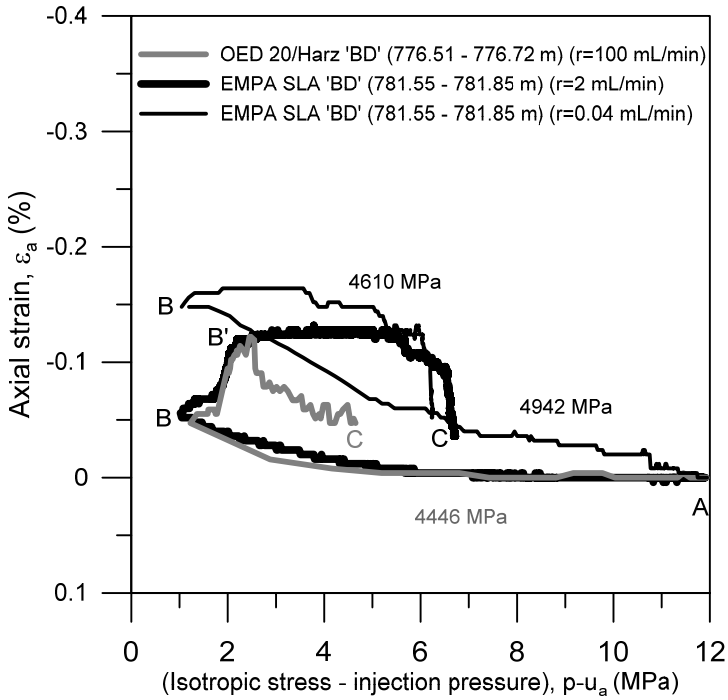

Figure 5-39. Comparison of axial strain changes associated with constitutive (effective) stress changes during air tests at *p* = 15 MPa between EMPA and OED 20/Harz 'Brauner Dogger' samples.

A lower compressibility of 'Brauner Dogger' has been systematically observed during air dissipation tests and loading paths in relation with results for Opalinus Clay samples. In terms of the stiffness of the materials, the drained bulk modulus during the air dissipation stage, calculated as $E^* = (\delta p - u_a)/\delta\varepsilon_a$, is shown in comparison with de drained constrained modulus on loading and unloading paths under oedometer conditions (Figure 5-40). A good agreement is found for 'Brauner Dogger' while the stiffness during air dissipation is higher than during loading/unloading for Opalinus Clay, given values very close to the 'Brauner Dogger' ones.

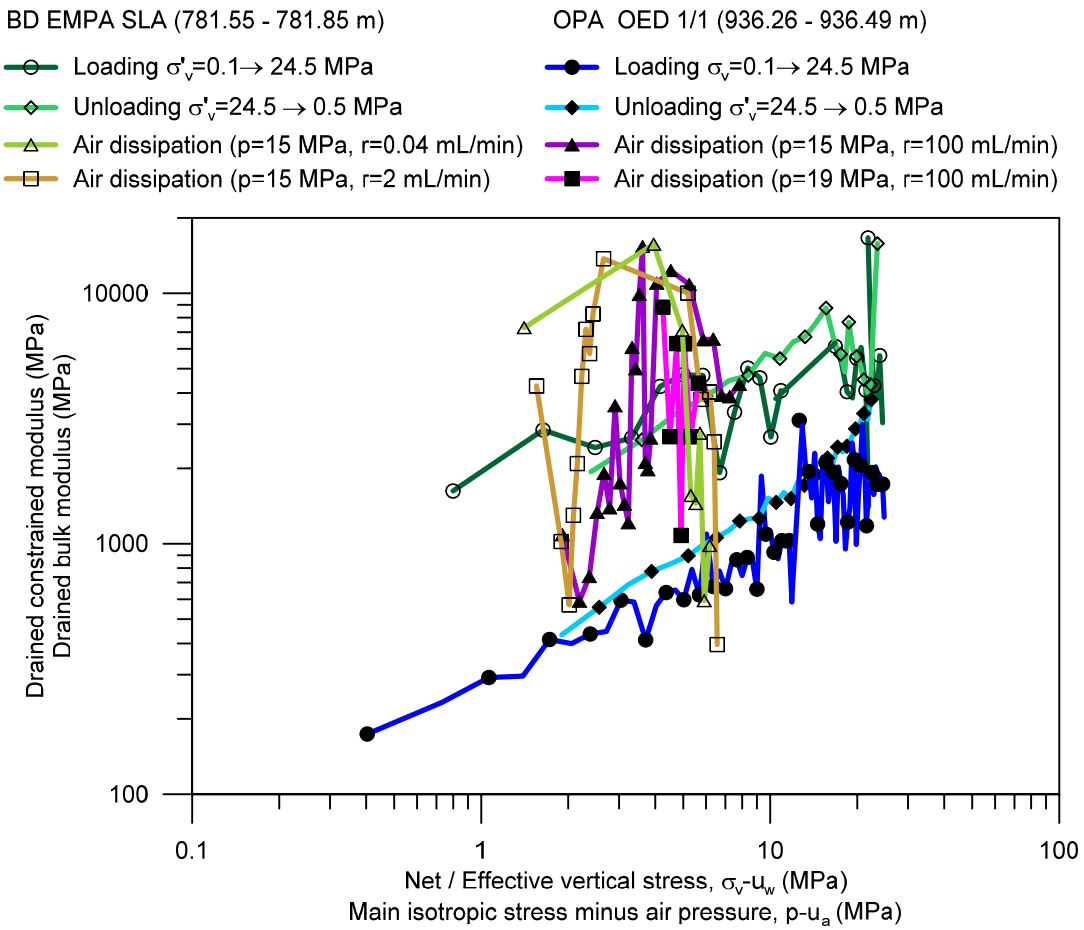

Figure 5-40. Stiffness of the materials during loading/unloading paths under oedometer conditions and during air dissipation stages under isotropic conditions.

5.4. Comparison

Results of gas injection and dissipation experiments have been shown for different argillaceous formations: plastic Boom Clay; and indurated clays: deep Opalinus Clay and 'Brauner Dogger' in two different setups. Despite its inherent differences, common features can be identified regarding its behaviour along gas migration process.

The air injection tests were performed in oedometer and isotropic cells at constant vertical or isotropic stress, on samples with a pre-defined orientation of bedding planes. The deformational response during the process was fully coupled with the hydraulic process. All samples underwent expansion during the air pressure propagation and compression when the air pressure decayed. Initially, the samples were able to maintain the air pressure, but at some point, large amounts of fluid volume were measured at the downstream reservoir which indicated the breakthrough point was exceeded.

Injection rate appeared to be one of the most influential factors in the behaviour. At faster injection rates, the deformational response of these clays is delayed in time,

whereas at slower injections, the expansion induced by air pressurization occurred more progressively and finished when maximum air pressure was reached. However, it is worthy of mention that, for Boom Clay, 2 mL/min was a rate enough slow to present this behaviour, whilst for indurated clays, due to its low porosity, the rate was decreased 50 times more, until 0.04 mL/min.

Boom Clay results on air permeability were clearly higher than those obtained for water. By contrast, indurated clays did not present a clear tendency in this regard.

5.5. Concluding remarks

In this Chapter, gas injection experiments have been described and analysed. Some preliminary conclusions can be drawn:

- Stress state of the samples influenced gas transport. In the case of tests under oedometer conditions, knowing the value of the lateral stress is a keystone to define maximum gas pressure so that to avoid gas passage through the sample-ring interface. Time-dependent effects such as lateral stress relaxation would merit more investigation.
- The studied materials were able to stand high gas pressures (lower than the minimum principal stress and generally larger than their air entry value) during a period, but after some time, the materials were not able to maintain the pressure anymore and large amounts of outflow fluid were recorded (breakthrough).
- Deformational behaviour during gas injection and dissipation was determined by the injection rate. At slower rates expansions occurred during the injection stage, since pore pressure was nearly equilibrated, whereas, at faster rates, this response was delayed in time.
- Bedding orientation in Boom Clay samples tested under oedometer conditions played a fundamental role in the volume change behaviour during gas migration. Samples with bedding normal to flow, less constrained, consistently displayed larger expansions than samples with bedding parallel to flow.
- Intrinsic permeability to gas flow in these nearly saturated clayey materials did not correlate with the porosity in the way that water permeability did. Moreover, bedding orientation did not seem to influence in the obtained values. Therefore, two-phase flow concepts did not apply in the gas transport process.
- Gas transport properties were clearly dependent on the deformation of the materials along the injection and dissipation stages and flow through preferential pathways is expected.

6
MICROSTRUCTURAL CHANGES INDUCED BY GAS MIGRATION

6.1. Introduction

Within the long-term safety analysis of the geological radioactive waste repositories a crucial issue to address is the evolution of the transport properties of the formations, in particular, the gas permeability since preferential gas pathways may develop taking advantage of the material heterogeneity, anisotropy or rock discontinuities, and thus, it may lead to the release of the produced gases.

Gas permeability is much sensitive than water permeability to microstructure changes due to the growth of micro-cracks or fissures in the rock mass. In order to analyse these effects, three different techniques were used to study the microstructure of the Boom Clay before (intact state) and after the air injection/dissipation experiments.

Mercury Intrusion Porosimetry (MIP) enables to find evidence of fissure opening induce by air injection. This technique presents data on entrance pore sizes and their distribution, but does not provide information on their shape (pore or fissure) – unless the fractal analysis is used – or on their connectivity.

Analysis of the surface of samples in the intact state and after being tested by Field-Emission Scanning Electron Microscopy (FESEM) qualitatively complements the information of the MIP given high-resolution images and also provides quantitative data regarding the magnitude of fissure apertures and the separation between them.

Additionally, use of new tomographic techniques in the geotechnical field, such as X-ray Micro-Computed Tomography (μ-CT), Nuclear Magnetic Resonance (NMR) or Focussed Ion Beam-Scanning Electron Microscopy (FIB-SEM), appear to be encouraging to complement the microstructural characterisation (Muurinen et al. 2013; Fleury & Canet 2014; Desbois et al. 2014; Bruchon et al. 2014; Hemes et al. 2015). In this work, μ-CT was selected since μ-CT images facilitate visualizing in 3D the fissure pattern and quantifying their volume and connectivity.

The microstructural information provides with these techniques such as fissure aperture, separation, volume, and connectivity will help to better understand the air transport mechanism through stress-dependant pathways, and furthermore, will provide experimental data to define model parameters of numerical analysis on gas flow through argillaceous materials.

This Chapter is organised in seven blocks mostly dedicated to Boom Clay since microstructural tests on indurated clays were not performed, with the exception of some porosimetry tests in Opalinus Clay. The first three contain a brief description of each technique together with the procedure for sample preparation and the obtained results, following by a section dedicated to comparing the obtained results. Prior to the concluding remarks, effects of microstructural changes in air transport properties are analysed.

6.2. Mercury Intrusion Porosimetry Tests

6.2.1. Description of the technique

MIP has been widespread used in the microstructural characterization of porous geomaterials (see for instance Hemes et al. 2015; Desbois et al. 2014; Seiphoori et al. 2014; Delage et al. 2006; Romero 2013).

The basic principle of the MIP technique is based on the Washburn equation (Eq. 6.1) in which an absolute pressure p_{Hg} is applied to a non-wetting liquid (mercury) in order to enter the empty pores. The equation applies for pores of cylindrical shape and parallel infinite plates (fissure-like microstructure) (Webb 2001):

$$p_{Hg} = -\frac{n\sigma_{Hg}cos\theta_{Hg}}{x} \quad (6.1)$$

where σ_{Hg} is the surface tension of mercury (σ_{Hg}= 0.484 N/m at 25 ºC), θ_{Hg} the contact angle between mercury and the pore wall, and x the entrance or throat pore diameter (n = 4) or the entrance width between parallel plates (n = 2). The value n = 4 is often used in MIP. The contact angle, which is very sensitive to surface roughness, is usually taken between 139º and 147º for clay minerals

The mercury intrusion procedure can be used to obtain data on the retention behaviour. It can become assimilated to the desorption path of the soil moisture characteristic curve by applying to an initially saturated sample an increasing external air pressure (non-wetting fluid) to gradually dry the soil (Romero 1999). Thus the injection of non-wetting mercury with a contact angle of θ_{nw} is equivalent to the ejection

of water from the pores (desorption curve) by the non-wetting front advance of air with θ_{nw} = 180° for the same diameter of pores being intruded. Therefore, the volume of pores not intruded by mercury could be used to evaluate the water content or degree of saturation corresponding to the equivalent applied air overpressure. The relationship between the equilibrium mercury intrusion pressure p_{Hg} and air overpressure or matric suction $(u_a - u_w)$ can be obtained applying Eq. (6.2) for the same diameter x of pores being intruded:

$$(u_a - u_w) = \frac{4\sigma_w cos\theta_w}{x} \quad \text{and} \quad p_{Hg} = -\frac{4\sigma_{Hg} cos\theta_{nw}}{x} \tag{6.2}$$

$$(u_a - u_w) = -\frac{\sigma_w cos\theta_w}{\sigma_{Hg} cos\theta_{nw}} p_{Hg} \approx 0.196 p_{Hg} \tag{6.3}$$

where σ is the surface tension and $cos\theta_w = 1$ the wetting coefficient for the air-water interface.

The corresponding water content (w) can be estimated by means of the following expressions (6.4):

$$Sr_{nw} + Sr = 1; \;\; Sr \cdot e = G_s \cdot w; \;\; w = \frac{e}{G_s}(1 - Sr_{nw}) = w_{sat}(1 - Sr_{nw}) \tag{6.4}$$

where Sr is the water degree of saturation, Sr_{nw} the degree of saturation of the non-wetting mercury, w_{sat} the water content at $Sr = 1$, e the void ratio and Gs the specific gravity of the soil grains

Romero & Simms (2008) presented the main limitations of MIP: (a) isolated pores enclosed by surrounding solids are not measured— this enclosed porosity is not significant in soils; (b) pores that are accessible only through smaller ones (constricted porosity) are not detected until the smaller pores are penetrated; (c) the apparatus may not have the capacity to enter the smallest pores of the sample (non-intruded porosity); and (d) the minimum practical pressure of the apparatus limits the maximum pore size to be detected (non-detected porosity). In this way, when the clay sample is intruded by mercury, the intruded void ratio estimated under the maximum applied pressure does not coincide with the estimated void ratio of the sample. Differences mainly arise due to the non-intruded porosity with entrance pore sizes lower than 10 nm and the non-detectable porosity for pore sizes larger than 400 μm. In addition, intrusion (pressure increase) and extrusion (pressure decrease) cycle does not close when the initial pressure is restored, indicating that some mercury has been permanently entrapped in the constricted porosity.

The device used for MIP tests is an 'AutoPore IV 9500 – Micrometrics Instrument Corp' porosimeter (Figure 6-1).

Figure 6-1. Mercury intrusion porosimetry equipment.

6.2.2. Sample preparation

Cubical samples of 1 cm^3 of volume were trimmed from intact core samples or from oedometer samples after being tested. These samples required a pre-treatment before being installed in the porosimeter. Instantaneous freezing is carried out by plunging the samples into liquid nitrogen (-196 ºC) and then applying vacuum in order to remove the pore water of the microstructure before the MIP test (Figure 6-2). In such conditions, water freezing occurs with very small ice crystals, and the 9% volume expansion occurring in normal freezing conditions does not take place, optimising the preservation of the microstructure during dehydration (Delage et al. 2006). Desbois et al. (2014) also showed that no significant changes in the quantification of pore sizes and pore morphologies were produced due to this sublimation process and therefore good microstructure preservation is ensured.

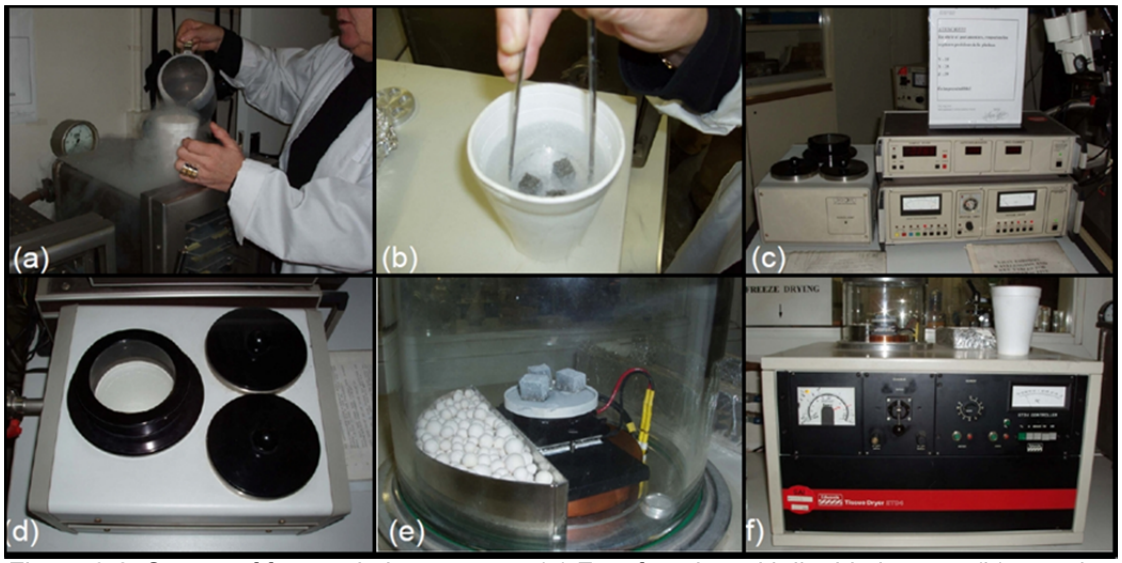

Figure 6-2. Stages of freeze-drying process. (a) Fast freezing with liquid nitrogen; (b) samples inside liquid nitrogen; (c) and (d) temperature stabilization at -120ºC; (e) vacuum drying; (f) freeze-drying equipment (after Lima 2011).

6.2.3. Results

MIP tests were performed in Boom Clay intact samples, in samples after gas injection tests under oedometer conditions (following Protocol 3) and in samples subjected to the same stress paths under oedometer conditions but without the injection stage (following Protocol 4). This way, it was possible tracking the changes in the microstructure induced by air migration. Firstly, obtained results after the air injection tests are shown in comparison with those corresponding to the intact sample (see Chapter 2 Section 2.2.6). Afterwards, results of MIP tests after non-injection experiments are presented.

Study of microstructural changes induced by gas migration in deep indurated clays only consists of MIP tests in the intact state, after gas injection test on Opalinus Clay as well as after compressibility tests in the oedometer cell, which are presented at the end of this section.

6.2.3.1. Results before and after air injection tests on Boom Clay

Figure 6-3 presents the pore size density functions for the intact material and after the air tests in terms of the intruded volume of mercury referred to the volume of solids (non-wetting void ratio e_{nw}) for different entrance pore sizes x. As indicated in the figure, a new family of large pores, which was not detected on intact samples, was observed after the air tests. This new dominant pore size at entrance sizes larger than 2 μm appeared to be associated with the expansion undergone by the material during the air injection and early shut-off stages and the possible opening of fissures

(Gonzalez-Blanco et al. 2016). This new family of porosity was consistently found in all samples after gas injection tests.

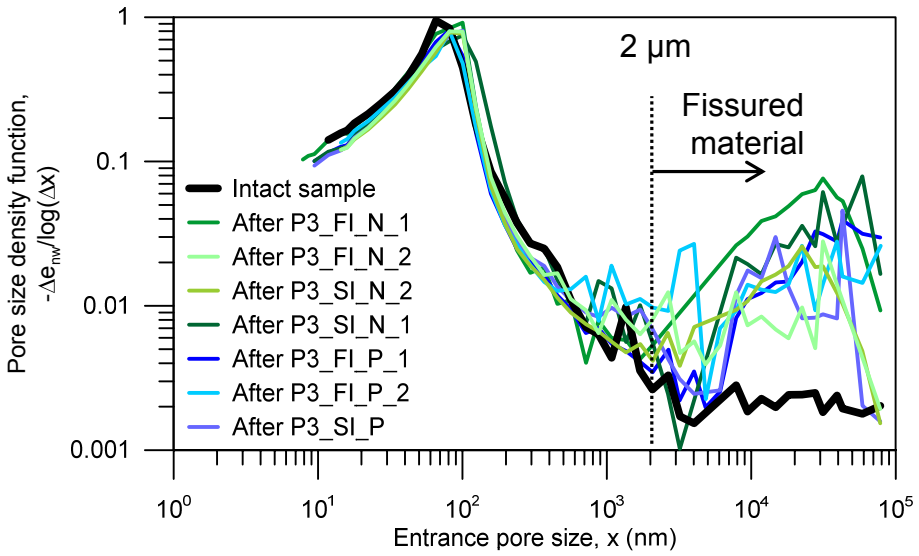

Figure 6-3. Pore size distribution curves from MIP on intact samples and after air injection tests

MIP technique does not directly provide information on the shape of the pores; however, a fractal analysis of the results can contribute to it. To this end, MIP data were also interpreted in terms of the fractal character of the porous network, admitting self-similarity of the hierarchical void structure (Romero & Simms 2008). Figure 6-4 shows the fractal dimension D_s of the porous medium that was obtained from the derivative of the pore volume (non-wetting degree of saturation $S_{r\,nw}$ of intruded mercury) with respect to the mercury intrusion pressure p (Eq. 6.5).

$$log\left(\frac{dSr_{nw}}{dp}\right) = -(D_s - 4)\log(p) \qquad (6.5)$$

The fractal analysis of intact material indicated a dominant fissure-like microporosity ($D_s \approx 2$) for pore sizes lower than 100 nm (applied pressure higher than 10 MPa) and a volumetric structure ($D_s \approx 3$) for the less developed macroporosity (pore sizes larger than 900 nm - applied pressure lower than 2 MPa -). After the air tests, the fractal analyses indicated a decrease of the fractal dimension $D_s \approx 2.5$ of the new family of pores developed in the macroporosity domain. It appeared that this macroporosity tended to a fissure-like structure consistent with the opening of fissures during the expansion undergone by the material along the air injection stage.

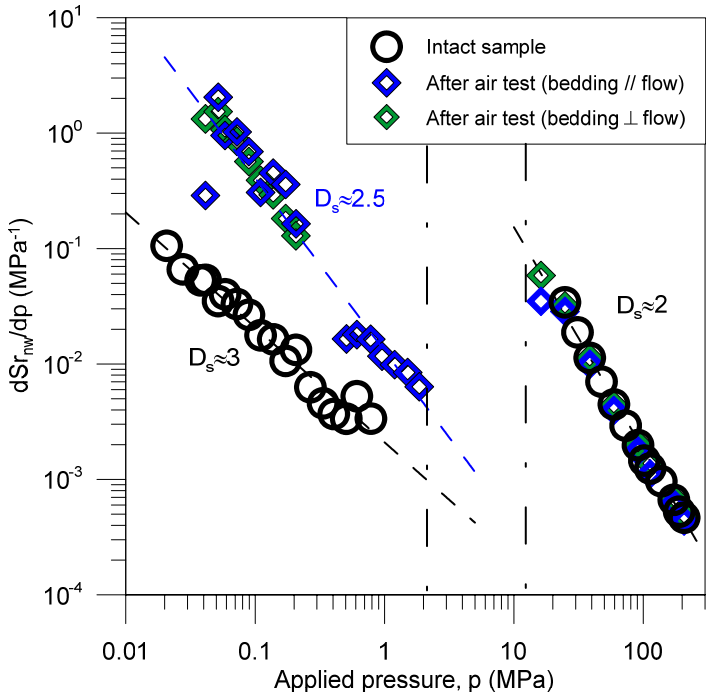

Figure 6-4. Fractal analyses using MIP data on intact material and after air tests.

Additional analysis of MIP data was conducted to get the permeability of the fabric, obtaining the microstructure and the macrostructure permeability using the method proposed by García-Bengochea et al. (1979) in which it is assumed that the permeability of the pores with diameter x can be calculated with Eq. 6.6:

$$K_p = \frac{\rho g n}{32\mu} x^2 \tag{6.6}$$

where ρ is the water density, n is the porosity, μ is the absolute viscosity and x is the entrance pore size. Therefore, the permeability of m connected pores with a diameter of x_m is given by Eq. 6.7:

$$K_m = \sum_1^m K_p \cdot f(x) = \frac{\rho g n}{32\mu} \sum_1^m (x^2 \cdot f(x)) \tag{6.7}$$

where $f(x)$ is the frequency histogram of the pore size distribution obtained following the scheme in Figure 6-5.

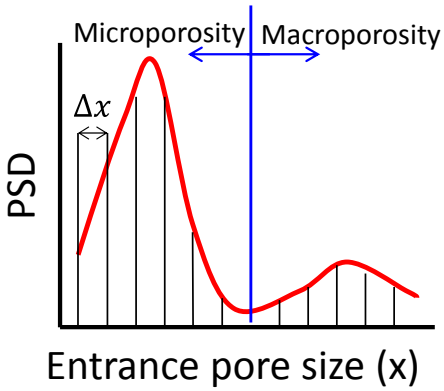

Figure 6-5. Scheme of the frequency histogram of the pore size distribution.

Figure 6-6 depicts the fabric permeability, normalized by the intact sample one. The permeability of the microporosity (Figure 6-6a) is in the same order of magnitude for all the samples (intact and after be tested) while the permeability obtained for the macroporosity (Figure 6-6b) is around one order of magnitude higher in samples after testing. This is in concordance with the permeability measurements obtained in air and water injection tests (see in Figure 5-16 Chapter 5), in which permeability to air was approximately one order of magnitude higher than permeability to water.

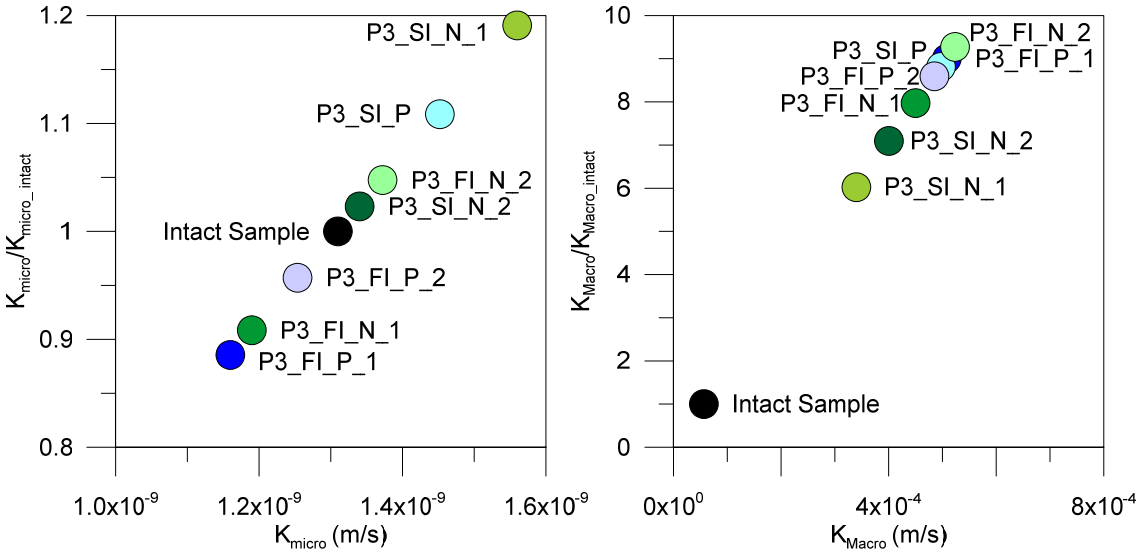

Figure 6-6. Permeability of the fabric: permeability of the microporosity (left) and permeability of the macroporosity (right).

6.2.3.2. Results of non-injection tests on Boom Clay

MIP tests on samples after air injection clearly show an opening in the macrostructure, but some concerning about the influence of the unloading process regarding the preservation of the microstructure after air tests arose at this point. Therefore, a set of non-injection tests was performed in order to discern the effects due to the air migration from the ones due to the unloading.

These tests followed the same protocol as the oedometer ones (see Protocol 4 in Chapter 3) but deleting the air injection stage with the aim of being sure about the formation of a new family of pores in samples after testing, and how the unloading process affects to the final microstructure, so that, three different unloading paths were chosen.

Figure 6-7 shows the pore size distribution of the non-injection tests in comparison with the intact sample. In the first one (P4_NI_N_1) unloading process was carried out at drained conditions: the sample was in contact with water and the unloading rate was at 0.9 kPa/min. In this test, the sample experimented a high swelling and as a consequence, an opening of the macroporosity can be observed in the pore size distribution. In the second test (P4_NI_N_2), a quasi-drained unloading was carried out. Faster unloading rate was chosen (30 kPa/min) but the sample was able to absorb some water. The pore size distribution is very similar to the first one despite having less expansion. For the third case (P4_NI_N_3), an undrained unloading was performed since the vertical pressure was reduced instantaneously, so the sample did not adsorb any water. The pore size distribution remained as the intact one since negligible expansion occurred during this process. This last one follows the same unloading path as the air injection tests.

The fractal dimension analysis was also performed with the new data (Figure 6-8), which confirms the change in the macroporosity after a drained unloading (mechanical unloading or increase on gas pressure during the injection) tending to a fissure-like shape -fractal dimension D_S around 2.5-. In contrast, undrained unloading shows the same patron as the intact sample with a volumetric fractal dimension at the macro scale.

Some remarks should be highlighted from these results:

- The registered opening at the macro scale in the pore size distribution after the air injection tests was caused by the air migration process.
- The undrained unloading did not modify the pore network.
- The hydro-mechanical loading paths followed in Protocol 3 did not affect the structure of the sample, which means that no plastic deformation occurred during these processes since pore size distribution after test P4_NI_N_3 is similar to the intact one.
- The drained and quasi-drained unloading processes produced some damage in the structure, as well as the air flow did.

- The hypothesis that the gas pressurization process acts as an unloading stage, producing some damage in the samples, is validated by the changes in the microstructure.

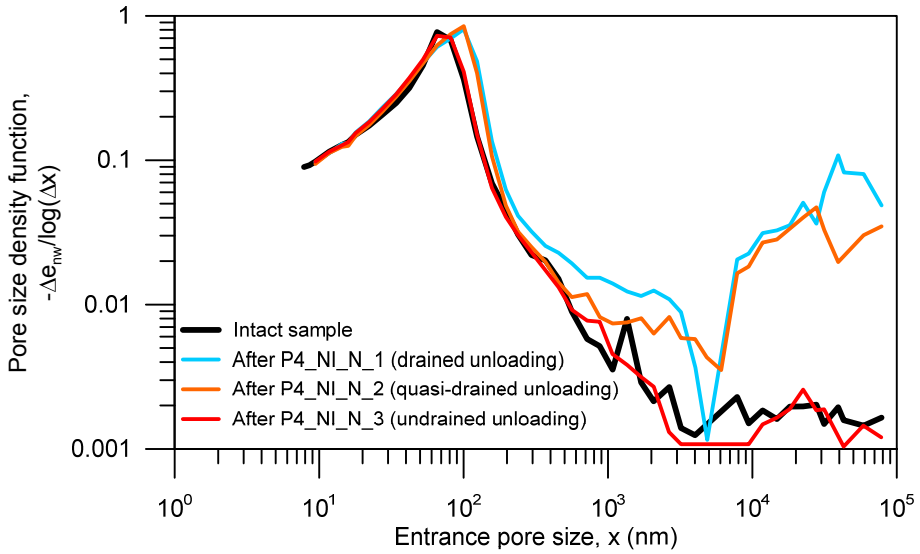

Figure 6-7. Pore size distribution curves from MIP on intact sample and after non-injection tests.

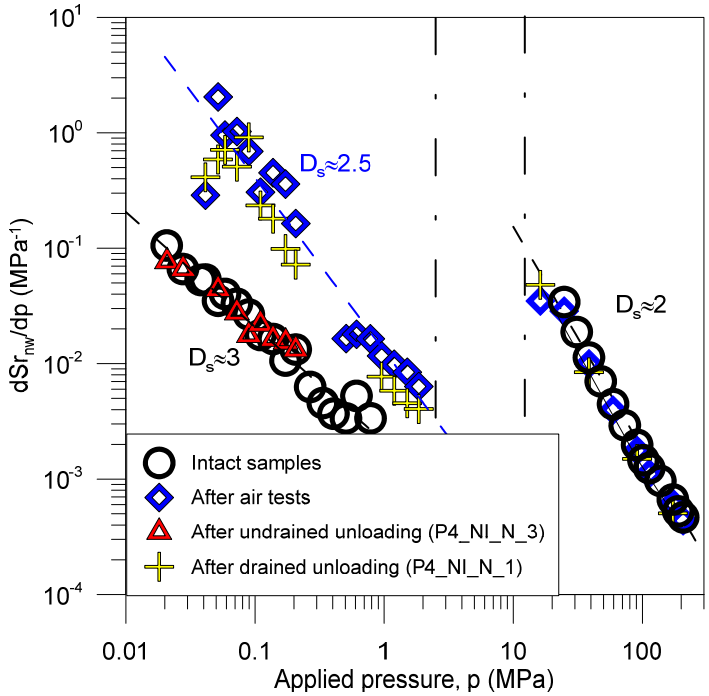

Figure 6-8. Fractal analyses using MIP data of the intact material, after air injection tests, and after non-injection tests.

6.2.3.3. Results before and after air injection tests on Opalinus Clay

At the end of the isotropic test on Opalinus Clay OED 1/1 (936.26 - 936.49 m), MIP test was performed to follow the evolution of the microstructure after air injections. The

obtained results are shown in Figure 6-9 in comparison with the PSD for the intact state. It can be observed some reduction of the microporosity as well as an aperture which is indicated by the change of the dominant pore mode, slightly higher after injections. Moreover, some macroporosity was detected after the injection tests, which could be developed during the expansion produced at the early stage of injection experiments. This could be an important fact on the gas transport properties of the indurated clays because suggest some degradation of the material due to the air passage. Despite scarce data on these materials, drawing this conclusion is reasonable since this change in the pore network turned out to resemble Boom Clay.

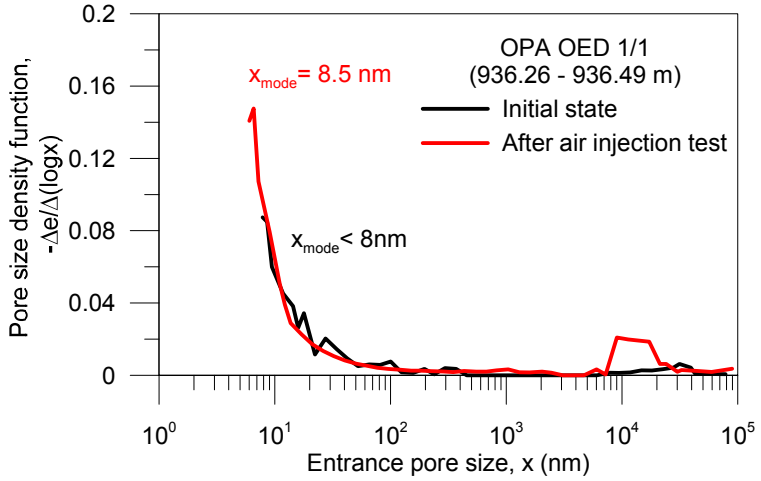

Figure 6-9. PSD functions on intact sample and after triaxial test for OED 1/1 Opalinus Clay.

6.2.3.4. Results after drained unloading on Opalinus Clay

At the end of the oedometer test, MIP test was performed to follow the evolution of the microstructure after loading/unloading paths. The obtained result is shown in Figure 6-10 together with PSD for the intact sample. After drained unloading Opalinus Clay shows some reduction of the microporosity with respect to the initial state, as well as an aperture which is indicated by the change of the dominant pore mode, slightly higher after the loading/unloading path. Also, some expansion of the pores bigger than 1 μm is observed in the double logarithmic scale. By comparison with the results after air injection test (Figure 6-11), same behaviour on the microscale level was found, whereas the opening at the macrostructure level occurred in both cases, being large when it was due to gas passage.

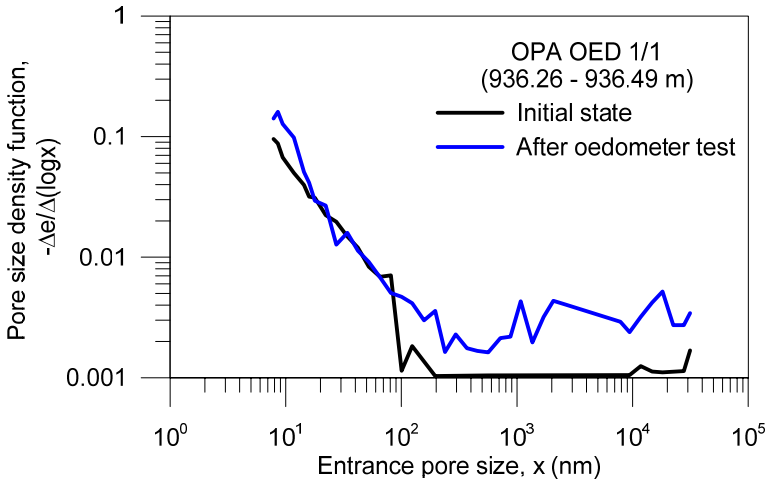

Figure 6-10. PSD functions on intact sample and after oedometer test for OED 1/1 Opalinus Clay.

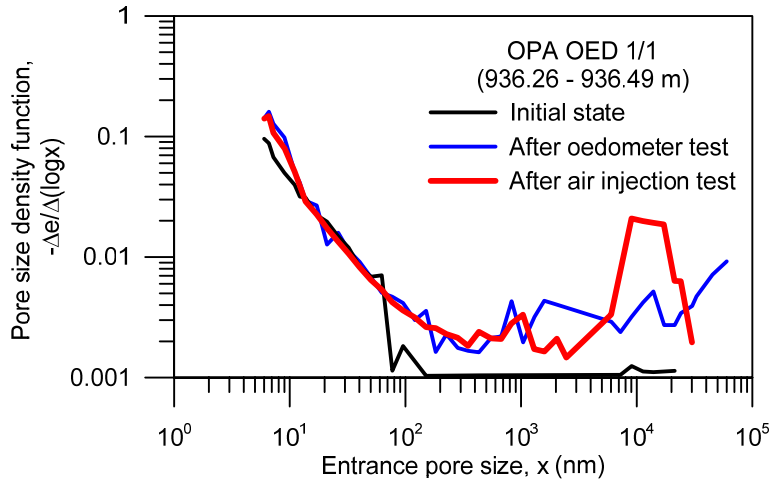

Figure 6-11. Comparison of PSD functions: intact state, after oedometer test and after air injection test for OED 1/1 Opalinus Clay.

6.3. Field-Emission Scanning Electron Microscopy

6.3.1. Description of the technique

Scanning Electron Microscopy is an experimental subject of interest for geologists, soil scientists and geotechnical engineers (Cotecchia et al. 2016; Romero & Simms 2008; Desbois et al. 2010; C. Liu et al. 2011; Delage et al. 2006). It is a qualitative method for studying and, where possible quantifying, the arrangements of aggregations/particles and voids in soils. In this work, Field-Emission Scanning Electron Microscopy (FESEM) was used to visualize very small topographic details on the surface of the material, in particular, the formation of fissures after gas migration suggested by MIP results, so that samples of intact material and after an air injection test were examined.

This technique is basically a microscope that works with electrons instead of light. These electrons are liberated by a field emission source according to a zig-zag pattern

and accelerated in a high electrical field gradient. Within the high vacuum column, these so-called primary electrons are focussed and deflected by electronic lenses to produce narrow scan beam that bombards the object. As a result, secondary electrons are emitted from each spot on the object. The angle and velocity of these secondary electrons relate to the surface structure of the object. A detector catches the secondary electrons and produces an electronic signal which is amplified and transformed to a scan-image.

The microscope used for FESEM was a JSM-7001F (JEOL) with a magnification range from 10 to 1,000,000, with a virtually unlimited depth of field (Figure 6-12). Compared with conventional scanning electron microscopy (SEM), FESEM produces clearer, less electrostatically distorted images with better spatial resolution (three to six times).

Figure 6-12. FESEM equipment.

6.3.2. Sample preparation

Small cubical samples of 10 mm length were manually trimmed and freeze-dried following the same procedure as in the MIP (Section 6.2.2). Afterwards, in order to be observed with the FESEM, samples were made conductive for current. This was done by coating them with an extremely thin layer of silver.

6.3.3. Results

FESEM images were taken from one intact sample (from Core 8 CGR66-67W_Core8_Section_a) and another one after a fast injection test on the sample with bedding planes normal to air flow (P3_FI_N_2).

The following figures (Figure 6-13 and Figure 6-14) show four images of each samples corresponding to magnifications of 100, 300 1,000 and 3,000 times (A to D respectively). The scale in μm is indicated in the bottom of the images and the coloured rectangles represent the area shown in the next image.

Images of intact sample (Figure 6-13) show very uniform material apart from some linear irregularities which are most likely due to the trimming process.

In contrast to the intact one, in the first FESEM image of the sample after air injection (100 times magnification, Figure 6-14A), several fissures can easily be distinguished. Their direction seems to mainly follow a preferential direction indicated in the figure even though some of them are connected. It is reasonable to think that gas flow takes advantage of the natural discontinuities (bedding planes) which were initially closed, and the fissures developed in that direction. Although it is difficult to ensure it based on these images, tomography images will confirm this statement. Besides the fissure direction, this image was used to quantify the distance between them (Figure 6-15) ranging from 150 to 270 nm.

The subsequent magnifications were done in two different areas so as to obtain different measurements of fissure aperture (Figure 6-14D). As it can be appreciated, the aperture is not constant along the same fissure, presenting narrow and wider zones. Fissure apertures of 3.6 and 10 μm were measured in good agreement with those detected by MIP.

It is also interesting to note that the material surrounding the fissures seems to be more folded and altered than the farther areas. On account of the fact that samples underwent expansion during the injection, this must be a consequence of the local compression deformations around the area in expansion.

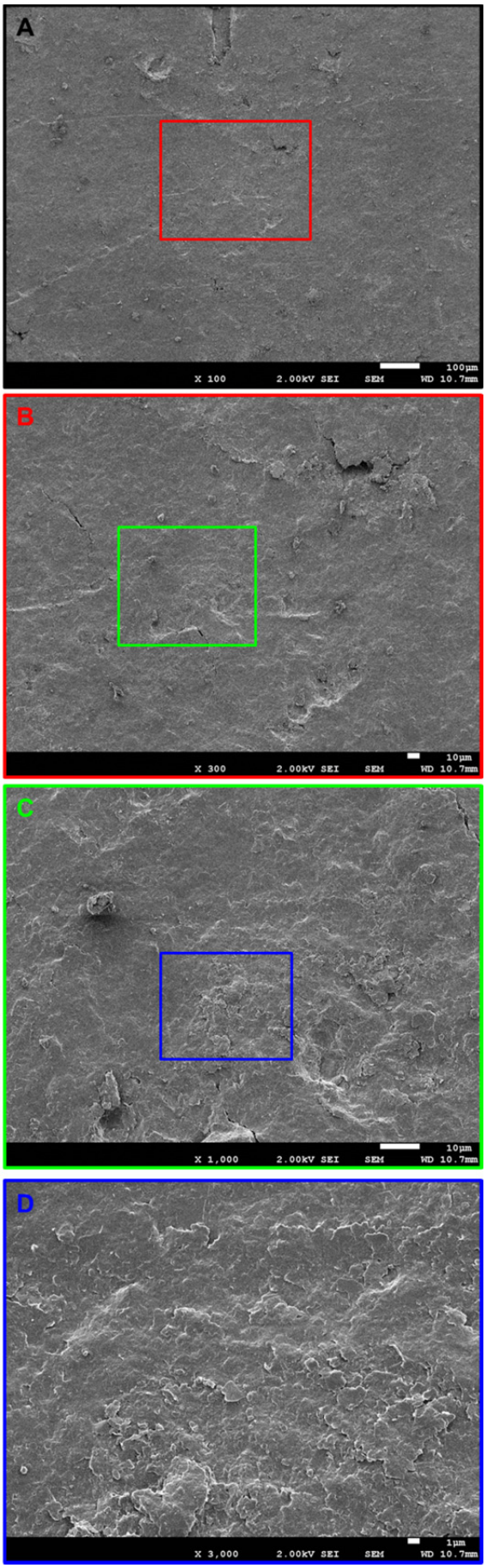

Figure 6-13. FESEM images of the intact sample. Magnifications of: A) 100; B) 300; C) 1,000 and D) 3,000 times.

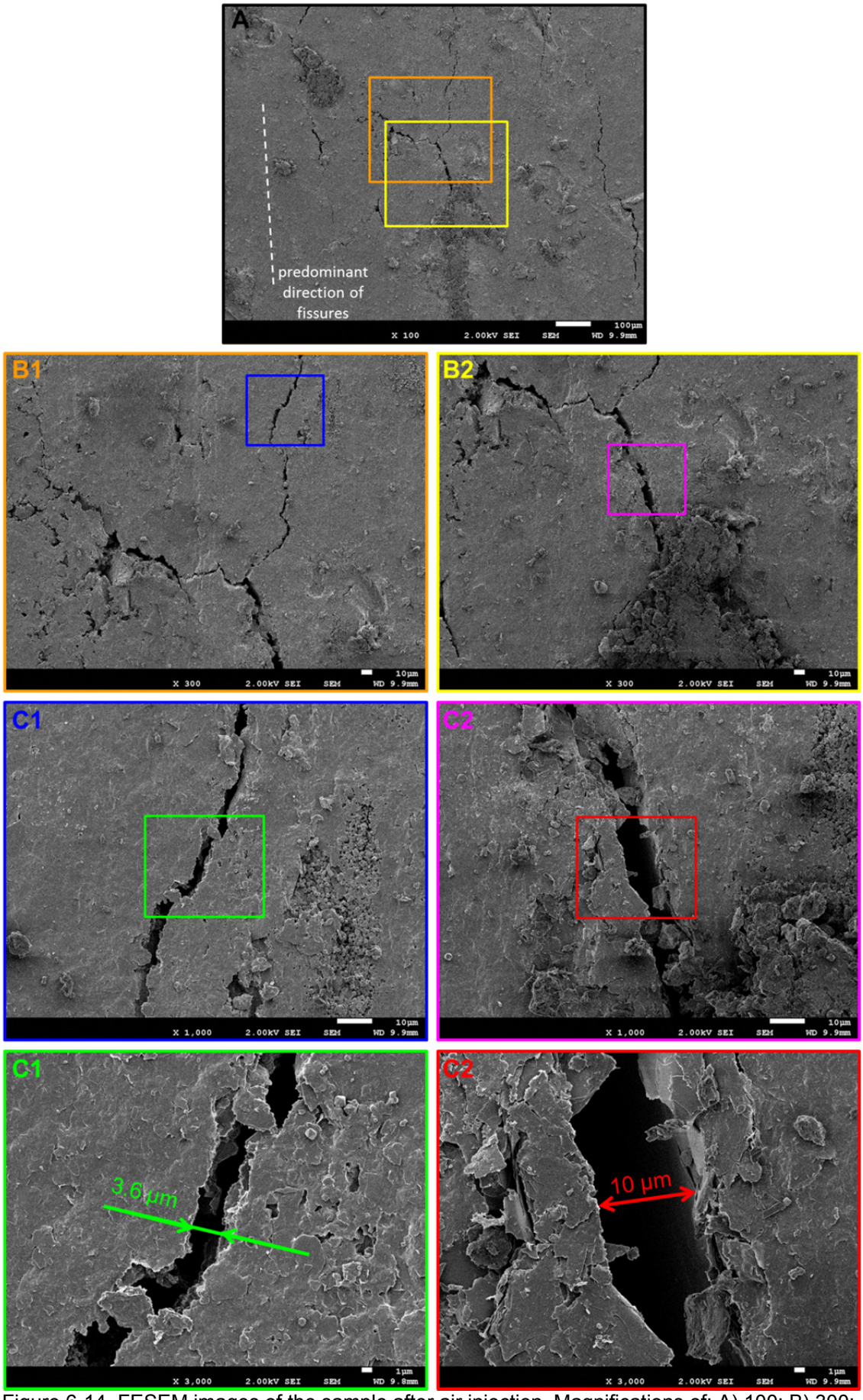

Figure 6-14. FESEM images of the sample after air injection. Magnifications of: A) 100; B) 300; C) 1,000 and D) 3,000 times.

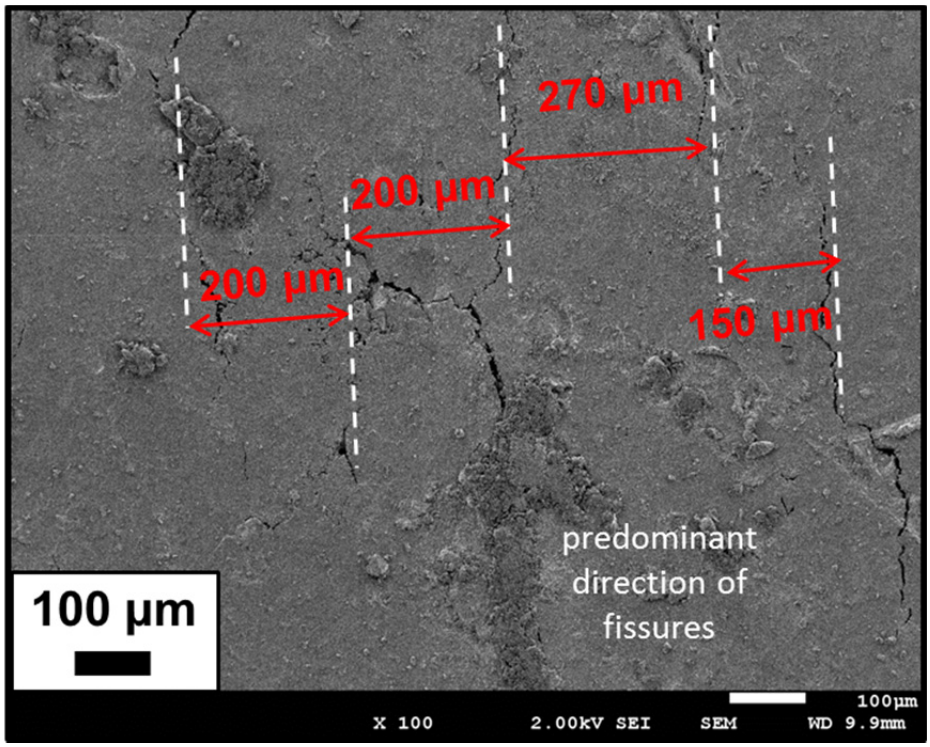

Figure 6-15. Measurements of distance between fissures detected on FESEM image of the sample after air injection (100 times magnification).

6.4. Micro-Focus X-ray Computed Tomography

6.4.1. Description of the technique

Micro-focus X-ray computed tomography (µ-CT) was used to examine in three dimensions the internal microstructure of intact Boom Clay and after air injection tests.

µ-CT is a non-destructive observation technique that has been proven to be useful in the investigation of various geological porous media including compacted bentonite (Kozaki et al. 2001), compacted sand/bentonite mixtures (Kawaragi et al. 2009; Saba et al. 2014), sand (Andò et al. 2012), or shales (Josh et al. 2012).

The principles of CT scanning have been extensively described (Wellington & Vinegar 1987). In brief, CT-scan imagery corresponds to a 2-D or 3-D linear X-ray attenuation pixel matrix, where the attenuation is a function of the density, the atomic number and the thickness of the sample analysed. When the X-ray hits the object only part of the photons goes through the material. The rate of removal of photons from the original X-ray is a function of the linear attenuation coefficient (μ) which depends on the photon energy (X-ray energy), the chemical composition, and physical density of the material. Dense materials (i.e., materials with high atomic numbers) attenuate more the X-ray beam energy than less dense materials and this difference in attenuation provides the contrast that forms the image. The basic equation for attenuation of a monochromatic

beam that travels through a medium to a depth z is given by Beer-Lambert's law as follows:

$$I = I_0 e^{-\mu z} \tag{6.8}$$

where I_0 is the initial or incident X-ray radiation, μ is the linear attenuation coefficient of the material, z is the length of the X-ray path through the material and I is the transmitted radiation (photons per area per unit time).

µ-CT works on the same principles but using smaller samples and a shorter distance between source and detector which allows much higher resolution. A micro-focus X-ray source illuminates the object under investigation and a planar X-ray detector collects magnified projection images (Figure 6-16). Based on hundreds of angular views acquired while the object rotates, a computer synthesises a stack of virtual cross section slices through the object.

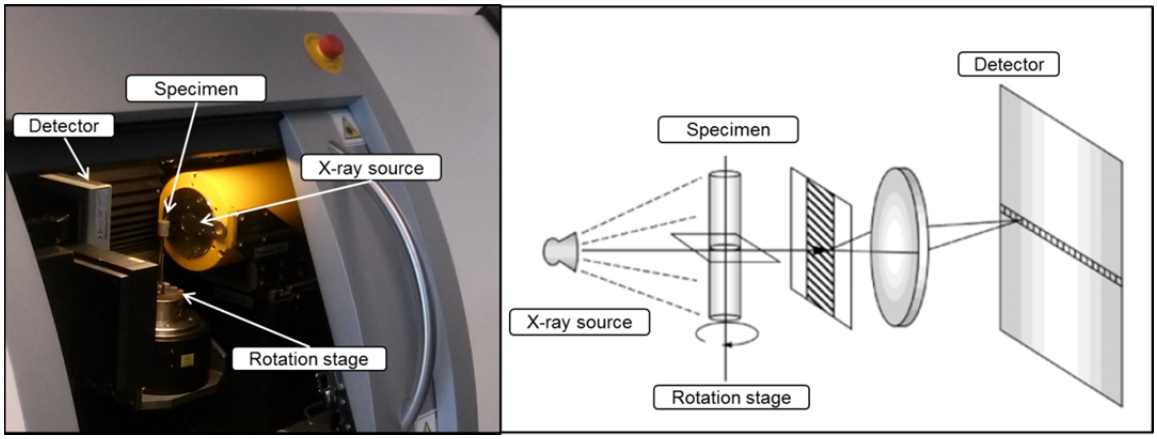

Figure 6-16. Photo and schematic representation of the µ-CT scan.

The device used for the µ-CT scans was a Phoenix Nanotom (GE Oil & Gas) from Delft University of Technology. The scan uses an open 180 kV / 15 W high-power nano-focus X-ray tube with up to 200 nm detail detectability and internal cooling – optimized for long-term stability.

Samples of intact Boom Clay and after being tested were scanned using 720 projections on 360º with a voxel size of 20 µm (a voxel describes a Volume Pixel which is the smallest distinguishable box-shaped portion of a three-dimensional image). The final 3D images are a 16 bits' greyscale type with a size of 835 x 874 x n voxels, where n is the number of slices (different for each test). The data obtained from the µ-CT consist on '*.dcm' file extension for each slide which is frequently used for images saved in the Digital Imaging and Communications in Medicine (DICOM) image format.

This format was created by the National Electrical Manufacturers Association (NEMA) as a standard for distributing and viewing medical images, such as MRIs, CT scans, and ultrasound images. DICOM files contain metadata that provide information about the image data, such as the size, dimensions, bit depth, modality used to create the data, and equipment settings used to capture the image. Table 6-1 shows most relevant metadata information of one of the DICOM files.

Table 6-1. Metadata information of a DICOM file.

File size	1460228
Format	DICOM
Format version	9
Width	835
Height	874
Bit depth	16
Colour type	'greyscale'
File meta-information group length	196
Image position patient	3x1 double
Image orientation patient	6x1 double
Rows	874
Columns	835
Pixel spacing	2x1 double
Bits allocated	16

6.4.2. Sample preparation

The size of the samples was determined by the required resolution, and thus, to achieve a voxel size of 20 μm, the samples should measure 15 mm of height and 15 mm in diameter (Figure 6-17). A cylindrical shape is recommended in order to avoid corner artefacts (Ketcham & Carlson 2001).

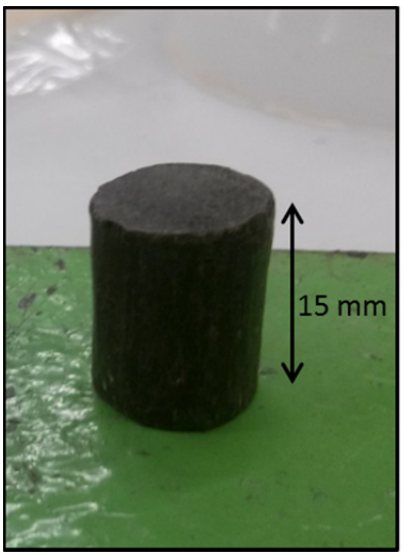

Figure 6-17. The sample for the μ-CT scan.

Samples of intact Boom Clay were directly trimmed from undisturbed cores (Core 8 CGR66-67_Core_8_Section_a) in both directions, bedding parallel and orthogonal to the axis. In the same manner, after dismounting two of injection tests (Tests P3_FI_P_2 and P3_FI_N_2) other two samples were obtained to scan them. Eventually, consequences of gas passage can be detected with this technique. After testing, samples were trimmed as is indicated in Figure 6-18. Hence, bedding planes were orthogonal to axis and loss of resolution due to the rendering was avoided.

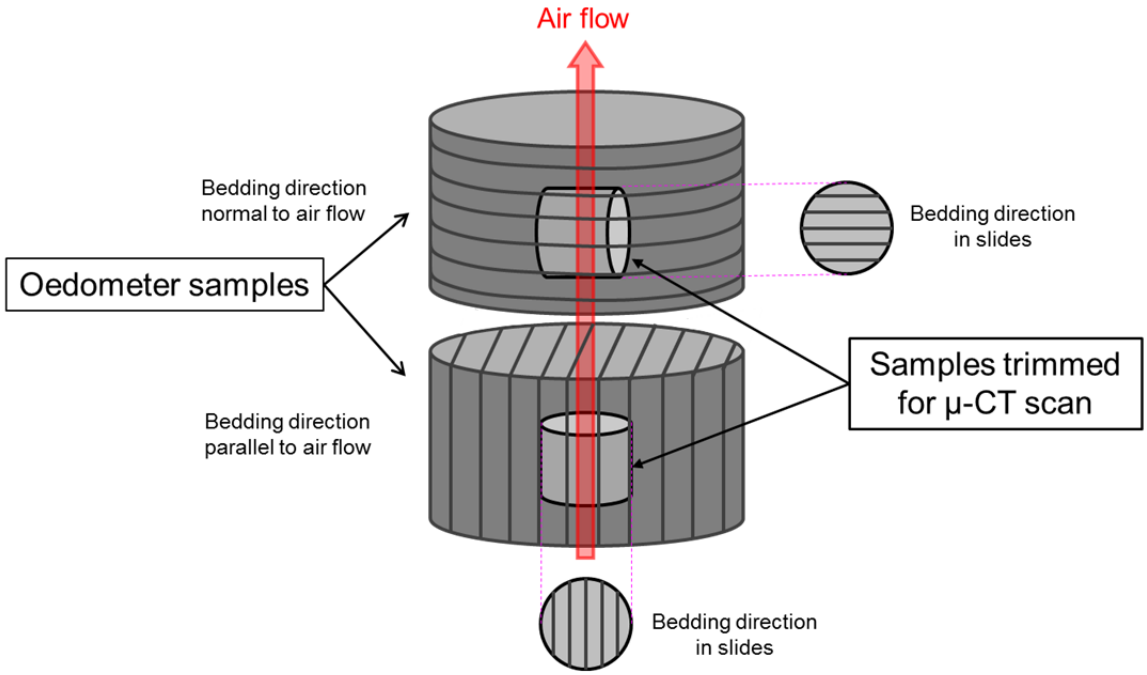

Figure 6-18. Scheme of how samples for µ-CT scan were trimmed from oedometer samples.

Although µ-CT does not need any samples pre-treatment, in this study, it was decided to subject the sample to the same process as in the MIP tests to allow its further comparison. After trimming all samples were freeze-dried by plunging the samples into liquid nitrogen and then applying vacuum in order to remove the pore water of the microstructure. Afterwards, samples were preserved in a vacuum packed until they were scanned.

6.4.3. Image post-processing procedure

6.4.3.1. Software

Currently, there are many software programs which allow image displaying of DICOM standard files, but not all of them offer the possibility of analysing them (measurements, histograms, etc.) and obtain rendering volumes. Consequently, in this study, image

post-processing was done with ImageJ software (Schneider et al. 2012) since it enables to achieve these purposes.

ImageJ is a public domain Java image processing and analysis program. It can display, edit, analyse, process, save and print 8-bit, 16-bit and 32-bit images. It can read many image formats including TIFF, GIF, JPEG, BMP, DICOM, FITS and 'raw'. It supports 'stacks' (and hyper-stacks) which are series of images that share a single window. It can calculate area and pixel value statistics of user-defined selections. It can measure distances and angles; create density histograms and line profile plots. It supports standard image processing functions such as contrast manipulation, sharpening, smoothing, edge detection and median filtering.

ImageJ, a multiplatform of public domain software, was designed with an open architecture that provides extensibility via Java plugins. Custom acquisition, analysis, and processing plugins can be developed using ImageJ's built in editor and Java compiler. User-written plugins make it possible to solve almost any image processing or analysis problem.

6.4.3.2. Volume reconstruction

Volume reconstruction, usually knows as volume rendering is used to describe techniques which allow the visualization of three-dimensional data. Volume rendering is a technique for visualizing sampled functions of three spatial dimensions by computing 2-D projections of a semi-transparent volume.

CT scanners produce three-dimensional stacks of parallel plane images, each of which consists of an array of X-ray absorption coefficients. In this study, X-ray μ-CT images have a resolution of 835 x 874 x 16 bits and there will be up to 1000 slides in a stack. The slides are spaced 20 μm apart (the resolution). In the two-dimensional domain, these slides can be viewed one at a time. The advantage of CT images is that they contain information from all the planes. The availability of the stacks of parallel data produced by CT scanners prompted the development of techniques for viewing the data as a three-dimensional field rather than as individual planes. This gave the immediate advantage that the information could be viewed from any view point.

ImageJ software includes several plugins for 3D visualization and also permits selecting between different methods of interpolation to create the rendering: "Nearest neighbour", "Trilinear", "Tricubic sharp" or "Tricubic smooth". Here, a trilinear interpolation method was chosen to 3D visualization.

6.4.3.3. Fissure filtering analysis description

The main goal of the image analysis is to verify the existence of fissures/fractures induced by air passage and quantify the total volume and its connectivity.

The easiest way to define features such as fractures is by simplifying the original (greyscale image) information. This is often done by segmentation, where a distinct set of classes is created using threshold values and every single datapoint is assigned to a class. However, global thresholding techniques are usually not successful on extracting narrow fractures from the dataset, and manual digitizing is not practical in such large dataset. Various approaches exist in the literature to process fractures in 3D datasets (Keller 1997; van Geet & Swennen 2001; Landis et al. 2003; Sellers et al. 2003; Ketcham et al. 2010; Deng et al. 2016). However, these techniques present several problems: often they do not work for narrow fractures or are not generally applicable because only work on a single fracture; and others have not published codes or required expensive commercial software packages. For these reasons, the multiscale Hessian fracture filtering, published by Voorn et al. (2013), has been used to analyse our μ-CT-scan images. It was thought to obtain the enhancement and segmentation on narrow fractures in 3D image data, and consequently, it adapts perfectly to our case of study. Moreover, it was implemented in ImageJ (Schneider et al. 2012). This approach also includes a connectivity filtering through a MATLAB® (The Mathworks, Inc., 2011) script to improve the representation of the data.

The Hessian fracture filtering is based on a Hessian matrix. For 3D image data, it is a 3 x 3 symmetric matrix containing the second order partial derivatives of the input data $I(x, y, z)$:

$$H = \begin{pmatrix} I_{xx} & I_{xy} & I_{xz} \\ I_{yx} & I_{yy} & I_{yz} \\ I_{zx} & I_{zy} & I_{zz} \end{pmatrix} \tag{6.9}$$

The Hessian matrix, therefore, describes the second order of intensity variation around each point of a 3D image. Since the second order information describes curvature, another way to think about it is that the Hessian matrix represents the local curvature of the data in a small neighbourhood surrounding each voxel (Voorn et al. 2013). Once the matrix is calculated, its eigenvectors describe the local principal directions of curvature, while the eigenvalues represent the magnitudes of the largest local contrast changes. The eigenvalues decomposition of the Hessian matrix can, therefore, be used to distinguish between blob-like, tube-like and plane-like features in the database.

Other steps of filtering, calibration and additional post-processing can be used to refine the results in order to reduce noise or emphasising high intensity values. Also, a connectivity MATLAB script is provided to improve the representation of the data, filtering the connected porous clusters throughout the sample in a certain direction. A complete description of the multiscale Hessian fracture filtering can be consulted on the original paper (Voorn et al. 2013) which also includes a user guide to use implementations and data processing steps in ImageJ.

6.4.4. Results

6.4.4.1. Features identification and volume rendering

Previously to any analysis, a region of interest (ROI) was applied to all image stacks to obtain well-defined and regular contours and volumes since samples were manually trimmed and thus, presented irregular shapes (Figure 6-19). Once the ROI was defined, the exterior of this region was set to Not a Number (NaN), so that it did not influence in the following analysis.

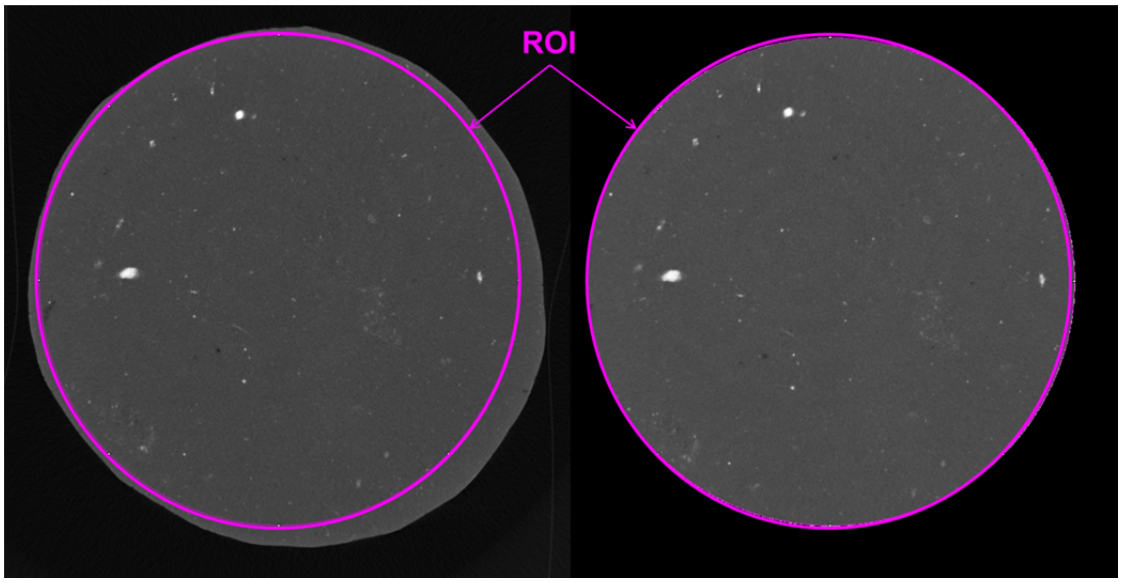

Figure 6-19. Slice before (left) and after (right) applying ROI.

Figure 6-20 presents three slices that corresponded to intact material and to samples after being tested with bedding planes parallel and normal to flow respectively. Differences between them could be readily observed: the intact sample presented a homogeneous aspect (except for calcium carbonate inclusions in white due to their higher density), whereas after the air injection tests some fissures were visible throughout the cross-section that was oriented along bedding planes. Hence, the presence of fissures induced by air migration, initially suggested by enhancement of

the entrance pore size at the macroscale in MIP results and afterwards, demonstrated with the fractal analysis, is now confirmed by image observations with this technique.

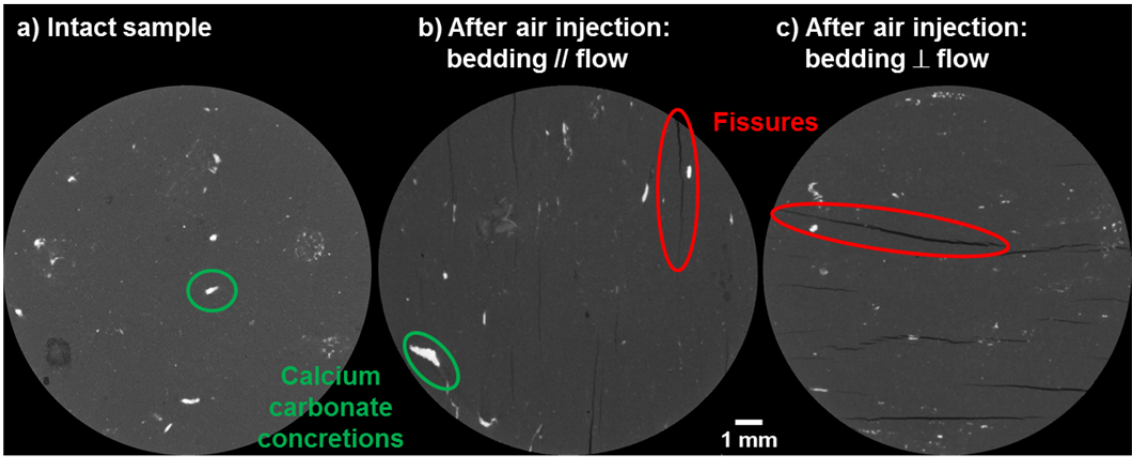

Figure 6-20. µ-CT images of intact sample (left) and after the air tests with bedding parallel (centre) and normal (right) to flow.

CT-value profile plots of the three samples highlight variations in density at the microscale which will be used to identify the parameters required in the fissure filtering analysis. Here, only a profile plot per sample is presented for the vertical middle section of the same slides as in the previous figure (Figure 6-21), but there is a good agreement along the stacks. The average CT-value was found around 10,000 in all the analysed profiles, which indicated homogeneous matrix in all samples. Higher CT-values correspond to denser minerals (mainly calcium carbonate concretions) whereas fissures present fairly lower values.

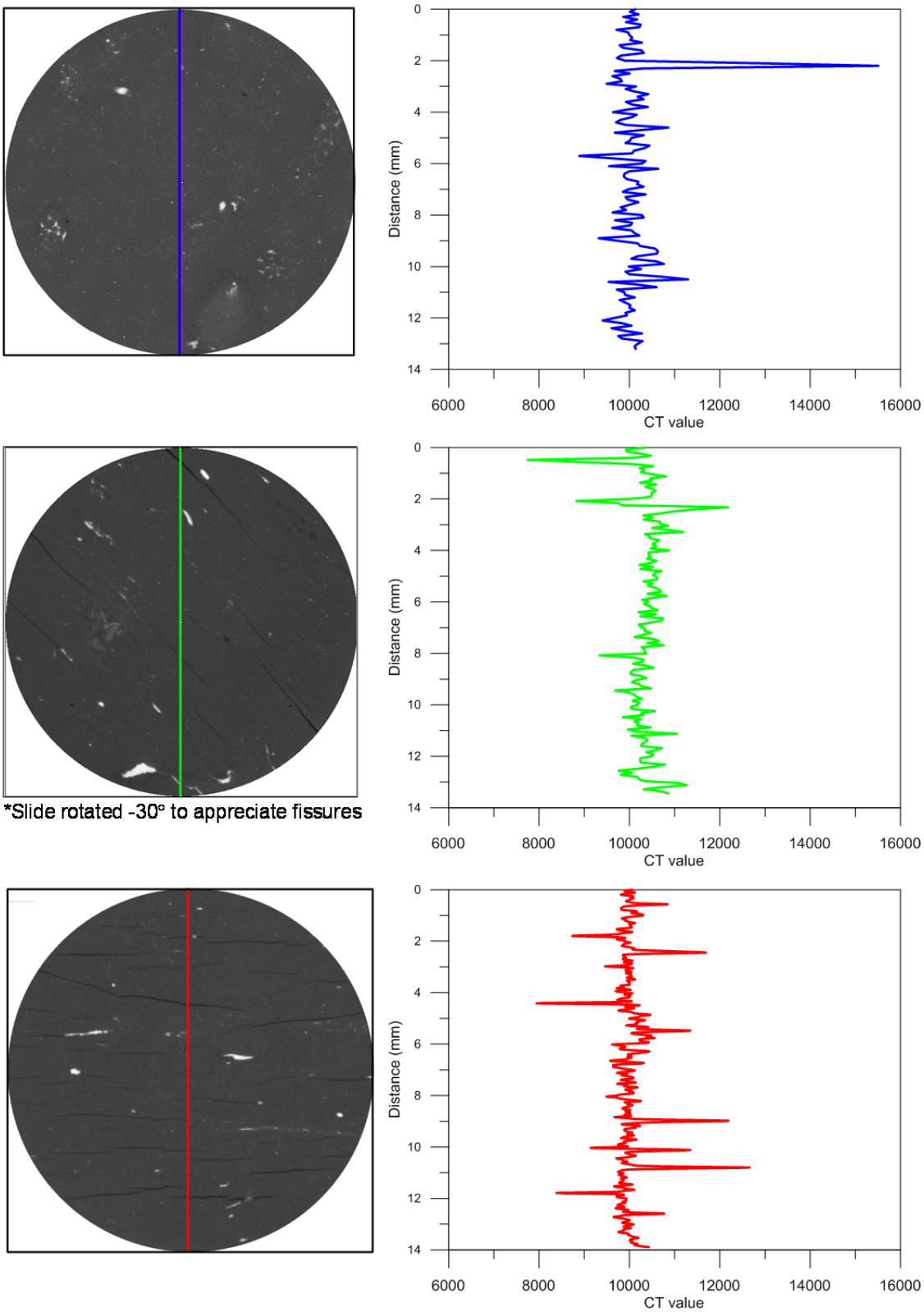

Figure 6-21. CT-values profile plots: intact sample (top); after gas injection with bedding parallel to flow (middle); and after gas injection with bedding normal to flow (bottom).

Volume rendering was performed with the 3D Viewer plugin using a trilinear interpolation. The following figures (Figure 6-22 to Figure 6-25) show the volume reconstruction for the intact sample and after air injection tests. Neither bedding planes

nor fissures are visible in the natural samples which indicate that, even though these natural discontinuities exist, they are initially closed or cannot be observed with the used techniques. In contrast, the fissure pattern is clearly visible in the volume reconstruction of samples after being tested mainly following the bedding orientation which is displayed in the figures together with the flow direction.

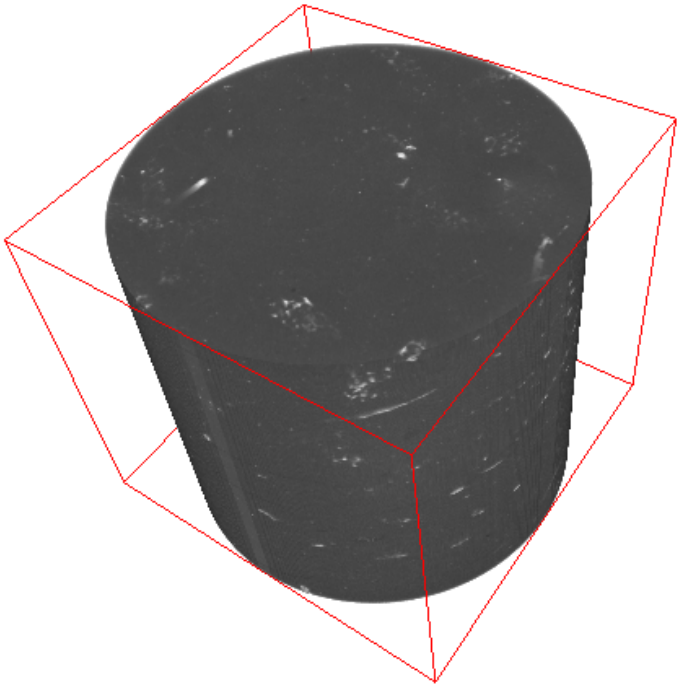

Figure 6-22. Volume reconstruction of intact sample with bedding planes normal to the sample axis.

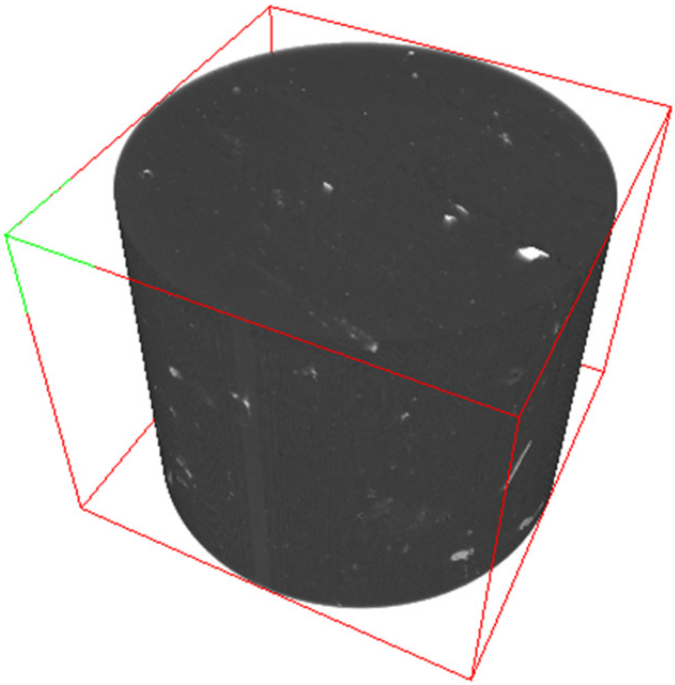

Figure 6-23. Volume reconstruction of intact sample with bedding planes parallel to the sample axis.

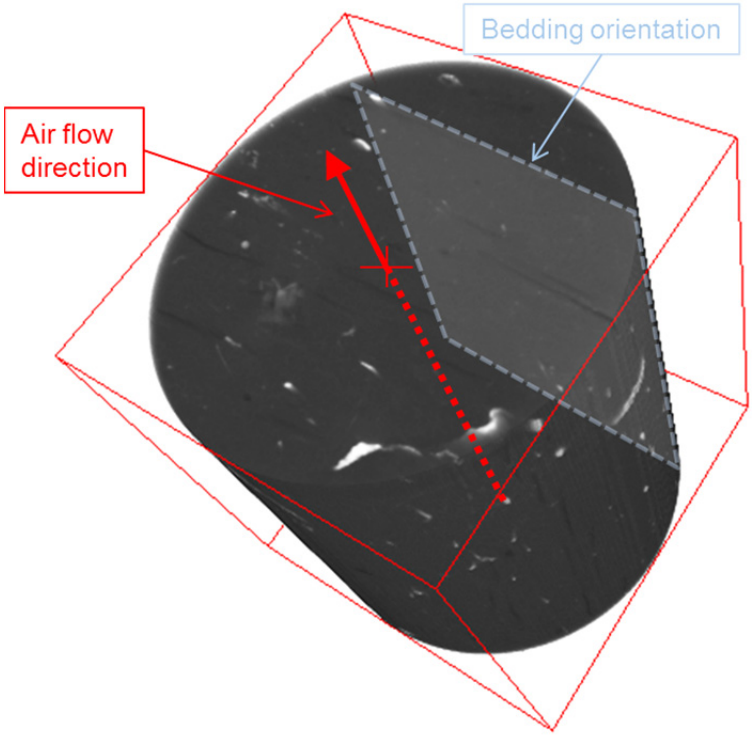

Figure 6-24. Volume reconstruction of the sample after air injection tests with bedding parallel to flow.

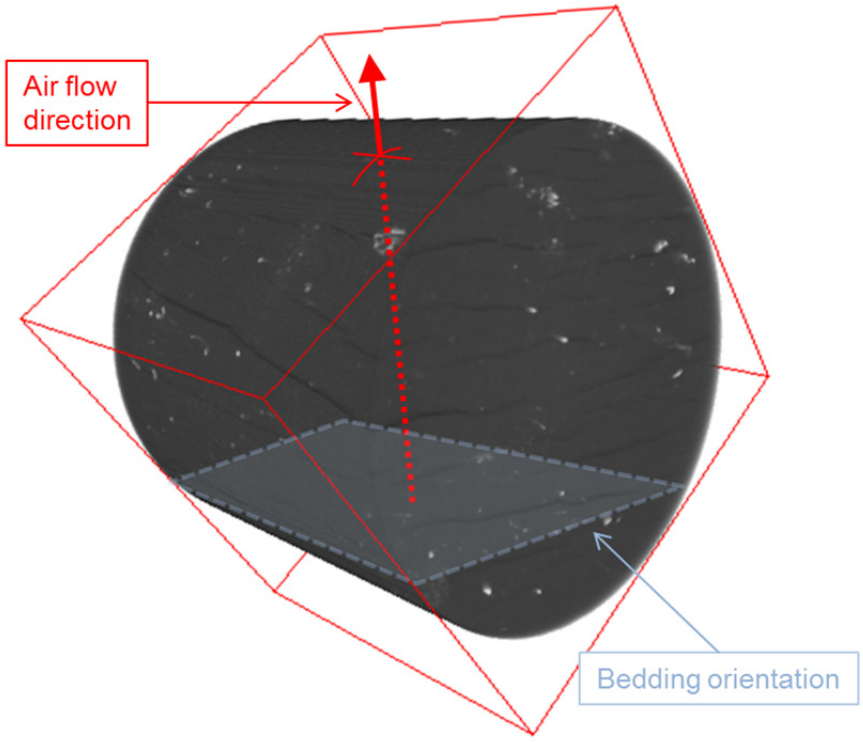

Figure 6-25. Volume reconstruction of the sample after air injection tests with bedding normal to flow.

6.4.4.2. Fissure filtering results

Images of samples after air injection were analysed with the multiscale Hessian fracture filtering (Voorn et al. 2013) in order to isolate the fissure network and hence, to quantify its volume and look for their connectivity. To apply it, it is firstly required defining a set of parameters which acts as threshold values in the different steps and are briefly described in Table 6-2. The last three are optional but improve the analysis.

Table 6-2. Parameters required for multiscale Hessian fissure filtering.

Parameter	Description
s_{min}	Minimum Gaussian smoothing scale: relates to the minimum aperture to detect (in pixels)
s_{max}	Maximum Gaussian smoothing scale: relates to the maximum aperture to detect (in pixels)
s_{step}	Steps between Gaussian smoothing scales: controls the intervals between the apertures to detect
$blocksize$	Blocksize in amount of slices: amount of data to be analysed per consecutive step in order to compensate for lack of RAM memory (if it is enough it will be the total number of slides)
$avgmat$	Average material greyscale: CT-value which characterises the material outside the fractures
$consthresh$	Conservative threshold of fractures: estimates the greyscale value present in the fractures
$maxmat$	Maximum material grey scale: removes bright spots in the dataset to prevent artefacts in the final output

Parameters s_{min} and s_{max} were defined taking into account the aperture in pixels of a representative number of fissures. Figure 6-26 shows one of these measurements. Parameter s_{step} was chosen equal to one in order to run the entire set of Gaussian scales; while $blocksize$ was the total number of slides since there were enough RAM memory in the computer.

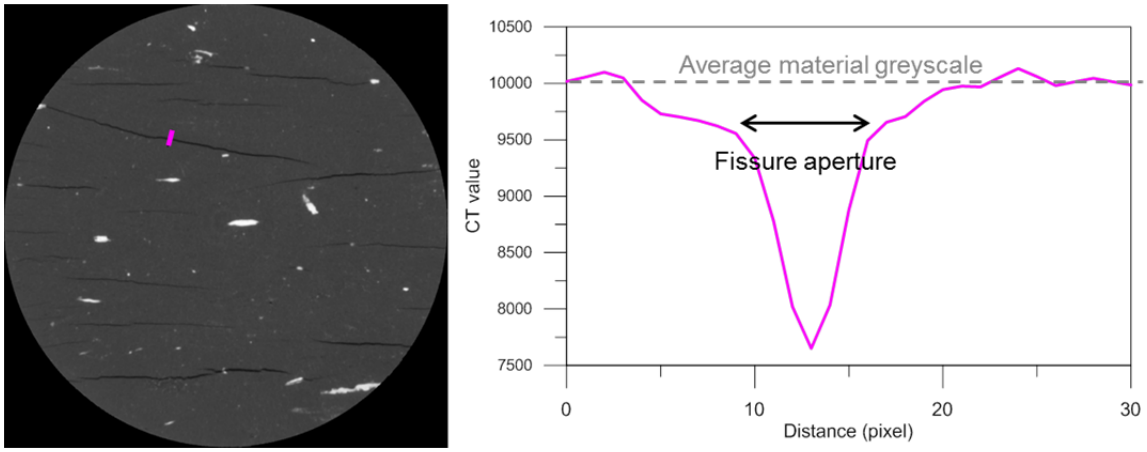

Figure 6-26. The aperture of a fissure measured in pixels.

As mention in the previous section, numerous profile plots in different slides were used to calculate the average material greyscale parameter, $avgmat$, given a value of 10,000 for both samples (see Figure 6-21). These plots also served to obtain $matmax$ value as a threshold parameter which permits deleting the brighter pixels. Although it is optional, in our dataset, is important to use it because there are several white areas that can be confused with fissures in the filtering process. Remember that the Hessian

matrix represents variations of local curvature of the data in a small neighbourhood surrounding each voxel, so it would identify the changes of curvature whatever from brighter to darker or vice versa. Thereby, $matmax$ was set in 10,600. Finally, $consthresh$ was selected as the greyscale inside the fissures, given a CT value of 9,000.

Obviously, the selection of these parameters introduces some ambiguity in the analysis. There is no a single answer on how to choose them, and it is depending on the desired results (Voorn et al. 2013). Several analyses were run changing parameters, but discussion about their sensitivity is out of the scope of this Thesis, and therefore, only the best approach is shown (less noisy and more accuracy).

The different steps of the multiscale Hessian fracture filtering: preparation, filtering, and calibration; were performed following the original paper. Figure 6-27 and Figure 6-28 show one slide of each sample before (input image) and after the filtering process. The 3D volume reconstruction of the fissure pattern is shown in Figure 6-29 and Figure 6-30 jointly with it overlapped with the 3D volume of the original input stack of images for samples on both orientations. As can be observed in the figures, it is reasonable to believe that gas flow occurs through preferential pathways which are developed taking advantage of the bedding, though initially closed, still a weakness within the clay matrix.

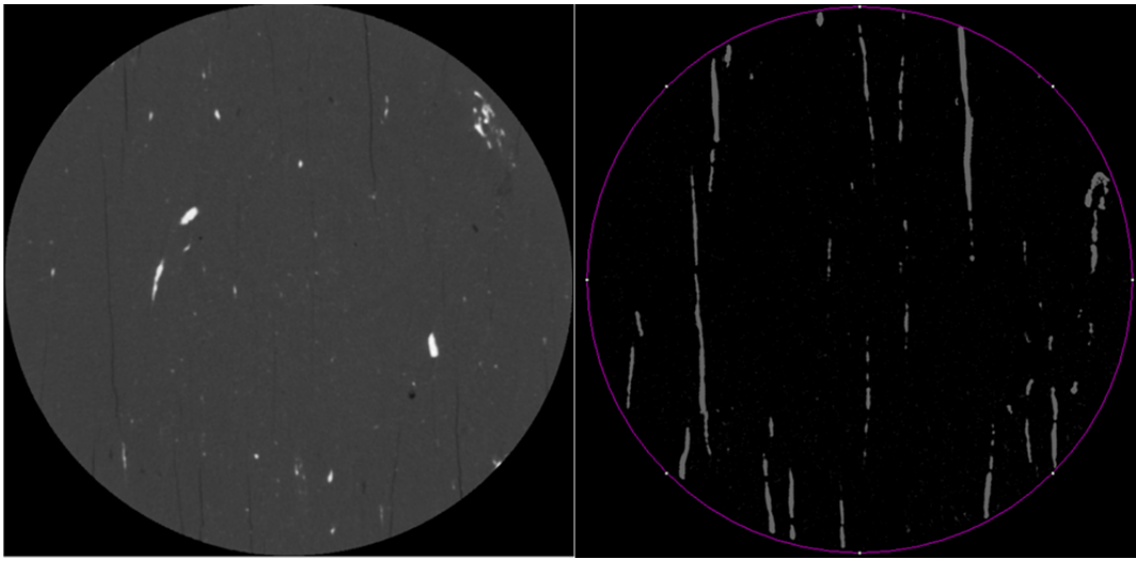

Figure 6-27. Original input image (left) and after filtering process (right) for the sample with bedding parallel to flow.

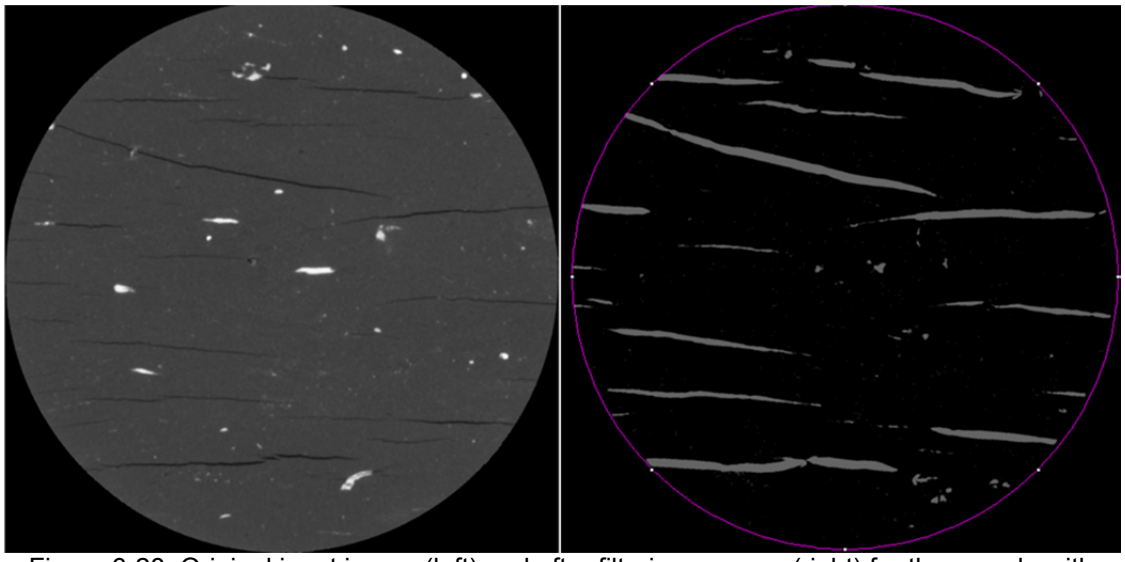

Figure 6-28. Original input image (left) and after filtering process (right) for the sample with bedding normal to flow.

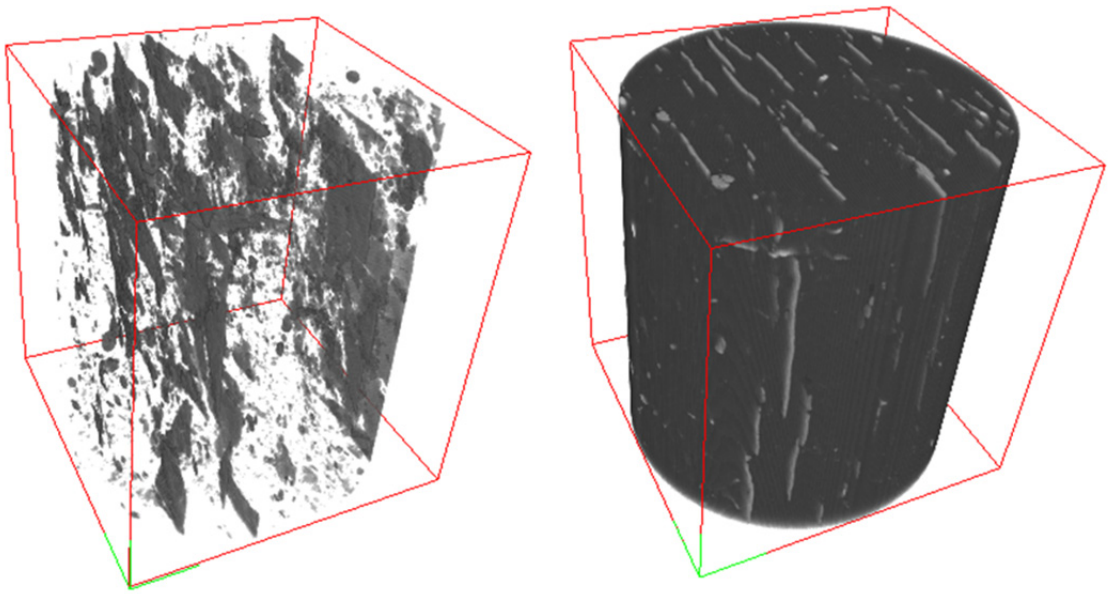

Figure 6-29. 3D reconstruction of the fissure pattern after filtering process (left) and overlapped to the 3D volume of the input stack (right) for the sample with bedding planes parallel to flow.

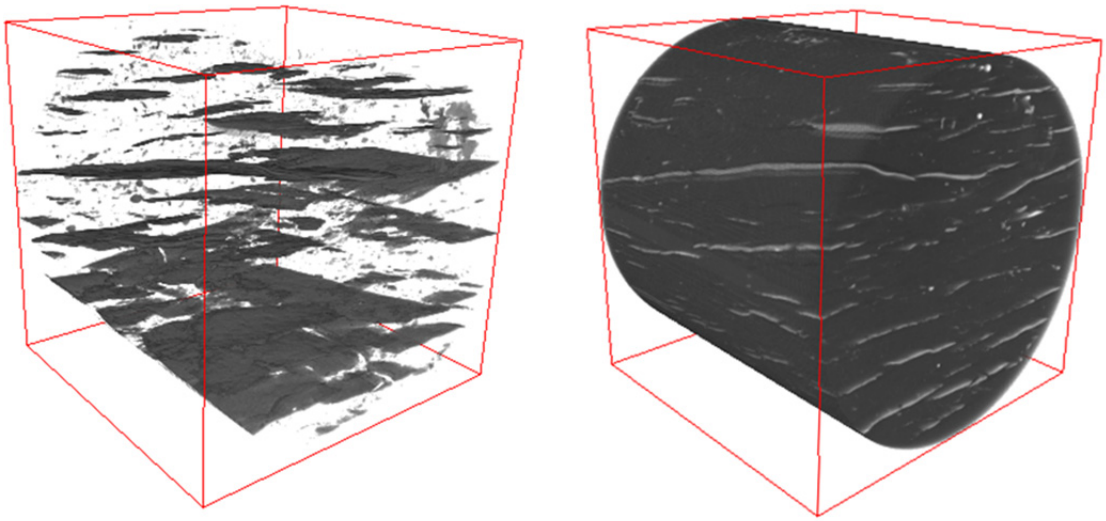

Figure 6-30. 3D reconstruction of the fissure pattern after filtering process (left) and overlapped to the 3D volume of the input stack (right) for the sample with bedding planes normal to flow.

The Hessian fracture filtering also provides the potential to obtain the connectivity of the fissure pattern throughout the sample in the direction orthogonal to the slides. This is the reason why only connectivity of sample with bedding parallel to flow can be obtained. Sample with bedding normal to flow was decided to be prepared so as the fissures were seen in the plane of the slides, renouncing to investigate the connectivity in that disposition.

Figure 6-31 shows the 3D reconstruction of the connected fissures in the sample after the connectivity filtering (left) together with the entire fissure volume (middle) and also, overlapped to the volume of the sample (right). It can be observed that only a small fraction of the volume is connected. Nonetheless, it stands to reason that the vast majority of fissures were connected during the air passage (expansion of the sample) and afterwards, during the dissipation stage, fissures closed up according to the recorded compression. Yet, they did not close completely and consequently, it can be asserted that air migration in Boom Clay produces irreversible damage.

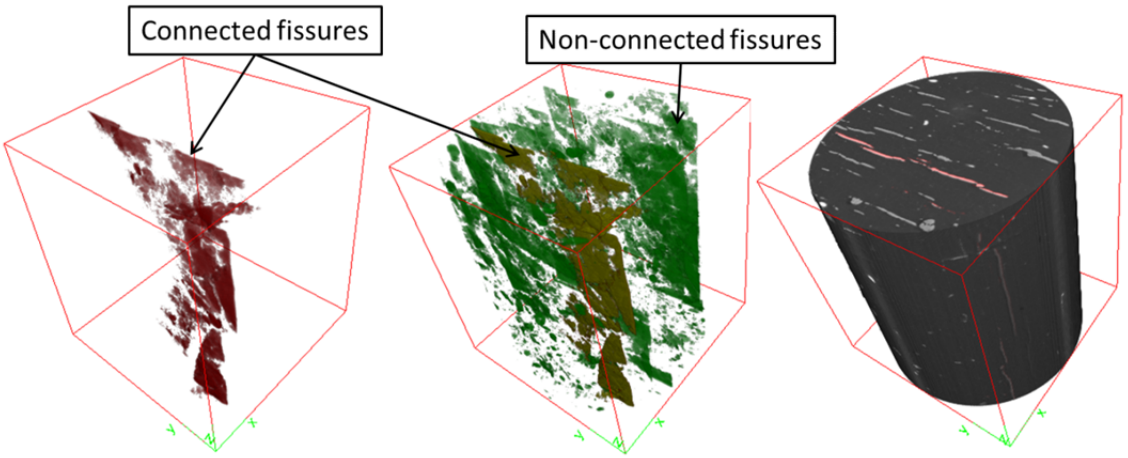

Figure 6-31. 3D reconstruction of the connected fissure pattern after connectivity filtering (left); connected and non-connected fissure pattern (middle); and fissure pattern overlapped to the 3D volume of the input stack (right) for the sample with bedding planes parallel to flow.

On the basis of the 3D volume reconstruction, it is possible to obtain the total volume of the fissure network using 3D Object Counter plugin as well as the corresponding to the connected fissures. Table 6-3 lists these volumes. For the sample with bedding parallel to flow, the fissured volume resulted in 34.5 mm^3, of which only 8.6 mm^3 were connected. The total volume of the analysed sample was 1924 mm^3 (volume of solids: 1233 mm^3). As observed, only 25% of the fissures were connected. Differently, fissured volume of sample with bedding planes normal to flow was inferior, 14 mm^3, for a total volume of 1600 mm^3 (volume of solids: 1020 mm^3).

Table 6-3. Volumes of fissure and sample

Volumes	Sample with bedding // flow	Sample with bedding ⊥ flow
$V_{total}\ (mm^3)$	1924.6	1595.54
$V_{fissures}\ (mm^3)$	34.45	13.92
$V_{connected\ fissures}\ (mm^3)$	8.59	

Additionally, µ-CT scan images were used to obtain measurements of fissure aperture and their separation (distance between consecutive fissures). Due to the large amount of data (many fissures in each slide), a statistical distribution of the aperture and the distance are shown in Figure 6-32 and Figure 6-33 respectively for both samples. The aperture was calculated as the double of distance from the geometric centre of the fissure to the surface's pixels since the width is not constant. Average aperture turned out to be 90 µm for the sample with bedding parallel to flow while after test with bedding planes normal to flow, the mean aperture was 153 µm. Regarding the separation which followed a normal distribution, its average values were 410 and 558 µm for each one.

It can be noticed that fissures of the sample with bedding parallel to flow are closer and narrower than in the case of bedding normal to flow. That seems logical since in the former air paths can easily develop due to the favourable orientation, yet, in the latter, air must open pathways going through from one bedding plane to another. This fact implies that, on the one hand, while the connections between each plane are not established, the air will accumulate in one plane, so the aperture will be larger (consistent with higher expansion recorded in the tests). On the other hand, it is highly probable that once the connection was established, air could skip some of the planes because they are not perfectly parallel (see Figure 6-28). However, connectivity filtering on the sample with bedding in this orientation was not possible due to its features, hence, further tests are necessary to study this issue.

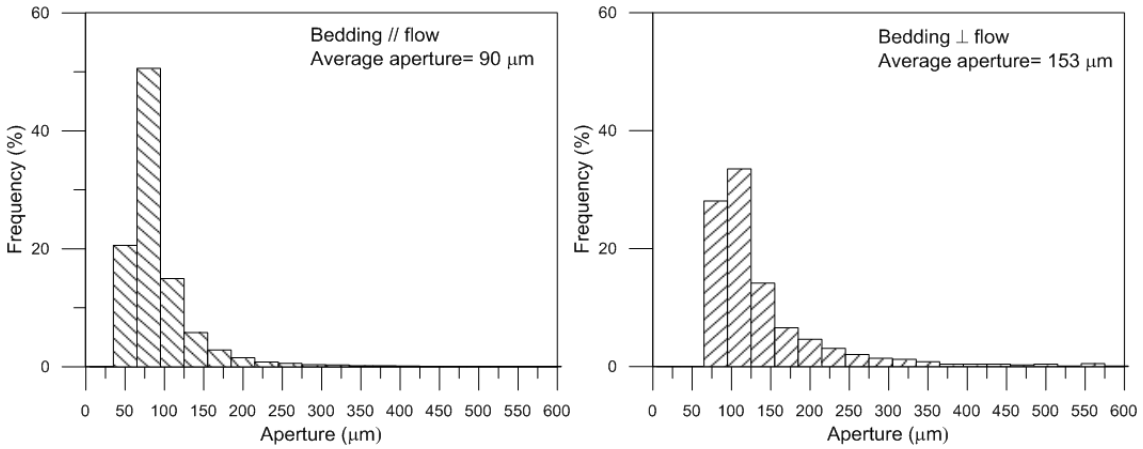

Figure 6-32. Frequency of fissure aperture for both samples: with bedding parallel to flow (left) and bedding normal to flow (right).

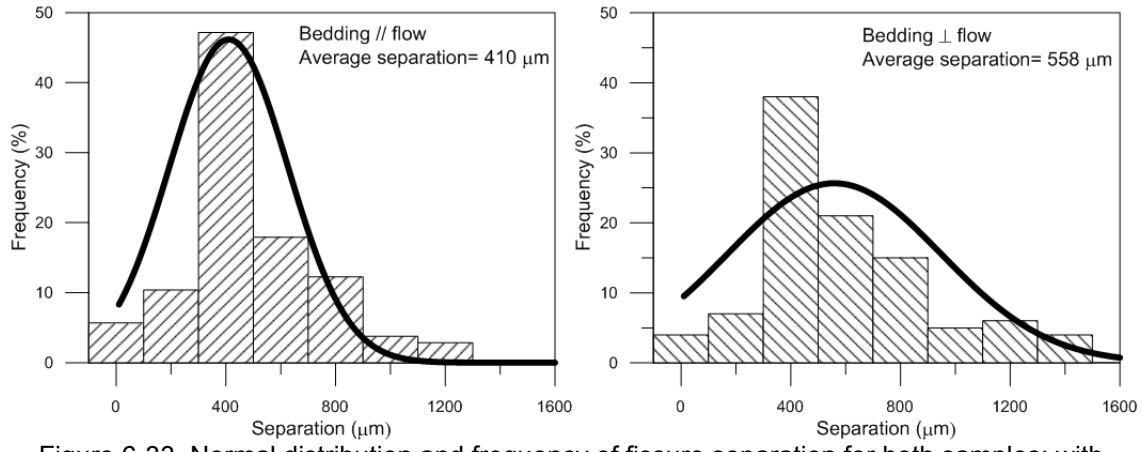

Figure 6-33. Normal distribution and frequency of fissure separation for both samples: with bedding parallel to flow (left) and bedding normal to flow (right).

6.5. Quantitative comparison of the techniques

The three different techniques used for tracking the evolution of the microstructure provide useful information about preferential pathways induced by the air migration. Therefore, it is worth comparing the obtained results.

6.5.1. Fissure features: aperture and separation

Experimental information on aperture and separation of fissures induced by air migration in argillaceous materials is still very poor, but for the study presented by Harrington et al. (2012) dealing with gas-induced pathways using a nanoparticle injection technique in Boom Clay samples. It showed that the minimum aperture of the pathways (usually developed parallel to bedding) was typically between 0.5 and 4 μm (though up to 10 μm) which, indeed, were the size of the transported nanoparticles, still there are not quantitative data about the real size of the apertures during the transport process. Moreover, the air pressure in these experiments was larger than the confining pressure and thus, these data must be taken with caution because the air transport mechanisms could differ from the ones of concern in this study.

Providing experimental measurements on fissure aperture and separation seems to be a clear necessity since they are used as parameters in numerical models such the proposed by Olivella & Alonso (2008) or Gerard et al. (2014) in which fracture aperture controls the coupling between the mechanical and the hydraulic response but the exact geometry, thickness and number of pathways is unknown. While the hydro-mechanical model leads to convincing numerical results, they remain arbitrary, dependent on the definition of the initial fracture geometry. The paucity of data limits further development and validation of these models, and thus, the importance of using microstructural techniques that could help to place quantitative values on such parameters. Table 6-4 presents some examples of values given to these fissure parameters obtained by calibration of the model: initial aperture (b_0), maximum aperture (b_{max}) and separation (a) but some of these are not explicitly indicated.

Nevertheless, there are others numerical approaches for damaged rocks as the reported in Arson & Pereira (2013) which relates permeability to porosity measurements though pore size distribution curves. The PSD curves are updated with strains and damage and thus, the only material parameters that are required to describe the microstructure are the lower and upper bounds of the pores size for both natural pores and cracks.

Table 6-4. Fissure aperture and separation values used in numerical modelling

Publication	Material	b_0 (μm)	b_{max} (μm)	a (μm)
Olivella & Alonso 2008	Opalinus Clay	0.1	-	600
Arnedo et al. 2008	Sand/bentonite	0.1		-
Arnedo et al. 2013a	Tertiary Mudstone Norwegian Shelf	0.001	0.3 - 0.5	-
Gonzalez-Blanco et al. 2016	Boom Clay	0.1	0.5	30
Romero et al. 2016	Ypresian clay	0.7		95

Table 6-5 shows fissure aperture (b) and separation (a) values experimentally obtained with the three techniques. It must be taken into account that the measured aperture is in between the initial and the maximum aperture of the generated pathways during gas migration, since it is expected that the fissures closed up during the air pressure dissipation (samples underwent compression during this process). In fact, in view of the results of this investigation, it can be considered that the bedding aperture, initially very small or closed, corresponds with the initial aperture. As a result, dominant entrance pore size of the intact material is considered to be representative of the bedding aperture and thus, the initial aperture. In the case of intact samples of Boom Clay, this value is of the order of 0.1 μm (exactly 70 nm). Another factor to consider when regarding the experimental results is the different resolution of the techniques. With MIP and FESEM apertures of 1 μm can be detected. Actually, changes in entrance pore size distribution with respect the intact sample where detected above 2 μm, and measured apertures in FESEM images were lower than 10 μm. On the other hand, in μ-CT images, the pixel size is 20 μm, and therefore, to detect a fissure with this technique it should be larger than 2 or 3 pixels which means 40 or 60 μm. That is why the fissure aperture and also the separation, obtained with this technique are larger. In reality, there are narrower fissures that are not detected and consequently the distance between them should be shorter. Besides, values presented in the table are average values (see Figure 6-32 and Figure 6-33).

Table 6-5. Fissure aperture and separation values.

	MIP	FESEM	μ-CT
Aperture: $b\ (\mu m)$	> 2	3 - 10	$90^{//}$ - $150^{\perp}$
Separation: $a\ (\mu m)$	-	150 - 270	$410^{//}$ - $560^{\perp}$

$^{//}$ Average value for the sample with bedding parallel to flow; $^{\perp}$ Average value for the sample with bedding normal to flow.

In view of thereof and taking into account the observations mentioned above, obtained results turn out to be rather consistent and reliable. Comparing them with the calibrated parameters presented in Table 6-4, the initial aperture is, in general, in good

agreement with the dominant pore mode of the intact materials. However, maximum aperture seems to be too low as well as the majority of separation values. This fact will be further analysed in Chapter 7 because it is related to how this kind of embedded fracture models works. The law which controls the intrinsic permeability is very efficient with the fracture aperture, and therefore maximum aperture must be limited.

6.5.2. Fissured volume and final degree of saturation

Both MIP and μ-CT techniques supplied quantitative data of the volume of fissures. As previously indicated, fissures in MIP curves were considered above entrance sizes larger than 2 μm, whereas μ-CT voxel resolution was limited to 20 μm. For that reason, only fissures larger than 20 μm were considered to obtain comparable results between both techniques.

A fissured void ratio ($e_{fissured}$) defined as the area below the pore size distribution curve (see Figure 6-34), was used to quantify the volume of fissures (respect to the volume of solids) induced by air migration with MIP results. This fissured void ratio was normalised with respect to the total void ratio (e). Then, a relationship that established the proportion of fissured material can be set as $e_{fissured}/e$. This ratio was useful to provide information on the expected value of the final degree of saturation of the clay after the air tests, $S_r = 1 - e_{fissured}/e$, when all fissures were desaturated (and clay matrix pores were still saturated). Final degree of saturation of sample with bedding planes parallel to flow of 0.932 and 0.953 could be estimated when all fissures larger than 2 μm and 20 μm, respectively, were desaturated. In the case of sample with bedding normal to flow these values are slightly higher, given 0.949 and 0.962.

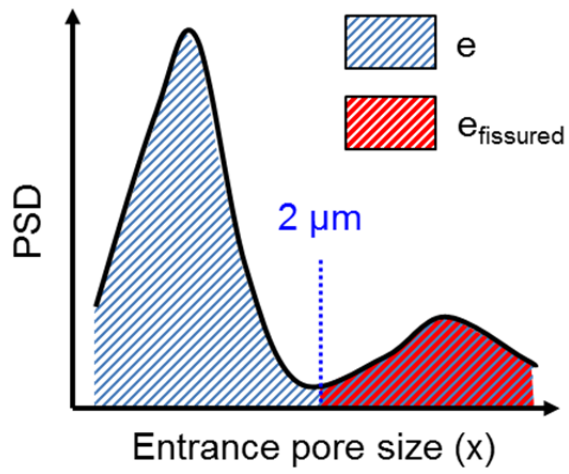

Figure 6-34. Scheme of how to obtain the fissured void ratio.

The volume of the fissures (x>20 μm) obtained after the filtering process of the μ-CT images were also analyse in terms of $e_{fissured} = V_{fissures}/V_{solids}$. Again, the normalisation with respect to the total void ratio permits to calculate the final degree of saturation after the tests. As a result, S_r=0.950 was estimated for sample with bedding parallel to flow assuming the desaturation of all the fissures, and 0.988 if only connected fissures larger than 20 μm were desaturated. For sample with bedding planes normal to flow, the final degree of saturation was 0.976 accounting the desaturation of all fissures.

A good consistency is observed in Table 6-6 for $e_{fissured}$ when comparing both techniques at the same range of fissure sizes (x>20 μm) for sample with bedding planes parallel to flow. Results for sample with bedding plane normal to flow differ somewhat among both techniques. It would appear that there is some loss of information in the images of the μ-CT with respect to the connectivity of the fissures that might be the cause of that difference.

Table 6-6. Fissured void ratios and final degree of saturation using MIP and μ-CT results.

Sample	Technique	$e_{fissured}$	$e_{fissured}/e$	S_r
Bedding // flow ($e = 0.560$)	MIP (x>2 μm)	0.038	0.068	0.932
	MIP (x>20 μm)	0.026	0.047	0.953
	μ-CT (x>20 μm, all fissures)	0.028	0.050	0.950
	μ-CT (x>20 μm, connected fissures)	0.007	0.012	0.988
Bedding ⊥ flow ($e = 0.563$)	MIP (x>2 μm)	0.029	0.051	0.949
	MIP (x>20 μm)	0.021	0.038	0.962
	μ-CT (x>20 μm, all fissures)	0.014	0.024	0.976

6.6. Effects of fissure opening in air transport properties

Experimental data collected from air injection experiments and microstructural analysis are interpreted together, with the goal of better understanding the Boom Clay behaviour during the gas migration.

It seems now clear that the passage of air causes some damage in the samples, opening the macrostructure. Previous analysis of fractal dimension showed that this opening has a fissure-like shape and FESEM and μ-CT images have confirmed it. There is also evidence of fissure opening by direct observation of some of the samples after dismantling because of its desaturation (Figure 6-35); whereas the matrix of the clay which presented a darker colour seemed to be fully saturated. It was noticeable that some of the fissures formed pathways, but other were not completely developed.

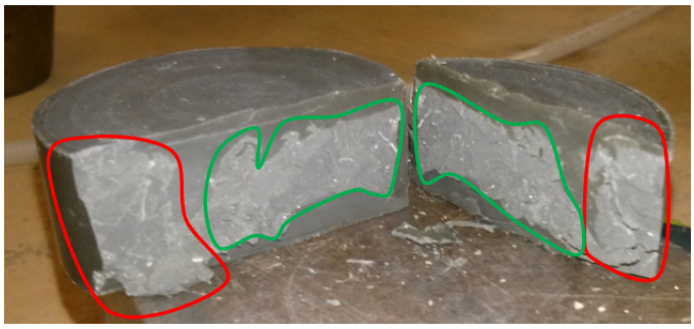

Figure 6-35. Detail of fissure desaturation in a post-mortem sample after air injection test.

MIP data were processed according to procedure explained in Section 6.2.1 to obtain the water retention curves of intact samples and after being tested (Figure 6-36) with the aim of checking the final degree of saturation obtained in the previous section as well as examining the variation of the air entry value due to the development of the fissure pattern. After air injection tests, the clay presented a degree of saturation between 0.89 and 1 being the values obtained with MIP and μ-CT data in between this range (see Table 6-6). In addition, and crucially, the air entry value (P_0) dropped substantially. Rather than using van Genuchten's equation to evaluate it, dominant entrance pore size was employed. Air entry value was found to be around 100 nm for the intact samples (mono-modal distribution); while for samples after air injection, which present a bi-modal distribution, the dominant entrance pore size was considered the largest one (around 30-50 μm). Figure 6-37 presents the air entry values against the dominant void ratio normalized by the total one. It clearly shows the remarkably change in the air entry pressure after the air migration.

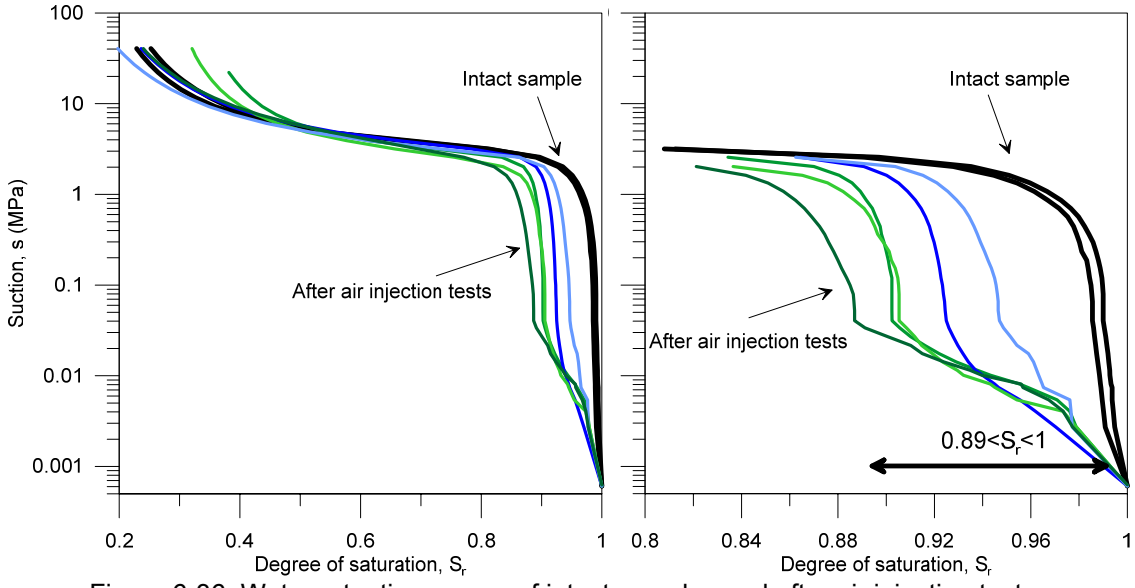

Figure 6-36. Water retention curves of intact samples and after air injection tests.

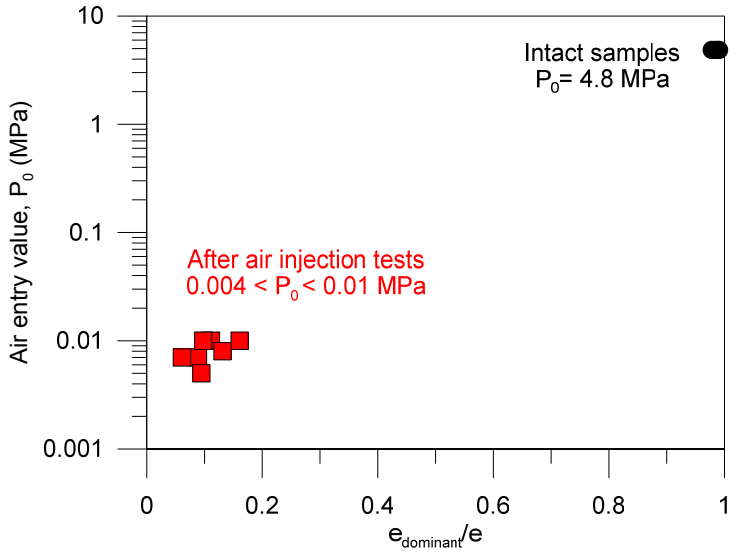

Figure 6-37. Air entry value determined with the dominant entrance pore size.

Gathering all these information, it seems now clear that intrinsic permeability to air is controlled by the opening of fissures. As suggested in Chapter 5 Section 5.2.4, intrinsic permeability is affected by deformational response during air injection and dissipation and consequently, two-phase flow models cannot explain its large variations with a small porosity changes (see Figure 5-22 and Figure 5-23). Consequently, intrinsic permeability to air is expressed in terms of the proportion of fissured material (the above defined ratio $e_{fissured}/e.$) instead of being a function of the total porosity. Figure 6-38 relates it with $e_{fissured}/e$ calculated with MIP data for sizes larger than 2 μm, whereas Figure 6-39 contains information of MIP and μ-CT for sizes larger than 20 μm. Either way, the analysis shows that the highest the proportion of fissures is, the highest the intrinsic permeability to air is obtained. For both cases, the exponential fittings of the experimental data, Equations 6.10 and 6.11 respectively, reflect the dependency of the intrinsic permeability with the opening of fissures during gas migration.

$$K = 3.6 \cdot 10^{-19} \exp(10.2 \cdot e_{fissured}/e) \;\; if \;\; e_{fissured} > 2\mu m \qquad (6.10)$$

$$K = 3.9 \cdot 10^{-19} \exp(10.4 \cdot e_{fissured}/e) \;\; if \;\; e_{fissured} > 20\mu m \qquad (6.11)$$

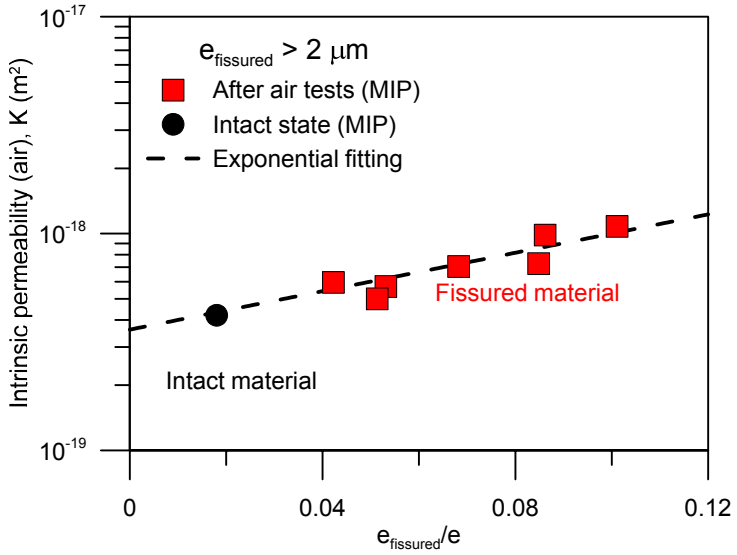

Figure 6-38. Variation of intrinsic permeability to air with fissured ratio (fissures larger than 2 μm detected with MIP).

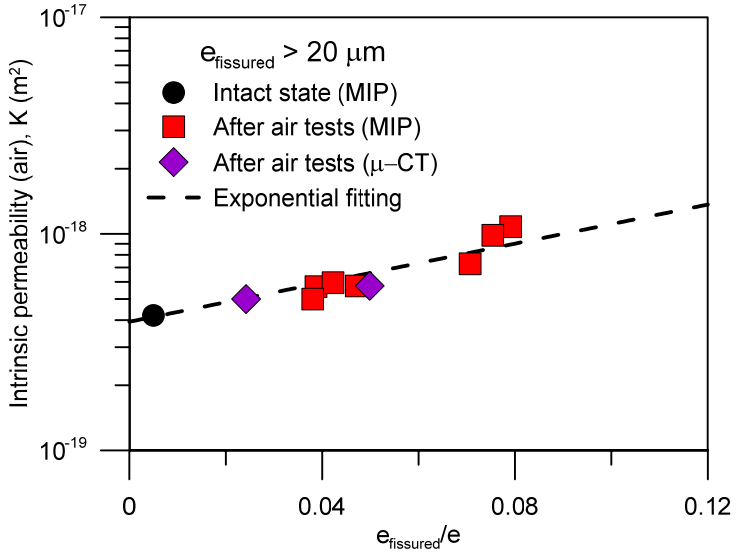

Figure 6-39. Variation of intrinsic permeability to air with fissured ratio (fissures larger than 20 μm detected with MIP and μ-CT).

6.7. Concluding remarks

Air injection/dissipation experiments systematically displayed expansion strains that induced damage on the material and it was expected the opening of preferential air pathways (fissures). These fissures played a major role on the dissipation stage, in which the air injection pressure started to decline with a sharp increase in the outflow air volume. Microstructural techniques provided crucial information regarding this matter and confirmed the opening of these stress-dependant pathways.

Three different microstructural techniques were used to analyse the changes in the pore network before (on intact material) and after the air test in Boom Clay, namely

mercury intrusion porosimetry (MIP), filed-emission scanning electron microscopy (FESEM) and micro-computed tomography (μ-CT). For indurated clays, only MIP tests were performed. However, these results presented the same tendency as the Boom Clay ones and therefore similar behaviour is expected. Henceforth, the text will refer to Boom Clay.

MIP provided information on the entrance pore sizes and the distribution of the pore space (pore size density function), which resulted in the detection of a new family of pores at entrance sizes larger than 2 μm after the air passage. The technique also allowed the quantification of the volume of fissures larger than 2 μm. A fractal analysis of the mercury intrusion data confirmed this fissure-like structure after the air test. In order to discern the effects due to the air migration from the ones due to the unloading, MIP tests were carried out in samples after non-injection tests. The microstructure was not modified after undrained unloading, conversely, drained unloading induced an opening of the porosity as the macroscale, similar to the caused by the air injection process.

FESEM images clearly showed fissures after the tests, not observed in the intact sample. Distances between consecutive fissures following the same direction were measured in the images ranging between 150 and 270 μm. With increasing magnification, also fissure apertures were quantified, given values of 3.6 and 10 μm, comparable with MIP results.

μ-CT images also confirmed the existence of fissures after the air tests and, as expected, they followed the orientation of the bedding planes which were initially closed or with apertures not detectable with this technique. Image analysis through multiscale Hessian fracture filtering allowed the quantification of the volume of fissures after the air tests. A statistical distribution of their aperture and separation was obtained in the analysis. Fissures on the sample with bedding orientated parallel to the air flow direction were narrower and closer than the developed in the sample with bedding orientated normal to the flow. Apart from this, the fissure pattern of the sample with bedding parallel to flow was analysed in terms of its connectivity. Only the 25% of the fissures were connected at the end of the test. Nonetheless, the vast majority of fissures should have been connected during the air passage (expansion of the sample) and afterwards, during the dissipation stage, fissures closed up according to the recorded compression.

When comparing data obtained with these techniques, in terms of fissured void ratio, a general good agreement was found. This information was useful to provide the

expected values of the degree of saturation of the clay after the air tests which were consistent with the measured.

Finally, changes in air transport properties as the air entry pressure or the intrinsic permeability were evaluated before and after injection tests. The opening of fissures clearly modified these parameters, considered constant in classic two-phase flow models. The air entry value presented a drastic reduction whereas the intrinsic permeability was larger than the measurements obtained with water flow. Intrinsic permeability to air is then greatly affected by the proportion of fissures in terms of the total pore volume ($e_{fissured}/e$) and an exponential relationship appears to fit these experimental observations.

7
NUMERICAL SIMULATION OF THE RESULTS

7.1. Background on modelling gas migration

Modelling gas injection experiments is a challenging task and involves several aspects. The main objective of the tests' simulations is to better understand the coupled hydro-mechanical consequences of the gas flow passage through the material by analysing the deformational response recorded in the experimental tests.

In most cases, the used models to simulate gas migration processes are based on the concept of two-phase flow through continuous porous media. Stress-dependent porosity and permeability are often used as a way to better reproduce rapid increase of gas flow above a threshold injection pressure (Senger et al. 2014). Other approaches suggest to couple explicitly two-phase flow transport models with poro-mechanics models (Yamamoto et al. 2015; Fall et al. 2014) to better take into account the role of the evolving stress field. The latter models are claimed to better reproduce the effect of pathway dilation on gas transport at the relevant scale of the system. The Two-Part Hooke's Model (TPHM) has been used as a possible alternative, which assumes that sedimentary rocks can be thought as a superposition of 'soft' and 'hard' parts (Liu et al. 2009; H. H. Liu et al. 2011). The model applied to a layered structure is conceived with soft layers undergoing relatively large strains, thus, showing higher permeability, and hard layers, which undergo small strains (Senger et al. 2015). To take into account material anisotropy and the possible presence of preferential gas transport pathways along a given orientation, other authors used embedded fracture permeability models or added joint elements to a continuum model (Arnedo et al. 2013a; Gerard et al. 2014). In many cases, the experimental data could be reproduced reasonably well by the previous approaches for what concerns gas pressure evolution. On the contrary, the deformational behaviour during the gas transport process has been seldom tackled.

In this work, an embedded fracture model in a fully coupled hydro-mechanical approach was adopted to simulate the gas injection tests on Boom Clay. The coupled solution of the mechanical and two-phase flow equations is performed using finite elements with Code_Bright (Olivella et al. 1996). The adopted approach for gas and

water flow through discontinuities including mechanical interactions was described and demonstrated on some synthetic cases in Alonso et al. (2006) and in Olivella & Alonso (2008), and afterwards applied to some experimental results on sand/bentonite Arnedo et al. (2008) and claystone Arnedo et al. (2013).

Initially, a simplified geometry of the problem was selected to confirm the usefulness and validity of the selected constitutive model. This first approximation was still able to capture the consequences of preferential path development. The sample was modelled by two zones having different hydraulic properties: the matrix and the zone of fracture development (ZFD) in which the dominant advective flow of gas occurs. In the choice of the latter, a single predefined central zone was chosen, renouncing to investigate the local distribution of the fractures, but still keeping the possibility of reproducing the global effect of the localised preferential paths on the sample response. For the matrix and the embedded fracture zone, the same mechanical parameters were chosen, but different hydraulic models were used.

The embedded fracture permeability model permits to track the degradation of the soil sample under gas pressurisation (increasing gas permeability) and helps in the comprehension of the local coupled processes dominating the response of the material. However, realistic modelling in a more general geometric configuration can be achieved only by integrating the embedded fracture model in all the elements. Therefore, in a second stage of the numerical analysis, a step forward was done introducing the heterogeneity of the material through random porosity field that allows heterogeneity to automatically develop fracture patterns, without the need for a pre-defined fracture zone.

7.2. Numerical formulation

The finite element code CODE_BRIGHT (Olivella et al. 1996) allows solving thermo-hydro-mechanical boundary values problems in porous media. In the most general case, five coupled equations can be considered: the mass balances of solid, water, and air, the balance of energy and the equilibrium equations. For problems involving less coupling, a reduced number of equations can be solved.

7.2.1. Balance equations

In this section, only a brief description of the formulation presented in (Olivella et al. 1996) for unsaturated media is accomplished. For the simulations performed in this chapter, an unsaturated porous medium constituted by solid grains, water, and air is assumed, since the soil underwent some desaturation throughout the air injection stage. Hydraulic and mechanical aspects are considered and the coupling between

them in all possible directions is taken into account (thermal effects do not take part of the problem although the code can take into account them). In this way, three species are considered: mineral, water (w) and air (a) which are presented in three different phases: solid (s) - mineral -; liquid (l) - water and dissolved air - and gas (g) -air-.

The solution of a coupled THM problem requires the simultaneous solution of the following balance equations

- *Solid mass balance:*

$$\frac{\partial}{\partial t}\left(\rho_s(1-\phi)\right) + \nabla \cdot (\boldsymbol{j_s}) = 0 \qquad (7.1)$$

- *Water mass balance:*

$$\frac{\partial}{\partial t}(\omega_l^w \rho_l S_l \phi) + \nabla \cdot (\boldsymbol{j_l^w}) = f^w \qquad (7.2)$$

- *Air mass balance:*

$$\frac{\partial}{\partial t}\left(\omega_l^a \rho_l S_l \phi + \omega_g^a \rho_g S_g \phi\right) + \nabla \cdot \left(j_l^a + j_g^a\right) = f^a \qquad (7.3)$$

- *Momentum balance for the medium:*

$$\nabla \cdot \boldsymbol{\sigma} + \boldsymbol{b} = 0 \qquad (7.4)$$

where ϕ is the porosity; ρ_α the density; ω_α^i is the mass fraction; S_α the degree of saturation; $\boldsymbol{j^i}$ the total mass flux; f^i an external supply; $\boldsymbol{\sigma}$ the stress tensor; $\boldsymbol{b}$ the body forces vector (in this notation, α may stand for each phase s, l or g depending on whether solid, liquid or gas flow is considered while i denotes the different species solid/mineral (s) water (w) and air (a).

7.2.2. Hydraulic constitutive laws

Liquid and gas flows follow Darcy's law

$$\boldsymbol{q_l} = -\boldsymbol{K_l}(\nabla P_l - \rho_l \boldsymbol{g}) \qquad (7.5)$$

$$\boldsymbol{q_g} = -\boldsymbol{K_g}(\nabla P_g - \rho_g \boldsymbol{g}) \qquad (7.6)$$

where P_l and P_g are absolute liquid and gas pressures, respectively, $\rho_l = \rho_{l0}\, exp\,(\beta\,(P_l - P_{l0}))$ (β = liquid compressibility) is the liquid density, ρ_g is the gas density and $\boldsymbol{K}_\alpha = \boldsymbol{k} \cdot k_{r\alpha}/\mu_\alpha$ is the permeability tensor. The intrinsic permeability tensor, $\boldsymbol{k}$, depends on the porosity ϕ through Kozeny's law

$$\boldsymbol{k} = \boldsymbol{k_0} \frac{\phi^3}{(1-\phi)^2} \frac{(1-\phi_0)^2}{\phi_0^3} \tag{7.7}$$

where $\boldsymbol{k_0}$ is the intrinsic permeability for the matrix with a reference porosity ϕ_0.

In this expressions, α may stand for either l or g depending on whether liquid or gas flow is considered. Both relative permeability of liquid phase and relative permeability of gas phase depend on the degree of saturation using empirical relationships. $\boldsymbol{g}$ is the gravity vector.

The relative permeability of liquid (k_{rl}) and gaseous (k_{rg}) phases are made dependent on S_e (effective degree of saturation) according to

$$S_e = \frac{S_l - S_{lr}}{S_{ls} - S_{lr}} \leq 1 \tag{7.8}$$

$$k_{lr} = S_e^n \qquad \text{(generalised power law)} \tag{7.9}$$

$$k_{gr} = A\,(1 - S_e)^\beta \qquad \text{(generalised power law)} \tag{7.10}$$

where S_l is degree of saturation, S_{lr} and S_{ls} are residual and maximum degrees of saturation, respectively, and A, n, and β are material parameters.

It is also necessary to define the retention curve of the materials by relating degree of saturation with suction ($s = (P_g - P_l) \geq 0$). The expression selected (van Genuchten's model) is:

$$S_e = \frac{S_l - S_{lr}}{S_{ls} - S_{lr}} = \left(1 + \left(\frac{s}{P_0}\right)^{1/1-\lambda}\right)^{-\lambda} \tag{7.11}$$

where P_0 is a parameter related to the capillary pressure and λ is a parameter which controls the shape of the curve. Hysteresis effects have not been taken into account in the analysis.

Molecular diffusion of dry gas in a liquid is governed by Fick's law:

$$\boldsymbol{i}_l^a = -(\tau \phi \rho_l S_l D_m^a \boldsymbol{I}) \nabla \omega_l^a \tag{7.12}$$

where $\boldsymbol{i}_l^a$ is the non-advective mass flux of gas in liquid, τ is the tortuosity, ϕ is the porosity, ω_l^a is the mass fraction of gas in liquid and D_m^a is the molecular diffusion coefficient of dry gas in liquid.

To model the effects of the localised fissures along the bedding planes, the embedded fracture permeability model was applied (Olivella & Alonso 2008). This hydraulic model, coupled with the mechanical part, can take into account the variation of the intrinsic permeability and the capillary air entry pressure with fracture aperture, which depends

on the strain. This model was applied to different domains depending on the selected geometry and the approached solution, as it is explained latter.

Two of the magnitudes that appear in the hydraulic equations explained above are modified in this new set of equations. The intrinsic permeability not only depends on the porosity but also of the fracture aperture while the capillary pressure is not constant anymore, if not it varies with the fracture aperture too.

In the single fracture, liquid and gas flow are also computed using Darcy´s law, with the intrinsic permeability calculated assuming laminar flow, as

$$\boldsymbol{k_{fracture}} = \frac{b^2}{12} \tag{7.13}$$

where b is the fracture aperture.

The equivalent element permeability is computed as follows

$$\boldsymbol{k} = \boldsymbol{k_{matrix}} + \frac{b^3}{12\mathrm{a}} \tag{7.14}$$

where $\boldsymbol{k_{matrix}}$. is the permeability tensor obtained with the Kozeny's model and a is a characteristic dimension for a specific rock accounting for the separation between fractures. This parameter, which weights the role of the fractures on the hydraulic response, governs the constitutive functions for permeability and capillary pressure variations.

The current aperture b can be estimated as a function of the strain $\boldsymbol{\varepsilon}$ (positive when describing expansion in the model) from

$$b = b_0 + \Delta b \qquad \text{for} \qquad \Delta b \geq 0 \tag{7.15}$$

$$\Delta b = s\Delta\boldsymbol{\varepsilon} = a(\boldsymbol{\varepsilon} - \boldsymbol{\varepsilon_0}) \qquad \text{for} \qquad \boldsymbol{\varepsilon} > \boldsymbol{\varepsilon_0} \tag{7.16}$$

Therefore, the local strain causes changes in aperture resulting in a coupling equation with the mechanical laws. The threshold strain ε_0 is associated with fracture initiation. In this study, an existing fracture is considered with an initial aperture b_0, and is assumed to be initially open at $\varepsilon = 0$ $(\mathrm{i.e.}, \varepsilon_0 < 0 \text{ and } b = b_0 + a(-\varepsilon_0) > b_0)$. Extension will induce further aperture opening ($\varepsilon > \varepsilon_0$). Unloading will imply fracture closure, but a residual aperture is expected owing to irreversible strains. Also a maximum aperture is defined as an upper bound of aperture, b_{max}.

The variation of capillary air entry pressure caused by changes in the aperture is also included. The capillary air entry pressure, P, necessary to desaturate a fracture is given by:

$$P = \frac{2\sigma \cos\theta}{b} \tag{7.17}$$

where σ is the surface tension and θ the contact angle.

This equation can be used directly to calculate the air entry value of the element. If Eq. 7.17 is combined with Eq. 7.14, then the capillary air entry pressure to start desaturation is obtained as

$$P = P_0 \sqrt[3]{\frac{k_o}{k}} \tag{7.18}$$

where $P_0$is the capillary pressure for a reference permeability k_0, which eventually can be the initial permeability.

Additional details of the embedded fracture permeability model are given in Olivella & Alonso (2008).

7.2.3. Mechanical constitutive laws

The mechanical model adopted for the simulations is the elasto-plastic Barcelona Basic Model (BBM) for unsaturated soils (Alonso et al. 1990) which includes the effect of effective or net stresses and the suction as:

$$d\boldsymbol{\sigma}' = \boldsymbol{D} d\boldsymbol{\varepsilon} + \boldsymbol{h} ds \tag{7.19}$$

where the suction can be defined as $s = max(p_g - p_l, 0)$ and the net stress as $\boldsymbol{\sigma}' = \boldsymbol{\sigma} + \max(p_g, p_l)\, \boldsymbol{I}$ (in terms of the following stress variables: $p' = (\sigma_1' + 2\sigma_3')/3$; $q' = q = \sigma_1 - \sigma_3$). The model parameters are included in $\boldsymbol{D}$ which is the stiffness tensor or constitutive matrix for changes in net or effective stress and $\boldsymbol{h}$ is the constitutive vector for changes in suction.

The elastic part of the deformation tensor ($\boldsymbol{\varepsilon}$) can be written in the following way (for isothermal conditions):

$$d\varepsilon_v^e = \frac{\kappa\, dp'}{(1+e)\, p'} + \frac{\kappa_s\, ds}{(1+e)(s+p_{at})} \tag{7.20}$$

$$d\varepsilon_q^e = \frac{1}{3G} dq \tag{7.21}$$

where κ and κ_s are the elastic stiffness parameters for changes in net stress and changes in suction respectively G is the shear modulus and e is the void ratio of the porous material.

The yield surface is defined so that the preconsolidation stress is dependent on the suction:

$$f(p', q, s, p_0^*) \equiv q^2 - M^2(p' + p_s)(p_0 - p') = 0 \quad (7.22)$$

where

$$p_s = ks \quad (7.23)$$

$$p_0 = p_c \left(\frac{p_0^*}{p_c}\right)^{[\lambda(0)-\kappa]/[\lambda(s)-\kappa]} \quad (7.24)$$

$$\lambda(s) = \lambda(0)[(1 - r)\exp(-\beta s) + r] \quad (7.25)$$

In these equations, p_0 and p_0^* are the preconsolidation stresses for suction and for saturated conditions respectively; k is the parameter to define the increase of cohesion with suction; p_c is a reference stress; $\lambda(0)$ and $\lambda(s)$ are the stiffness parameters for changes in net stress and suction; r and β are the parameters to define the loading-collapse curve.

The hardening law depends on plastic volumetric strain according to:

$$dp_0^* = \frac{(1+e)p_0^*}{\lambda(0)-\kappa} d\varepsilon_v^p \quad (7.26)$$

The plastic potential is taken as:

$$G \equiv \frac{3\alpha J^2}{g_p^2} - L_p^2(p' + p_s)(p_0 - p') = 0 \quad (7.27)$$

where g_p is a function of the Lode angle; $L_p = M/g_p\big|_{\theta=-\pi/6}$ (being M the slope of the critical state line) and α is a non-associativity parameter .

7.3. Results and interpretation

Initially, the hydro-mechanical loading paths carried out in the oedometer cell (see Chapter 4) were simulated. In such manner, the parameters for the mechanical constitutive model were obtained. Afterwards, regarding the gas injection experiments, two different approaches were considered. Initially, a numerical model with a localized fracture zone was developed in order to see the usefulness of the embedded fracture permeability model to simulate the experimental results regarding the gas transport process. Hereafter, once that model was validated, a more realistic approach was intended applying the embedded fracture permeability model to all the domain without

the need of pre-define a fracture zone. In this way, the fracture pattern will develop automatically due to the heterogeneity of the material which is applied through a porosity random field.

7.3.1. Numerical simulation of hydro-mechanical paths

The numerical simulation of the hydro-mechanical paths, including the pre-conditioning path, the saturation, the water pressurization and the drained loading, allows the determination of the parameters required to simulate the gas injection. Following the test Protocol 1 (see Chapter 3 Section 3.3.1), a full set of mechanical parameters for the BBM was successfully obtained, since during these tests plasticity took place due to its range of stresses. Additionally, hydraulic parameters were also fitted based on the experimental results.

Two different simulations were performed, one for each orientation (samples with bedding planes parallel and normal to flow) changing the mechanical parameters in order to reflect the anisotropy features of the Boom Clay. As a result, compressibility parameters were obtained depending on sample orientation.

7.3.1.1. Geometry and boundary conditions

A picture of the geometry and spatial discretisation adopted for the numerical analyses are shown in Figure 7-1. Taking advantage of the radial symmetry of the oedometer sample, the model used a 2D axisymmetric representation with linear quadrilateral elements with four integration points.

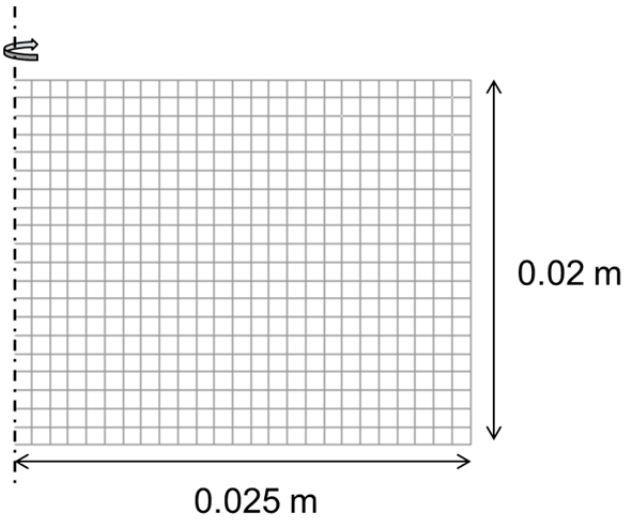

Figure 7-1. Geometry and mesh for the numerical simulation of the loading paths.

To simulate oedometer conditions, null vertical displacements at the bottom of the system and null radial displacement on the sample lateral wall were imposed.

Mechanical and hydraulic conditions were applied following the test protocol. Table 7-1 compile the simulation stages for the loading paths.

Table 7-1. Boundary conditions for each stage of the loading path simulation (Test P1_FI_N).

Time (min)	**Stage**	**Boundary conditions**
0-360	Loading at constant water content	Vertical stress increases from 0.1 to 3.1 MPa Atmospheric pressure at upstream and downstream boundaries
360-420	Flooding	Vertical stress remains constant Atmospheric pressure at upstream and downstream boundaries
420-15000	Water pressure increase and water permeability	Vertical stress remains constant Upstream pressure increases up to 0.7 MPa Downstream pressure increases up to 0.6 MPa
15000-21000	Water pressure equalization	Vertical stress remains constant Upstream pressure decreases to 0.6 MPa Downstream pressure remains constant (0.6 MPa)
21000-33000	Drained loading	Vertical stress increases from 3.1 to 9.1 MPa Upstream and downstream pressures remain constant (0.6 MPa)

Fluid pressures and stress referring to the modelling are expressed in absolute terms (it is zero-referenced against perfect vacuum)

7.3.1.2. Model parameters

Table 7-2 lists the mechanical parameters required for the BBM model used in the calculations and determined from tests performed at high stress level, P1_FI_N and P1_FI_P. This set of parameters is in accordance with those reported in Li et al. (2007) for Boom Clay.

Table 7-2. Parameters for the BBM model used in the simulation

Definition parameter	Symbol	Bedding normal	Bedding parallel
Elastic behaviour			
Elastic compressibility (against mean stress changes)	κ	0.020	0.005
Volumetric compressibility against suction changes	κ_s	0.005	0.002
Poisson ratio	ν	0.33	0.33
Plastic and shear strength behaviour			
Elastoplastic volumetric compressibility	$\lambda(0)$	0.10	0.10
Parameters to define loading-collapse yield curve	r	0.95	0.95
	β	4 MPa^{-1}	4 MPa^{-1}
Parameter to define increase in cohesion with suction	k	0.01	0.01
Reference stress	P_c	0.1 MPa	0.1 MPa
Slope of critical state line	M	0.73	0.73
Parameter for the plastic potential	α	0.333	0.304
Initial state			
Initial preconsolidation stress for saturated conditions	p_0^*	6 MPa	6 MPa
Lateral earth pressure at rest	K_0	0.84	0.84
Initial void ratio	e_0	0.57	0.58

The hydraulic parameters used in these simulations were also fitted with experimental data. For the retention properties, the van Genuchten's model was adopted (Figure 7-2). A power law is considered for both liquid and gas relative permeability fitting the experimental data reported by Volckaert et al. (1995) despite its dispersion. In the absence of harder experimental results, these data have been used as in Delahaye & Alonso (2002). However in this study, not only the gas relative permeability has been fitted with a generalized power law, but also the liquid relative permeability (Figure 7-3). The diffusion coefficient was selected according to Jacops et al. (2015) for samples with bedding planes orthogonal and parallel to the flow direction. In Figure 7-4 the fitted Kozeny's model for the intrinsic permeability changes of the material as a function of the void ratio is shown, together with the experimental measurements for samples with bedding planes orthogonal and parallel to water flow. Table 7-3 shows the hydraulic constitutive parameters considered in the analysis.

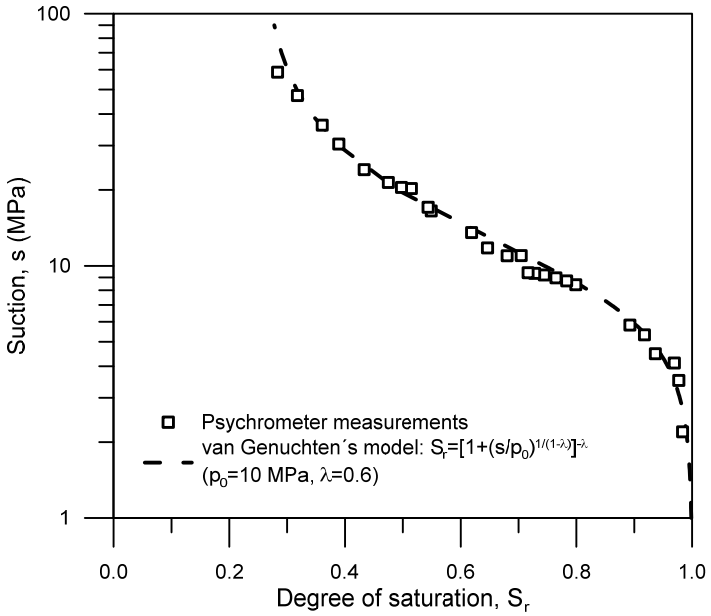

Figure 7-2. Drying branch of the water retention curve. Experimental data and van Genuchten's fitting.

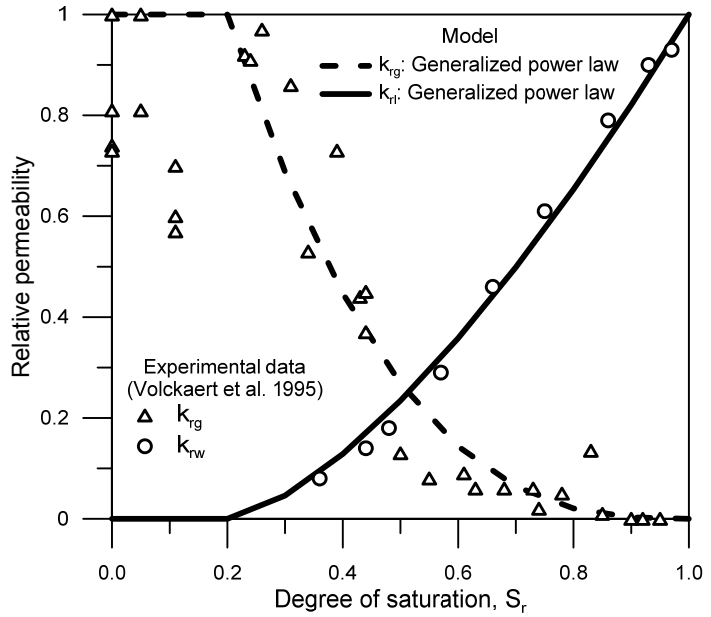

Figure 7-3. Experimental data for relative permeability in Boom Clay (after Volckaert et al. 1995) together with model fitting (after Delahaye & Alonso 2002).

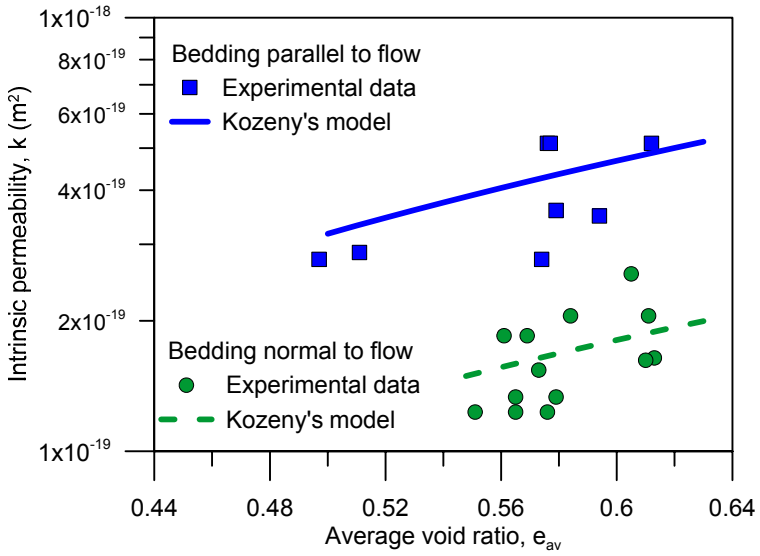

Figure 7-4. Water permeability as a function of the void ratio. Experimental data and Kozeny's fitting.

Table 7-3. Hydraulic constitutive parameters for both orientations

Definition parameter	Symbol	Bedding normal	Bedding parallel
Kozeny´s model			
Reference intrinsic permeability	k_0	$4.2 \cdot 10^{-19}$ m^2	$4.2 \cdot 10^{-19}$ m^2
Reference porosity	ϕ_0	0.380	0.300
Retention curve (van Genuchten's model)			
Shape function for retention curve	λ	0.6	0.6
Material parameter related to air entry value	P	10 MPa	10 MPa
Residual saturation	S_{rl}	0.2	0.2
Maximum saturation	S_{ls}	1	1
Liquid relative permeability			
Power	n	1.48	1.48
Gas relative permeability			
Power	β	2.8	2.8
Diffusion of dissolved air			
Molecular diffusion coefficient	D_m^a	$2.6 \cdot 10^{-10}$ m^2/s	$5 \cdot 10^{-10}$ m^2/s

7.3.1.3. Results of hydro-mechanical paths

Figure 7-5 shows the results of the numerical simulation of the mechanical compression paths for both orientations together with the experimental data. The model with the fitted parameters is capable of reproducing the initial loading, the swelling upon contact of the sample with the SBCW and the drained loading very well. In order to simulate the elastic loading and the swelling of the sample during the contact with SBCW, different elastic parameters were used, which evidenced the anisotropy behaviour of the Boom Clay in the elastic domain. In contrast, the elastoplastic compressibility turned out to be equal for both orientations.

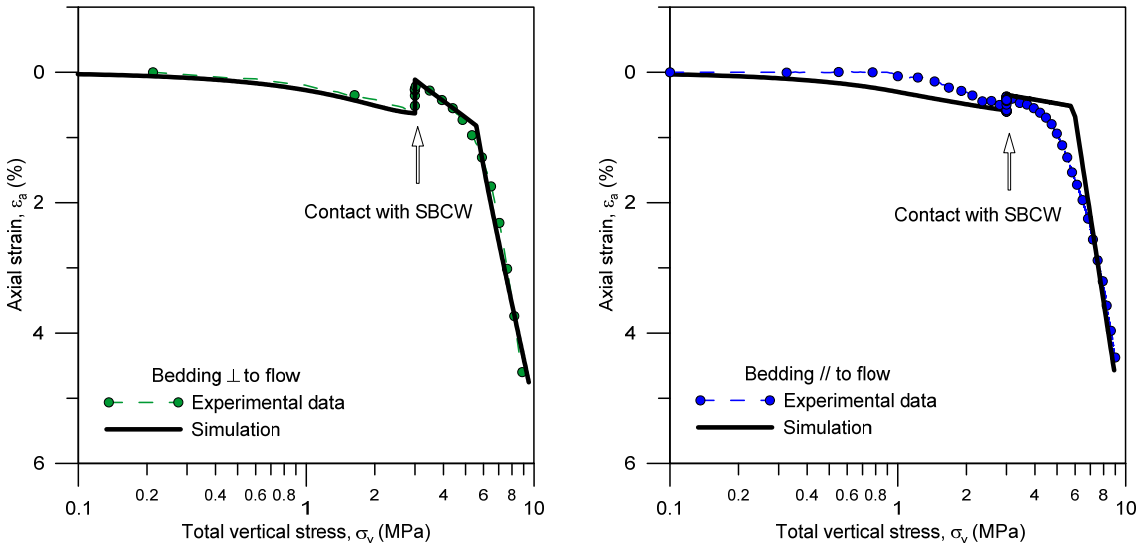

Figure 7-5. Computed versus measured axial strains during hydro-mechanical loading for samples a) with bedding planes normal to flow; b) with bedding planes parallel to flow.

The simulation also provides interesting information in relation to the suction reduction during the pre-conditioned path which confirmed the hypothesis that after the first loading some suction remained in the sample and thus, samples underwent expansion during flooding. The formulation of the BBM model takes into account that changes in suction produce a deformational response and provides complementary information to the experimental data regarding the pore pressure in this stage.

Figure 7-6 shows the reduction of the initial suction during the loading and the flooding of the samples for both orientations. At the end of the loading at constant water content, suction reduction in the sample with bedding planes normal to flow was more effective, nonetheless, as the elastic compressibility against the suction changes is higher, it underwent a large swelling during the flooding (Figure 7-7).

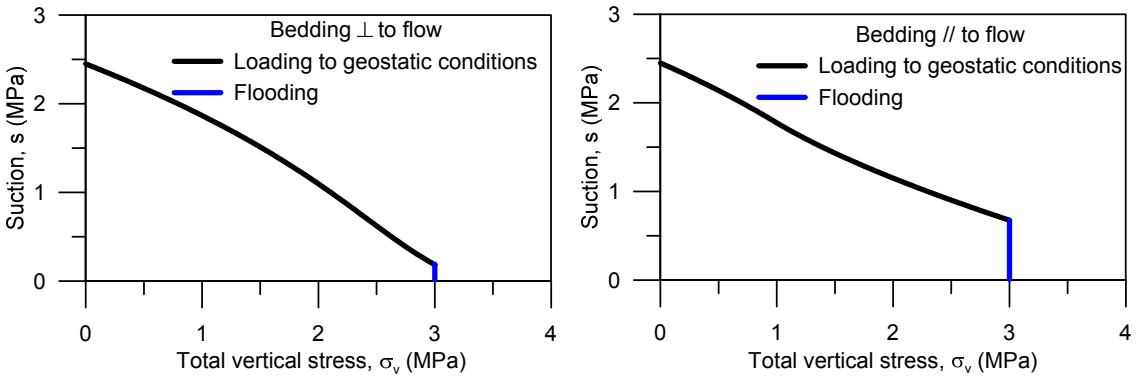

Figure 7-6. Suction reduction during initial loading and flooding for both sample orientations.

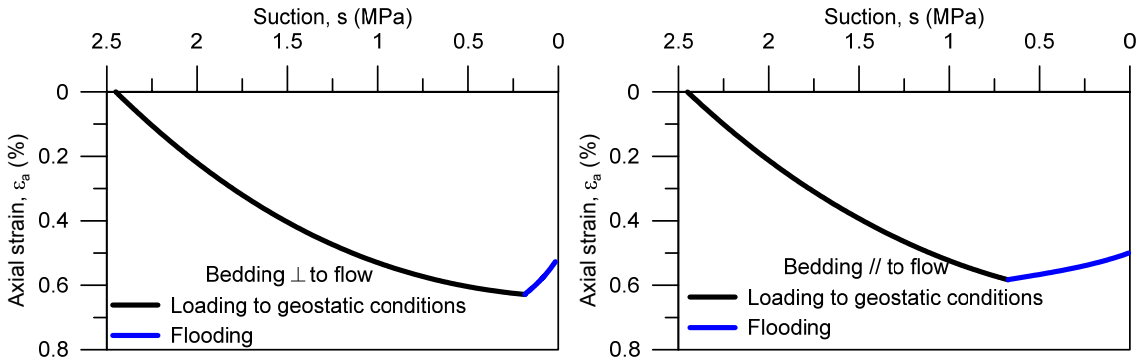

Figure 7-7. Deformational response against suction changes for both sample orientations.

7.3.2. Numerical simulation of gas injection with localized fracture zone

In order to perform the air injection stage in the simulation, some modifications had to be made with respect to the hydro-mechanical one. A 2D axisymmetric representation of the sample was also selected; however, the sample was modelled by two zones having different hydraulic properties: the matrix and the zone of fracture development (ZFD) in which the dominant advective flow of gas occurs. In the choice of the latter, a single predefined central zone was chosen, renouncing to investigate the local distribution of the fractures, but still keeping the possibility of reproducing the global effect of the localised preferential paths on the sample response. For this reason, only gas migration on samples with bedding planes parallel to flow was simulated, since this geometry for samples with bedding planes normal to flow was not representative. Experimental results of two test carried out with being planes parallel to flow following Protocol 3 (P3_FI_P_2 and P3_SI_P) were used. For both the matrix and the embedded fracture zone the same mechanical parameters were chosen, but different hydraulic models were used. Both for the constitutive model and the geometry of the problem simple approximations were made, but still able to capture the consequences of preferential path development.

Initially, a simulation for the slow injection test (P3_SI_P) was performed obtaining the required parameters for the embedded fracture permeability model, and afterwards, a simulation of the fast injection test (P3_FI_P_2) was launched as a blind test using the same set of parameters.

7.3.2.1. Geometry and boundary conditions

To properly simulate the gas injection stage of tests, it was necessary to include both the injection and recovery systems in the model, which correspond to the drainage lines of the experimental setup. If these were not explicitly included in the numerical model, the actual injection and outflow pressures history at the boundaries of the sample would not be properly assigned, because the change in the density of the

pressurised mass of air would be disregarded. After the shut-off, the mass of pressurised air in the upstream injection system is significant and cannot be disregarded. Accounting for the controlling system flexibility was achieved by adding to the model two reservoirs, which represent the injection and recovery pistons, lines and coarse porous rings. These elements were idealised with a porosity of 0.5 (the code cannot simulate non-porous materials), high conductivity (permeability of 10^{-10} m^2) and a flat retention curve with a very low air entry value ($P_0 = 0.001$ MPa). The total volume of each system corresponds to the dead volumes obtained from calibration tests of the equipment (see Chapter 3). The mechanical constitutive law for these stiff elements was linear elasticity with a very high Young modulus. The final geometry of the discretised problem is depicted in Figure 7-8.

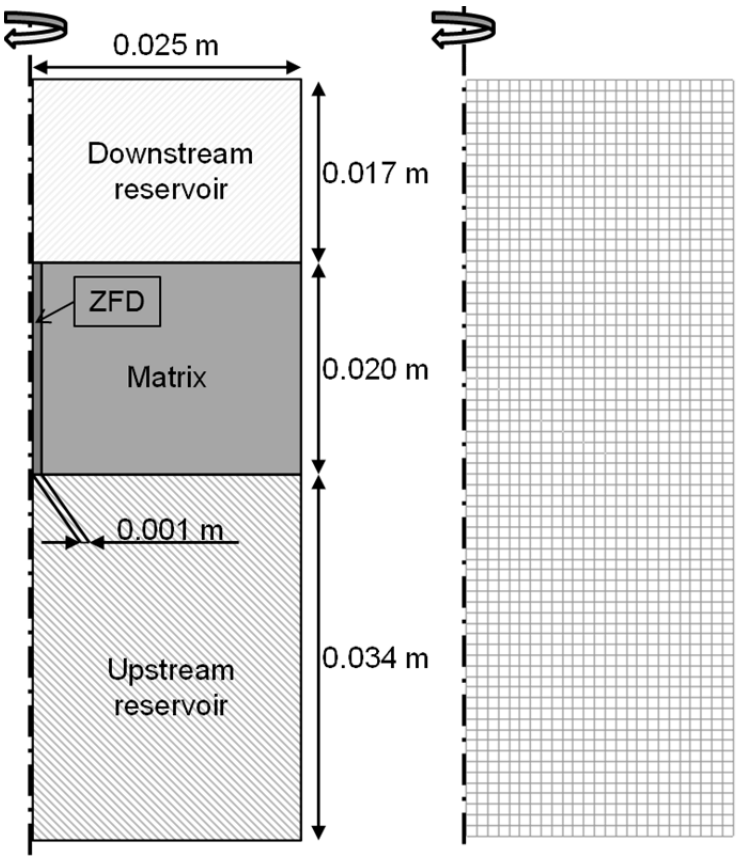

Figure 7-8. Materials, geometry, and mesh for air injection numerical simulation.

Before the air injection starts, the sample was fully saturated, as well as both reservoirs. The first stage of the injection consisted of replacing the water in the upstream reservoir by air at 0.5 MPa pressure. An injection pressure ramp was then applied at the bottom of the injection reservoir, which followed the recorded data during the test. The dissipation stage started once the injection pressure reached the

maximum pressure of 4 MPa. The bottom boundary became impermeable during this dissipation stage forcing the accumulated air in the reservoir to flow upwards.

The pressure of the downstream pressure/volume controller was kept constant at 0.5 MPa during the tests. This device is capable of maintaining this pressure by changing the volume as the air flows through the sample. However, when the tank of the controller is full, it is not able to keep the pressure anymore if the air flow continues and thus the pressure begins to rise. In contrast, the upper reservoir in the simulation has a fixed volume. As a result, an increase in the outflow pressure must be imposed in the numerical model to properly model the boundary conditions. Accordingly, the pressure boundary condition in the downstream reservoir was set constant in the first stage of the simulation - water pressure at 0.5 MPa - and was increased up to 1.5 MPa in the last stage. A schematic picture of the boundary conditions is shown in Figure 7-9. Table 7-4 summarises the simulation stages for the air injection.

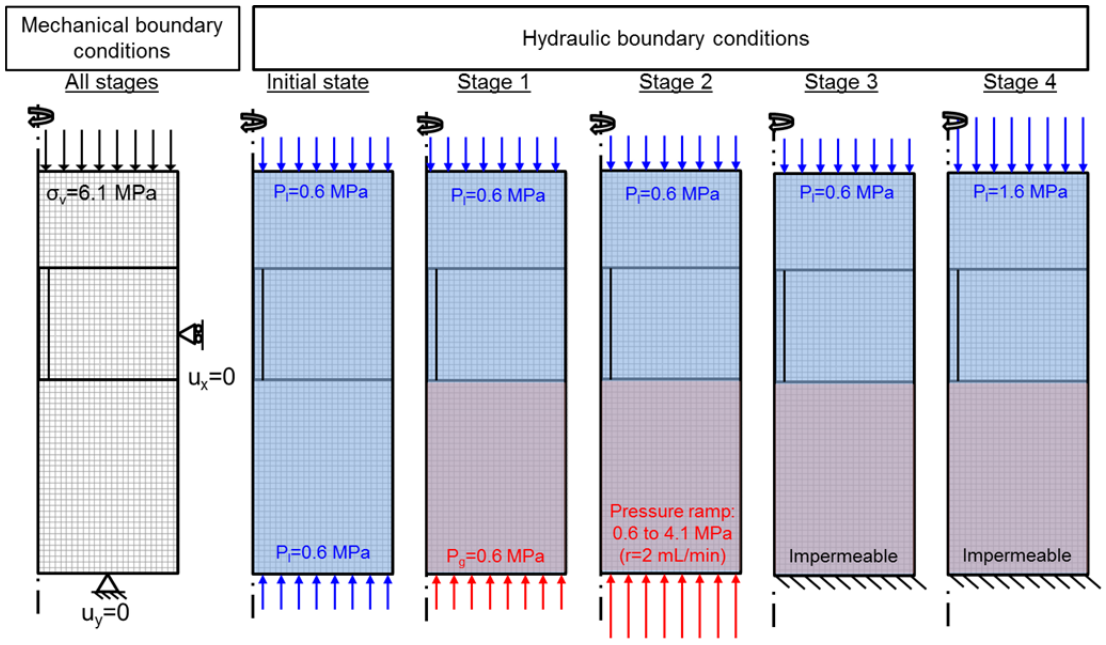

Figure 7-9. Mechanical and hydraulic boundary conditions used in the gas injection simulation (pressures are zero-referenced against the perfect vacuum - absolute pressures).

Table 7-4. Stages and pressure boundary conditions for the simulation of slow air injection test.

Time (min)	Stage	Boundary conditions
0-500	Replace water by air	Upstream air pressure increases up to 0.6 MPa Downstream pressure constant (0.6 MPa)
500-745	Air injection (*r*=2 mL/min)	Upstream pressure increases from 0.6 to 4.1 MPa Downstream pressure constant (0.6 MPa)
745-1080	Air dissipation	Upstream boundary becomes impermeable Downstream pressure constant (0.6 MPa)
1080-2300	Air dissipation	Upstream boundary remains impermeable Downstream pressure increases up to 1.6 MPa

Fluid pressures referring to the modelling are expressed in absolute terms (it is zero-referenced against perfect vacuum)

Gas pressures in the code indicate the mixture of dry and saturated vapour and are presented in terms of absolute pressures (it is zero-referenced against perfect vacuum). In the numerical results presented below, gas pressures shown in comparison with the experimental pressures are expressed as relative pressure (it is zero-referenced against the atmospheric pressure) except when it is specifically indicated.

7.3.2.2. Model parameters

The mechanical parameters for both, the matrix and the zone of fracture development were the same as the set determined for the loading path (Table 7-2). Note that the stress level during these tests did not reach the yield stress so that only elastic regime took place in the simulations of gas injection.

Elastic parameters of the reservoirs are presented in Table 7-5.

Table 7-5. Mechanical parameter of the reservoirs

Definition parameter	Symbol	Value
Linear elasticity		
Young modulus	E	10000 MPa
Poisson ratio	υ	0.3
Initial void ratio	e	1.0

For the matrix material, the same set of hydraulic parameters presented in Table 7-3 were employed.

The required parameters for the embedded fracture permeability model applied to the zone of fracture development were fitted by using some of the experimental data presented in Chapter 6. An initial aperture $b_0 = 100\ \mathrm{nm}$ – slightly higher than the dominant pore mode of the matrix – was selected (as discussed in Chapter 6 Section 6.5.1). The threshold strain (ε_0), the maximum aperture (b_{max}) and the characteristic dimension (a) were fitted so as to achieve a final capillary pressure in the ZFD similar

to the one determined by MIP after the air injection tests. Although experimental data on fissure aperture and separation are available from measurements in FESEM and μ-CT images, these data cannot be directly applied in this case. Firstly because in the selected geometry, fracture development is restricted to a small zone; secondly, it cannot be ensured that measured apertures were the maximum because as discussed in Chapter 6 Section 6.5.1 the compression underwent by the samples in the pressure dissipation stage could produce some closure; and finally and most important, the model does not take into account the roughness and tortuosity of the fissure pattern, and thus, the increase of permeability is too efficient with fracture aperture.

The theoretical variation of the intrinsic permeability and the capillary pressure with the selected parameters – according to Eq. 7.14 and Eq. 7.18 – is depicted in Figure 7-10 together with the corresponding initial and final values. The initial and the final water retention curves of the ZFD – obtained with the initial and final value of the capillary pressures, respectively – are in good agreement with the experimental data (Figure 7-11).

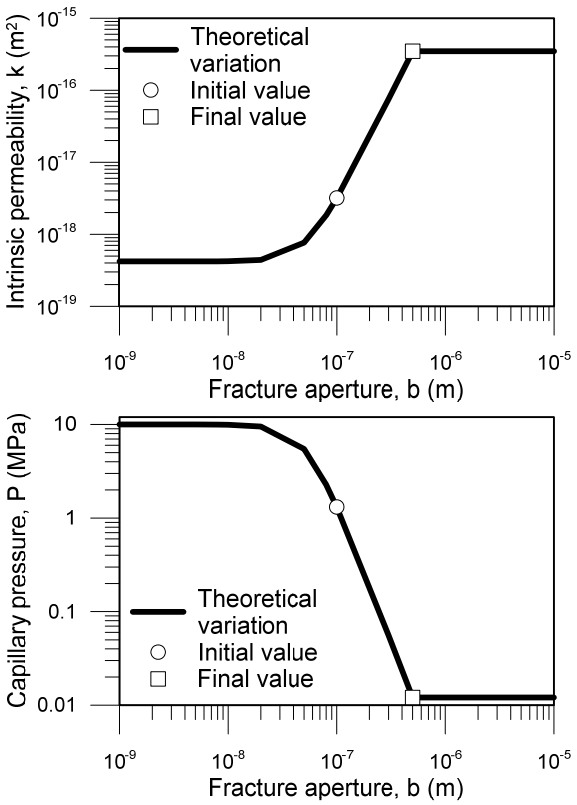

Figure 7-10. Theoretical variation of intrinsic permeability and capillary pressure in the ZFD with initial and final values for the set of parameters indicated in Table 7-6.

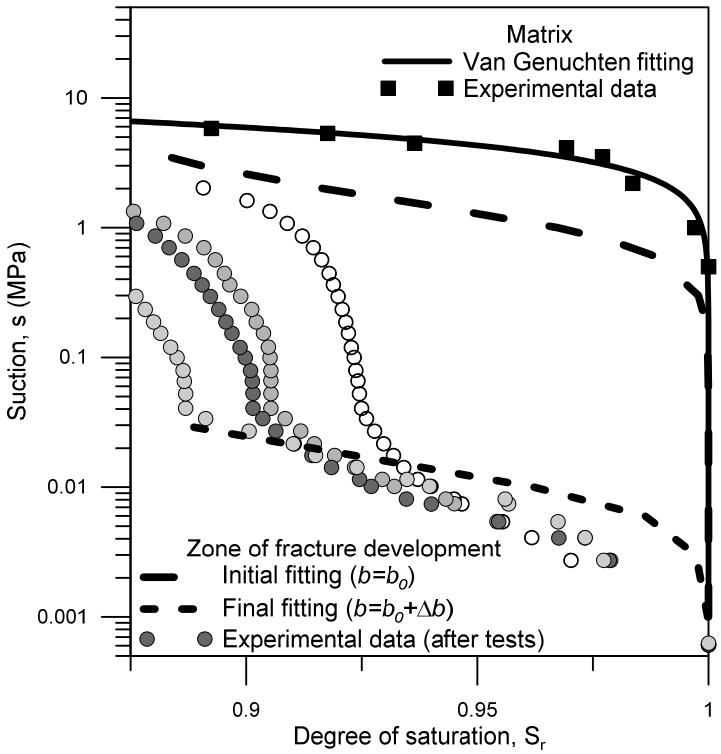

Figure 7-11. Experimental water retention curves before (matrix) and after (ZFD) air tests together with their modelling curves.

Table 7-6 shows the hydraulic constitutive parameters of the zone of fracture development considered in the analysis. Those which are not explicitly referred in the text were the same as in the matrix.

Table 7-6. Hydraulic parameters of the ZFD used in the simulations.

Definition parameter	Symbol	Bedding parallel
Embedded fracture permeability model		
Reference intrinsic permeability	k_0	$4.2 \cdot 10^{-19}$ m^2
Reference porosity	ϕ_0	0.363
Initial aperture	b_0	$1 \cdot 10^{-7}$ m
Threshold strain	ε_0	$-1 \cdot 10^{-4}$
Characteristic dimension	a	$3 \cdot 10^{-5}$ m
Maximum aperture	b_{max}	$5 \cdot 10^{-7}$
Liquid relative permeability		
Power	n	1.48
Gas relative permeability		
Power	β	2.8
Diffusion of dissolved air		
Molecular diffusion coefficient	D_m^a	$5 \cdot 10^{-10}$ m^2/s

7.3.2.3. Results of the simulation of the slow air injection test

The results of the computed injection and outflow pressure response in the ZFD (at 0.0005 m from the axis) as a function of time together with the outflow volume and the

average axial strain along the sample height are shown in Figure 7-12 compared with experimental results for the sample tested at slow injection rate (P3_SI_P).

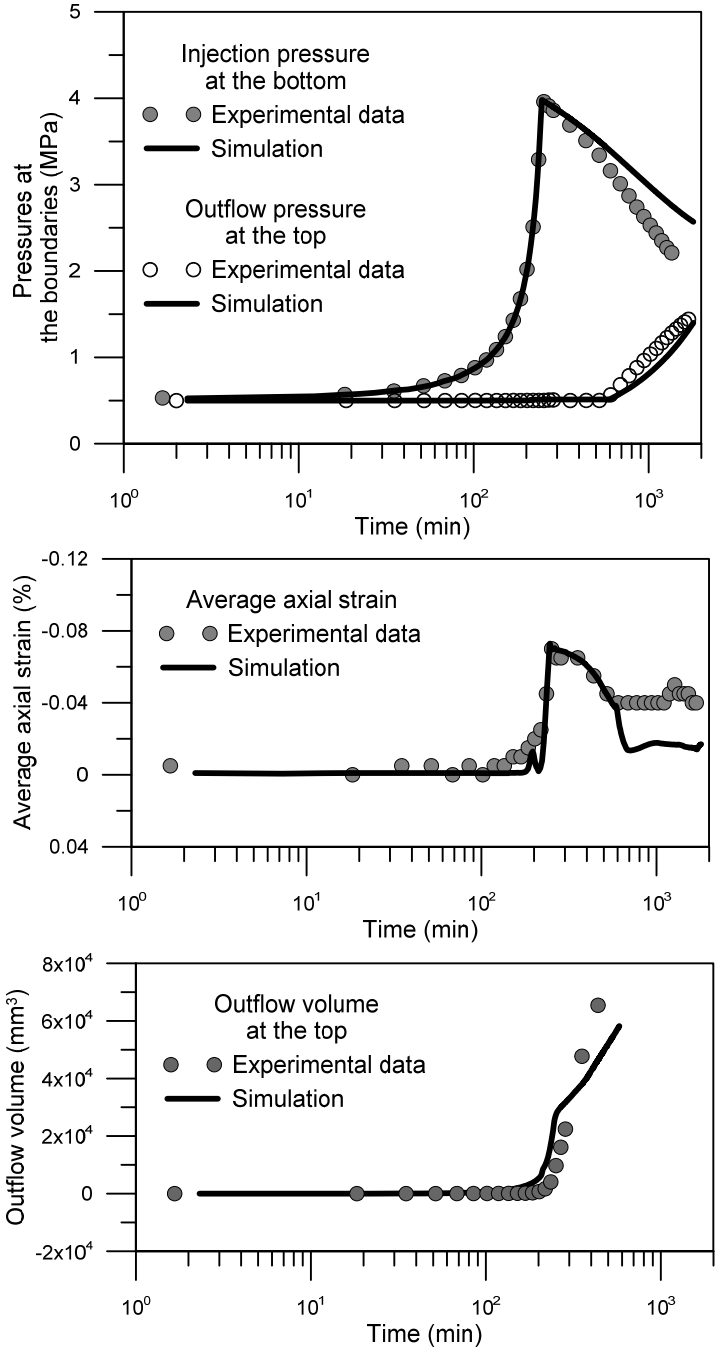

Figure 7-12. Computed versus measured in the ZFD (at 0.0005 m from the axis): a) injection and recovery pressures; b) average axial strains; c) outflow volumes. Slow air injection test

Figure 7-12a shows that the air pressure decay at the bottom of the sample during the dissipation stage is acceptably well fitted. Good agreement is also found in the fluid pressure at the top, computed as the maximum between air and water pressure. The computed sample volume change represented by the average axial strain is also reasonably well reproduced (Figure 7-12b). The sample at an air injection rate of 2

mL/min undergoes expansion during the injection stage followed by compression during air dissipation. The computed results show the same expansion, while a slightly larger compression than the measured one is predicted.

Moreover, the time in which the outflow takes place (Figure 7-12c) compares well with the measured one. Fixing the pressure boundary conditions at the downstream reservoir as explained above, the outflow volume, computed as the sum of water and air volumes, fits well with the experimental measurements.

The local sample response is depicted in Figure 7-13, with contour plots to better understand the influence of the embedded fracture response. Absolute gas pressure, porosity and liquid degree of saturation are represented at three different time steps. The first one refers to 150 minutes after the start of gas injection, the second at the end of the gas injection (shut-off) and finally during the dissipation stage. It is worth noting that the opening of the fracture plays an important role in terms of air dissipation. On the one hand, only when the air pressure increased enough, the fracture opens and becomes desaturated, allowing the air to flow. On the other hand, as the air pressure decreases due to the outflow, the fracture gradually closes up over the time.

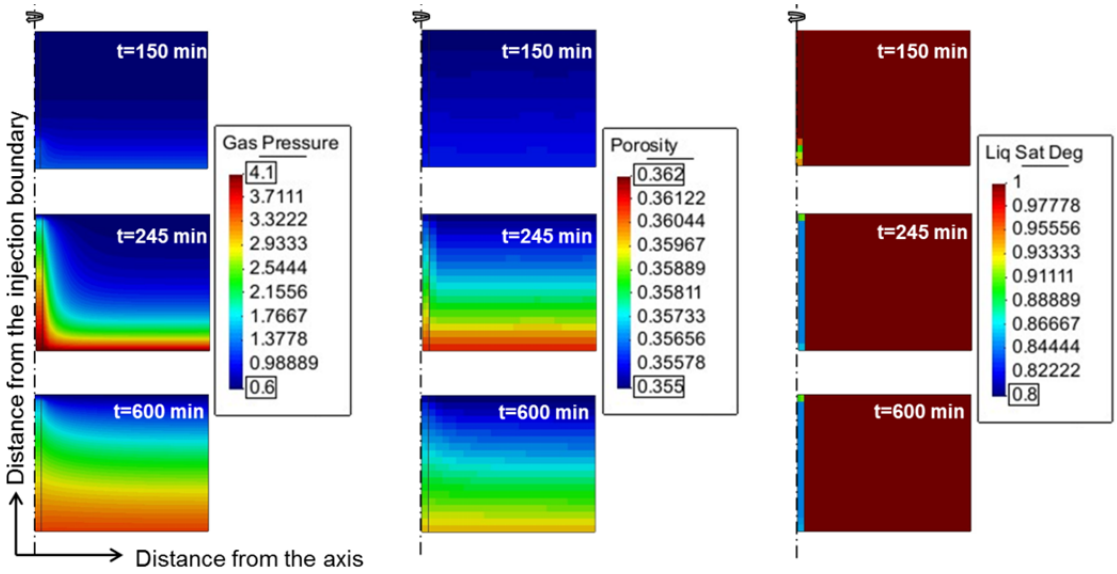

Figure 7-13. Simulated distribution of absolute gas pressure (left, in MPa), porosity (middle) and liquid degree of saturation (right) during the air injection (t=150 min), at shut-off (t=245 min) and during the dissipation (t=600 min).

The matrix of the clay presents a significant delay in its behaviour, as its permeability does not change at the same rate. Moreover, it remains fully saturated after the air passage. Indeed, within the matrix, the dominant transport mechanism is the diffusion of dissolved air. Figure 7-14 shows the contribution of the diffusive and advective flows in the matrix and in the ZFD at three different elapsed times. The dominant advective

flow in the ZFD is clearly observed. The simulated vertical profiles in the ZFD of the gas and the liquid pressures at the same elapsed times are shown in Figure 7-15, where the evolution of the gas pressure front along the ZFD can be clearly appreciated.

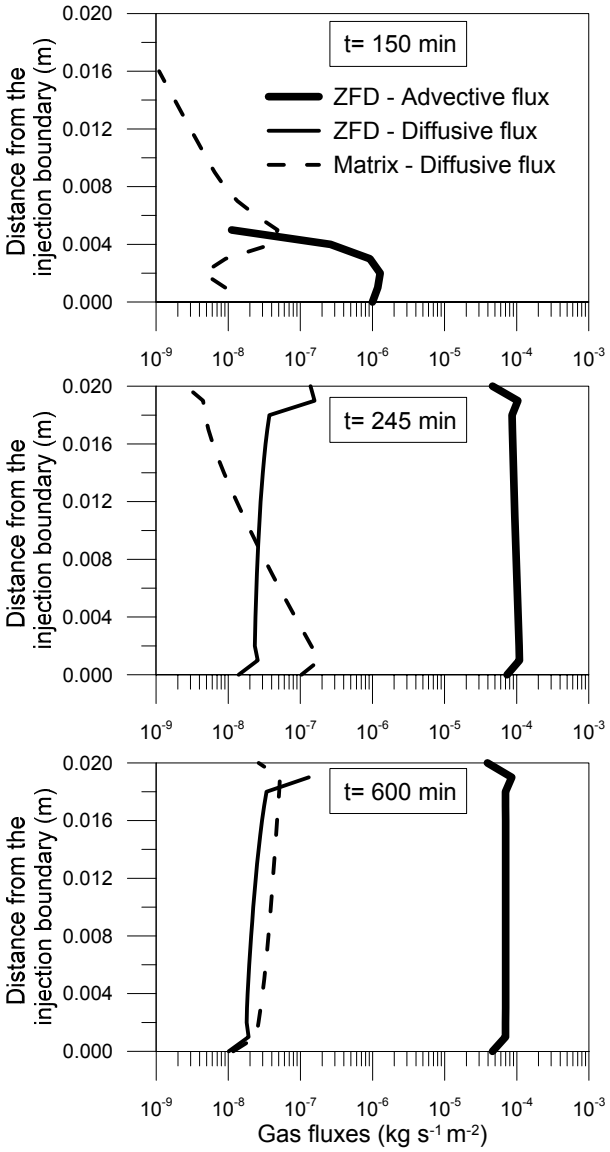

Figure 7-14. Diffusive and advective fluxes along the core height in the ZFD (at 0.0005 m from the axis) and in the matrix (at 0.0125 m from the axis) at air injection (t=150 min), shut-off (t=245 min) and dissipation (t=600 min) stages.

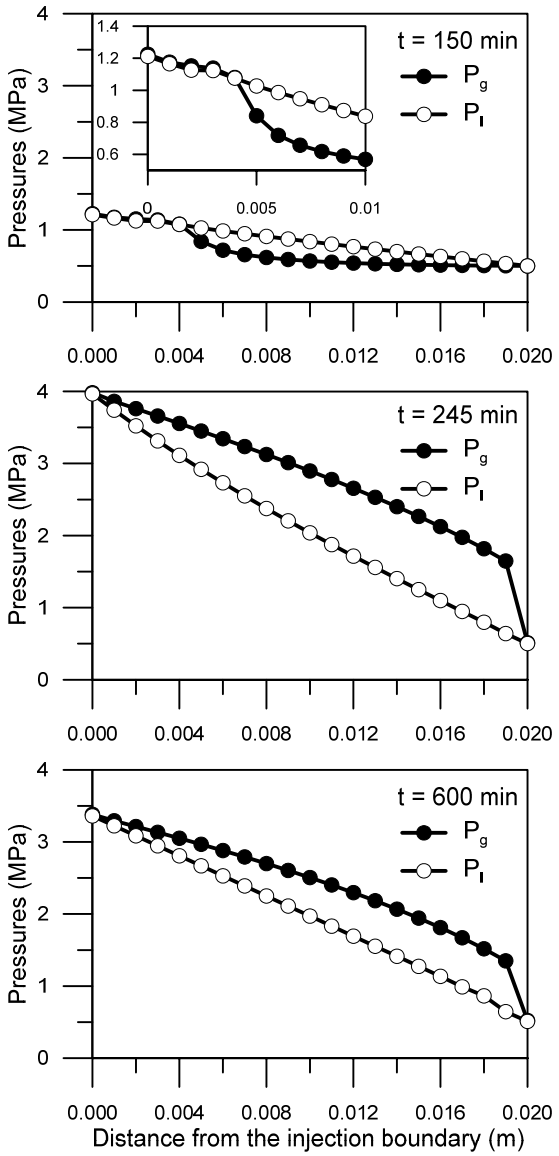

Figure 7-15. Simulated vertical profiles of gas pressure, P_g, and liquid pressure, P_l, throughout the core height in the ZFD (at 0.0005 m from the axis) at air injection (t=150 min), shut-off (t=245 min) and dissipation (t=600 min) stages.

In Figure 7-16 the computed local radial strains (positive in compression) show that the oedometer constraint does not prevent local radial strains associated with the aperture of the fracture. The local strains start developing at the beginning of the gas injection and clearly reach their maximum in correspondence of the maximum aperture of the fracture. The intact matrix is subjected to compressive strains which compensate the extension strains of the ZFD. Afterwards, they decrease during the dissipation stage. It is worth noting that the non-null radial strain at the boundary of the sample is a numerical artefact due to the calculation of strains at the Gauss points. The position of the maximum radial displacement moves towards the external boundary during the injection tests, and its value at the boundary is correctly null, as shown in the same figure.

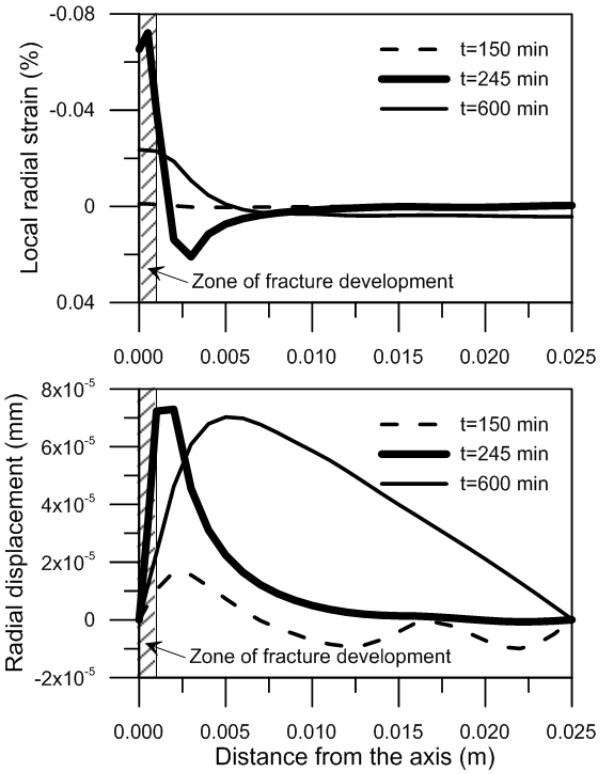

Figure 7-16. Computed local radial strains and radial displacements at the mid-height of the sample as a function of the distance from the symmetry axis at air injection (t=150 min), shut-off (t=245 min) and dissipation (t=600 min) stages.

7.3.2.4. Prediction test: simulation of the fast air injection test

The parameters of the embedded fracture model were calibrated by comparison with the slow injection test. To demonstrate the predictive capability of the numerical model, the air injection test at 100 mL/min (P3_FI_P_2) was simulated with the previous set of parameters, representing a blind test. The stages of the simulation were changed to adapt them to the faster injection as the injection stage lasted only 4.87 minutes, but keeping the same criteria regarding boundary conditions as before (Table 7-7).

Table 7-7. Stages and pressure boundary conditions for the simulation of fast air injection test.

Time (min)	Stage	Boundary conditions
0-500	Replace water by air	Upstream air pressure increases up to 0.6 MPa Downstream pressure constant (0.6 MPa)
500-504.87	Air injection (*r*=100 mL/min)	Upstream pressure increases from 0.6 to 4.1 MPa Downstream pressure constant (0.6 MPa)
504.87-535.68	Air dissipation	Upstream boundary becomes impermeable Downstream pressure constant (0.6 MPa)
535.68-541.68	Air dissipation	Upstream boundary remains impermeable Downstream pressure increases up to 1.9 MPa
541.68-2000	Air dissipation	Upstream boundary remains impermeable Downstream pressure constant (1.9 MPa)

Fluid pressures referring to the modelling are expressed in absolute terms (it is zero-referenced against perfect vacuum)

Figure 7-17 presents the computed results together with the experimental ones (P3_FI_P_2) showing a general good agreement. The pressure release in the simulation was slower than the measured, and thus the average expansion axial strain is slightly higher. However, the overall deformation behaviour is well captured, displaying some expansion at the early injection stage which continues after the shut-off, while the air pressure front propagates into the sample. Afterwards, during the air pressure dissipation stage, progressive compression of the sample is well caught. The outflow volume breakthrough at the top of the sample is well reproduced, although the amount of outflow is slightly overestimated.

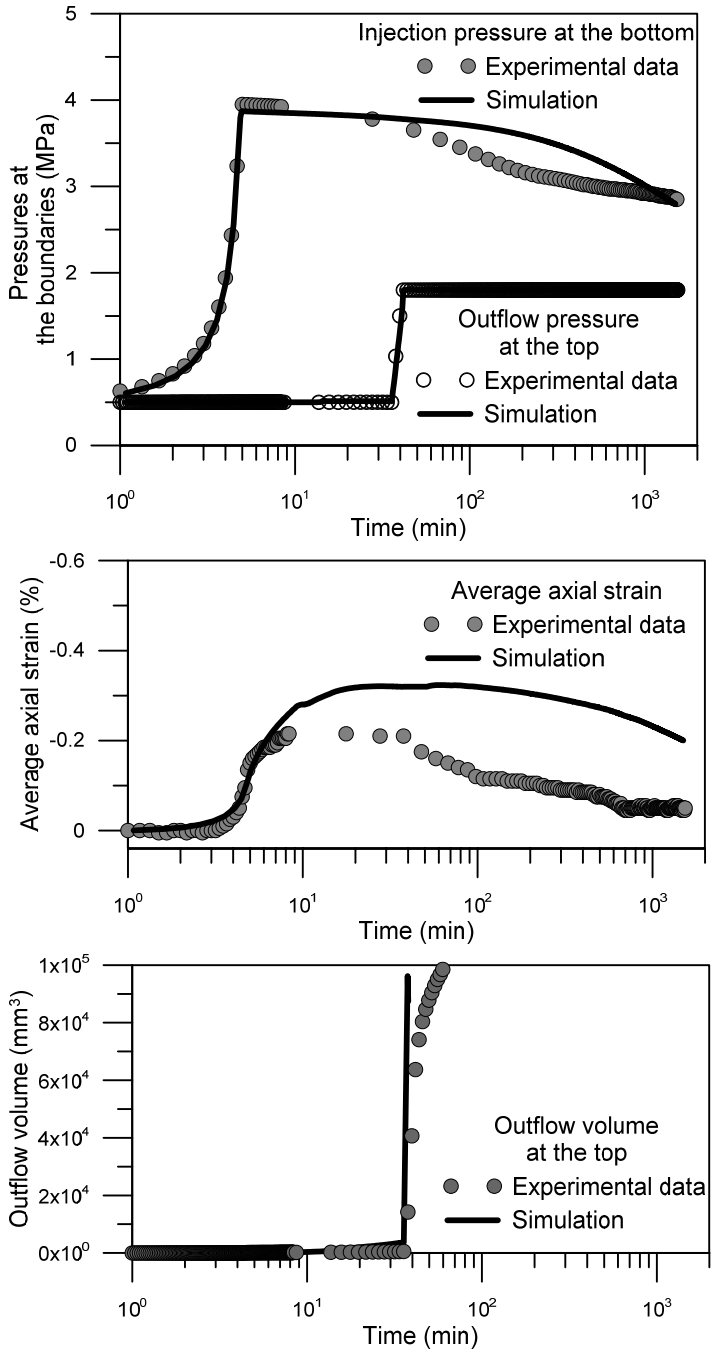

Figure 7-17. Computed versus measured in the ZFD (at 0.0005 m from the axis): a) injection and recovery pressures; b) axial strains; c) outflow volumes. Fast air injection test.

7.3.3. Numerical simulation of gas injection with random porosity field

The comparison between the experimental data and the model predictions with a localized fracture zone shows encouraging agreement. The simple numerical model implemented for the analysis of these oedometer tests provided some interesting information on the local hydro-mechanical coupled response of Boom Clay subjected to gas pressurisation and transport. However, it was though that more realistic modelling in a more general geometric configuration could be achieved only by integrating the embedded fracture model in all the elements. This can be done including random

permeability (or porosity) fields, like the ones proposed by Delahaye & Alonso (2002) or Arnedo et al. (2013). This way, heterogeneity can automatically develop fracture patterns, without the need for a pre-defined fracture zone. In the case of study, small scale heterogeneity of the material was considered including a random porosity field.

Nevertheless, in view of the experimental results of the microstructure evolution, this approach does not completely tally with the formation of preferential pathways following the bedding direction, and thus, further improvements are required in the sense of introducing spatial correlation throughout the information of micro-tomography images.

7.3.3.1. Random porosity field calculation

To address the issue, the strategy adopted in this work was to start from a simple approach, using porosity data with no spatial correlation.

The initial porosity field was obtained from a collection of porosity data of Boom Clay samples retrieved at the HADES level in Mol. A total of 99 values of porosity were gathered from Le (2008); Lima (2011); Dao (2015) and this study. A normal distribution with no spatial correlation (Figure 7-18) was obtained in order to calculate the mean value and its standard deviation, given: $\bar{n} = 0.386; \sigma = 0.012$. These data allowed creating initial random uniformly distributed porosity field shown in Figure 7-19.

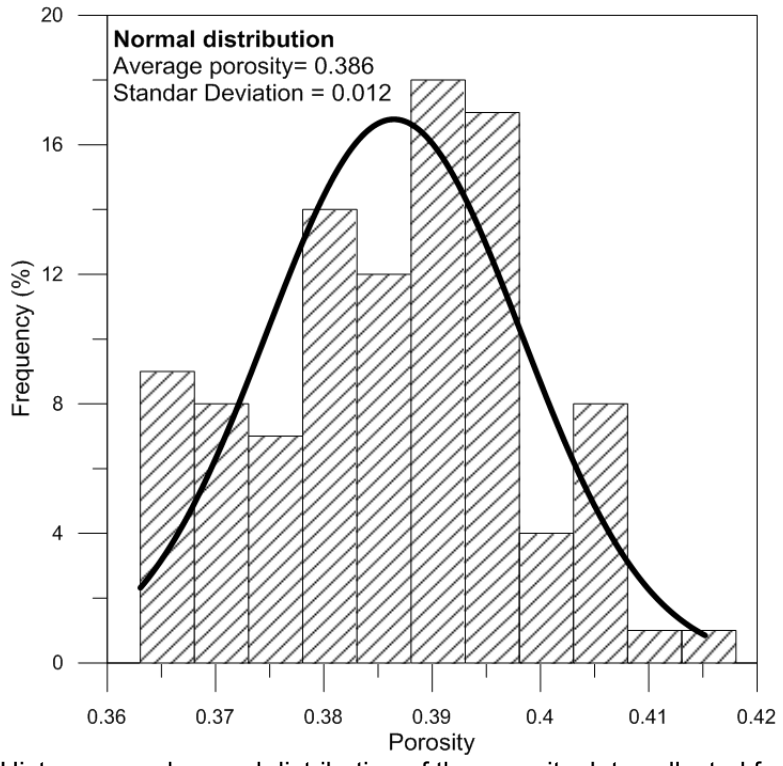

Figure 7-18. Histogram and normal distribution of the porosity data collected from Le (2008); Lima (2011); Dao (2015) and this study.

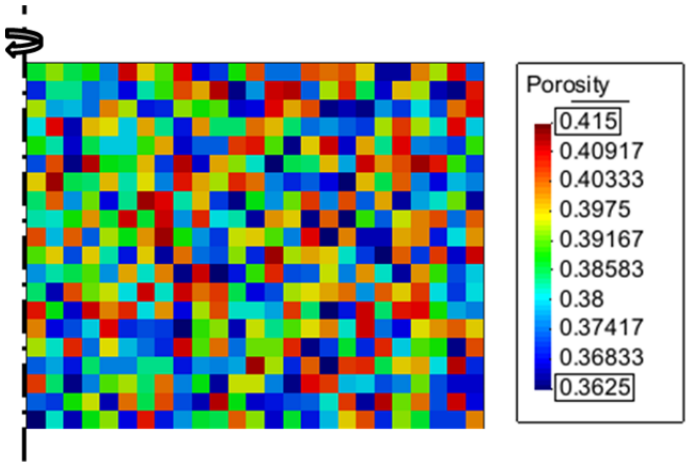

Figure 7-19. Initial porosity field.

Figure 7-20 shows the initial permeability field obtained from the porosity field by means of Kozeny's law (as initial fracture aperture are small). Note that, due to small variations in porosity considered, initial permeability of all elements is in the same order of magnitude, so initially there is no marked heterogeneity in the hydraulic properties. This situation will change as the elements deform in response to change in net stress (effect of pressurization, saturation and gas injection).

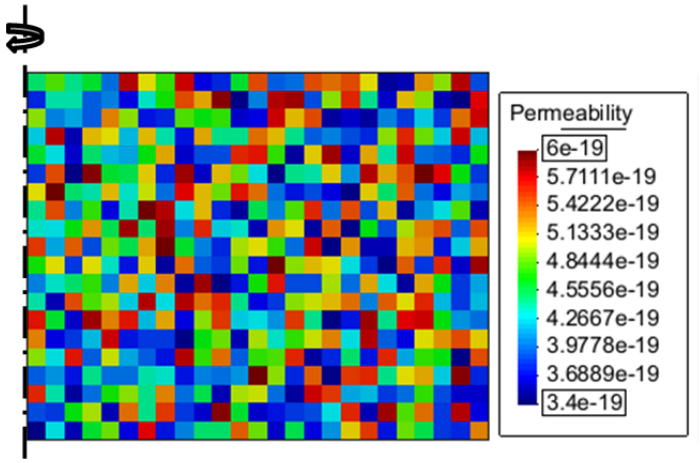

Figure 7-20. Initial permeability field.

7.3.3.2. Geometry, boundary conditions and model parameters

Features of this simulation were equal from the used in the simulation with a localized fracture. Same stages were imposed, but in contrast to the initial simulation, the parameters of the zone fracture of fracture development (Table 7-6) were adopted for the entire domain which means that the embedded fracture permeability model was applied in all elements representing the material.

7.3.3.3. Results of the simulation with random porosity field

Figure 7-21 presents the computed results together with the experimental ones (P3_SI_P) for the simulation performed with the random porosity field. As in the simulation with the ZFD, a general good agreement is shown. The pressure release in the simulation is slower than the measured, but it is slightly improved with respect to the previous simulation. The overall deformation behaviour is well captured, presenting expansion during the injection stage, reaching the maximum value of the average strain very accurately and also predicting the compression during the dissipation. In contrast to the previous simulation, this compression is underestimated. Good agreement is also found in the fluid pressure at the top, computed as the maximum between air and water pressure. Moreover, the time in which the outflow takes place compares well with the measured one.

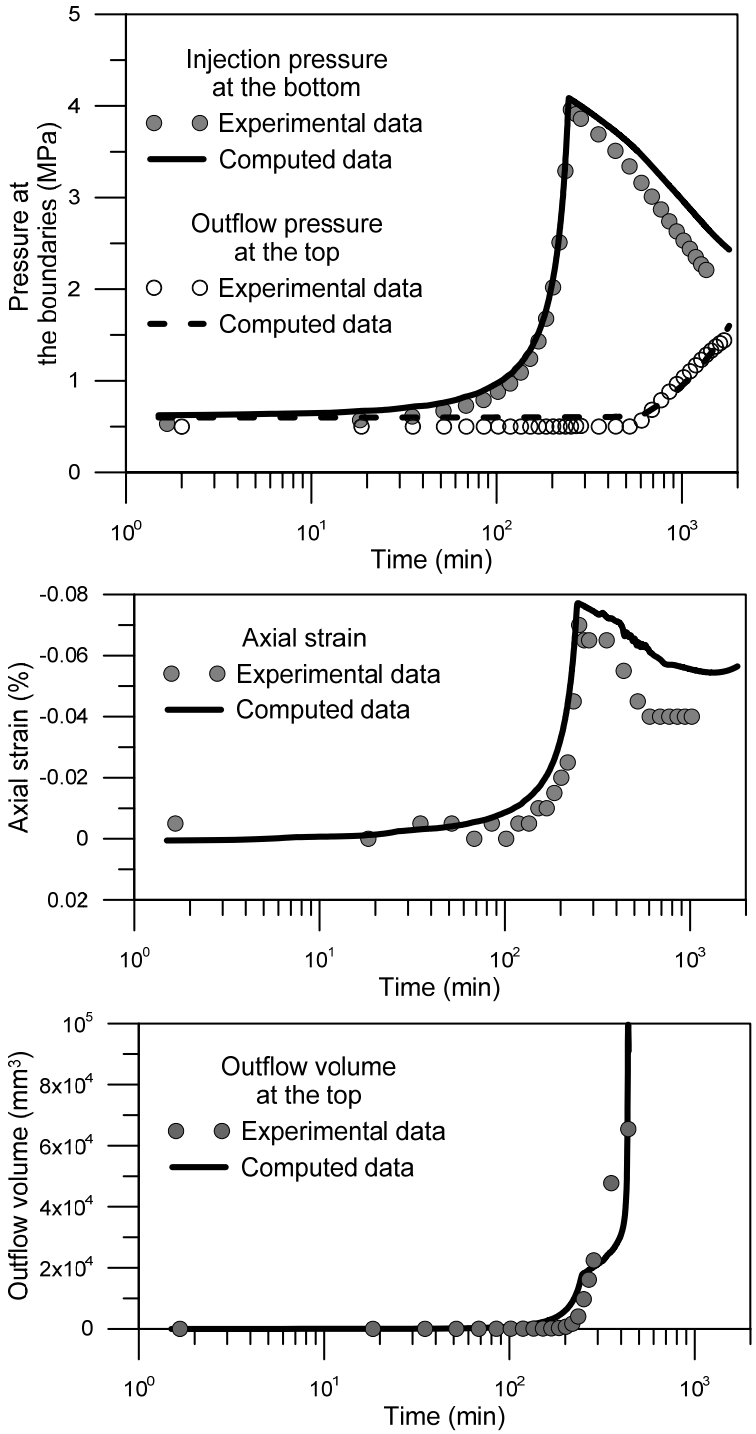

Figure 7-21. Computed versus measured in the middle section (at 0.0125m from the axis): a) injection and recovery pressures; b) axial strains; c) outflow volumes. Slow air injection test.

The following figure (Figure 7-22) presents contour and vector plots to examine the influence of the porosity field in the gas migration behaviour. To that end, the liquid degree of saturation, the absolute gas pressure, and the gas flux are presented at two different and representative times (330 and 400 minutes after the start of the injection). Initially, the desaturation front is rather uniform, but with increasing gas pressure, several preferential paths developed within the domain, clearly noticeable in gas flux vectors (gas flows are one order of magnitude higher in the preferential paths). The

degree of saturation contour plot allows observing that the opening (S_r decrease) and closure (S_r increase) of the fractures. However, this response with the random porosity is far from the experimental evidences which show that fractures open in the bedding direction. For this reason, none further analyses of this simulation were performed and major efforts to introduce special correlation accounting for the bedding direction are being carried out.

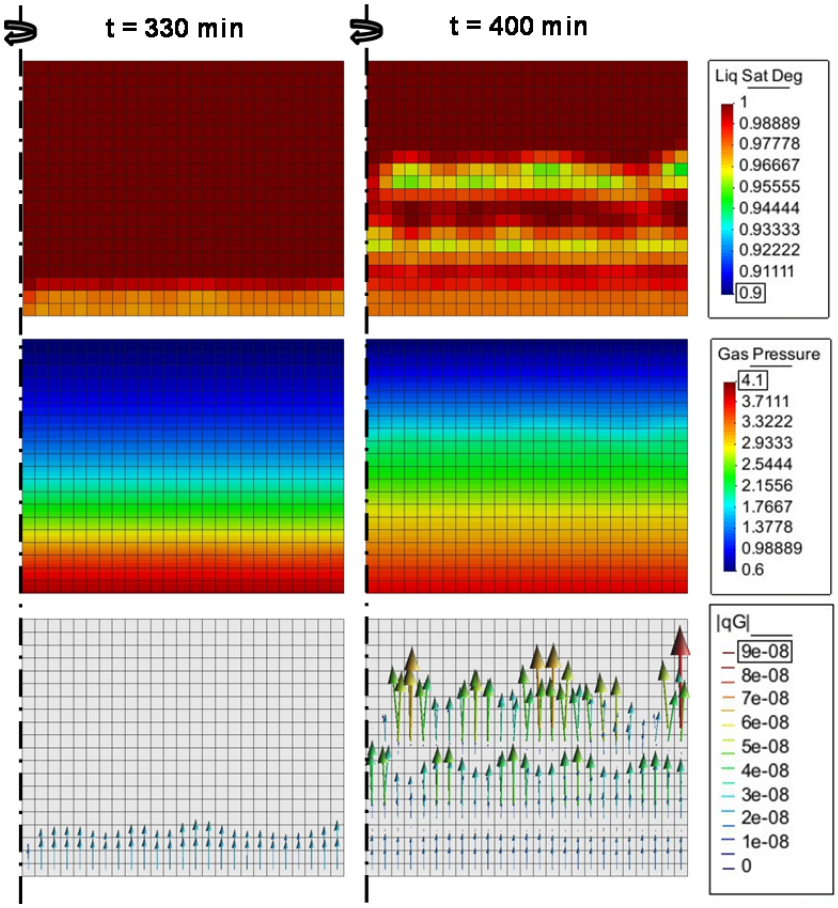

Figure 7-22. Simulated distribution of the liquid degree of saturation (top), the absolute gas pressure (middle, in MPa), the gas flux vectors (bottom) after 330 min and 400 min.

7.4. Concluding remarks

Experimental techniques used to study coupled multi-physics process (tracking relevant fields in time) do not always present the complete picture of understanding because the control conditions are usually imposed only on the boundaries of the specimen at the macroscopic (phenomenological) level. Moreover, these control conditions are applied to direct fields, but indirect processes (arising as a consequence of primary gradients) may evolve independently from any external control. Also, the homogeneity of the relevant fields inside the specimen is not ensured when transport processes occur (particularly from gas migration viewpoint). In addition, information on

local behaviour (and at the microscopic level) usually remains unknown, unless special experimental techniques are used. Consequently, the use of theoretical and/or numerical models must accompany the interpretation of the physical tests to better exploit the information provided by measurements and to offer additional confidence on the experimental results.

In this Thesis, a FE coupled hydro-mechanical numerical code was used to analyse the experimental results in order to validate the experimental techniques and to give greater confidence in the considered processes, besides providing complementary information on local processes during gas migration.

Initially, the hydro-mechanical loading paths carried out in the oedometer cell, including the pre-conditioning path, the saturation, the water pressurization, and the drained loading were simulated so that to obtain adequate hydro-mechanical parameters. Barcelona Basic Model was selected as the mechanical constitutive model and a full set of mechanical parameters was successfully obtained, as well as the required for classic equations of visco-capillary two-phase flow. Then, air migration stages on samples with bedding planes parallel to flow were simulated by introducing the embedded fracture permeability model, firstly in a pre-defined zone, and later in the entire domain. In both cases, a 2D axisymmetric representation of the sample was selected.

For the first simulation, the sample was modelled by two zones having different hydraulic properties: the matrix and the zone of fracture development (ZFD) in which the dominant advective flow of gas occurs. For both the matrix and the embedded fracture zone, the same mechanical parameters were chosen. Both for the constitutive model and the geometry of the problem simple approximations were made, but still able to capture the consequences of preferential path development.

The initial aperture of the fracture was set based on the dominant entrance pore size detected by MIP, and the current aperture was assumed to be governed by the local normal strain, once this overran a threshold strain. One of the experimental tests was used to calibrate the unknown parameters, while a second one was performed as a blind prediction test. It is worth noted that including the upstream and downstream reservoirs explicitly was necessary to simulate the flexibility of the experimental system and to accomplish reliable results, by properly assigning the conditions time history at the boundaries of the sample. The comparison between the experimental data and the model predictions showed encouraging agreement specially refer to volume change behaviour with has been seldom tackled. Besides the experimental data, numerical

modelling provided complementary information on gas and liquid pressures propagation into the sample or local stains which helped to better understand the consequences of air migration.

In the second case, the embedded fracture model was integrated into all the elements in a more general geometric configuration. For that purpose, a random porosity field with no spatial correlation was included, and thus, heterogeneity of the sample allowed automatically development of fracture patterns, without the need for a pre-defined fracture zone. Good agreement was also found when comparing with the experimental data, however, this approach moves away from the evidence of preferential pathways formation following the bedding direction. So that, random porosity filed with spatial correlation introduced by means of micro-tomography images can improve the simulations.

8
CONCLUSIONS

8.1. Summary

Deep geological disposal constitutes one of the most promising solutions for the safe isolation of long-lived and high-level radioactive waste high-level. The isolation of the radioactive wastes from the biosphere relies on a multi-barrier concept whose design offers several protective layers, natural or artificial, of which the highest level is the geological formation itself. Most of this research work in these materials concerns the initial transient processes of hydration under the combined action of the infiltrating water from the host rock and the heat generated by the canister. The experimental information concerning this transient process covers only a short time period of the expected lifetime of an engineered barrier. The long-term behaviour of clay barriers has received comparatively less attention. A significant issue in the long-term performance of clay buffers and the surrounding host rock concerns the generation of gases due to mainly anaerobic corrosion of metal parts of the disposal and their migration throughout the system.

Yet, gas transport through low-permeability rock formations seems to be controlled not only by the hydraulic and mechanical properties of the rock mass (intrinsic permeability, porosity, rock strength) but also by the gas pressure at the generation locus and the hydro-mechanical state of the rock but still there are many uncertainties. The present work was motivated by the challenging task of better understanding the gas migration process on argillaceous formations that are intended to host radioactive waste in geological disposals.

To this aim, laboratory scale experiments, which are clearly necessary to provide data for understanding theoretical frameworks and for validating predictive tools, were launched. Tests under oedometric and isotropic conditions followed robust protocols given priority to re-establish *in situ* conditions of the materials and their full saturation. Hydro-mechanical parameters were obtained during the initial stages. Relatively fast controlled-volume rate air injections tests (air pulse tests) were performed in order to study single-phase air flow mechanisms associated with the opening of stress-

dependent discontinuities, rather than on slower two-phase flow and air diffusion mechanisms through the matrix. The tests were designed specifically on samples with oriented bedding planes to investigate their effects on the coupled hydro-mechanical mechanisms dominating gas migration, pressurisation, and release in the clay. Influence of the injection rate was also studied. Volume changes were allowed in the experimental setups, and the deformation response was analysed during air injection, air pressure increase and dissipation. Air permeability was measured during the last stage.

Particular attention was given to the change in the pore network in order to detect the opening of fissures or discontinuities due to the air migration, by using three different techniques. Pore size distribution obtained from mercury intrusion porosimetry before and after the gas injection tests showed the evidence of preferential pathways formed during gas injection and pressurisation. Images from scanning electron microscopy and micro-focus computed tomography revealed the opening of fissures induced by gas passage following the bedding direction. These techniques allow the quantification of mean fissure features: aperture, separation, volume and connectivity.

The results of the experimental tests were further evaluated with the aid of numerical analysis, which gives preliminary suggestion on the local stress–strain response along gas injection and dissipation. A FE coupled hydro-mechanical code was used to analyse the results, adopting an embedded fracture permeability model within the continuous elements of the matrix in order to simulate the fracture opening in the material. The model allows tracking the degradation of the clay under gas pressurisation (increasing gas permeability) and helps in the comprehension of the local coupled processes dominating the response of the material. The comparison between the experimental data and the model predictions shows encouraging agreement.

8.2. Original contributions

The main original contributions of this PhD work include:

- Well-posed test protocols were developed to perform air injection tests on nearly saturated clayey materials given particular emphasis to the pre-conditioning paths in order to restore the *in situ* conditions.
- The coupled hydro-mechanical coupled response of the materials during gas transport process was studied. For that, volume change behaviour of the samples was measured along air pressurization and dissipation. Expansions

were consistently recorded during gas pressurization suggesting the opening of stress-dependent pathways. Afterwards, during gas pressure dissipation samples underwent compression which could partially close them.

- Deformational behaviour during gas injection and dissipation was determined by the injection rate. At slower rates expansions occurred during the injection stage, since pore pressure was nearly equilibrated, whereas, at faster rates, this response was delayed in time.
- Bedding orientation in Boom Clay samples tested under oedometer conditions played a fundamental role in the volume change behaviour during gas migration. Samples with bedding normal to flow, less constrained, consistently displayed larger expansions than samples with bedding parallel to flow.
- Estimation of the intrinsic permeability to air flow of the materials during the dissipation stages was found to be higher that the measured for water flow.
- Evaluation of microstructural changes induced by air migration was performed with three different techniques. The opening of fissures following the bedding direction was detected after air tests. The techniques used allow quantifying the volume of damage material which enables to establish a relationship with values of intrinsic permeability. Furthermore, aperture and separation of the fissures and also their connectivity were measured.
- Differences in fissure patterns detected with micro computed tomography were observed depending on the bedding orientation. Fissures of samples with bedding planes parallel to flow were narrower and closer than the ones detected in the sample tested with bedding normal to flow.
- Numerical simulations of the experimental results were performed using an embedded fracture permeability model which takes into account the air flow through preferential pathways. Experimental data at the micro-scale were used to fit the required parameters. The analysis provides complementary information on gas and liquid pressures propagation into the sample or local stains and helps to better understand the consequences of air migration.

8.3. Outlooks

The research work carried out in this PhD has enabled a better comprehension of the gas migration process in argillaceous rock formations. However, several aspects would merit additional investigations in order to further improve our understanding. The different outlooks are detailed hereafter.

8.3.1. Experimental research

Gas transport in clay-based materials is rapidly gaining importance in the context of energy-related geomechanics (disposal of radioactive waste, production of shale gas, CO_2 sequestration). However, the experimental characterization of argillaceous formations is indeed complex and time demanding which makes vital to develop simple and well-set experimental protocols to easily identify the main gas transport mechanisms and their coupling with the stress-strain response.

The complexity of this problem justifies the realisation of oedometer tests. Still, oedometer tests do not provide a full description of the material behaviour, as the lateral stress state is rarely measured and therefore, it is not possible to have a complete picture of the stress state of the materials. Then, using oedometer cells with lateral stress measurements would be very interesting. On the other hand, the use of isotropic cells in which stress state is well known comes across other concerns such as measuring radial displacement at high confining stress or reproducing anisotropy of the *in situ* stress field. Triaxial tests appear to be most appropiate to properly reproduce the stress state, yet, are complex to carry out, the measurement of displacement could be tricky, and their interpretation is not often straightforward. Added to that, pore pressure measurements during the gas migration are a keystone to better comprehend the pressurization mechanisms and how the pressure front propagates through the samples, but the installation of pressure transductors could produce some troubles to ensure the gas tightness and prevent leakages.

Additionally, the study of the pore network on intact samples and after injection tests provides interesting data on the development of the stress-dependant fractures. The uses of microscopy and/or tomography with higher resolutions would suppose an improvement in the quality of the measurements. A step forward would be to track the evolution of the microstructure during the gas injection tests. Integration of CT scanner in the experimental setup or using emerging techniques such as nanoparticle injection into the gas stream or acoustic emission can be used to study the origin and developments of pathways through clay and provide additional insights into the processes governing gas flow to help guide future numerical modelling.

Another concern that would merit increasing attention is the gas migration along interfaces, whether between the canister and clay-based materials or different clays (bentonite/host rock) because they can represent a weak point in the repositories since gas flow could take advantage of these technological gaps or discontinuities.

As more confidence is gained in understanding the gas transport process, laboratory experiments would evolve to study the long-term behaviour of the repositories by reproducing firstly the short-term. Initial transient combined processes of hydration and heat generated by the canisters could affect the response of the material along gas migration. Hence, experimental tests with hydration, temperature pulses, and gas injection stages would provide information to adequately evaluate the long-term safety of the disposal system.

8.3.2. Constitutive modelling

Modelling of gas migration in clayey materials remains an issue because gas injection experiments highlight that the migration occurs along localized gas pathways through the sample. Such behaviour is difficult to reproduce. Nonetheless, models dealing with equivalent continuum medium associated with the development of advective gas pathways through predefined localised fractures within the material seem to be promising. They can explain the continuous increase in permeability and subsequent decrease in gas entry pressure generated by the fracture opening which depends on the local strains.

Even so, these approaches are very dependent on the definition of the initial fracture geometry which is somewhat arbitrary, in many cases based on qualitative experimental data and only in a few on quantitative data. Therefore, introducing the exact geometry, thickness, number of pathways and proper separation between them, which involves the need of more experimental data on microstructure evolution, would improve the predictive capabilities of these models.

Another question that arises is that the opening of pathways generates an excessive increase of permeability. Although embedded fracture models limit its increase including a maximum aperture, it is still very effective. Accounting for fracture roughness and tortuosity would help to restrict its response.

REFERENCES

Albert, W., Bläsi, H.R., Madritsch, H., Vogt, T., & Weber, H.P., 2012. Geologie, Stratigraphie, Strukturgeologie, bohrlochgeophysikalisches Logging und Wasserproben der Geothermiebohrung Schlattingen SLA-1 (Rohdaten). *Nagra Project Report NPB 12-16*.

Alonso, E.E., Gens, A., & Josa, A., 1990. A constitutive model for partially saturated soils. *Géotechnique*, 40(3), pp.405–430.

Alonso, E.E., Olivella, S., & Arnedo, D., 2006. Mechanisms of gas transport in clay barriers. *Journal of Iberian Geology*, 32(2), pp.175–196.

Amann, F. & Vogelhuber, M., 2015. Expert Report - Assessment of Geomechanical Properties of Intact Opalinus Clay. *Expert Report ENSI 33/461*, p.69.

Andò, E., Bésuelle, P., Hall, S. a., Viggiani, G., & Desrues, J., 2012. Experimental micromechanics: grain-scale observation of sand deformation. *Géotechnique Letters*, 2, pp.107–112.

Arnedo, D., Alonso, E.E., & Olivella, S., 2013a. Gas flow in anisotropic claystone: modelling triaxial experiments. *International Journal for Numerical and Analytical Methods in Geomechanics*, 37, pp.2239–2256.

Arnedo, D., Alonso, E.E., & Olivella, S., 2013b. Gas flow in anisotropic claystone: modelling triaxial experiments. *International Journal for Numerical and Analytical Methods in Geomechanics*, 37, pp.2239–2256.

Arnedo, D., Alonso, E.E., Olivella, S., & Romero, E., 2008. Gas injection tests on sand/bentonite mixtures in the laboratory. Experimental results and numerical modelling. *Physics and Chemistry of the Earth*, 33, pp.237–247.

Arson, C. & Pereira, J.-M., 2013. Particle Shape Effect on Macro-and Micro Behaviours of Monodisperse Ellipsoids. *International Journal for Numerical and Analytical Methods in Geomechanics*, 37, pp.810–831.

Bear, J., 1972. *Dynamics of Fluids in Porous Media*, Elsevier, New York.

Bésuelle, P., Viggiani, G., Desrues, J., Coll, C., & Charrier, P., 2014. A Laboratory Experimental Study of the Hydromechanical Behavior of Boom Clay. *Rock*

Mechanics and Rock Engineering, 47, pp.143–155.

Blümling, P., Bernier, F., Lebon, P., & Derek Martin, C., 2007. The excavation damaged zone in clay formations time-dependent behaviour and influence on performance assessment. *Physics and Chemistry of the Earth*, 32(8–14), pp.588–599.

Bruchon, J.-F., Vandamme, M., Pereira, J.-M., Lenoir, N., Bornert, M., & Delage, P., 2014. A μCT investigation of the collapse of a loose unsaturated sand specimen: Comparison between macroscopic and mesoscopic scale. In K. Soga et al., eds. *Geomechanics from Micro to Macro*. Taylor & Francis Group, London, pp. 1171–1176.

Cardoso, R., Romero, E., Lima, A., & Ferrari, A., 2007. A Comparative Study of Soil Suction Measurement Using Two Different High-Range Psychrometers. *Experimental Unsaturated Soil Mechanics*, 112, pp.79–93.

Chen, G.J., Sillen, X., Verstricht, J., & Li, X.L., 2011. ATLAS III in situ heating test in boom clay: Field data, observation and interpretation. *Computers and Geotechnics*, 38, pp.683–696.

Coll, C., 2005. *Endommagement des roches argileuses et perméabilité induite au voisinage d ' ouvrages souterrains*. PhD Thesis, Universite Joseph Fourier–Grenoble I, France.

Cornet, F.., 2009. In-situ Stress measurement Campaign. *SCK•CEN Underground Laboratory Boerentang, Mol, March 2009, Final report, Ecole et Observatoire des Sciences de la Terre, Université de Strasbourg*.

Cotecchia, F., Cafaro, F., & Guglielmi, S., 2016. Microstructural Changes in Clays Generated by Compression Explored by Means of SEM and Image Processing. *Procedia Engineering*, 158, pp.57–62.

Cui, Y.-J., Delage, P., & Sultan, N., 2010. Yielding and plastic behaviour of Boom clay. *Géotechnique*, 60(9), pp.657–666.

Cui, Y.-J., Le, T.T., Tang, A.-M., Delage, P., & Li, X.-L., 2009. Investigating the time-dependent behaviour of Boom clay under thermo-mechanical loading. *Géotechnique*, 59(4), pp.319–329.

Cui, Y.-J. & Tang, A.M., 2013. On the chemo-thermo-hydro-mechanical behaviour of

geological and engineered barriers. *Journal of Rock Mechanics and Geotechnical Engineering*, 5, pp.169–178.

Cuss, R., Harrington, J., Giot, R., & Auvray, C., 2014. Experimental observations of mechanical dilation at the onset of gas flow in Callovo-Oxfordian claystone. *Geological Society, London, Special Publications*, 400, pp.507–519.

Dao, L.Q., 2015. *Etude du comportement anisotrope de l'argile de Boom*. PhD Thesis, Université Paris-Est, Paris, France.

Davy, C.A., Skoczylas, F., Lebon, P., & Dubois, T., 2009. Gas migration properties through a bentonite / argillite interface. *Applied Clay Science*, 42, pp.639–648.

DeCraen, M., 1998. *The formation of septarian carbonate concretions in organic - rich argillaceous sediments*. PhD Thesis, KULeuven , Belgium.

DeCraen, M., Wang, L., Van Geet, M., & Moors, H., 2004. Geochemistry of Boom Clay pore water at the Mol site. *Scientific Report SCK·CEN-BLG-990*, p.181.

Delage, P., Le, T.T., Tang, A.-M., Cui, Y.-J., & Li, X.-L., 2008. Suction effects in deep Boom clay block samples. *Géotechnique*, 57(1), pp.239–244.

Delage, P., Marcial, D., Cui, Y.J., & Ruiz, X., 2006. Ageing effects in a compacted bentonite: a microstructure approach. *Géotechnique*, 56(5), pp.291–304.

Delage, P., Romero, E., & Tarantino, A., 2008. Recent developments in the techniques of controlling and measuring suction in unsaturated soils. In *Keynote Lecture, Proc. 1st Eur. Conf. on Unsaturated Soils, Durham, United Kingdom, July 2-4*. pp. 33–52.

Delahaye, C.H. & Alonso, E.E., 2002. Soil heterogeneity and preferential paths for gas migration. *Engineering Geology*, 64, pp.251–271.

Deng, H., Fitts, J.P., & Peters, C.A., 2016. Quantifying fracture geometry with X-ray tomography: Technique of Iterative Local Thresholding (TILT) for 3D image segmentation. *Computational Geosciences*, 20, pp.231–244.

Deng, Y.F., Tang, A.M., Cui, Y.J., & Li, X.L., 2011. Study on the hydraulic conductivity of Boom clay. *Canadian Geotechnical Journal*, 48, pp.1461–1470.

Desbois, G., Urai, J.L., Hemes, S., Brassinnes, S., De Craen, M., & Sillen, X., 2014. Nanometer-scale pore fluid distribution and drying damage in preserved clay

cores from Belgian clay formations inferred by BIB-cryo-SEM. *Engineering Geology*, 179, pp.117–131.

Desbois, G., Urai, J.L., Houben, M.E., & Sholokhova, Y., 2010. Typology, morphology and connectivity of pore space in claystones from reference site for research using BIB, FIB and cryo-SEM methods. *EPJ Web of Conferences*, 6, p.22005.

Fall, M., Nasir, O., & Nguyen, T.S., 2014. A coupled hydro-mechanical model for simulation of gas migration in host sedimentary rocks for nuclear waste repositories. *Engineering Geology*, 176, pp.24–44.

Ferrari, A., Favero, V., & Laloui, L., 2014. Experimental analysis of the retention behavior of shales. *International Journal of Rock Mechanics and Mining Sciences*, 72, pp.61–70.

Ferrari, A., Favero, V., Manca, D., & Laloui, L., 2012. Geotechnical characterization of core samples from the geothermal well Schlattingen SLA-1 by LMS/EPFL. *NAGRA Technical Report NAB 12-50*, p.79.

Ferrari, A. & Laloui, L., 2013. Advances in the Testing of the Hydro-mechanical Behaviour of Shales. In *Multiphysical Testing of Soils and Shales*. pp. 57–68.

Fleury, M. & Canet, D., 2014. Water orientation in smectites using NMR nutation experiments. *Journal of Physical Chemistry C*, 118, pp.4733–4740.

François, B., Laloui, L., & Laurent, C., 2009. Thermo-hydro-mechanical simulation of ATLAS in situ large scale test in Boom Clay. *Computers and Geotechnics*, 36, pp.626–640.

Frieg, B., Grob, H., Hertrich, M., Madritsch, H., Müller, H., Vietor, T., Vogt, T., & Weber, H., 2015. Novel Approach for the Exploration of the Muschelkalk Aquifer in Switzerland for the CO2-free Production of Vegetables. In *World Geothermal Congress, Melbourne, Australia, 19-25 April 2015*.

Gallé, C., 2000. Gas breakthrough pressure in compacted Fo-Ca clay and interfacial gas overpressure in waste disposal context. *Applied Clay Science*, 17, pp.85–97.

García-Bengochea, I., Lovell, C.W., & Altschaeffl, A.G., 1979. Pore distribution and permeability of silty clays. *Journal Geotechnical Engineering, ASCE*, 105(7), pp.839–856.

van Geet, M. & Swennen, R., 2001. Quantitative 3D-fracture analysis by means of microfocus X-ray computer tomography (μ-CT): an example from coal. *Geophysical Research Letters*, 28(17), pp.3333–3336.

Gens, A., Sánchez, M., Guimarães, L.D.N., Alonso, E.E., Lloret, A., Olivella, S., Villar, M.V., & Huertas, F., 2009. A full-scale in situ heating test for high-level nuclear waste disposal: observations, analysis and interpretation. *Géotechnique*, 59(4), pp.377–399.

Gerard, P., Harrington, J., Charlier, R., & Collin, F., 2014. Modelling of localised gas preferential pathways in claystone. *International Journal of Rock Mechanics and Mining Sciences*, 67, pp.104–114.

Giger, S. & Marschall, P., 2014. Geomechanical properties, rock models and in-situ stress conditions fo Opalinus Clay in Northern Switzerland. *NAGRA Technical Report NAB 14-01*, p.108.

Gonzalez-Blanco, L., Romero, E., Jommi, C., Li, X., & Sillen, X., 2016. Gas migration in a cenozoic clay: Experimental results and numerical modelling. *Geomechanics for Energy and the Environment*, 6, pp.81–100.

Gonzalez-Blanco, L., Romero, E., Li, X.-L., & Sillen, X., 2014. Importance of sample volume changes and material degradation on gas transport properties in Boom Clay. In *International Congress on Environmental Geotechnics. "7th International Congress on Enviromental Geotechnics: Lessons, Learnings & Challenges*. pp. 850–857.

Graham, J., Halayko, K.G., Hume, H., Kirkham, T., Gray, M., & Oscarson, D., 2002. A capillarity-advective model for gas break-through in clays. *Engineering Geology*, 64, pp.273–286.

Gutiérrez-Rodrigo, V., Villar, M.V., Martín, P.L., Romero, F.J., & Barcala, J.M., 2015. Gas-breakthrough pressure of FEBEX bentonite. *Geological Society , London , Special Publications*, 415, pp.47–57.

Harrington, J., Volckaert, G., Jacobs, E., Maes, N., Areias, L., Charlier, R., Frédéric, C., Gerard, P., Radu, J.P., Svoboda, J., Granet, S., Alcoverro, J., Arnedo, D., Olivella, S., Alonso, E., Marschall, P., Gaus, I., Rüedi, J., Cuss, R., et al., 2013. Summary report : Experiments and modelling of excavation damage zone (EDZ) behaviour in argillaceous and crystalline rocks (Work Package 4). *EC FORGE Project*

Report D4.24-R, p.129.

Harrington, J.F., Cuss, R.J., Noy, D.J., Graham, C.C., Milodowski, A.E., Hall, M., & Talandier, J., 2015. Stress coupling in Callovo-Oxfordian claystone during gas and water flow. In *6th International Conference Clays in Natural and Engineered Barriers for Radioactive Waste Confinement, Brussels, March 23-26*. pp. 162–163.

Harrington, J.F. & Horseman, S.T., 2003. Gas migration in KBS-3 buffer bentonite. *SKB Technical Report TR-03-02*, p.53.

Harrington, J.F. & Horseman, S.T., 1999. Gas transport properties of clays and mudrocks. *Geological Society, London, Special Publications*, 158(1), pp.107–124.

Harrington, J.F., Milodowski, A.E., Graham, C.C., Rushton, J.C., & Cuss, R.J., 2012. Evidence for gas-induced pathways in clay using a nanoparticle injection technique. *Mineralogical Magazine*, 76(8), pp.3327–3336.

Hemes, S., Desbois, G., Urai, J.L., Schröppel, B., & Schwarz, J.O., 2015. Multi-scale characterization of porosity in Boom Clay (HADES-level, Mol, Belgium) using a combination of X-ray μ-CT, 2D BIB-SEM and FIB-SEM tomography. *Microporous and Mesoporous Materials*, 208, pp.1–20.

Hildenbrand, A., Schlömer, S., & Krooss, B.M., 2002. Gas breakthrough experiments on fine-grained sedimentary rocks. *Geofluids*, 2, pp.3–23.

Hildenbrand, a, Schlömer, S., Krooss, B.M., & Littke, R., 2004. Gas breakthrough experiments on pelitics rocks: comparitive study with N2, CO2 and CH4. *Geofluids*, 4, pp.61–80.

Horseman, S.T., Harrington, J.F., & Sellin, P., 1999. Gas migration in clay barriers. *Engineering Geology*, 54, pp.139–149.

Horseman, S.T., Higgo, J.J.W., Alexander, J., & Harrington, J.F., 1996. Water, Gas and Solute Movement Through Argillaceous Media. *Report CC-91/1 OECD*, p.290.

Horseman, S.T., Winter, M.G., & Entwistle, D.C., 1987. Geotechnical characterization of Boom Clay in relation to the disposal of radioactive waste. *Final report EUR 10987*, p.100.

Jacops, E., Volckaert, G., Maes, N., Weetjens, E., & Govaerts, J., 2013. Determination of gas diffusion coefficients in saturated porous media: He and CH4 diffusion in

Boom Clay. *Applied Clay Science*, 83–84, pp.217–223.

Jacops, E., Wouters, K., Volckaert, G., Moors, H., Maes, N., Bruggeman, C., Swennen, R., & Littke, R., 2015. Measuring the effective diffusion coefficient of dissolved hydrogen in saturated Boom Clay. *Applied Geochemistry*, 61, pp.175–184.

Jahns, E., 2013. Geomechanical laboratory tests on Opalinus Clay cores from the bore hole Schlattingen SLA-1. *NAGRA Technical Report NAB 13-18*, p.117.

Josh, M., Esteban, L., Delle Piane, C., Sarout, J., Dewhurst, D.N., & Clennell, M.B., 2012. Laboratory characterisation of shale properties. *Journal of Petroleum Science and Engineering*, 88–89, pp.107–124.

Kawaragi, C., Yoneda, T., Sato, T., & Kaneko, K., 2009. Microstructure of saturated bentonites characterized by X-ray CT observations. *Engineering Geology*, 106, pp.51–57.

Keller, A.A., 1997. High resolution CAT imaging of fractures in consolidated materials. *Int. J. Rock Mech. Min. Sci.*, 34(3–4), p.358.

Ketcham, R.A. & Carlson, W.D., 2001. Acquisition, optimization and interpretation of x-ray computed tomographic imagery: Applications to the geosciences. *Computers and Geosciences*, 27, pp.381–400.

Ketcham, R.A., Slottke, D.T., & Sharp, J.M., 2010. Three-dimensional measurement of fractures in heterogeneous materials using high-resolution X-ray computed tomography. *Geosphere*, 6(5).

Kozaki, T., Suzuki, S., Kozai, N., Sato, S., & Ohashi, H., 2001. Observation of Microstructures of Compacted Bentonite by Microfocus X-Ray Computerized Tomography (Micro-CT). *Journal of Nuclear Science and Technology*, 38(8), pp.697–699.

Landis, E.N., Nagy, E.N., & Keane, D.T., 2003. Microstructure and fracture in three dimensions. *Engineering Fracture Mechanics*, 70(7), pp.911–925.

Le, T.T., 2008. *Comportement thermo-hydro-mécanique de l ' argile de Boom*. PhD Thesis, Ecole Nationale des Ponts et Chaussées, France.

Le, T.T., Delage, P., Cui, Y.J., Tang, a M., Lima, A., Romero, E.E., Gens, A., & Li, X.L., 2008. Water retention properties of Boom clay : A comparison between

different experimental techniques. In *Unsaturated Soils: Advances in Geo-Engineering- Toll et al. (eds)*. Taylor & Francis Group, London, pp. 229–234.

Li, X., Bernier, F., Vietor, T., & Lebon, P., 2007. TIMODAZ: Thermal impact on the damaged zone around a radioactive waste disposal in clay host rocks. Deliverable 2. *TIMODAZ, FI6W-CT-036449, European Commision Project*, p.106.

Li, X.L., Chen, G.J., Verstricht, J., Troullinos, I., Dizier, A., Leysens, J., Van Marcke, P., & Sillen, X., 2015. The Praclay Experiment at URL Hades, Mol, Blegium. In *13th ISRM International Congress of Rock Mechanics, 10-13 May, Montreal, Canada*. Canadian Institute of Mining, Metallurgy and Petroleum.

Lima, A., 2011. *Thermo-Hydro-Mechanical Behaviour of two deep Belgian clay Formations: Boom and Ypresian clays*. PhD Thesis, Universitat Politècnica de Catalunya, Barcelona, Spain.

Liu, C., Shi, B., Zhou, J., & Tang, C., 2011. Quantification and characterization of microporosity by image processing, geometric measurement and statistical methods: Application on SEM images of clay materials. *Applied Clay Science*, 54, pp.97–106.

Liu, H.H., Rutqvist, J., & Berryman, J.G., 2009. On the relationship between stress and elastic strain for porous and fractured rock. *International Journal of Rock Mechanics and Mining Sciences*, 46, pp.289–296.

Liu, H.H., Rutqvist, J., & Birkholzer, J.T., 2011. Constitutive relationships for elastic deformation of clay rock: Data analysis. *Rock Mechanics and Rock Engineering*, 44, pp.463–468.

Liu, J., Song, Y., Skoczylas, F., & Liu, J., 2016. Gas migration through water-saturated bentonite – sand mixtures , COx argillite , and their interfaces. *Canadian Geotechnical Journal*, 53, pp.60–71.

Liu, Z.B., Shao, J.F., Liu, T.G., Xie, S.Y., & Conil, N., 2016. Gas permeability evolution mechanism during creep of a low permeable claystone. *Applied Clay Science*, 129, pp.47–53.

Mäder, U., 2011. Recipe and preparation of a simplified artificial pore water for Opalinus Clay and Brown Dogger. *Nagra Report AN 11-159.*

Marschall, P., Horseman, S., & Gimmi, T., 2005. Characterisation of Gas Transport

Properties of the Opalinus Clay, a Potential Host Rock Formation for Radioactive Waste Disposal. *Oil & Gas Science and Technology*, 60(1), pp.121–139.

Monfared, M., Sulem, J., Delage, P., & Mohajerani, M., 2012. On the THM behaviour of a sheared Boom clay sample: Application to the behaviour and sealing properties of the EDZ. *Engineering Geology*, 124, pp.47–58.

Muurinen, A., Carlsson, T., & Root, A., 2013. Bentonite pore distribution based on SAXS, chloride exclusion and NMR studies. *Posiva Working Report 2013-53*, p.74.

Nagra, 2002. Opalinus Clay Project. Demonstration of feasibility of disposal ("Entsorgungsnachweis") for spent fuel, vitrified high-level waste and long-lived intermediate-level easte. *Nagra Report*, p.24.

Nguyen, X.P., 2013. *Étude Du Comportement Chimico-Hydro- Mécanique Des Argiles Raides Dans Le Contexte Du Stockage De Déchets Radioactifs*. PhD Thesis, Université Paris-Est, Pairs, France.

Olivella, S. & Alonso, E.E., 2008. Gas flow through clay barriers. *Géotechnique*, 58(3), pp.157–176.

Olivella, S., Gens, a., Carrera, J., & Alonso, E.E., 1996. Numerical formulation for a simulator (CODE_BRIGHT) for the coupled analysis of saline media. *Engineering Computations*, 13(7), pp.87–112.

ONDRAF/NIRAS, 2013. Research, Development and Demonstration (RD&D) Plan for the geological disposal of high-level and/or long-lived radioactive waste including irradiated fuel of considered as waste, State-of-the-art report as of December 2012. *ONDRAF/NIRAS, report NIROND-TR 2013-12 E*, p.413.

ONDRAF/NIRAS, 2001. Technical overview of the SAFIR 2 report. Safety Assessment and Feasibility Interim Report 2. *ONDRAF/NIRAS Technical Report NIROND 2001-05*, p.278.

Ortiz, L., Volckaert, G., & Mallants, D., 2002. Gas generation and migration in Boom Clay, a potential host rock formation for nuclear waste storage. *Engineering Geology*, 64, pp.287–296.

Pineda, J., Alonso, E.E., & Romero, E., 2014. Environmental degradation of claystones. *Géotechnique*, 64(1), pp.64–82.

Pineda, J., Romero, E., Alonso, E.E., & Pérez, T., 2014. A new high-pressure triaxial apparatus for inducing and tracking hydro-mechanical degradation of clayey rocks. *Geotechnical Testing Journal*, 37(6), pp.1–15.

Prime, N., Levasseur, S., Miny, L., Charlier, R., Léonard, A., & Collin, F., 2016. Drying induced shrinkage of Boom Clay: an experimental investigation. *Canadian Geotechnical Journal*, 53(3), pp.396–409.

Pusch, R. & Forsberg, T., 1983. Gas migration through bentonite. *SKB Technical Report TR 83-71*, p.31.

Rodwell, W., Norris, S., Cool, W., Cuñado, M., Johnson, L., Mäntynen, M., Müller, W., Sellin, P., Snellman, M., Talandier, J., Vieno, T., & Vines, S., 2003. A thematic network on gas issues in safety assessment of deep repositories for radioactive waste (Gasnet). *Final Report EUR 20620*, p.61.

Romero, E., 2013. A microstructural insight into compacted clayey soils and their hydraulic properties. *Engineering Geology*, 165, pp.3–19.

Romero, E., 1999. *Characterisation and Thermo-Hydro-Mechanical behaviour of unsaturated Boom Clay: an experimental study*. PhD TThesis, Universitat Politècnica de Catalunya, Barcelona, Spain.

Romero, E., Arnedo, D., Alonso, E.E., & Marschall, P., 2010. Gas Injection Laboratory Experiments on Opalinus Clay. In *Clays in Natural & Engineered Barriers for Radioactive Waste Confinement, 4th International Meeting, March 2010, Nantes, France*. pp. 113–114.

Romero, E. & Gómez, R., 2013. Water and air permeability tests on deep core samples from Schlattingen SLA-1 borehole. *NAGRA Technical Report NAB 13-51*, p.65.

Romero, E. & Gonzalez-Blanco, L., 2015. Complementary water and air permeability tests on core samples from Schlattingen SLA-1 borehole. *NAGRA Technical Report NAB 15-06*, p.79.

Romero, E., Sau, N., Lima, A., Van Baelen, H., Sillen, X., & Li, X., 2016. Studying the thermal conductivity of a deep Eocene clay formation: Direct measurements vs back-analysis results. *Geomechanics for Energy and the Environment*, pp.1–14.

Romero, E., Senger, R., Marschall, P., & Gómez, R., 2012. Air tests on low-permeability claystone formations. Experimental techniques, results and

simulations. In *International Workshop Advances in Multiphysical Testing of Soils and Shales, Lausanne*. Springer, pp. 69–83.

Romero, E. & Simms, P.H., 2008. Microstructure investigation in unsaturated soils: A review with special attention to contribution of Mercury Intrusion Porosimetry and Environmental Scanning Electron Microscopy. *Geotechnical and Geological Engineering*, 26, pp.705–727.

Saba, S., Delage, P., Lenoir, N., Cui, Y.J., Tang, A.M., & Barnichon, J.D., 2014. Further insight into the microstructure of compacted bentonite-sand mixture. *Engineering Geology*, 168, pp.141–148.

Schneider, C.A., Rasband, W.S., & Eliceiri, K.W., 2012. NIH Image to ImageJ: 25 years of image analysis. *Nature Methods*, 9(7), pp.671–675.

Seiphoori, A., Ferrari, A., & Laloui, L., 2014. Water retention behaviour and microstructural evolution of MX-80 bentonite during wetting and drying cycles. *Géotechnique*, 64(9), pp.721–734.

Sellers, E., Vervoort, A., & Van Cleynenbreugel, J., 2003. Three-dimensional visualization of fractures in rock test samples, simulating deep level mining excavations, using X-ray computed tomography. *Geological Society, London, Special Publications*, 215(1), pp.69–80.

Senger, R., Romero, E., Ferrari, A., & Marschall, P., 2014. Characterization of gas flow through low-permeability claystone: laboratory experiments and two-phase flow analyses. *Geological Society, London, Special Publications (Online)*, 400, pp.531–543.

Senger, R., Romero, E., & Marschall, P., 2015. Modeling of gas migration through low-prermeability clay using information on pressure and deformation from fast air injection tests. In *PROCEEDINGS, TOUGH Symposium 2012 Lawrence Berkeley National Laboratory, Berkeley, California, September 28-30, 2015*. pp. 1–5.

Shaw, R.P., 2013. *Gas Generation and Migration* Shaw RP (E.,

Sillen, X. & Marivoet, J., 2007. Thermal impact of a HLW repository in clay. *External Report SCK·CEN-ER-38*, p.63.

Tanai, K., Kanno, T., & Gallé, C., 1996. Experimental Study of Gas Permeabilities and Breakthrough Pressures in Clays. *MRS Proceedings*, 465, p.995.

Tanai, K. & Yamamoto, M., 2003. Experimental and Modeling Studies on Gas Migration in Kunigel V1 Bentonite. *JNC Technical Report TN8400 2003-024*, p.23.

Valkó, P. & Economides, M.J., 1997. Transient Behavior of Finite Conductivity Horizontal Fractures. *SPE Journal*, 2.

Vietor, T., Müller, H., Frieg, B., & Klee, G., 2012. Stress measurements in the geothermal well Schlattingen, Northern Switzerland. In *Veröffentlichung des Instituts für Geomechanik der Technischen Universität Bergakademie Freiberg, Heft 2012-1,Geomechanik-Kolloquium, Freiberg, 16 November 2012*. pp. 105–112.

Villar, M.V., Gutiérrez-Rodrigo, V., Martín, P.L., Romero, F.J., & Barcala, J.M., 2012. Results of the tests on bentonite (Part 2). FORGE. *FORGE Report D3.27*, p.60.

Villar, M.V., Martín, P.L., Romero, F.J., & Barcala, J.M., 2012. Results of the tests on bentonite (Part 1). FORGE. *FORGE Report D3.15*, p.30.

Volckaert, G., Bernier, F., Sillen, X., Van Geet, M., Mayor, J.C., Göbel, I., Blümling, P., Frieg, B., & Su, K., 2005. Similarities and Differences in the Behaviour of Plastic and Indurated Clays. In *Proceedings Euradwaste'04. Radioactive waste management community policy and research initiatives. EUR-21027*. pp. 281–291.

Volckaert, G., Mallants, D., Bush, R.A., & Lambers, L., 1998. Long-term environmental impact of underground disposal of P&T waste. In *Final Partitioning and Transmutation Workshop , SCK.CEN, Mol, Belgium*.

Volckaert, G., Ortiz, L., De Canniere, P., Put, M., Horseman, S.T., Harrington, J.F., Fioravante, V., & Impey, M., 1995. MEGAS Modelling and experiments on gas migration in repository host rocks. *EUR 16235 MEGAS Final Report Phase 1*, p.464.

Voorn, M., Exner, U., & Rath, A., 2013. Multiscale Hessian fracture filtering for the enhancement and segmentation of narrow fractures in 3D image data. *Computers and Geosciences*, 57, pp.44–53.

Webb, P.A., 2001. An Introduction To The Physical Characterization of Materials by Mercury Intrusion Porosimetry with Emphasis On Reduction And Presentation of Experimental Data. *Micrometrics Instrument Corp.*, p.23.

Webb, P.A. & Orr, C., 1997. Analytical methods in fine particle technology.

Micromeritics Instrument Corp., Norcross, GA, USA, p.301.

Wellington, S.L. & Vinegar, H.J., 1987. X-ray computerized tomography. *Journal of Petroleum Technology*, 39, pp.885–898.

Wiseall, A.C., Cuss, R.J., Graham, C.C., & Harrington, J.F., 2015. The visualization of flow paths in experimental studies of clay-rich materials. *Mineralogical Magazine*, 79(6), pp.1335–1342.

Yamamoto, S., Kumagai, M., Koga, K., & Sato, S., 2015. Mechanical Stability of Engineered Barriers in Sub-surface Disposal Facility during Gas Migration Based on Coupled Hydro-Mechanical Modelling. *Geological Society, London, Special Publications*, 415, pp.213–224.

Yoshimi, Y. & Osterberg, J.O., 1963. Compression of partially saturated cohesive soils. *ASCE J. of the Soil Mechanics and Foundations Div.*, 89(4), pp.1–24.

Zeelmaekers, E., 2011. *Computerized qualitative and quantitative clay mineralogy*. PhD Thesis, Katholieke Univeriteit Leuven, Belgium.

Appendix A
CALIBRATION OF LABORATORY EQUIPMENT

A.1. Axial displacement calibration of the oedometer cell

The vertical deformation of the structure of the oedometer cell was carefully calibrated for loading and unloading paths. To this aim, a solid steel disc that simulated the sample (2 cm in height and 5 cm in diameter) and the oedometer ring was placed inside the cell. The metallic disc deformation was considered negligible. A contact loading of 100 kPa was applied. Then, the vertical loading was increased up to 10 MPa at 0.5 kPa/min. The displacement was measured during this period as well as during the unloading path which was performed at a faster rate of 30 kPa/min (Figure A-1). A power law was fitted with the recorded displacements during loading and unloading which resulted very similar. This calibration was used to correct the loading and unloading paths performed with the oedometer cell.

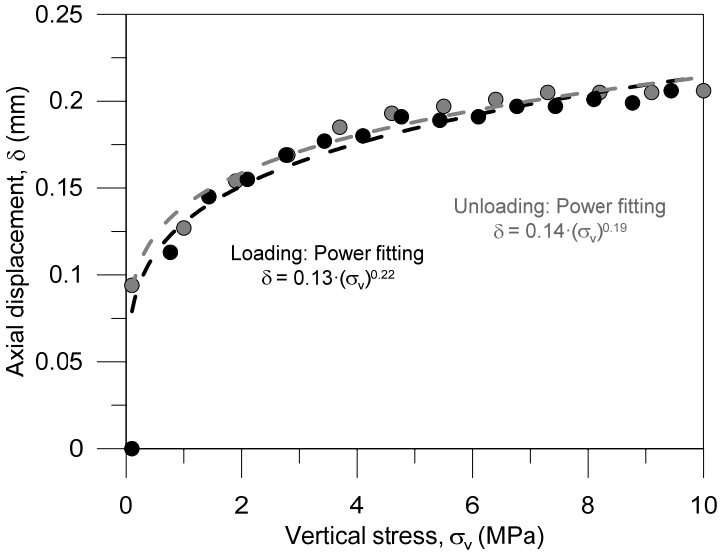

Figure A-1. Axial displacement due to the deformation of the structure of the oedometric cell.

A.2. Axial displacement calibration of the isotropic cell

The vertical displacement of the structure of the isotropic cell was carefully calibrated for loading and unloading paths. To this aim, a steel solid disc that simulates the sample (2.5 cm in height and 5 cm in diameter) was placed inside the cell. The metallic disc deformation was considered negligible. A contact loading of 100 kPa was applied.

Then the isotropic loading was increased up to 20 MPa at 30 kPa/min. The displacement was measured during this period as well as during the unloading path (Figure A-2). A power law was fitted with the recorded displacements during loading and a linear one with the unloading results. This calibration was also used to correct the loading/unloading paths presented in this work and also in Romero & Gómez (2013) since the same isotropic cell was used.

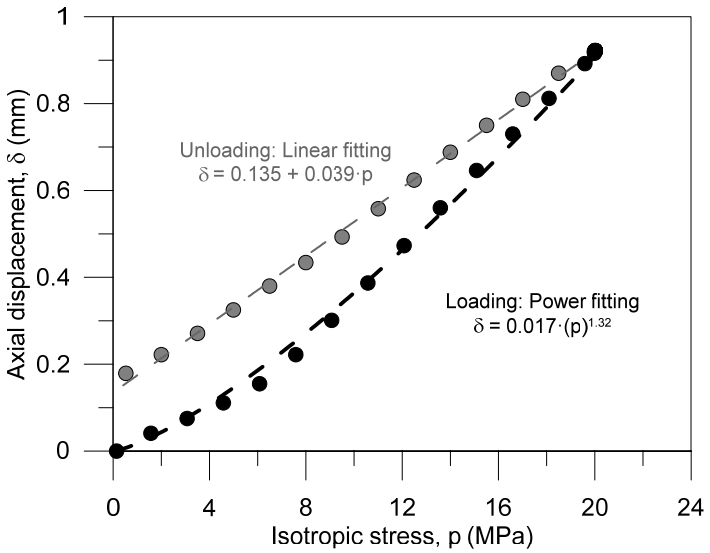

Figure A-2. Axial displacement due to the deformation of the structure of the isotropic cell.

Appendix B
COMPLEMENTARY TESTS

B.1. Splitting test

Tensile strength on Boom Clay samples was indirectly determined through splitting tests for samples with both orientations, parallel and normal to press axis.

Figure B-1 shows the equipment (real setup and a drawing) used to carry out these tests. It consists of two plates between which the sample was placed, having only two contact points for the application of the load. It also has a Perspex chamber to prevent desiccation of the sample during the test. This equipment was put inside a press with axial displacement control (1 mm/min).and measurements of the load cell were recorded during the experiments.

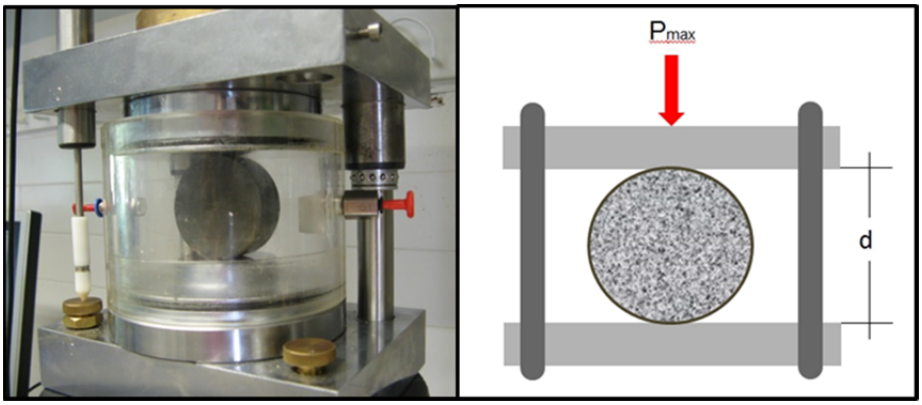

Figure B-1. Real setup and drawing of the equipment used to determine tensile strength.

Data obtained (load versus axial displacement) are shown in Figure B-2 for both tests. As expected, the sample with bedding planes parallel to the axis of applied load, early developed a fracture in the bedding direction; while in the sample with bedding planes normal to the axis developed a flattening in the contact point, but no fracture appeared despite a drop in the measured load. Figure B-3 shows a picture of both samples after the tests. From the maximum load, using Equation B.1, the tensile strength was obtained, giving a value of 0.63 MPa for the sample with bedding planes normal to load axis and 0.37 MPa for the sample with bedding planes parallel.

$$\sigma_t = \frac{2 \cdot P_{max}}{\pi \cdot L \cdot d} \qquad \text{(B.1)}$$

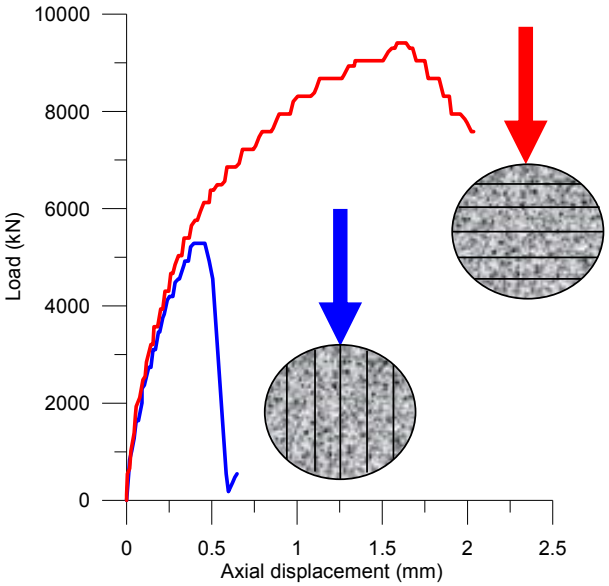

Figure B-2. Data recorded during the splitting test for both samples.

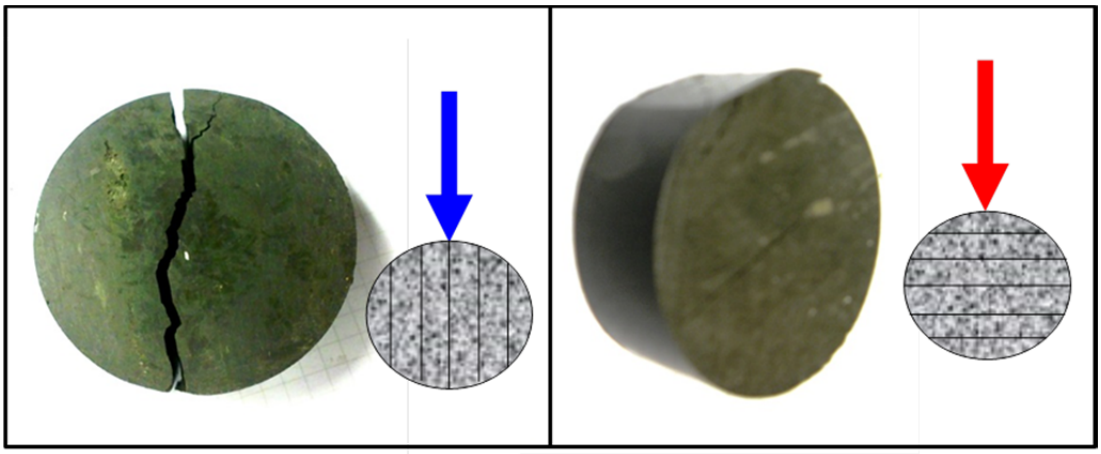

Figure B-3. Samples after the splitting tests.

B.2. Diffusion test

To analyse the air diffusion on Boom Clay, a test based on a 'ceramic concept' experiment was performed on the oedometer cell. This experiment consisted on pressurize with air a known volume of water in the top of the sample. The water went through the sample in a first step and water permeability could be calculated measuring the water volume in the bottom of the sample. Once the water ran out, a change was noticeable in the trend of the measured outflow, giving the value of the air diffusion.

Firstly, the sample was loaded up to 3 MPa to reach the *in situ* conditions. Secondly, the top and bottom caps of the sample were saturated at atmospheric conditions. Afterwards, a pressure of 0.1 MPa was imposed at the bottom of the sample through the automatic controller, meanwhile, the water in the top reservoir was pressurized

applying a constant air pressure of 2 MPa. Figure B-4 presents a sketch of it. This test was carried out in a sample trimmed with the bedding planes normal to flow (Dif_1_N).

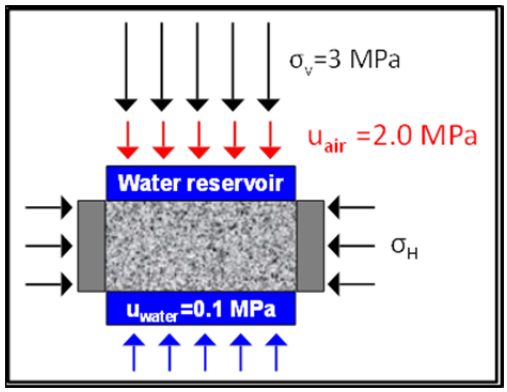

Figure B-4. Sketch of the diffusion test protocol.

The value of the diffusion coefficient was obtained with Eq. B.2:

$$D = \frac{H}{nAh}\frac{(u_w+u_{atm})}{(u_a-u_w)}\frac{\delta V}{\delta t} \quad \text{(B.2)}$$

where H is the sample thickness, n the porosity, u_w the water pressure, u_a the air pressure, h the volumetric coefficient of solubility of dissolved air in water (at T=22ºC, h=0.018) and $\delta V/\delta t$ was obtained from the experimental data depicted in Figure B-5.

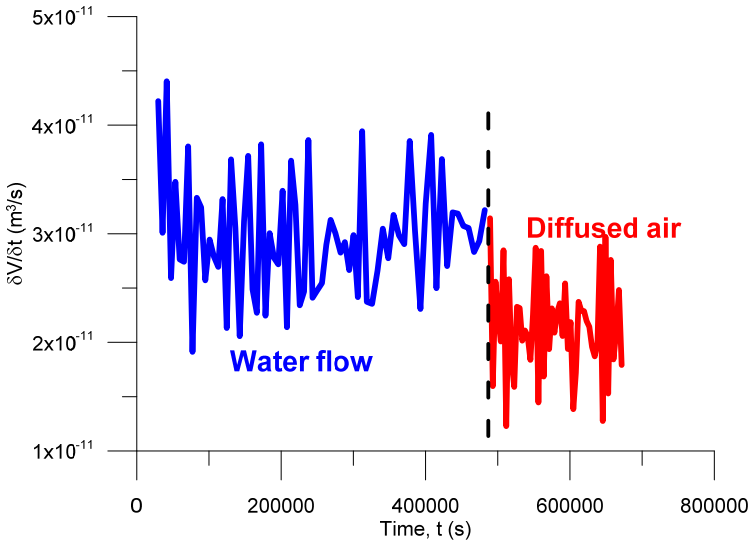

Figure B-5. Outflow volume variation during the diffusion test.

The value of water permeability measured in this test was $1.58 \cdot 10^{-12}$ m/s, which is in good agreement with reported values for samples with bedding planes normal to flow (see Figure 4-12). However, the value of air diffusion coefficient calculated through this method was $3.2 \cdot 10^{-9}$ m^2/s, higher than the reported by Jacops et al. (2015) for

hydrogen (between 2.4 and $7.5 \cdot 10^{-10}$ m^2/s) and which was finally used for the simulations.

Appendix C
RECORDED DATA DURING WATER PERMEABILITY STAGES

C.1. Results for Boom Clay samples

Figure C-1 to Figure C-13 show the evolution with time of the outflow volume during the water permeability determination stages for the entire set of tests in Boom Clay samples. The water permeability was determined at several stages of the oedometer tests based on the water outflow volume under steady-state conditions, at different stress states and pressure gradients which are indicated in each plot. For more information see Chapter 4 Section 4.1.3.

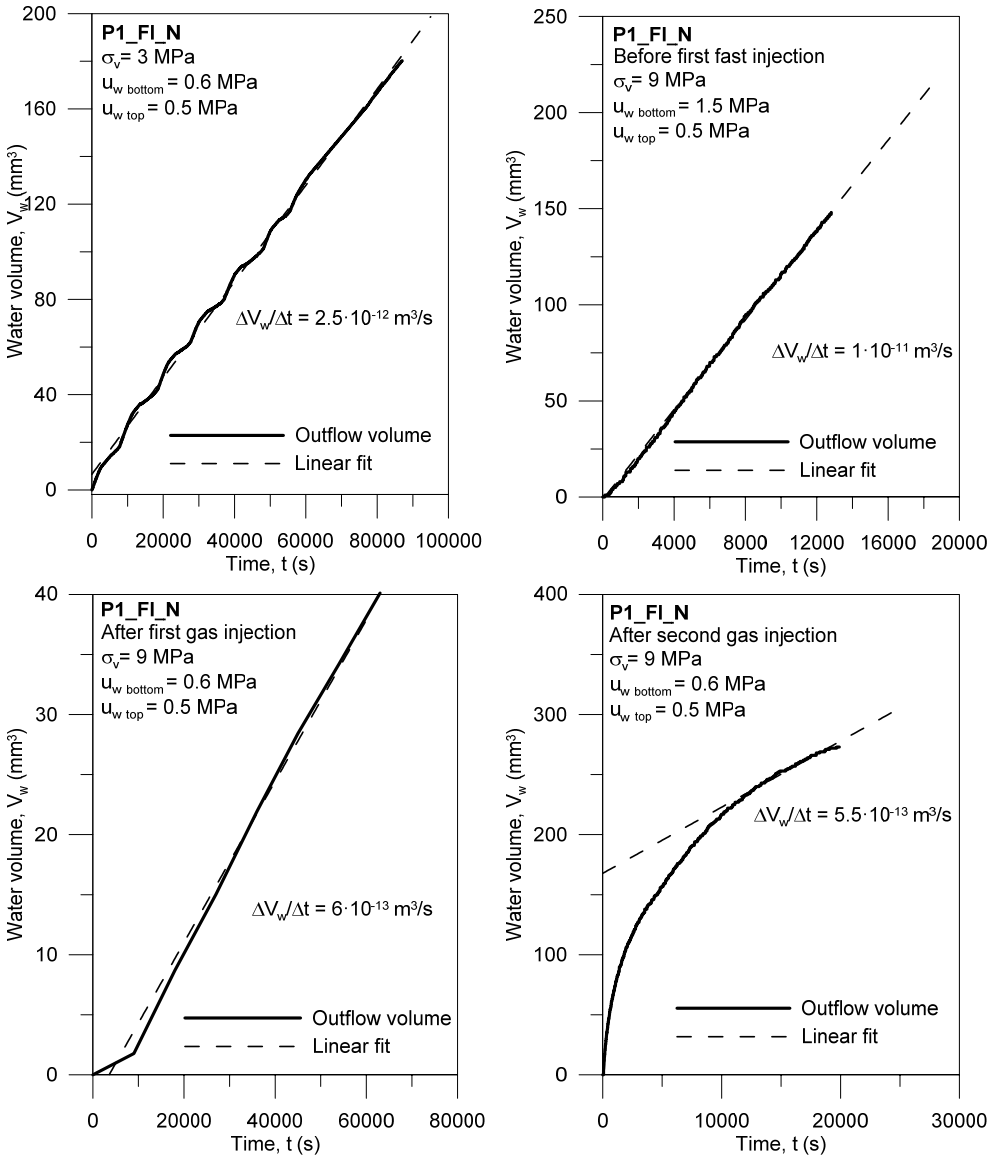

Figure C-1. Time evolution of water outflow volumes during the different stages of water injection for P1_FI_N test.

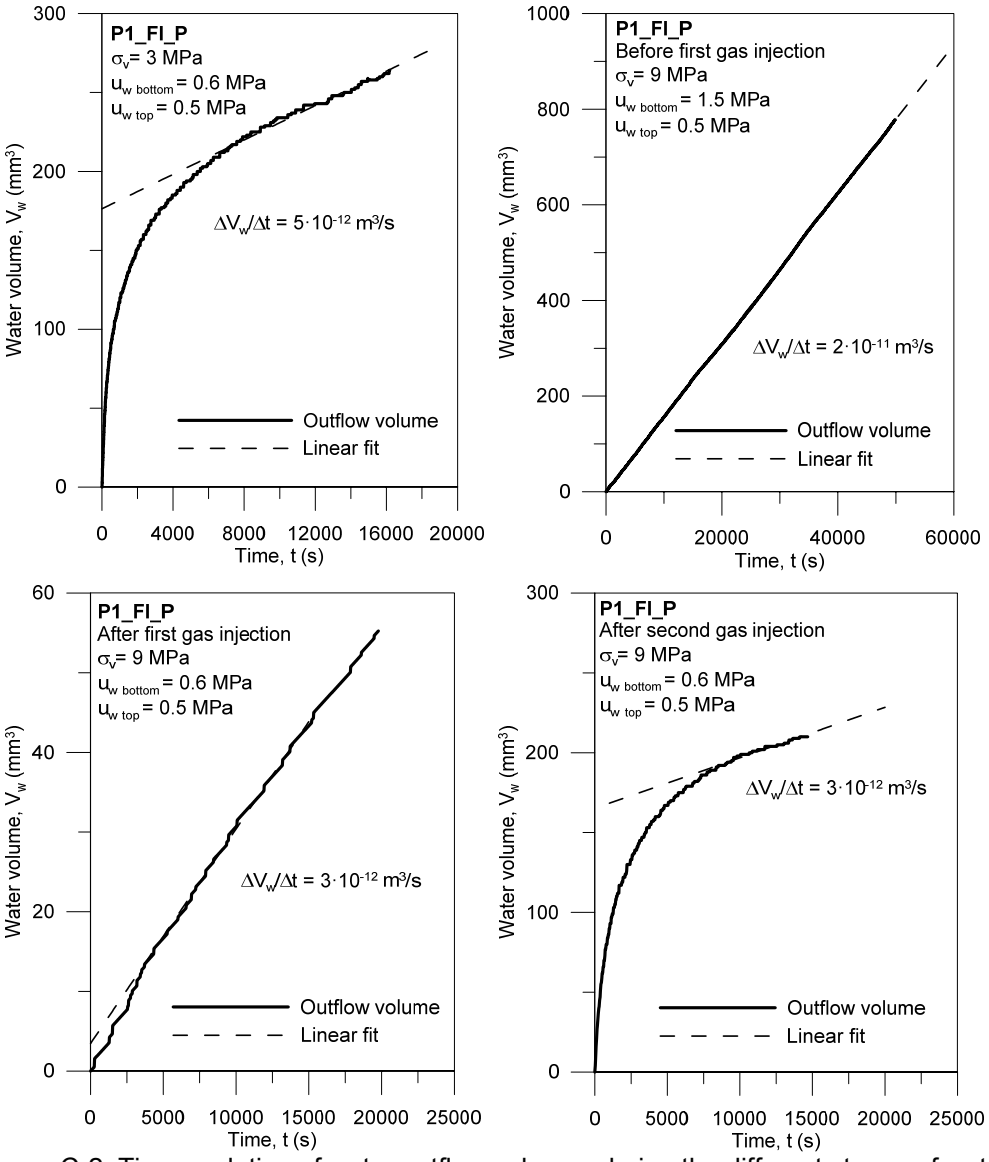

Figure C-2. Time evolution of water outflow volumes during the different stages of water injection for P1_FI_P test.

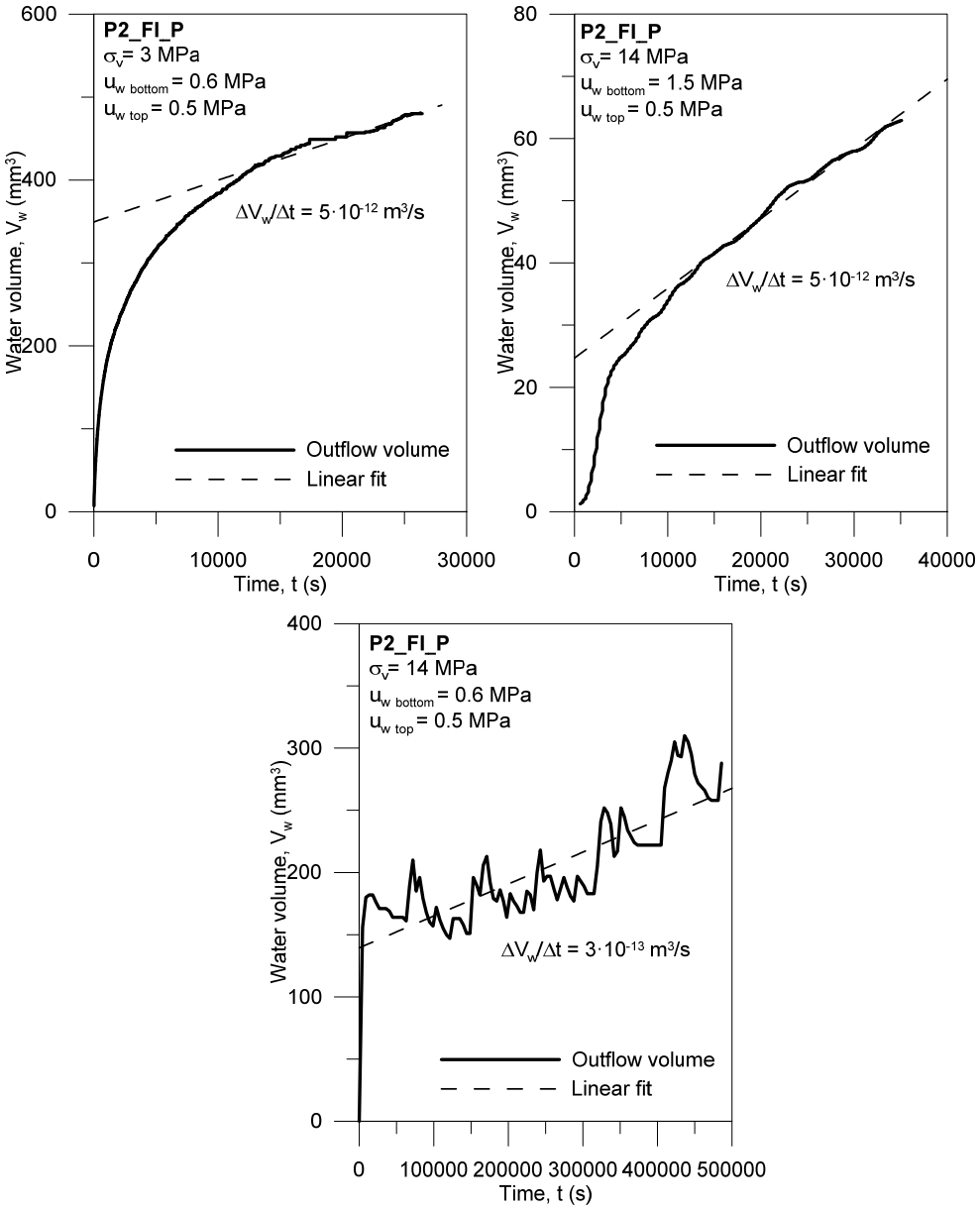

Figure C-3. Time evolution of water outflow volumes during the different stages of water injection for P2_FI_P test.

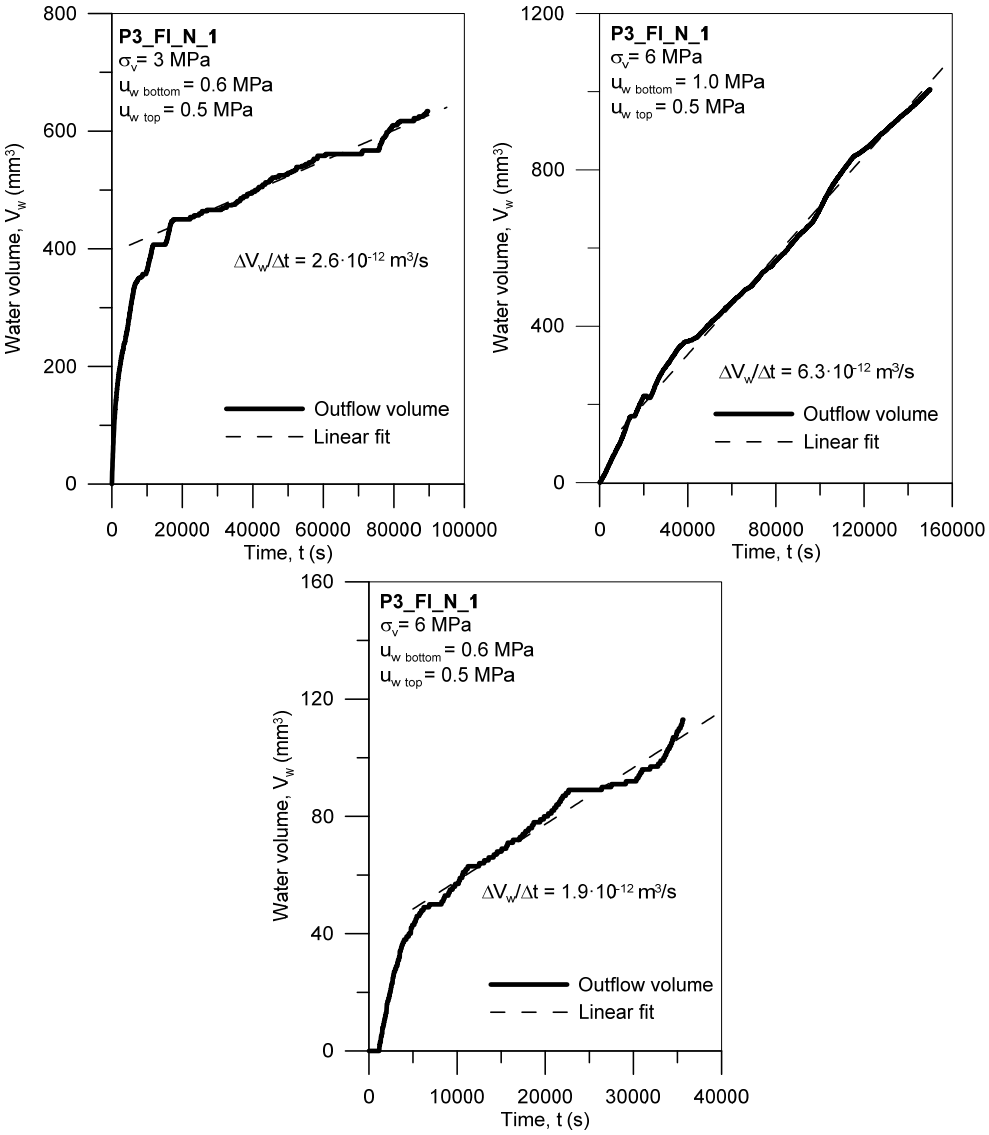

Figure C-4. Time evolution of water outflow volumes during the different stages of water injection for P3_FI_N_1 test.

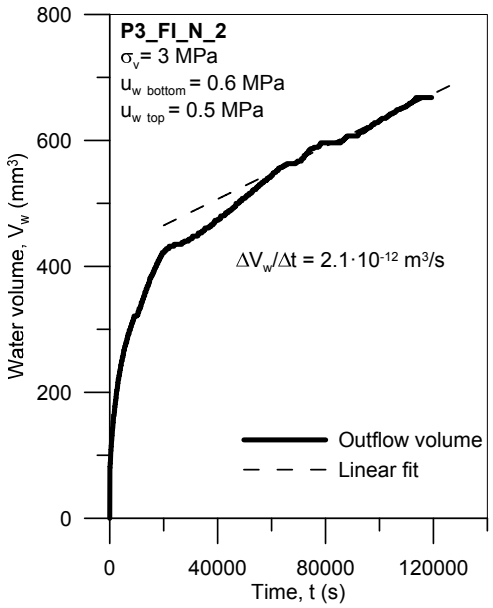

Figure C-5. Time evolution of water outflow volumes during the different stages of water injection for P3_FI_N_2 test.

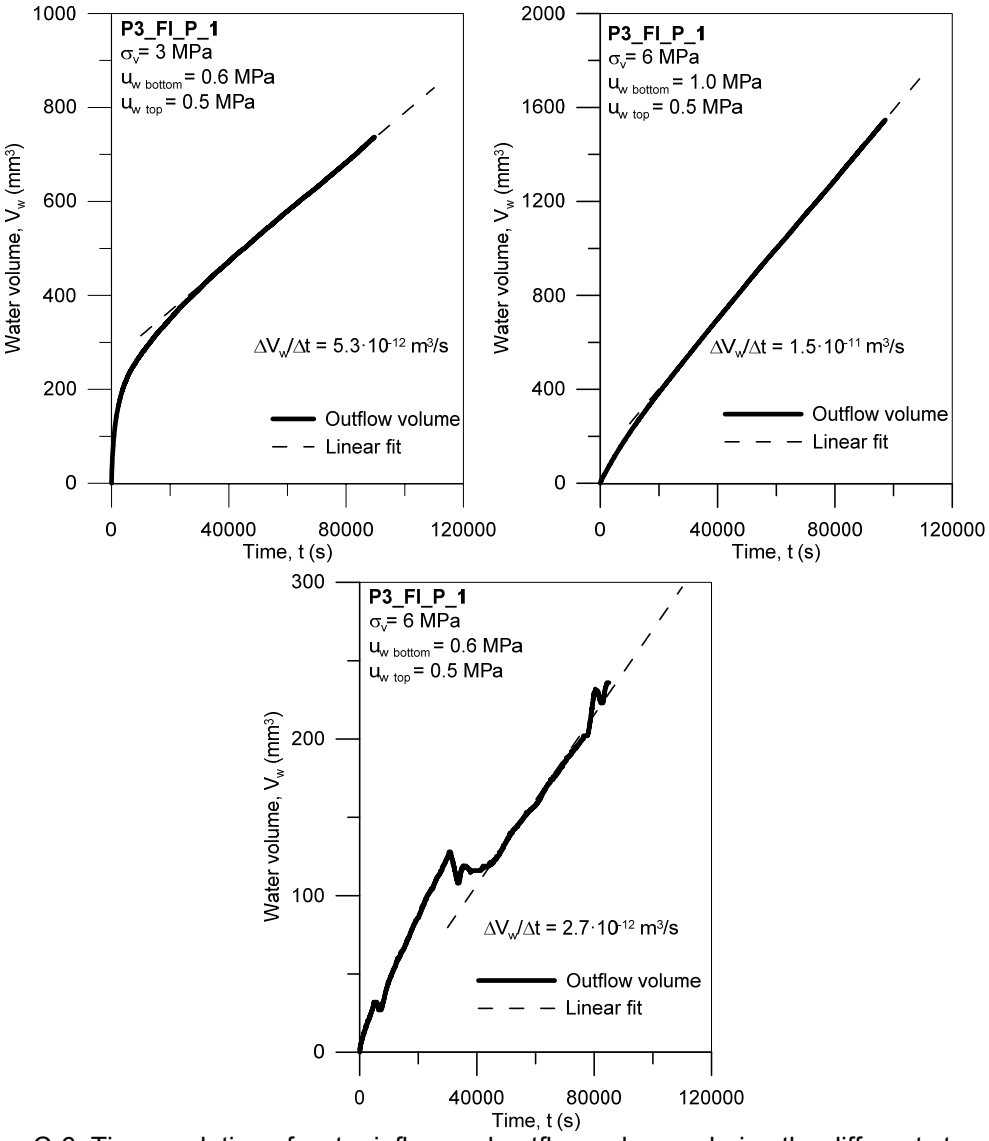

Figure C-6. Time evolution of water inflow and outflow volumes during the different stages of water injection for P3_FI_P_1.

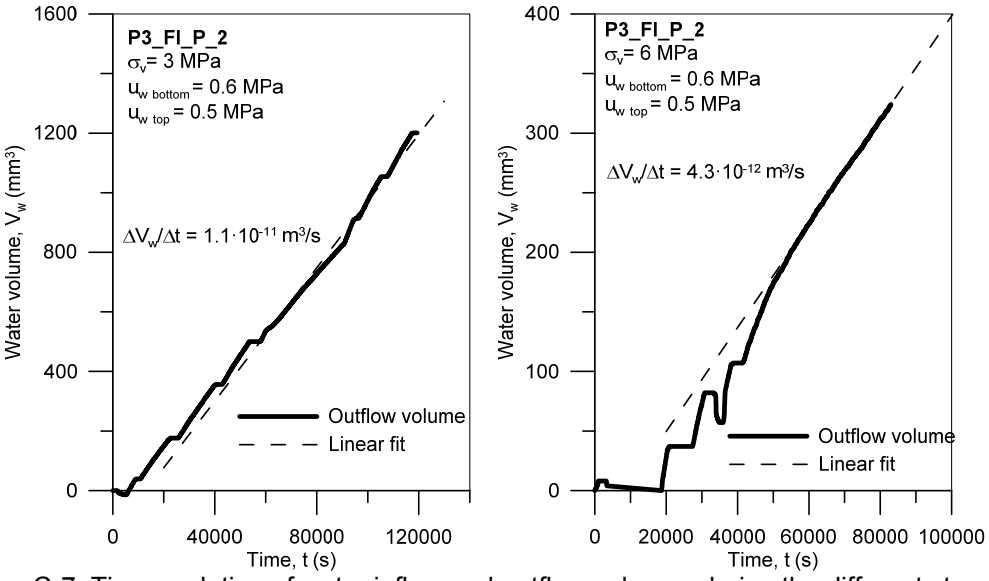

Figure C-7. Time evolution of water inflow and outflow volumes during the different stages of water injection for P3_FI_P_2.

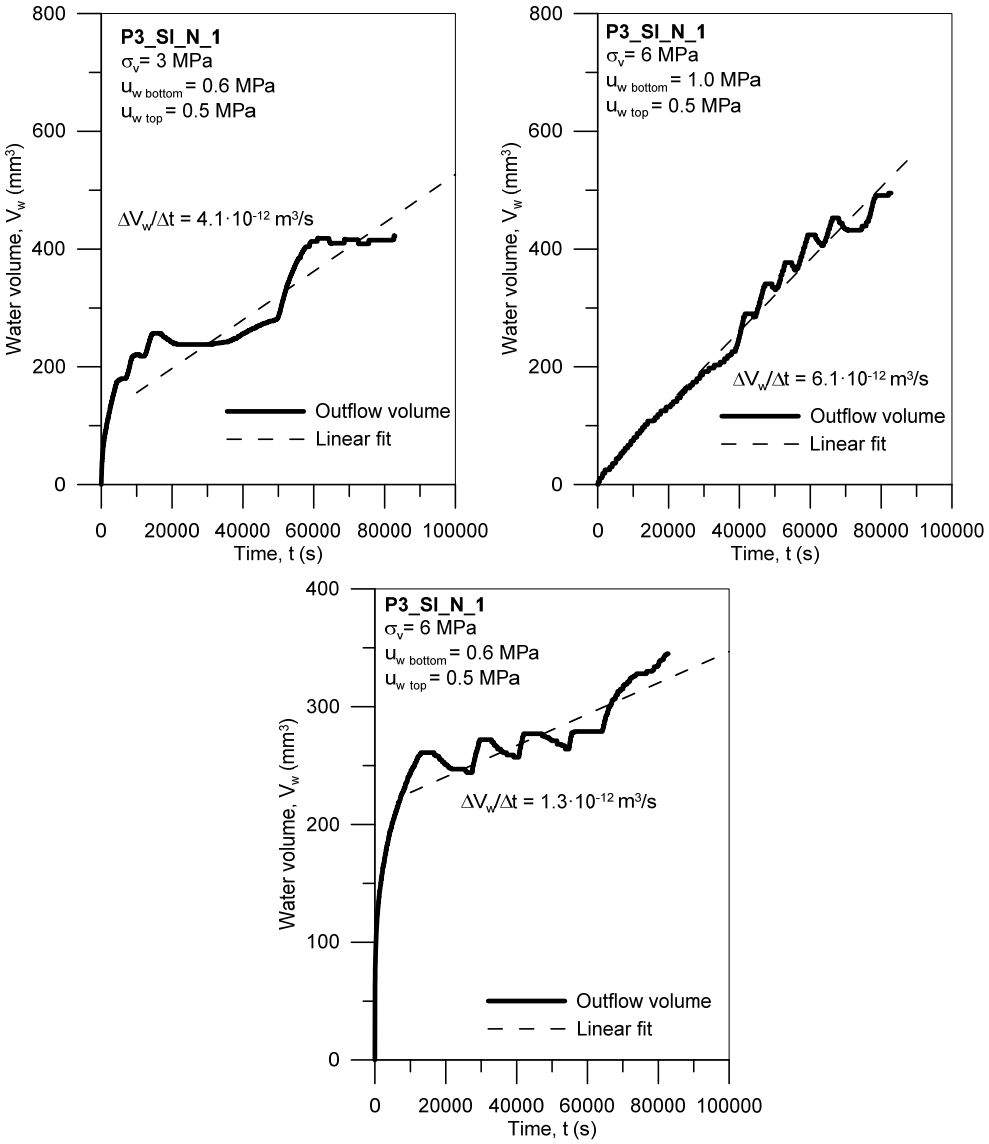

Figure C-8. Time evolution of water outflow volumes during the different stages of water injection for P3_SI_N_1.

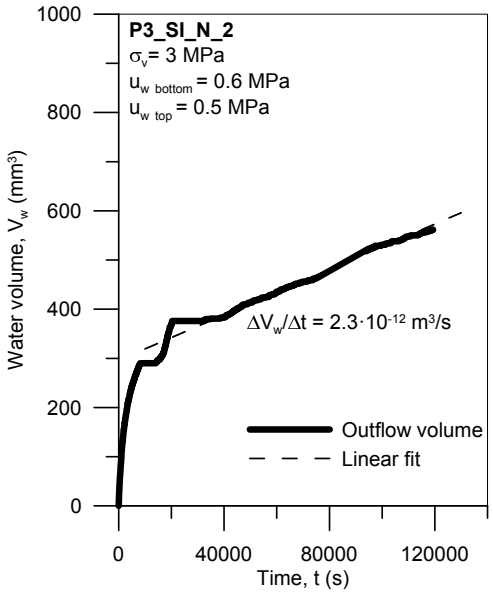

Figure C-9. Time evolution of water outflow volumes during the different stages of water injection for P3_SI_N_2.

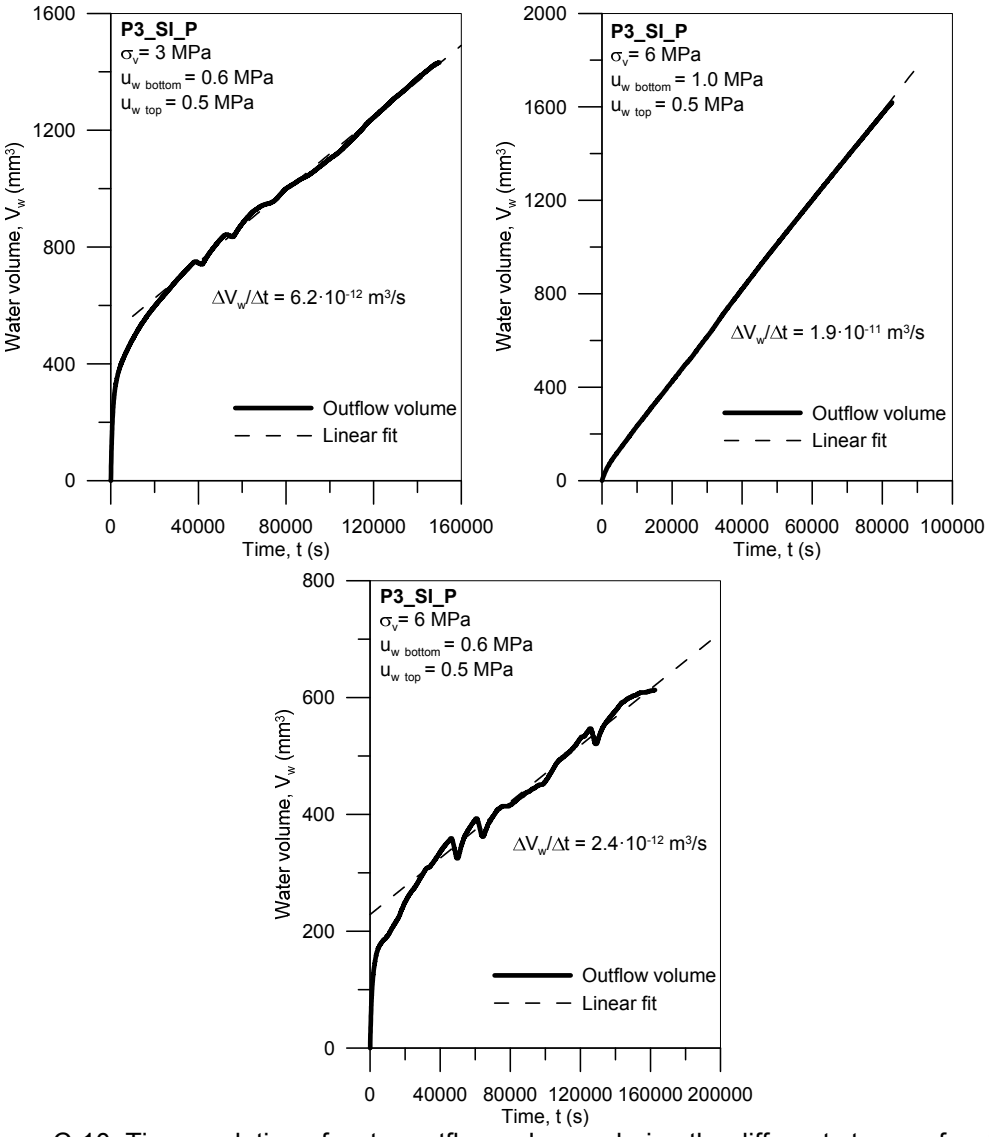

Figure C-10. Time evolution of water outflow volumes during the different stages of water injection for P3_SI_P.

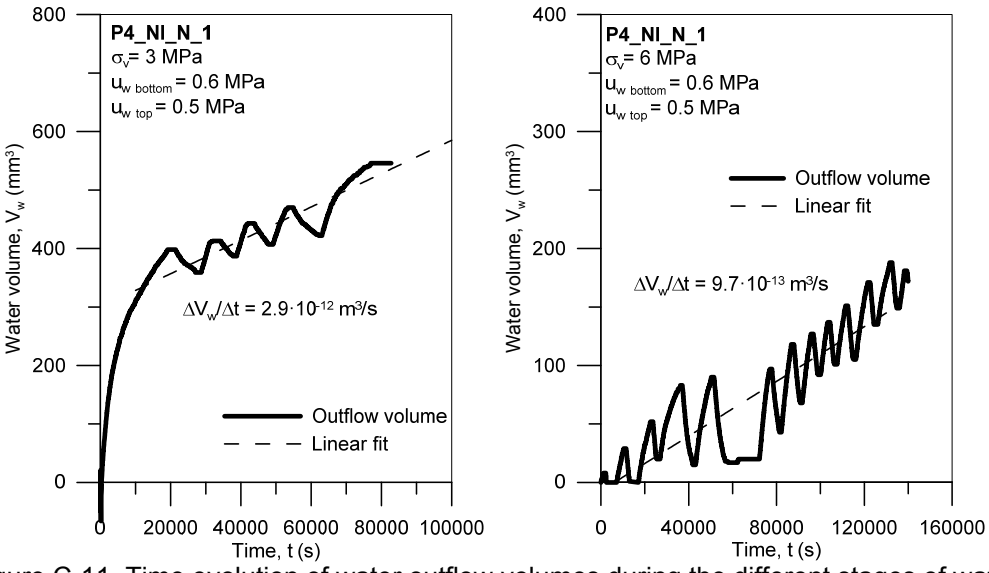

Figure C-11. Time evolution of water outflow volumes during the different stages of water injection for P4_NI_N_1.

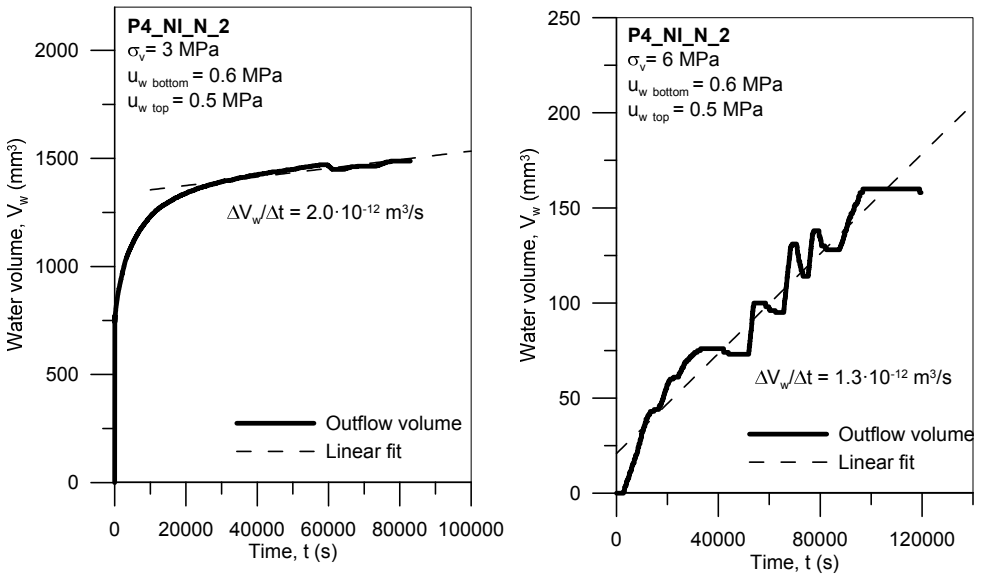

Figure C-12. Time evolution of water outflow volumes during the different stages of water injection for P4_NI_N_2.

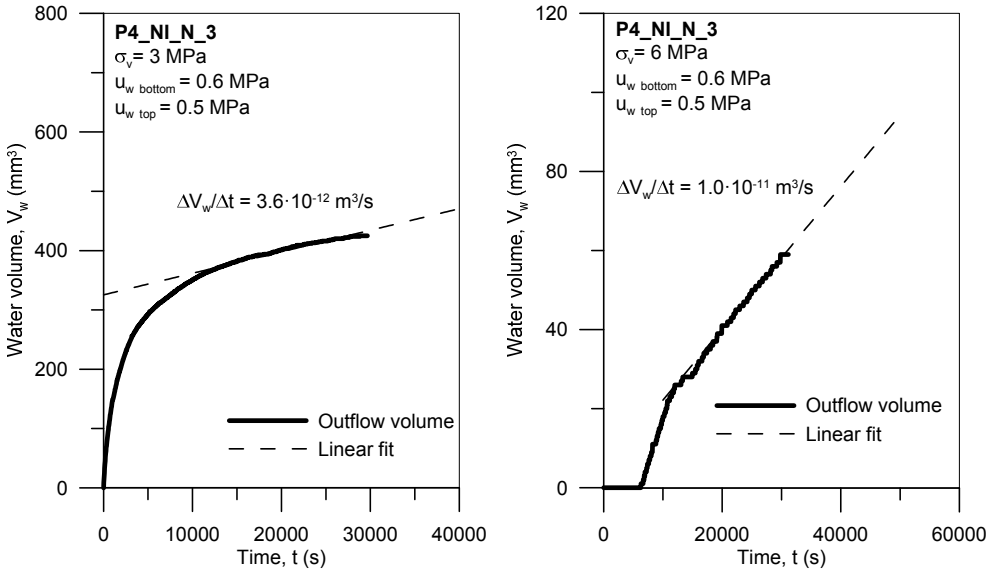

Figure C-13. Time evolution of water outflow volumes during the different stages of water injection for P4_NI_N_3.

C.2. Results for indurated clay samples

Figure C-14 to Figure C-16 show the time evolutions during the different stages of water permeability determination in terms of outflow volume, V_w, and $\Delta V_w/(A \cdot i \cdot \Delta t)$for Opalinus Clay sample, whereas Figure C-17 to Figure C-19 show them for 'Brauner Dogger' sample. For more information see Chapter 4 Section 4.2.3.

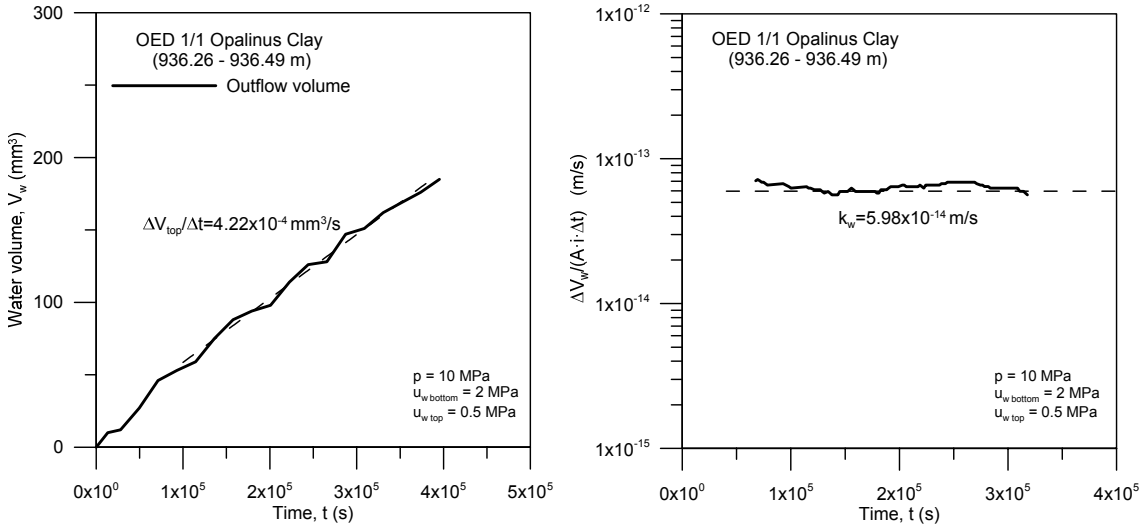

Figure C-14. Time evolution of water volume and permeability at a constant isotropic stress of 10 MPa. OED 1/1 Opalinus Clay sample.

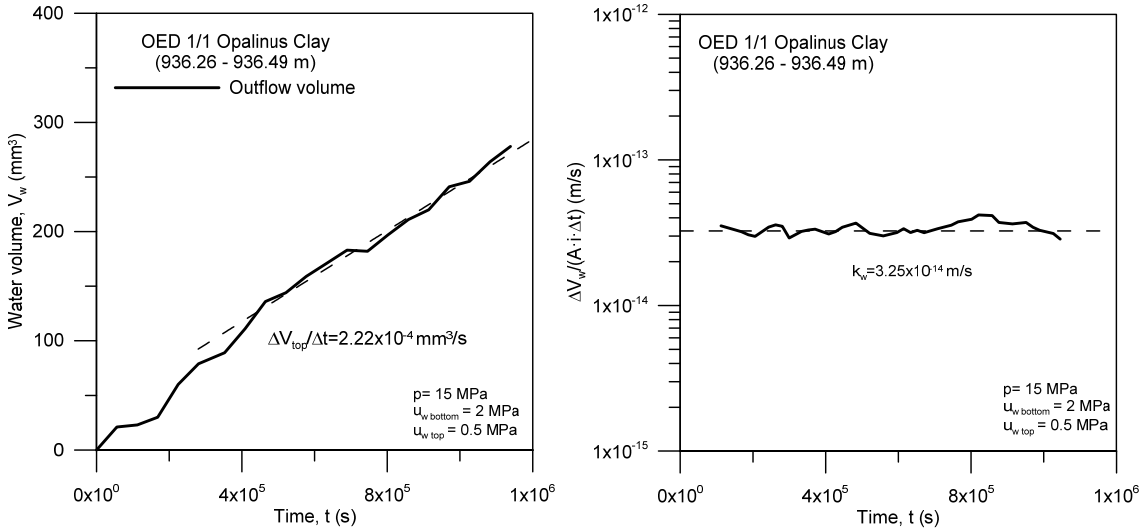

Figure C-15. Time evolution of water volume and permeability at a constant isotropic stress of 15 MPa. OED 1/1 Opalinus Clay sample.

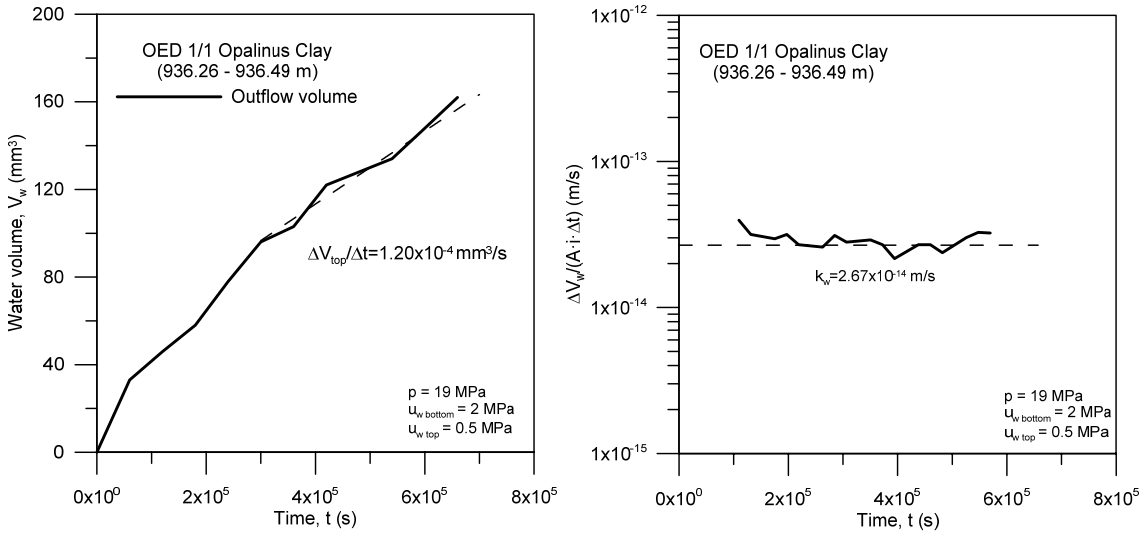

Figure C-16. Time evolution of water volume and permeability at a constant isotropic stress of 19 MPa. OED 1/1 Opalinus Clay sample.

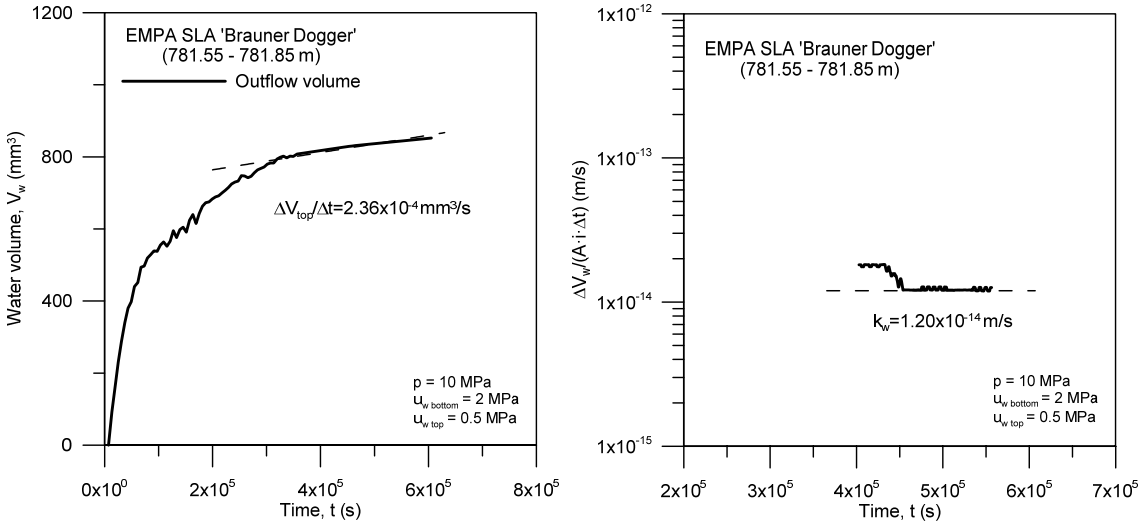

Figure C-17. Time evolution of water volume and permeability at a constant isotropic stress of 10 MPa. EMPA SLA 'Brauner Dogger' sample.

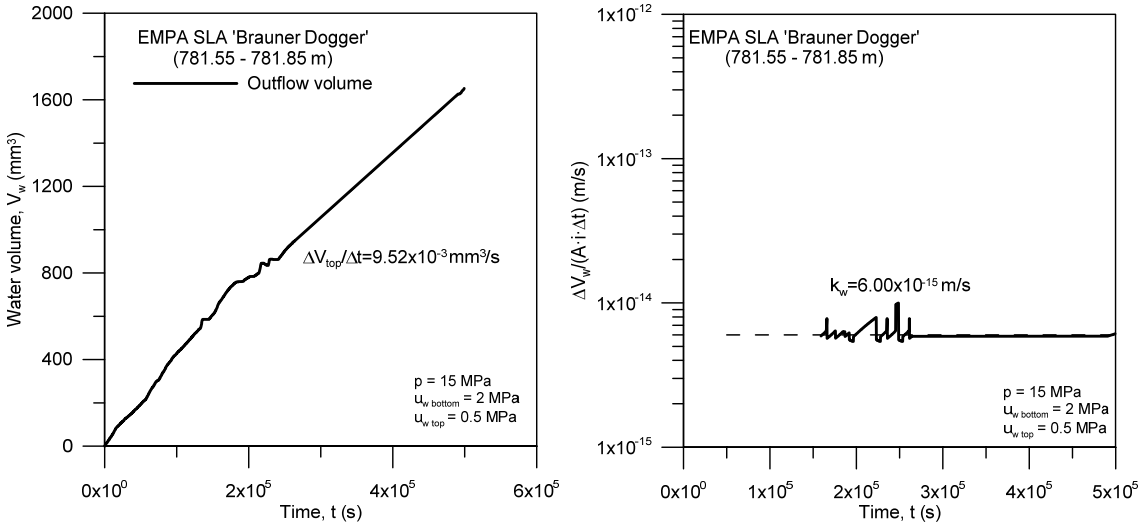

Figure C-18. Time evolution of water volume and permeability at a constant isotropic stress of 15 MPa before first air injection. EMPA SLA 'Brauner Dogger' sample.

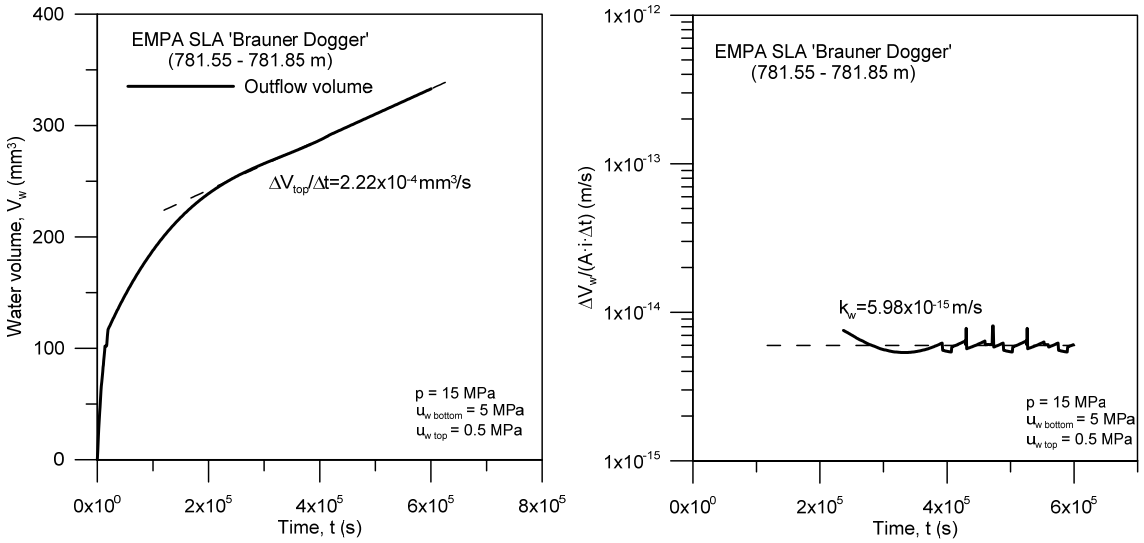

Figure C-19. Time evolution of water volume and permeability at a constant isotropic stress of 15 MPa after first air injection. EMPA SLA 'Brauner Dogger' sample.

Appendix D
RECORDED DATA DURING AIR INJECTION STAGES

This Appendix includes recorded data during the air injection stages on Boom Clay samples (Figure D-1 to Figure D-7) corresponding to low stress protocols which were not explicitly shown in Chapter 5.

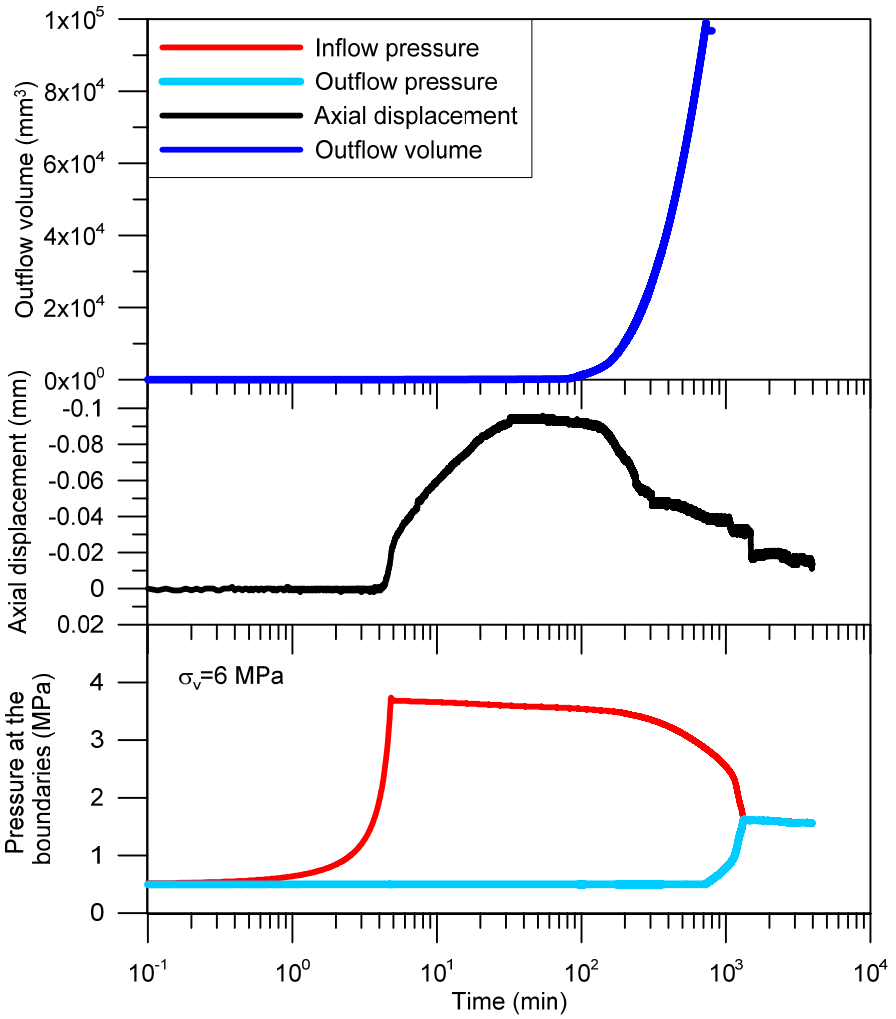

Figure D-1. Measured time evolution of pressures at the injection and recovery boundaries, outflow volume and axial displacements of test P3_FI_N_1.

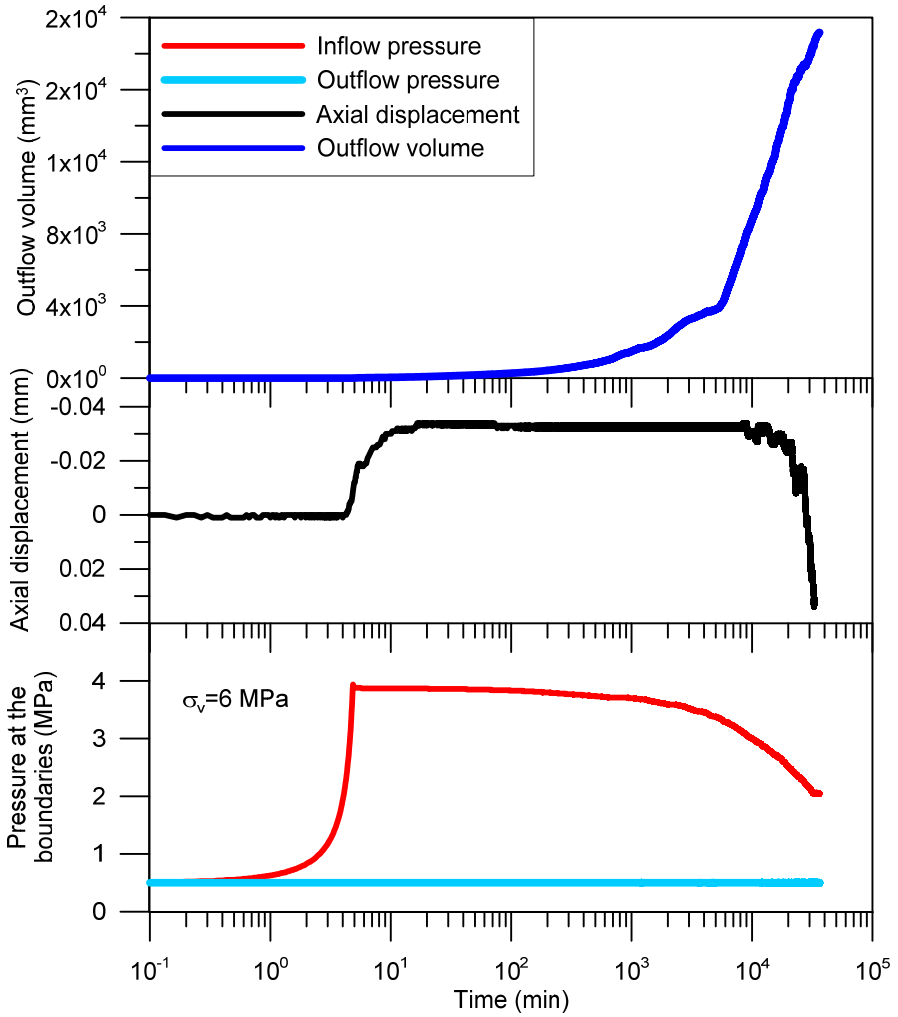

Figure D-2. Measured time evolution of pressures at the injection and recovery boundaries, outflow volume and axial displacements of test P3_FI_P_1.

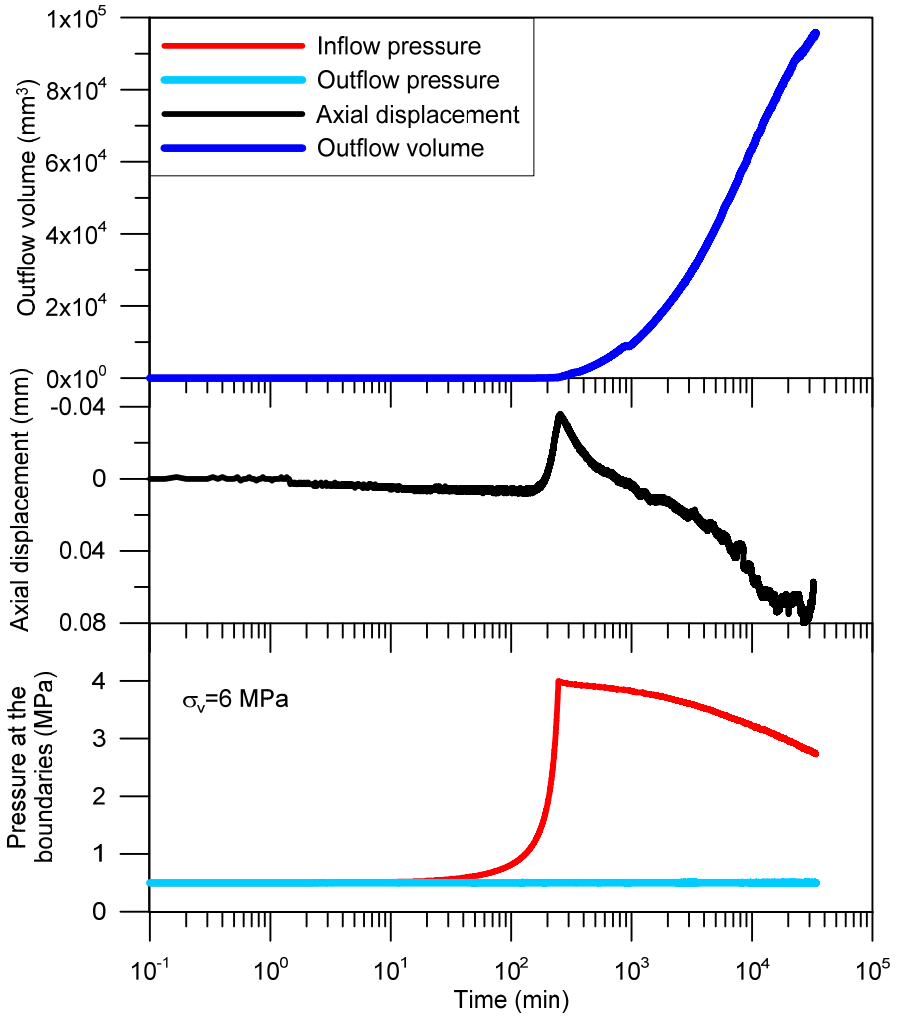

Figure D-3. Measured time evolution of pressures at the injection and recovery boundaries, outflow volume and axial displacements of test P3_SI_N_1.

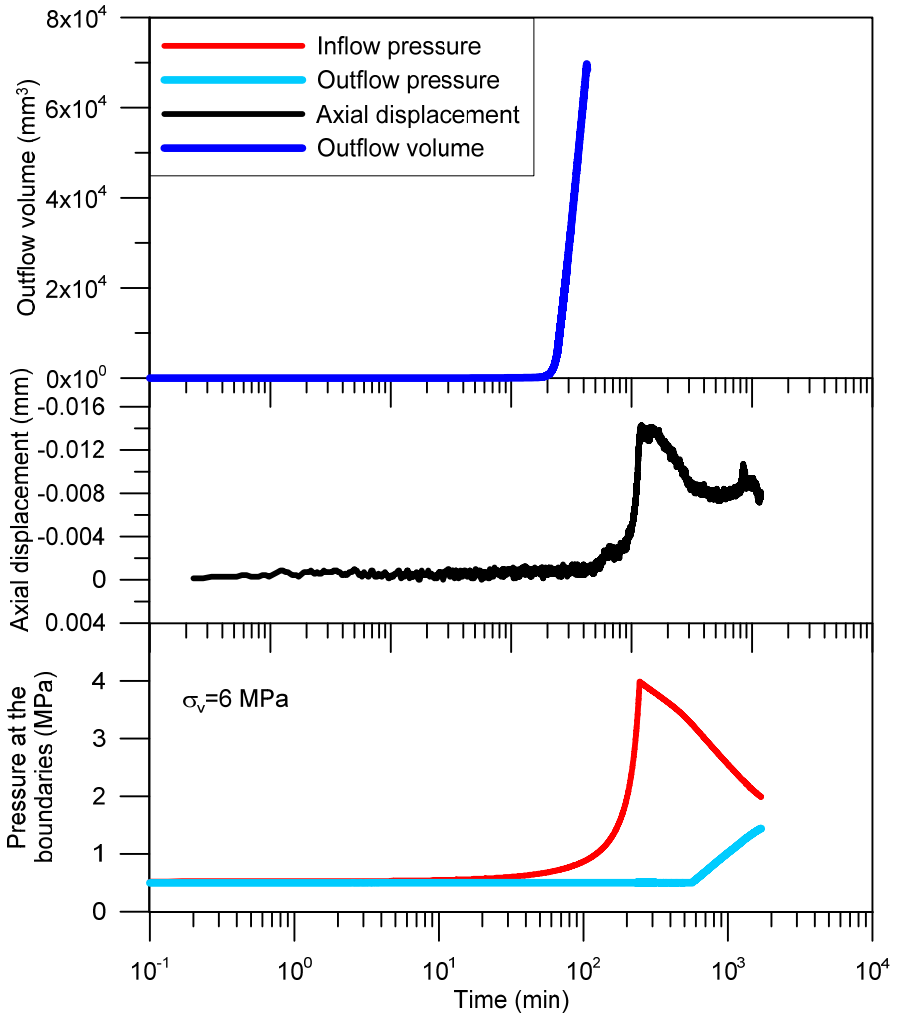

Figure D-4. Measured time evolution of pressures at the injection and recovery boundaries, outflow volume and axial displacements of test P3_SI_P.

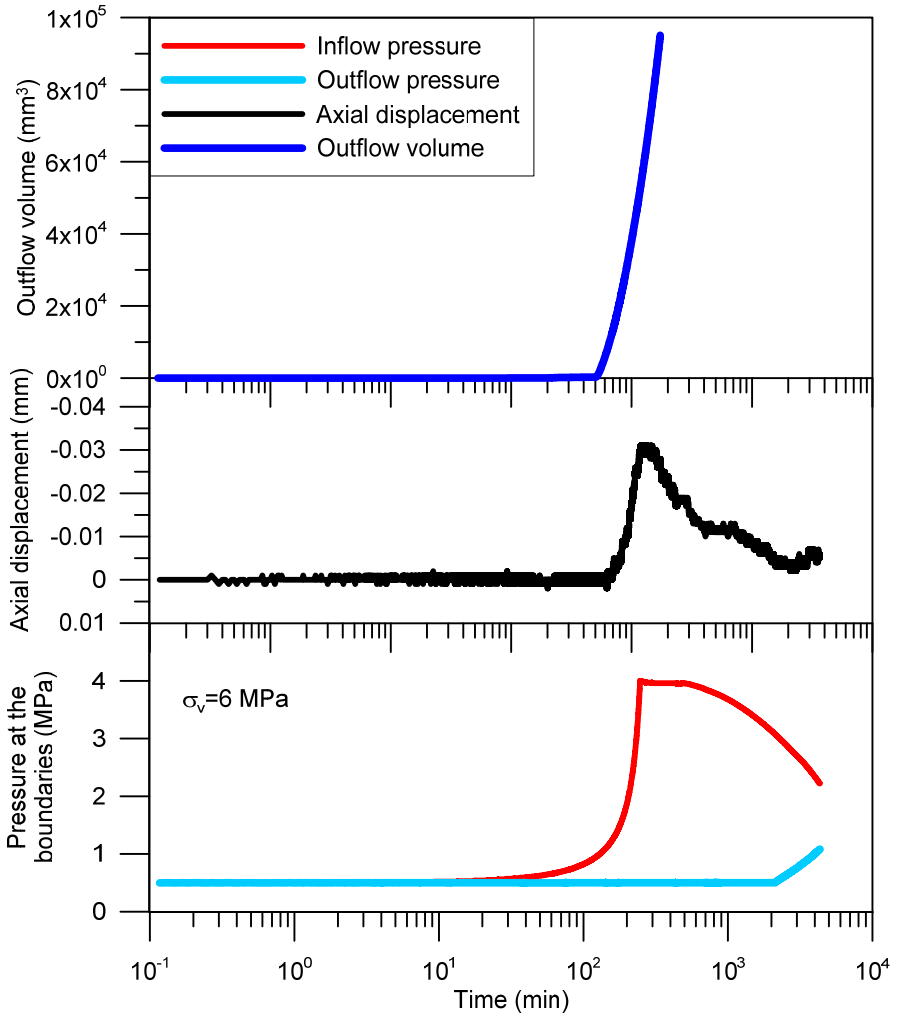

Figure D-5. Measured time evolution of pressures at the injection and recovery boundaries, outflow volume and axial displacements of test P3_SI_N_2.

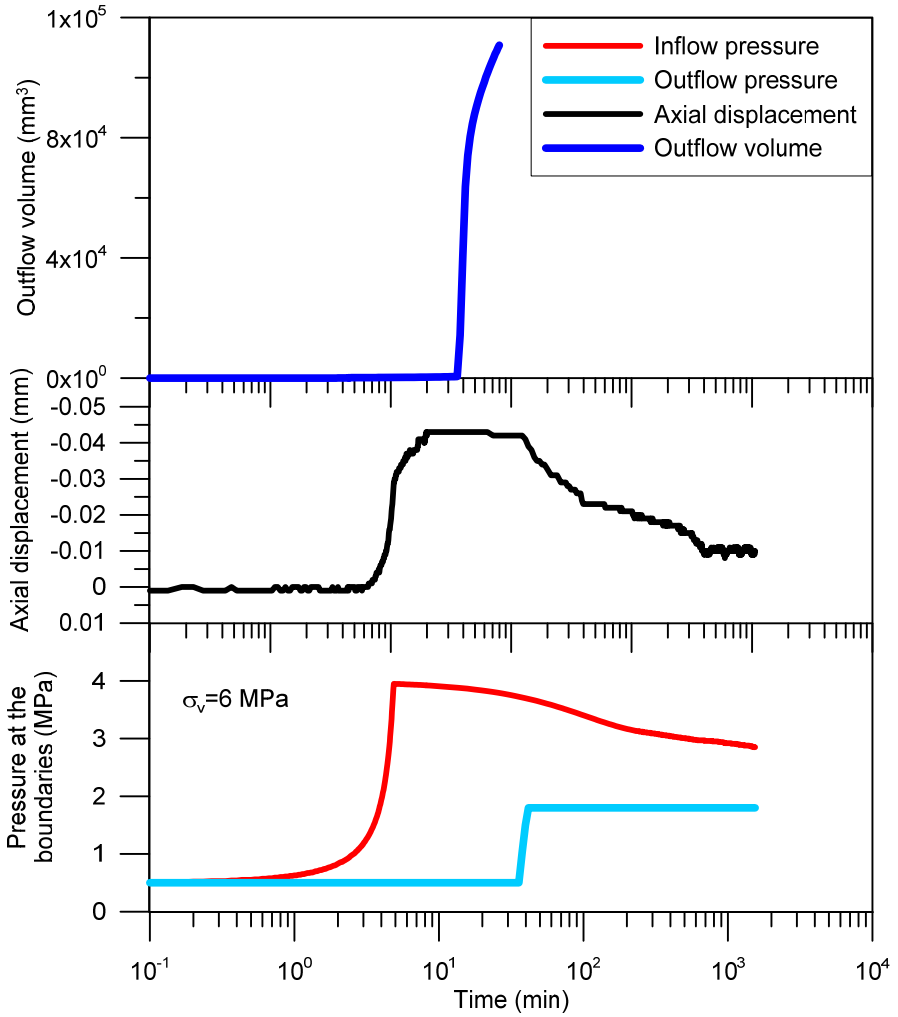

Figure D-6. Measured time evolution of pressures at the injection and recovery boundaries, outflow volume and axial displacements of test P3_FI_P_2.

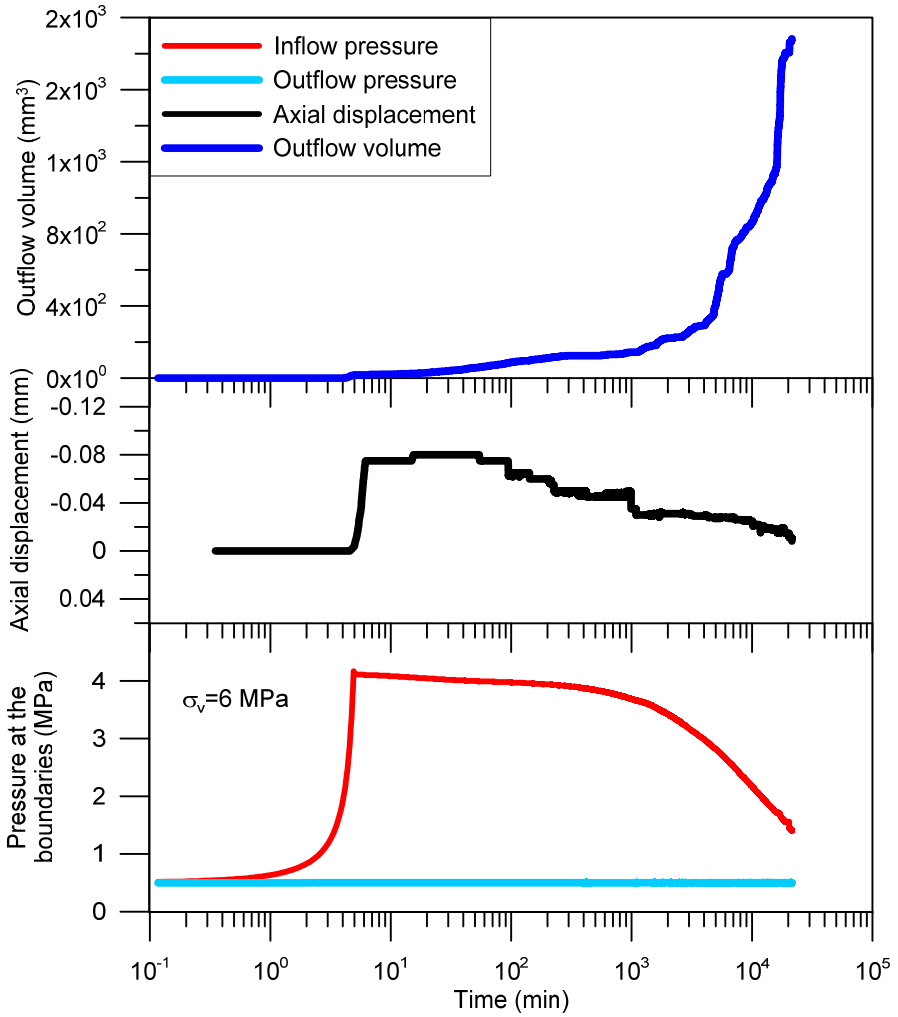

Figure D-7. Measured time evolution of pressures at the injection and recovery boundaries, outflow volume and axial displacements of test P3_FI_N_2.

Appendix E
AIR MASS BALANCE

The mass balance during the air dissipation stage was estimated considering the difference between injected air mass and the outflow air mass for each test (Eq. E.1).

$$m_{stored}(t) = m_{inj}(t) - m_{out}(t) \quad \text{(E.1)}$$

The injected air mass was determined from fitted and measured data (Eq. E.2) as the initial mass inside the system (m_{system}) minus the mass obtained from injection volume and pressure with the perfect gas law at each time ($m_t(t)$).

$$m_{inj}(t) = m_{system} - m_t(t) \rightarrow m_{inj}(t) = \frac{V_0}{\rho_{air}} - \frac{\bar{u}_{in\,meas}(t) M_{ma} V(t)}{RT} \quad \text{(E.2)}$$

where the initial volume of air (V_0) was fitted by considering a constant air mass system (M_a) during the initial stage of fast injection process -least squared method applied to the difference (S in Eq. E.3) between measured absolute air injection ($\bar{u}_{in\,meas}$) (Eq. E.3) and absolute air pressure estimated using perfect gas law ($\bar{u}_{in\,est}$) (Eq. E.4) for a given volume of air (V) at elapsed time (t):

$$S = \sum_{i=1}^{n} (\bar{u}_{in\,meas} - \bar{u}_{in\,est})_i^2 \quad \text{(E.3)}$$

$$\bar{u}_{in\,est} = \frac{M_a}{V M_{ma}} RT \rightarrow V = V_0 - rt \quad \text{(E.4)}$$

where M_{ma} is the molecular mass of dry air mixture (28.966 kg/kmol), R is the universal molar gas constant (8.31432 J/(mol·K)), T is the absolute temperature of test conditions (295.15 K) and r is the injection rate (100 mL/min or 2 mL/min).

Figure E-1 presents the evolution with time of the injected mass of air for some of the tests performed with Protocol 3.

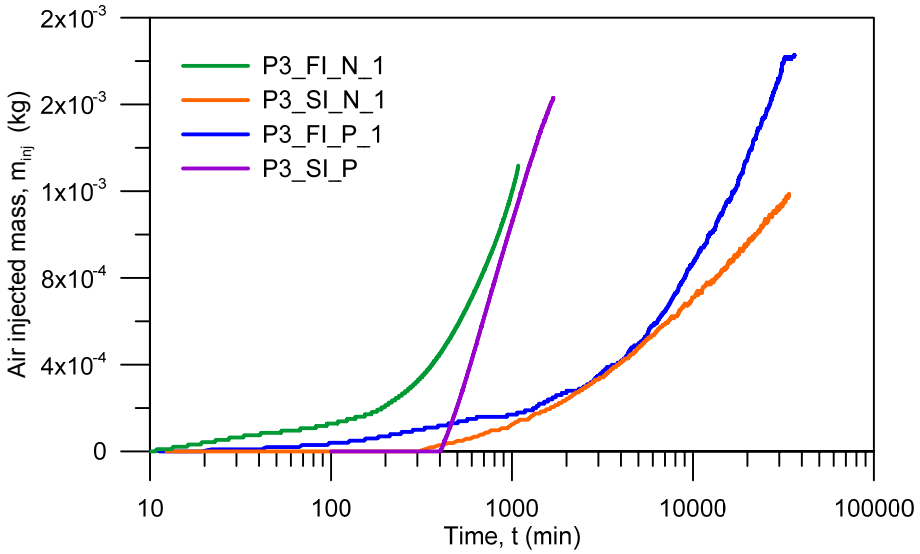

Figure E-1. Time evolution of injected air mass.

The outflow mass ($m_{out}(t)$) (Figure E-2) was calculated with outflow data recorded during the air dissipation stage ($u_{out}(t)$ and $V_{out}(t)$) admitting the perfect gas law (Eq. E.5);

$$m_{out}(t) = \frac{u_{out}(t) M_{ma} V_{out}(t)}{RT} \quad \text{(E.5)}$$

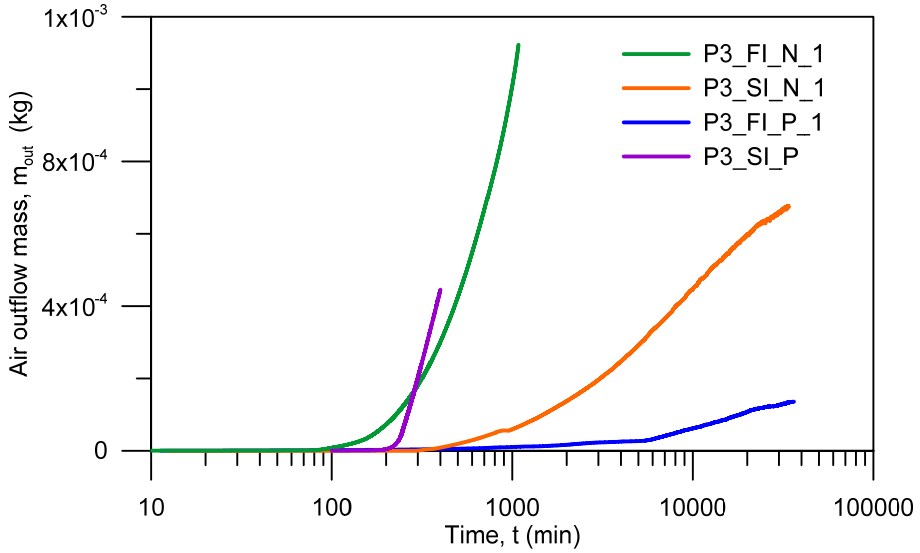

Figure E-2. Time evolution of outflow mass.

Figure E-3 shows the air mass stored in the samples with time. Nevertheless, a simple estimation of the maximum storage capacity of the pores shows that it would imply that all the porosity is filled with air at the end of the experiments. Then, the injected mass should be overestimated or the outflow mass underestimated. These calculations are based on the hypothesis of gas perfect without considering the influence of the pressure or the stress state, and therefore, they do not to fit with the real behaviour

experimentally observed, were the final degree of saturation is very high (between 0.85 and 1).

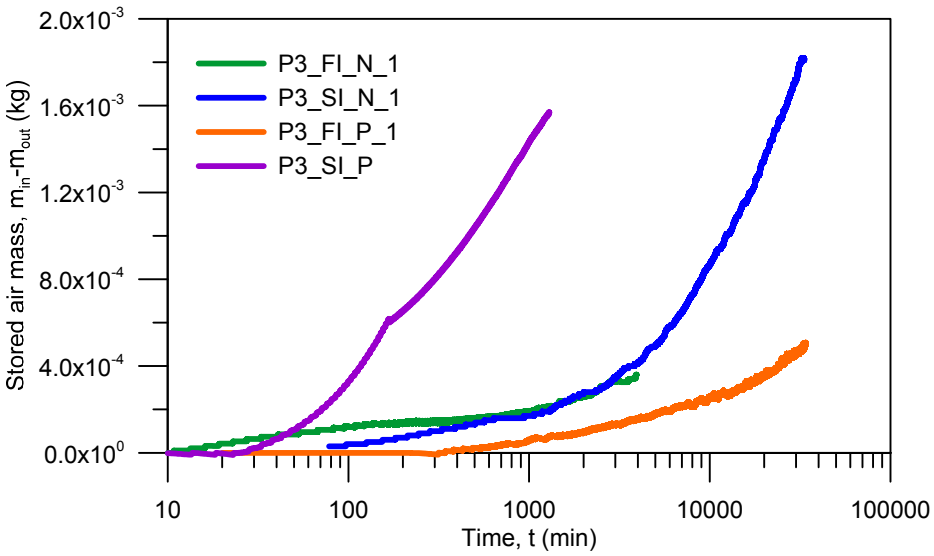

Figure E-3. Stored air mass.